Brunel
UNIVERSITY
LONDON

Genotype and Phenotype Characterisation of Friedreich Ataxia Mouse Models and Cells

A thesis submitted for the degree of Doctor of Philosophy by

Sara Anjomani Virmouni

Division of Biosciences
School of Health Sciences and Social Care
September 2013

Declaration

I hereby declare that the research presented in this thesis is my own work, except where otherwise specified, and has not been submitted for any other degree.

Sara Anjomani Virmouni

ABSTRACT

Friedreich ataxia (FRDA) is an autosomal recessive neurodegenerative disorder, caused by a GAA repeat expansion mutation within intron 1 of the *FXN* gene, resulting in reduced level of frataxin protein. Normal individuals have 5 to 40 GAA repeat sequences, whereas affected individuals have approximately 70 to more than 1000 GAA triplets. Frataxin is a mitochondrial protein involved in iron-sulphur cluster and heme biosynthesis. The reduction in frataxin expression leads to oxidative stress, mitochondrial iron accumulation and consequential cell death with the primary sites of neurons of the dorsal root ganglia and the dentate nucleus of the cerebellum. FRDA, which is the most common inherited ataxia, affecting 1:50,000 Caucasians, is characterised by neurodegeneration, cardiomyopathy, diabetes mellitus and skeletal deformities.

To investigate FRDA molecular disease mechanisms and therapy, several human *FXN* YAC transgenic mouse models have been established: Y47R, containing normal-sized $(GAA)_9$ repeats; YG8R and YG22R, which initially contained expanded GAA repeats of 90-190 units and 190 units, respectively, but which have subsequently been bred to now contain expanded GAA repeats of 120-220 units and 170-260 units, respectively, and YG8sR (YG8R with a small GAA band) that was recently generated from YG8R breeding. To determine the *FXN* transgene copy number in the enhanced GAA repeat expansion-based FRDA mouse lines, a TaqMan qPCR assay was developed. The results demonstrated that the YG22R and Y47R lines had a single copy of the *FXN* transgene while the YG8R line had two copies. The YG8s lines showed less than one copy of the target gene, suggesting potential deletion of the *FXN* gene. Single integration sites of all transgenes were confirmed by fluorescence *in situ* hybridisation (FISH) analysis of metaphase and interphase chromosomes. However, in the YG8s line, at least 25% of the YG8s cells had no signals, while the remaining cells showed one signal corresponding to the transgenic *FXN* gene. In addition, the analysis of *FXN* exons in YG8s rescue mice by PCR confirmed the presence of all *FXN* exons in these lines, suggesting the incidence of somatic mosaicism in these lines.

Extended functional analysis was carried out on these mice from 4 to 12 months of age. Coordination ability of YG8R, YG8sR and YG22R 'FRDA-like' mice, together with Y47R and C57BL6/J wild-type control mice, was assessed using accelerating rotarod

analysis. The results indicated a progressive decrease in the motor coordination of YG8R, YG22R and YG8sR mice compared to Y47R or C57BL6/J controls. Locomotor activity was also assessed using an open field beam-breaker apparatus followed by four additional functional analyses including beam-walk, hang wire, grip strength and foot print tests. The results indicated significant functional deficits in the FRDA mouse models. Glucose and insulin tolerance tests were also conducted in the FRDA mouse models, indicating glucose intolerance and insulin hypersensitivity in the aforementioned lines.

To investigate the correlation between the FRDA-like pathological phenotype and frataxin deficiency in the FRDA mouse models, frataxin mRNA and protein levels as well as somatic GAA repeat instability were examined. The results indicated that somatic GAA repeats increased in the cerebellum and brain of YG22R, YG8R and YG8sR mice, together with significantly reduced levels of *FXN* mRNA and protein in the liver of YG8R and YG22R compared to Y47R. However, YG8sR lines showed a significant decrease in *FXN* mRNA in all of the examined tissues compared to Y47R human *FXN* and C57BL6/J mouse *Fxn* mRNA. Protein expression levels were also considerably reduced in all the tissues of YG8sR mice compared to Y47R.

Subsequently, the telomere length of human and mouse FRDA and control fibroblasts was assessed using qPCR and Q-FISH. The results indicated that the FRDA cells had chromosomes with relatively longer telomeric repeats in comparison to the controls. FRDA cells were screened for expression of telomerase activity using the TRAP assay and a quantitative assay for hTERT mRNA expression using TaqMan qRT-PCR. The results indicated that telomerase activity was not present in the FRDA cells. To investigate whether FRDA cells maintained their telomeres by ALT associated PML bodies (APBs), co-localisation of PML bodies with telomeres was assessed in these cells using combined immunofluorescence to PML and Q-FISH for telomere detection. The results demonstrated that the FRDA cells had significantly higher co-localised PML foci with telomeric DNA compared to the normal cells. Moreover, telomere sister chromatid exchange (T-SCE) frequencies were analysed in the human FRDA cell lines using chromosome orientation FISH (CO-FISH). The results indicated a significant increase in T-SCE levels of the FRDA cell lines relative to the controls. Furthermore, growth curve and population doubling analysis of the human FRDA and control fibroblasts was carried out. The results showed that the FRDA fibroblast cell cultures

underwent growth arrest with higher cumulative population doubling compared to the controls. Though, further analysis of telomere length at different passage numbers revealed that the FRDA cells lost telomeres faster than the controls. Finally, the telomere dysfunction-induced foci (TIF) assay was performed to detect DNA damage in the human FRDA fibroblast cells using an antibody against DNA damage marker γ-H2AX and a synthetic PNA probe for telomeres. The frequency of γ-H2AX foci was significantly higher in the FRDA cells compared to the controls. Similarly, the FRDA cells had greater frequencies of TIFs in comparison to the controls, suggesting induced telomere dysfunction in the FRDA cells.

ACKNOWLEDGEMENTS

I would like to express my deepest gratitude to Dr. Mark Pook for his supervision, advice and guidance and also for his encouragement in the loneliest of times.

I would also like to thank Dr. Predrag Slijepcevic, Dr. Christopher Eskiw, Dr. Sahar Al-Mahdawi, Dr. Terry Roberts and Dr. Hemad Yasaei whose excellent supervision, support, guidance and expertise have helped me greatly with the design and interpretation of my experiments. I am also very grateful for Dr. Evgeny Makarov's continual support and advice as my second supervisor throughout the project.

I would like to thank my colleagues Dr. Chiranjeevi Sandi, Dr. Vahid Ezzatizadeh and Madhavi Sandi for their continual assistance during my study. I would also like to express my appreciation to Dr. Matthew Themis, Christine Newton and Alison Marriott for their incessant support, advice and assistance and all the other technical staff who have contributed to this work in many ways. I would also like to thank my friends Julie Davies, Azadeh Motevalli and Abdulbasit Naiel, and other PhD students who have helped me during my PhD.

Finally, I would like to thank my family and my husband Dr. Mohammad Reza Herfatmanesh for their continual support and endless love throughput this project.

TABLE OF CONTENTS

LIST OF FIGURES

CHAPTER I

CHAPTER II

CHAPTER III

CHAPTER IV

CHAPTER V

APPENDIX

LIST OF TABLES

LIST OF ABBREVIATIONS

aCGH	array Comparative Genomic Hybridisation	gDNA	Genomic Deoxyribonucleic Acid
AFT1	Activator of Iron Transcription	GWAS	Genome Wide Association Studies
ALT	Alternative Lengthening of Telomeres	H_2O	Water
APBs	ALT Associated Promyelocytic Leukemia Bodies	HAT	Histone Acetyltransferase
B6	C57BL/6J	HCl	Hydrochloric Acid
BAC	Bacterial Artificial Chromosome	HDACi	Histone Deacetylase Inhibitors
bp	Base Pair	HMTase	Histone Methyltransferase
BCA	Bicinchoninic Acid	HPA	Hybridisation Protection Assay
BSA	Bovine Serum Albumin	HR	Homologous Recombination
cDNA	Complementary DNA	HSC	Haematopoietic Stem Cell
ChIP	Chromatin Immunoprecipitation	hTERT	Human Telomerase Reverse Transcriptase
CNS	Central Nervous System	hTR	Human Telomerase RNA
CNV	Copy Number Variation	ISPs	Iron-Sulphur Cluster-Containing Proteins
CO-FISH	Chromosome Orientation FISH	IR	Ionizing Radiation
CoQ_{10}	Coenzyme Q_{10}	IRP1	Iron Regulatory Protein 1
CPD	Cumulative Population Doubling	IRS	Insulin Receptor Substrate
DAPI	4´,6-Diamidino-2-Phenylindole Dihydrochloride	KCl	Potassium Chloride
DDR	DNA Damage Response	MGB	Minor Groove Binder
DMEM	Dulbecco's Modified Eagle Medium	$MgCl_2$	Magnesium Chloride
DNA	Deoxyribonucleic Acid	MIP	Mitochondrial Intermediate Peptidase
dNTPs	Deoxynucleotide Triphosphate	MPP-β	Mitochondrial Processing Peptidase
DRG	Dorsal Root Ganglia	mRNP	Messenger Ribonucleoprotein
ds	Double-Stranded	NaCl	Sodium Chloride
DSBs	Double-Strand Breaks	NCS	Newborn Calf Serum
dsRNA	Double-Stranded RNA	NFQ	Nonfluorescent Quencher
ECTR	Extra-Chromosomal Telomeric DNA	NMR	Nuclear Magnetic Resonance
EDTA	Ethylene Diamine Tetra-Acetic Acid	nt	Nucleotides
EPC	Endothelial Progenitor Cell	NTC	No Template Control
EtBr	Ethidium Bromide	OH•	Hydroxyl Radical
FBS	Fetal Bovine Serum	PBL	Peripheral Blood Lymphocytes
Fe-S	Iron- Sulphur	PBS	Phosphate Buffered Saline
FMR 1	Fragile X Mental Retardation-1	PCR	Polymerase Chain Reaction
FITC	Fluorescein Isothiocyanate	PD	Population Doublings
FISH	Fluorescence *in situ* Hybridisation	PEV	Positive Effect Variegation
FRDA	Friedreich Ataxia	PML	Promyelocytic Leukemia
FXN	Human Frataxin	PNA	Peptide Nucleic Acid
Fxn	Mouse Frataxin	Q-FISH	Quantitative FISH
FXS	Fragile X Syndrome	qPCR	quantitative PCR
GDAS	Gel Documentation Analysis System	rcf	Relative Centrifugal Force

rhuEPO	Recombinant Human Erythropoietin
RNA	Ribonucleic Acid
RNase	Ribonuclease
RNAPol	RNA Polymerase
RNP	Ribonucleo Proteins
ROS	Reactive Oxygen Species
rpm	Revolutions Per Minute
RQ	Relative Quantitation
RT	Room Temperature
RT	Reverse Transcriptase
RT-PCR	Reverse Transcriptase PCR
SDS	Sodium Dodecyl Sulfate
SNP	Single Nucleotide Polymorphism
SOD	Superoxide Dismutase
ss	Single-Stranded
ssDNA	Single-Stranded DNA
TBE	Tris-Borate EDTA
Tert	Telomerase Reverse Transcriptase
TIF	Telomere Dysfunction-Induced Foci
T_m	Melting Temperature
TR	Triplet Repeat
TRAP	Telomeric Repeat Amplification Protocol
TRD	Telomere Rapid Deletion
TRF	Telomeric Restriction Fragment
Tris-HCl	Hydroxymethyl Aminomethane-HCl
T-SCE	Telomere-Sister Chromatid Exchange
STELA	Single Telomere Length Analysis
WT	Wild-Type
YAC	Yeast Artificial Chromosome
YFH1	Yeast Frataxin Homologue 1

CHAPTER I

GENERAL INTRODUCTION

1.1 History

In 1853, Nicholaus Friedreich, a German physician, described a degenerative atrophy of the posterior columns of the spinal cord leading to progressive ataxia, sensory loss, muscle weakness, often associated with scoliosis, foot deformity and cardiomyopathy. His publications in 1866 and 1867 further confirmed his previous work on the discovery of a new disease entity while some critics, particularly Charcot, had assumed that Friedreich's patients had tabes, associated with neurosyphilis [1-3]. Friedreich identified all the essential clinical and pathological features of the disease except the loss of deep tendon reflexes, which was later described by Erb in 1885. Brousse termed the new disease *Friedreich's ataxia* (currently abbreviated FRDA) in 1882 [2, 3]. In the late 1970s, Quebec Collaborative Group and Harding established the clinical features of the typical FRDA specifically recessive inheritance as an essential feature of FRDA [4, 5].

1.2 Clinical and Pathological Features

1.2.1. Epidemiology

FRDA is a progressive neurodegenerative disease inherited as an autosomal recessive trait with an estimated prevalence of 1 in 50,000 Caucasians [6]. It is the most common form of the hereditary ataxias accounted for half of the whole heredodegenerative ataxia cases and three-quarters of those with onset before age 25 [7]. The carrier rate has been approximated at 1:120-1:60 [6, 8, 9].

1.2.2. Pathology

FRDA is a progressive disease that initiates with gait abnormality within patients ranging from 2-3 years of age to later than 25 years of age. The essential clinical features of FRDA are autosomal recessive inheritance, onset before 25 years of age, progressive ataxia of gait and limbs, loss of tendon reflexes in the lower extremities, electrophysiologic evidence of axonal sensory neuropathy (within 5 years of onset), dysarthria, extensor plantar responses, areflexia at all four limbs, muscle wasting and loss of sensation, especially of vibration and joint position sense. Patients lose their ability to walk on average 15 years after onset and may be confined to a wheelchair in their early teens [3, 10].

There may be other clinical features, as the disease progresses, including nystagmus (involuntary rhythmic oscillations of the eyeballs, characterised by a smooth pursuit in

one direction and a fast movement in the opposite direction), saccadic-pursuit eye movements (rapid correction eye movements to redirect the line of site during smooth pursuit of an object), difficulty with swallowing and breathing as well as cardiomyopathy, diabetes mellitus and skeletal deformities [1, 3, 11, 12]. Some patients can develop optic atrophy (25%) and sensorineural hearing loss (20%) [13]. Slower disease progression is often observed in patients with late onset FRDA whereby tendon reflexes are often retained [11, 14-16]. Spinal cord atrophy associated with atrophy of the brainstem and cerebellum was detected in patients with typical and late onset FRDA using magnetic resonance imaging [17-20].

The neuropathologic discoveries differentiate FRDA from other hereditary ataxias. Degeneration of the posterior columns of the spinal cord is considered an early finding [13]. The posterior columns consist of the central branches of the axons of large dorsal root ganglia (DRG) sensory neurons. These axons extend and form the gracile (Goll) and Cuneate (Burdach) tracts which originate at the lumbosacral level and from cervicothoracic segments respectively. Demyelination, loss of fibers and fibrillary gliosis are more severe in the Goll than in the Burdach tract, indicating that the fibers originating from neurons located caudally are more severely affected. Atrophy in the spinocerebellar tracts is also observed, resulting in the dorsal being more affected than the ventral [6, 13, 20, 21]. Clarke's column, where the spinocerebellar tracts originate, is atrophied; whereas motor neurons in the ventral horns are unaffected. On the other hand, the long crossed and uncrossed corticospinal motor tracts are atrophied. In the brainstem, where the dorsal column tracts terminate, the gracile and cuneate nuclei, indicating transsynaptic degeneration with intense gliosis. The long tracts of fibers, particularly the corticospinal fibers, are severely atrophic in distal portions, suggesting a dying-back process. The entering roots of cranial sensory nerves are affected while cranial nerve nuclei remain normal. Cerebellar atrophy is not a major characteristic of FRDA. The cerebellum cortex shows Purkinje cell loss, typically late in the course of the disease. Conversely, the dentate nuclei are severely affected. Loss of pyramidal (Betz) cells in the primary motor areas of the cerebral cortex is observed provided that the pyramidal tract atrophy is advanced. In the peripheral nervous system, sensory axonal polyneuropathy is a characteristic of FRDA. The marked loss of large myelinated fibers has been observed in the peripheral nerves and also in the DRG cells. The features of the changes in the peripheral nerve system are not well understood.

Previous studies have indicated that there is a maturational defect in specific neurons that remain hypotrophic and subsequently die back gradually [22].

Enlargement of the heart accompanied by the thickening of the ventricular walls and interventricular septum leads to arrhythmias and heart failure, the most common causes of death in the majority of FRDA patients. The pathology of the cardiac degeneration consists of interstitial fibrosis, hypertrophy and degeneration of cardiac cells, muscle necrosis and intracellular accumulation of lipofuscin, iron and calcium deposits. In addition, diabetes mellitus associated with a decrease in the number of pancreatic β cells, is also observed in 10% of the patients [1, 4, 11, 23-25]. Furthermore, skeletal deformities are very common in FRDA patients including pes cavus (hammer toes) and kyphoscoliosis (abnormal lateral and posterior curvature of the vertebral column) [4, 11].

1.3 Identification of the FRDA Gene

The primary mapping of the FRDA gene was accomplished in 1988 by Chamberlain *et al.* [26]. The FRDA gene was mapped to chromosome 9 by linkage analysis in 20 families with at least three affected sibs. The locus was mapped with a closely linked marker at 9q13-q21.1, providing a region small enough for identification of candidate gene [27, 28]. The FRDA gene, initially referred to as *X25*, was one of the expressed genes in this region, identified by complementary DNA selection and sequence analysis. A mutation in *X25* was screened in a number of patients which resulted in the identification of an expanded trinucleotide repeat (GAA) within the first intron of the FRDA gene [6]. This gene encodes the protein called *Frataxin* which plays a crucial role in the development of FRDA.

1.4 Location and Structure of FRDA Gene

The Frataxin gene is located on the long arm (q) of chromosome 9 between the Giemsa bands 13 and 21.1 precisely from base pair 71,650,478 to base pair 71,715,093, Fig. 1.1 [6, 27, 29].

The FRDA gene is composed of seven exons, numbered 1 to 5a, 5b and 6, spread over 95kb of genomic DNA. Transcription goes in the centromere to telomere direction, Fig. 1.2. The major transcript, exons 1 to 5a, is a 1.3kb mRNA that encodes a 210 amino acid protein called *frataxin*. Exon 5b as a result of alternative splicing can be

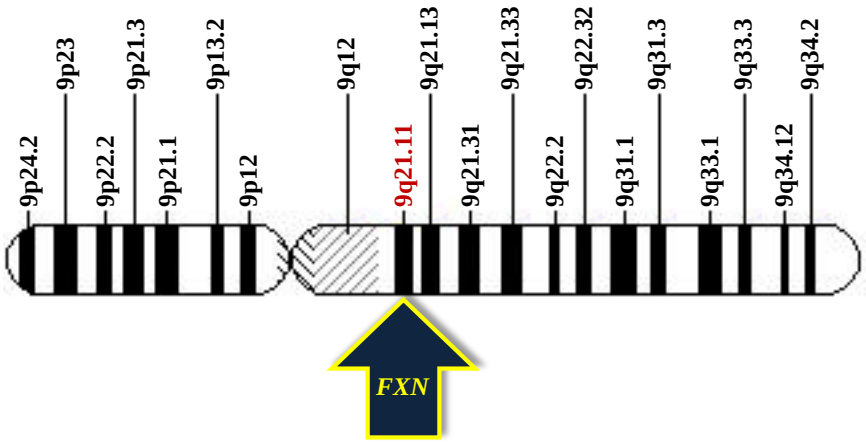

Fig. 1.1 Schematic representation of human chromosome 9. The blue arrow indicates the location of frataxin gene.

transcribed, leading to the synthesis of different protein isoforms. Exon 6 is entirely noncoding [6, 30].

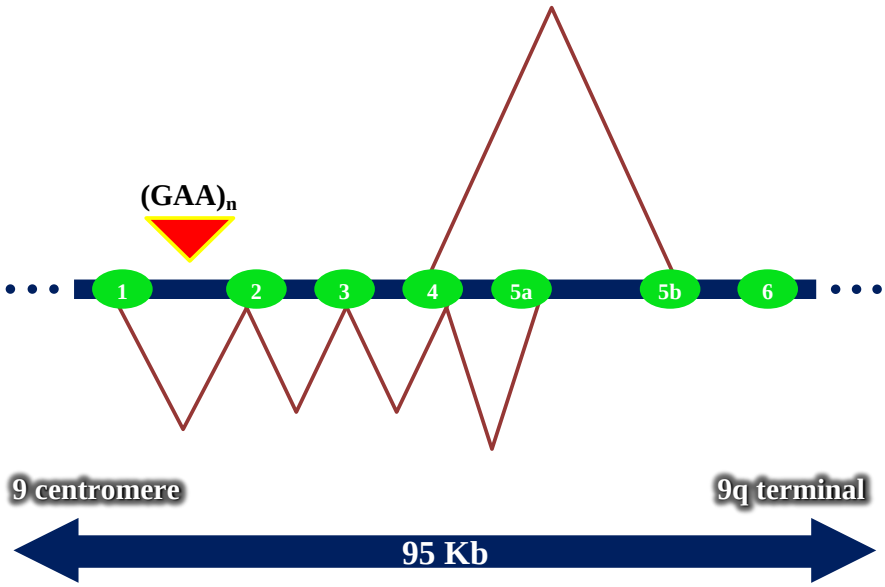

Fig. 1.2 Schematic representation of exons and splicing pattern of the *FXN* gene. The gene extends from centromere to telomere of the 9q chromosome. The GAA repeats are located in intron1, represented by the red triangle.

The FRDA gene demonstrates tissue-specific levels of expression. Among adult human, frataxin mRNA is considerably expressed in heart and central nervous system; intermediate levels in liver, skeletal muscle and pancreas; and minimal levels in other tissues. In the central nervous system (CNS), expression of frataxin appears to be the highest in the spinal cord, with less expression in the cerebellum and very little in the cerebral cortex [6, 31].

1.5 Gene Mutations in FRDA

1.5.1 Trinucleotide Repeat Expansion

In 98% of FRDA chromosomes, an abnormal trinucleotide repeat expansion (GAA) occurs within the first intron of the frataxin gene [6]. This intron is 12kb in size and the triplet repeat is localised within an Alu sequence, 1.4kb after exon 1. Normal chromosomes contain between 5 and 40 triplets [32], whereas FRDA chromosomes contain 70 to 1700 repeats [11]. The GAA expansion forms a triple helical DNA or R-loop structures which inhibits transcription of the FRDA gene by inducing heterochromatin formation, resulting in reduced frataxin levels [33, 34].

1.5.2 Point Mutations

Point mutations in the frataxin gene are a rare cause of FRDA. In all cases characterised so far, only 4% of affected individuals were heterozygous for their point mutation, with an expanded GAA repeat on the other homologue of chromosome 9. None of these patients harboured point mutations on both alleles [35-37].

The most common point mutations are I154F, M1I and G130V. Patients with the I154F mutation have a typical FRDA phenotype, whereas the other cases give rise to atypical phenotypes. Therefore, it can be concluded that point mutations associated with loss of functional frataxin protein result in a severe phenotype, whereas for other missense mutations, the severity of the disease course cannot be predicted [8, 29].

1.6 Origin of the Expanded GAA Repeat

Although, the origins of the GAA repeat expansion and its effects on frataxin expression are not fully understood, it has been manifested that alleles at the GAA repeat site depending on their length can be subdivided into three classes: short normal alleles (82%, containing 5-9 triplets), long normal (17%, containing 10-40 triplets) and pathological expanded alleles (1%, > 70 triplets). The length polymorphism of normal GAA alleles may be generated by small changes most likely due to occasional events of polymerase “stuttering” during DNA replication. Such small changes may cause limited size heterogeneity within the short normal and the large normal alleles. The jump from the short normal to the long normal group can be considered as a singular event with a rare recurrence. The linkage disequilibrium studies of the GAA repeat with different haplotype markers indicated that pathological expanded and long normal alleles are

genetically homogenous and related, whereas short normal alleles appear heterogeneous [30, 38, 39].

1.7 Effect of the GAA Repeat Expansion on Frataxin Gene Expression

FRDA can be defined as a deficiency of frataxin. The expanded GAA repeat has been shown to cause this deficiency by suppressing FRDA gene expression, Fig. 1.3. The data obtained from ribonuclease (RNase) protection assays in individuals with FRDA revealed a severe reduction in the level of mature frataxin mRNA proportional to the size of GAA repeats [30]. Western blot analysis of frataxin in FRDA patients also confirmed a severe frataxin deficiency inversely proportional to the expansion sizes, providing a biological basis for the correlation between expansion sizes and phenotypic features [40, 41].

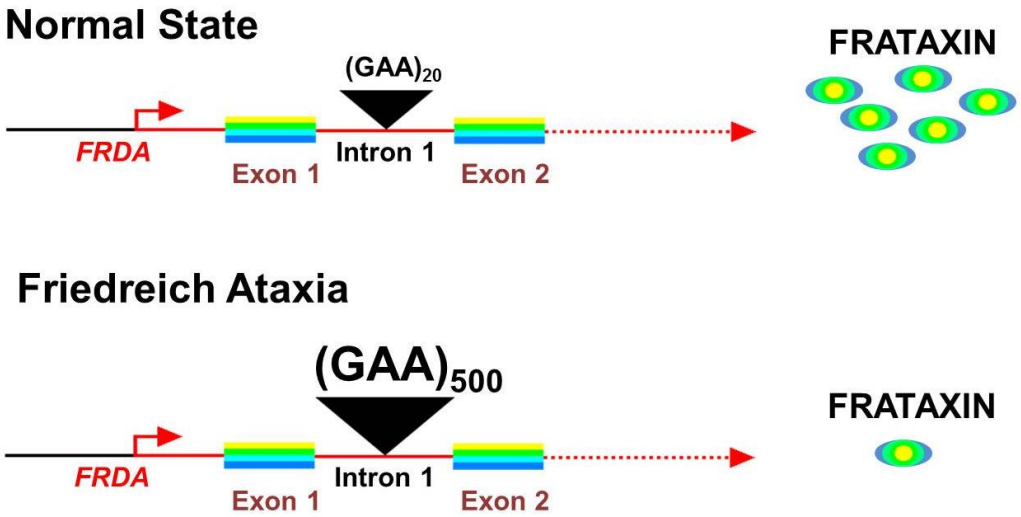

Fig. 1.3 Schematic presentation of the frataxin expression. Normal state indicates more frataxin protein, whereas affected state (FRDA) shows less frataxin.

1.8 Genotype-Phenotype Correlation

In the same manner as in the other repeat disorders, the size of the expanded repeat in FRDA is inversely related to age of onset and disease severity. However this correlation is more complex in FRDA than that in dominant or X-linked triplet-repeat diseases, since FRDA patients have two expanded alleles, whereas those suffering from dominant diseases only have one expanded allele. The size of the smaller FRDA allele is strongly correlated with age at onset and with the rate of disease progression. Montermini *et al.* reported a negative correlation between age at onset and the number of the repeats in both small and large alleles. Their results indicated that FRDA patients with larger

expansions tended to exhibit earlier onset whereas late-onset FRDA patients exhibited smaller alleles [32]. The relatively low correlation coefficients between disease severity and the GAA repeat expansion size indicate that other factors including somatic mosaicism, genetic and environmental modifiers may influence the phenotypic heterogeneity [8, 11, 32].

1.9 Role of Frataxin in Mitochondria

The mitochondrion is an essential organelle for cellular biochemistry and ATP generation as well as being a well-known location for dynamic electron transport and redox chemistry. Heme and iron-sulphur (Fe-S) cluster biosynthesis are the two major iron-related metabolic processes in the mitochondrion for the safe delivery, storage and usage of iron. Frataxin is a mitochondrial protein that is perceived as an important factor in either mitochondrial iron transport or iron-sulphur assembly and transport [42].

Homologous proteins of human frataxin have been identified in mouse and yeast with 73% and 31% amino acid sequence identity respectively, providing further insight into FRDA pathogenesis [43]. YFH1 is a yeast frataxin homologue that encodes a 174 amino acid protein with homology to frataxin, especially at the C-terminus, localised to the mitochondria. Studies of yeast strains deficient in YFH1 demonstrated that the frataxin is involved in mitochondria iron homeostasis [44]. In yeast, the AFT1 transcription factor regulates iron utilisation and homeostasis at the transcriptional level. This is mainly attributed to the activation of AFT1 in iron-poor media, resulting in an increased cytosolic iron level or inactivation in high cytosolic iron level in iron-rich media [45]. In yeast strains deficient cells, AFT1 is activated in both iron-poor and iron-rich medium, indicating low levels of cytosolic iron in these cells compared to wild-type cells. Hence, iron passes the plasma membrane into the cytosol through an activated high affinity transporter which ultimately leads to the mitochondrial iron accumulation. Such mechanism suggests that frataxin may be involved in iron transport either by regulating release of mitochondrial iron to the cytoplasm or by inhibiting iron transport into the mitochondria [45].

Molecular and biochemical analysis of fibroblasts from FRDA patients manifested mitochondrial iron overload in contrast to control cells [46]. Endomyocardial biopsies from these patients have shown a generalised deficiency of Fe-S cluster-containing proteins (ISPs) (i.e. respiratory chain complexes I, II and III; and mitochondrial and

cytosolic aconitase), reduced level of mitochondrial DNA and increased activity of iron regulatory protein 1 (IRP1) [47-49, 50, 51]. A similar deficiency in the activity of ISPs has been observed in heart muscle of conditional frataxin knockout mice. Since ISPs are very sensitive to reactive oxygen species (ROS), deficiency in the activity of ISPs suggests oxidative damage in frataxin deficient tissues [42, 52, 53]. Mitochondrial iron can react with ROS and generate more toxic ROS such as hydroxyl radical (OH•) via the Fenton reaction leading to the oxidation of cellular compounds, Fig. 1.4. Increased iron levels in conjunction with defects in respiratory chain complexes result in free-radical accumulation, ultimately leading to cellular injury and death [47]. According to results from mouse models, deficiencies in ISPs occur in the initial phase of the pathology, whereas mitochondrial iron accumulation occurs later, indicating that mitochondrial iron accumulation cannot be the causative pathological mechanism. Moreover, low superoxide dismutase (SOD) induction observed in the diseased mouse confirms that either decreased or absent frataxin impairs early antioxidant defences with no SOD induction resulting in higher cell lethality in response to oxidative stress [54].

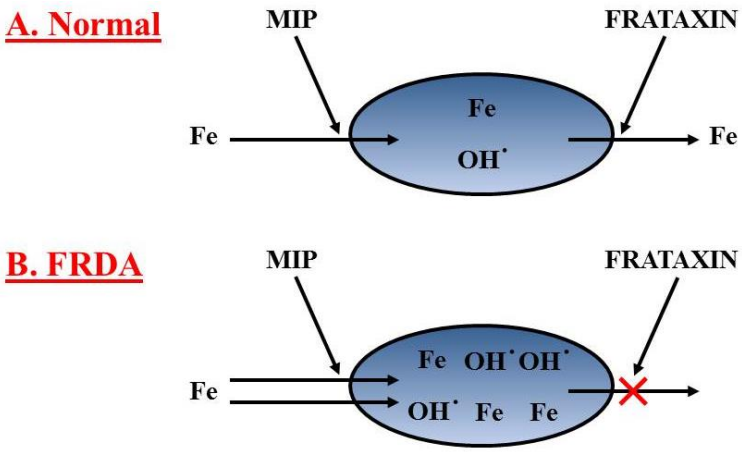

Fig. 1.4 Schematic representation of the likely pathogenesis of FRDA. **A)** The normal situation in the mitochondrion is shown with iron influx and efflux maintaining low mitochondrial iron (Fe) and free radical ($OH^{\cdot}$) levels. Frataxin is likely to be acting directly at the level of iron efflux. Yeast data suggest that frataxin may also be indirectly limiting the influx of iron into mitochondria by reducing mitochondrial intermediate peptidase (MIP) activity. **B)** In FRDA reduced frataxin results in inhibition of the efflux of mitochondrial iron. This leads to reduced cytosolic iron, which results in induction of iron uptake systems and this in turn results in further iron uptake into mitochondria. The increased iron uptake may be in part the result of over activity of MIP owing to the absence of frataxin. The excess mitochondrial iron leads to excess production of toxic free radicals by Fenton reaction ($Fe^{2+} + H_2O_2 \rightarrow Fe^{3+} + OH^- + OH^{\cdot}$) leading to cell damage and death [29].

The expression of frataxin is dependent on the type of tissue, indicating tissue-specific pathology in FRDA. Tissues such as liver, skeletal muscle and thymus are not affected by the disease yet they contain high levels of mitochondria and frataxin is significantly expressed in such tissues. While the aforementioned tissues can be replaced due to their inherent dividing nature, the affected tissues such as those in the central nervous system, heart and pancreas are typically nondividing [29, 42, 43]. Moreover, neurons and cardiac myocytes are more susceptible to mitochondrial defects and toxic effects of mitochondrial free-radical accumulation due to their high aerobic metabolism dependence [55].

1.10 Structure of Human Frataxin

Human frataxin, a 210 amino acid protein, contains a N-terminal mitochondrial targeting sequence that is proteolytically processed after frataxin is imported into the matrix. The mitochondrial processing peptidase, MPP-β, is responsible for cleavage of the frataxin mitochondrial targeting sequence, generating the human frataxin with 155 amino acids (residues 56-210) [56-58, 59]. Crystal and solution nuclear magnetic resonance (NMR) structures of frataxin show significant sequence similarity between the C-terminal domain of frataxin (residues 90-210) and the CyaY proteins of γ-purple bacteria [59-62], providing a common structural features to study possible structure and function of frataxin family. Frataxin has a unique fold that combines two terminal helices (α_1 and α_2) which are nearly parallel to each other and to the plane of the large β sheet, five antiparallel β-strands that interact with the two helices, and a sixth (and, in human frataxin, a seventh) β-strand that intersects the planes to give an overall compact

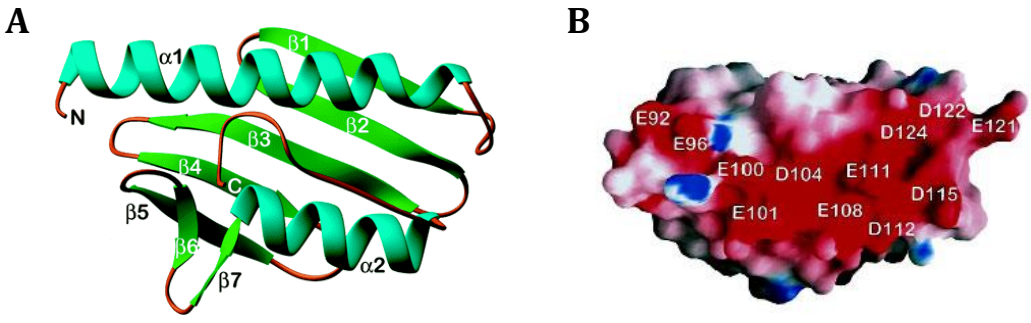

Fig. 1.5 Structure of frataxin. **A)** Crystal structure of human frataxin shows the fold of human frataxin, a compact αβ sandwich, with α helices and β sheets. Strands β1 – β5 formed a flat antiparallel construct that interact with the two helices, α1 and α2. **B)** Molecular surface representation of frataxin. Several anionic residues in α1 and β1 are shown in red. The anionic surface might be critical for the function of frataxin [60].

αβ sandwich structure, Fig. 1.5A [60]. However strand seven is only detected in human frataxin with structures extremely similar to those of frataxin orthologs due to high degree of amino acid sequence similarity [60].

A clustering of negatively charged side chains of 12 acidic residues projected from helix α1 and strand β1 creates an acidic patch of the surface of the protein, Fig. 1.5B. The general structure, including the anionic surface, is conserved in both eukaryotes and prokaryotes; however, the architecture of frataxin represents a new protein fold. The conserved outer surface of the β sheet might mediate a specific protein-protein interaction with partners that may be crucial for its biological functions. Different approaches such as NMR experiments and crystallographic experiments were used to study the potential binding properties of frataxin to iron, but no chemical changes were observed. These results indicate that frataxin does not have any feature resembling known iron-binding sites; however, the anionic surface of frataxin is considered to contain the putative iron-binding sites based on the resemblance to bacterial ferritin [60, 61].

Mapping the pathological mutations onto the structure provides an insight into possible function of frataxin. However, a small percentage (≈ 2%) of FRDA patients are compound heterozygotes, having a combination of increased GAA repeats in one allele and a point mutation in the other allele [37, 63-65]. Several mutations are in the protein core including L106S, I154F, L156P, W173G, L182H/L182F and H183R leading to interruption of the stable and compact structure [55]. Another mutation, D122Y, within the anionic patch alters charge within this surface and overall protein polarity. Mutants G130V, W155R and R165C are located within the flat, conserved external surface of the large β sheet. Therefore, the mutations associated with disease are not only located in the compact core structure, but are also located within two conserved surfaces including the anionic surface and the conserved outer β sheet surface. Thus, these surfaces are critical for frataxin function as the mutations within these surfaces showed several effects, including steric strain and electrostatic strain [60]. The mutations in FRDA patients have been summarised in Table 1.1 [61].

Table 1.1 Summary of the mutations described in FRDA patients

Mutation	Effect	References
L106S, W173G	Internal cavities with loss of packing energy	64,36
I154F, L182F	Steric strain by replacing a buried hydrophobic residue by a larger one	6,8
L156P	Disruption in the β-sheet hydrogen bonds by introducing a proline	36
L182H	Electrostatic strain by replacing a buried residue with a hydrophilic one	36
H183R	Electrostatic stain by replacing a partially uncharged buried residue with a bulky charged one	36
D122Y	Change of identity of a conserved negatively charged group on the surface	36
G130V	Steric stain by replacing a glycine which is in a conformation that is not allowed for other residues	63
W155R	Replacement of a bulky highly conserved aromatic side chain with a positively charged residue	66
R165C	Replacement of a conserved positively charged group with as exposed cysteine that might form intermolecular disulphide bound	37

1.11 Molecular Mechanisms of GAA Repeat Expansions

The exact mechanism through which the GAA repeat mutation inhibits frataxin expression is still unknown. However, several combined mechanisms have been identified to be involved in the establishment of epigenetic changes in FRDA. GAA repeats have been shown to form hairpins; these non-B DNA structures may induce DNA methylation. On the other hand, small double-stranded RNA (dsRNA) has also been reported to induce transcriptional gene silencing through DNA methylation. Therefore, better understanding of the mechanisms involved in GAA-induced inhibition of *FXN* gene transcription associated with FRDA can lead to the development of several novel for therapeutic approaches [67].

1.11.1 Hairpin Formation in FRDA Triplet Repeat Expansion

Triplet repeat (TR) tracts occur throughout the human genome [68]. Expansions of these tracts during their transmission from parent to child are closely associated with more than 14 hereditary neuromuscular diseases [69, 70]. TRs associated with FRDA include GAA/TTC repeats. The expansions produce an identical sequence to that of the repeat tract, varying from a few triplets in a coding region of the gene (type I) to hundreds of triplets in a noncoding region of the gene (type II). Repeat instability is dependent on the length of the repeat tract and its orientation in the genome. Consequently, long tracts of TRs are highly unstable, making them more susceptible to changes in the repeat size either through expansion or deletion. These instabilities are presumed to be due to the formation of unusual secondary structures such as hairpins, Fig. 1.6. TR expansion is predicted to occur as a result of DNA slippage of the Okazaki fragment and TR contraction by replication across hairpins formed in the template strand, occurring during DNA lagging strand replication of the TR tract [71-73]. The discontinuous nature of lagging strand replication, the presence of single-stranded regions (ssDNA) in the template and free 5´-ends in the growing strand (Okazaki fragment), presents the opportunity for the formation of hairpins [74-76].

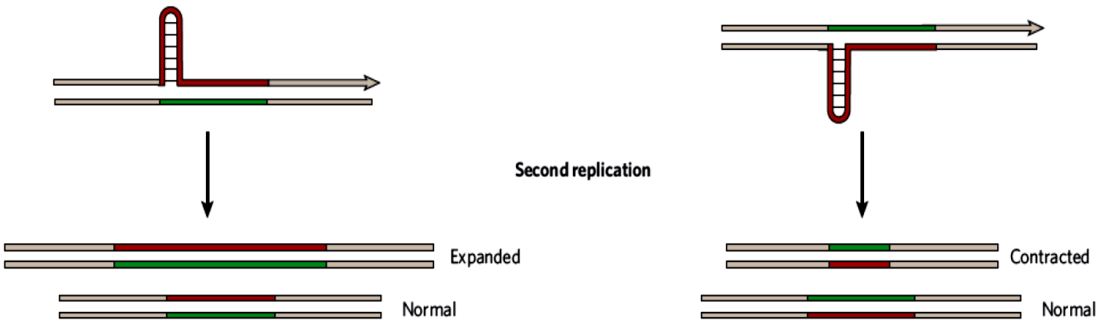

Fig. 1.6 Schematic representation of hairpin formation in FRDA patient DNA. After two rounds of replication, formation of a repetitive hairpin on the nascent strand results in repeat expansions (left panel), whereas the presence of the same structure on the template strand results in repeat contractions (right panel) [77].

CAG, CTG, GCC and GGC TR tracts synthesised *in vitro* were shown to form hairpin and hairpin-related tetraplex secondary structures through self-annealing [78-81]. Lagging strand replication model in bacteria and yeast demonstrated both contractions and expansions produced by hairpins during lagging strand replication of TR tracts [72, 73, 76, 82]. Although the single-stranded expansion products are a great potential target for DNA repair, secondary structure formation is believed to protect the expansion from

DNA repair activities of the cell, including mismatch repair and flap endonuclease [83-89]. Synthetic GAA and TTC single-stranded DNAs do not easily self-anneal and secondary structures adopted by these oligonucleotides are much less stable than the structures formed by single-stranded CAG, CTG, GCC and GGC TRs [78-81, 90-92]. The differences in repair presumably are caused by the different abilities of the repeat tracts to self-anneal to form hairpins [88].

Intermediate structures are perceived to be involved in FRDA TR expansions through pausing DNA replication and inducing DNA slippage within the repeat tracts. Such structures are commonly referred to as sticky DNAs, formed by triplex (purine-purine-pyrimidine and pyrimidine-purine-pyrimidine) and duplex structures of GAA and TTC TR tracts combination [91, 93-96].

1.11.2 Gene Silencing

The second characteristic of expanded GAA repeats is heterochromatin formation and subsequent gene silencing. Festenstein *et al.* generated artificial transgenes with a heterochromatin-sensitive lymphoid cell-surface marker protein (CD2) in order to investigate whether CTG repeats found in myotonic dystrophy or GAA repeats in FRDA could silence genes by inducing heterochromatin [97]. This study observed that both expanded GAA and CTG repeats could exert position effect variegation (PEV) on the CD2 reporter gene expression. PEV occurs when a gene is located within or near regions of heterochromatin and results in silencing of the affected gene in a subset of cells. Heterochromatin is controlled by the presence of particular types of histone modifications (for example, H3K9 methylation), the absence of acetylated histones, and the presence of HDACs, DNA methyltransferases, chromodomain proteins (such as members of the HP-1 family of repressors) and polycomb group proteins. It has been suggested that molecules that reverse *FXN* gene silencing could relieve the deficiency in *FXN* mRNA and protein in affected individuals [98].

Production of heterochromatin through triplet repeat expansions can be described by different models, Fig. 1.7. Triplet repeats form non-B DNA structures and sticky DNA at the *FXN* locus that may result in stalling of the RNA polymerase (RNAPol). In this case cellular checkpoint mechanisms could trigger heterochromatin formation, leading to inactivation of the locus. In addition to triplexes, there is also evidence to suggest that

R-loop (RNA•DNA hybrid) formation during transcription is intrinsic to long GAA-TTC repeats [99] in which the nascent transcript forms a duplex with the transcriptional template strand. R-loops can result in double-strand breaks (DSBs) and recombination via transcription associated recombination. Several factors may contribute to R-loop formation, such as defective biogenesis of messenger ribonucleoprotein (mRNP) particles, deficiency of proteins responsible for splicing and/or nuclear export of transcripts, and sequence composition of the non-template strand [99]. In addition, bidirectional transcription has also been shown to contribute to the formation of R-loops, Fig. 1.7. The newly formed R-loops are presumed to contribute to trinucleotide

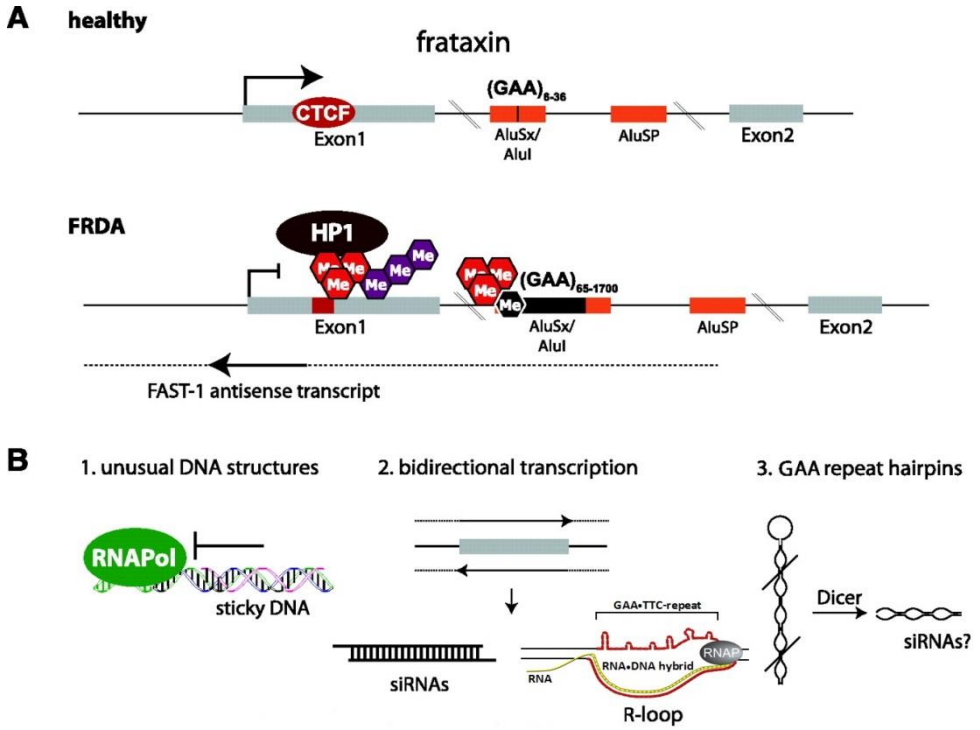

Fig. 1.7 Triplet repeat induced heterochromatin formation in FRDA. **A)** In healthy individuals, intron 1 of the frataxin gene contains only a small number of GAA repeats. The frataxin gene is transcribed and CTCF binding in exon 1 may be an important regulatory element for this locus. In FRDA patient cells, expanded GAA repeats lead to formation of a heterochromatic domain, coinciding with loss of CTCF binding and silencing of frataxin expression. Interestingly, repression of frataxin correlates with upregulation of the *FAST-1* antisense transcript, which may originate from the AluSP sequence in intron 1. **B)** Models for initiation of heterochromatin through triplet repeat expansions. 1) Triplet repeats form unusual DNA structures that may result in stalling of the RNA polymerase (RNAPol). This could trigger a damage signal leading to inactivation of the locus. 2) Bidirectional transcription across the frataxin locus may produce double stranded RNA, triggering siRNA-mediated heterochromatin formation. In addition, R-loops, RNA•DNA hybrids, can arise from bidirectional transcription through the trinucleotide repeat. 3) Transcripts containing large GAA triplet repeats form hairpin structures that can be cleaved by dicer. It is currently unclear if the cleavage products function as siRNAs [100].

repeat instability by aberrant processing via transcription-coupled nucleotide excision repair factors [101, 102]. Another model for induction of heterochromatin at trinucleotide repeat loci is antisense transcription across the *FXN* locus which generates double stranded RNA, triggering siRNA-mediated heterochromatin formation, Fig. 1.7. Thus, production of the *FAST-1* transcript could be crucial for the silencing mechanism in FRDA. A major regulator for antisense transcript production might be CTCF. In FRDA patients, loss of CTCF binding correlates with accumulation of *FAST-1* transcripts, which may originate from the AluSP sequence in intron 1. In a third model, transcripts containing expansions of CAG or CUG repeats, as found in fragile X syndrome (FXS) and DM1, are capable of forming hairpin structures that can be cleaved by dicer, Fig. 1.7. The cleavage products of CNG hairpins, or for FRDA GAA hairpins, might resemble siRNAs that potentially trigger heterochromatin formation using a similar mechanism [100].

1.12 Instability of the Expanded GAA Triplet Repeats

The GAA repeat sequence is unstable when transmitted from parent to child. Instability during patent-offspring transmission can also be indirectly demonstrated by the detection of two distinct alleles in affected children of consanguineous parents, who are expected to be homozygous by descent at the FRDA locus. Both expansions and contractions of expanded GAA repeats can be observed in FRDA. Fully expanded alleles most often contract during paternal transmission, but further expansion or contraction of the pathological GAA repeat can be detected equally during maternal transmission. The unstable dynamics of FRDA GAA repeats resembles that of other diseases associated with very large expansions in noncoding regions, such as fragile X syndrome and myotonic dystrophy, however smaller expansions of CAG repeats in coding regions, found in dominant ataxias or Huntington's disease, show size increases during paternal transmission [103].

In addition to the GAA repeat size, FRDA disease phenotypic variation can also be explained by other factors such as somatic mosaicism of the GAA repeat expansion, gene modifiers and epigenetic effects. Small-pool PCR analysis of central nervous system (CNS) tissues derived from autopsies of patients with FRDA revealed the somatic instability of the GAA repeat [38]. Various regions of the CNS demonstrated a similar mixture of GAA alleles, with the largest GAA repeats detected in the cerebellar

cortex of FRDA patients. However there was no overall relation between GAA repeat size and FRDA regions of pathology. In lymphoblastoid cell lines and blood samples from FRDA patients, a slight expansion bias and an instability threshold of 44 repeats were detected in alleles with <500 triplets and conversely a significant contraction bias in alleles with >500 triplets including complete reversion to normal length [104, 105].

Pook *et al.* created a transgenic mouse model with a yeast artificial chromosome (YAC) carrying the entire human *FXN* locus containing a 190-GAA repeat in intron 1 to investigate the pathogenic GAA repeat associated with FRDA. They generated two lines of human *FRDA* YAC GAA transgenic mice, designated YG8 and YG22, containing double motif of 190 and 90 GAA repeats and a single 190-GAA repeat sequence respectively. Both lines of transgenic mice exhibited intergenerational and somatic GAA repeat instability, with no significant differences in overall instability

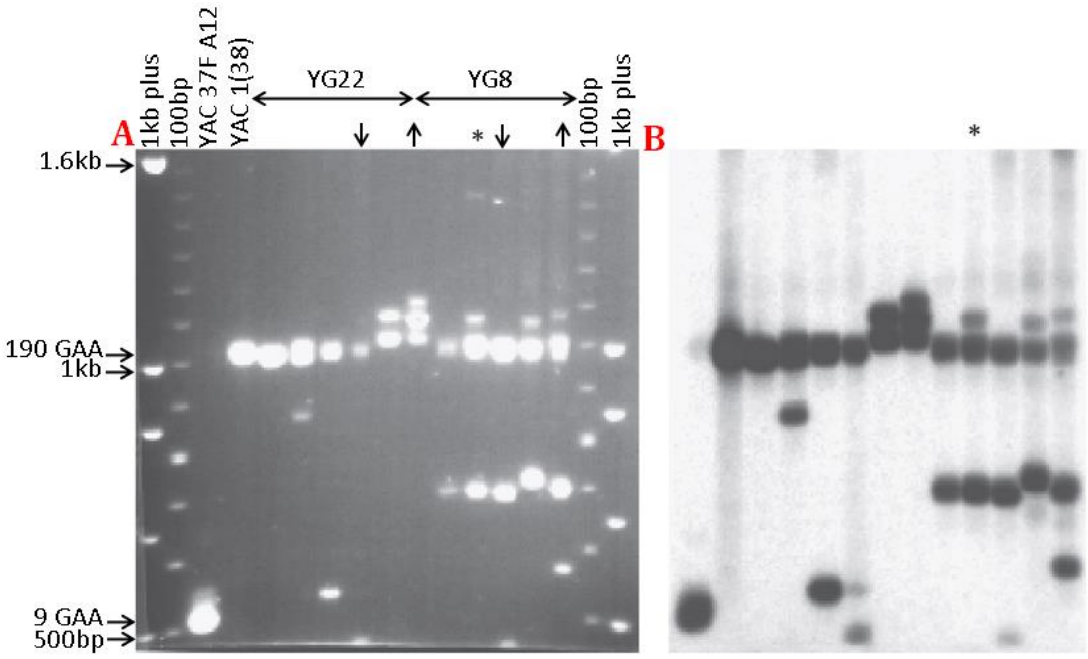

Fig. 1.8 Intergenerational GAA repeat instability in FRDA YAC transgenic mice. **A)** Ethidium bromide-stained agarose gel and **B)** Southern blot autoradiograph of GAA PCR products from representative YG22 and YG8 transgenic mice [103].

between the two lines, Fig. 1.8 [103]. Miranda *et al.* created another transgenic knock-in mouse model carrying a $(GAA)_{230}$ insert at the Frda locus which showed neither intergenerational nor somatic instability of a 230-GAA repeat sequence [106].

Studies of bacteria, yeast and mammalian cells indicated that both *cis* and *trans*-acting factors regulate the trinucleotide repeat sequences stability, including the position and

orientation of the repeats relative to the replication origins [41, 107, 108]. These studies suggested that the presence of replication-associated motifs and chromatin environment may be involved in instability mechanisms [109, 110].

To investigate whether somatic instability in FRDA is age dependent, Pook *et al.* compared the levels of somatic instability in tissues derived from young (2 months old; 2400 individual molecules) and old (12 months old; 2000 individual molecules) YG8 transgenic mice. The results showed less that 1% of somatic instability in the $(GAA)_{190}$ allele through 2 months of age whereas older mice showed a significant increase in mutation load due to the accumulation of expansions. The lower level of somatic mutations in blood and sperm compared to non-proliferative tissues such as cerebellum and DRG implies the role of cell type-specific *trans*-acting factors that modify specific triplet-repeat sequences [103].

1.13 Experimental Therapeutics for FRDA

Although there is no effective therapy for FRDA, some experimental therapeutic approaches such as antioxidant therapy are currently being exercised in clinical trials to increase frataxin expression. Considering the potential for the formation of free radicals and oxidative damage when frataxin levels are reduced, antioxidants including parabenzoquinones are being investigated as a potential FRDA therapy. Two such compounds are coenzyme Q10 (CoQ_{10}) and idebenone, a short-chain parabenzoquinone analogue of CoQ_{10} [111-114]. FRDA patients who were given CoQ_{10} in addition to vitamin E, an antioxidant compound, exhibited significant improvement of ATP production in cardiac and skeletal muscle after several months of treatment [115]. In addition, idebenone, a potential therapeutic agent to reduce oxidative stress and free radicals, has currently finished being tested in two phase III clinical trials in patients with FRDA. Rustin *et al.* reported on the effectiveness of idebenone in reducing hypertrophic cardiomyopathy in FRDA [116]. However, none of the pharmacological drugs tested had a significant beneficial effect on the neurological symptoms in FRDA patients [117]. Nevertheless, several clinical trials are currently being carried out to assess the effectiveness of promising antioxidant molecules. EPI-A0001 is a CoQ_{10} analogue which has completed phase II clinical trials. The results have shown improvements in neurological function in FRDA patients [118]. The EPI-743 (alpha-tocotrienol quinone) is a new drug based on vitamin E which targets improvement of

mitochondrial function and modifies disease progression in patients with inherited mitochondrial respiratory chain disorders [119]. This drug is currently being tested on FRDA patients in phase II clinical trial. OX1 (indole-3-propionic acid) is a natural compound that prevents oxidative stress through a combination of hydroxyl radical scavenging activity and metal chelation, currently in preclinical phase for toxicological safety.

Other therapeutic trials at the protein level include iron chelators such as desferrioxamine [120] and exogenous heme administration [121], which reduce intracellular iron. Interestingly, erythropoietin, a known stimulant of heme synthesis, can rescue defects in frataxin-deficient cells, but the mechanism(s) by which it increases frataxin levels is unknown [122]. Deferiprone, an oral chelating agent, has been established to be more effective than desferrioxamine in treating iron overlap in FRDA patients. However significant reduction in aconitase activity has been identified as the primary side effect of these drugs [123, 124]. Therefore, care should be taken when using iron chelators as a therapeutic agent.

Considering that the mutation leaves the coding region intact, gene-based strategies designed to increase the frataxin level would be an ideal therapy for FRDA, Fig. 1.9. Gene therapy is a viable option for FRDA and other recessive disorders. Recombinant adeno-associated viral and lentiviral vectors expressing frataxin cDNA have been revealed to partially correct sensitivity to oxidative stress in FRDA primary fibroblasts [125].

Grabczyk and Usdin conducted *in vitro* studies using T7 RNA polymerase to investigate the mechanisms by which expanded GAA repeats reduce FRDA gene transcription [126]. Their results provided additional confirmation for a model in which RNA polymerase was trapped in an R•R•Y intramolecular triplex. They further demonstrated that oligodeoxyribonucleotides specifically designed to block triplex structures were capable of increasing transcription through the GAA repeats [127]. This was the first proof of concept for the development of therapeutic agents in FRDA that targeted triplex formation. Numerous other studies have demonstrated that DNA-binding compounds, such as pyrrole-imidazole polyamides or pentamidine, are effective at increasing frataxin transcription in primary FRDA lymphocytes [128, 129].

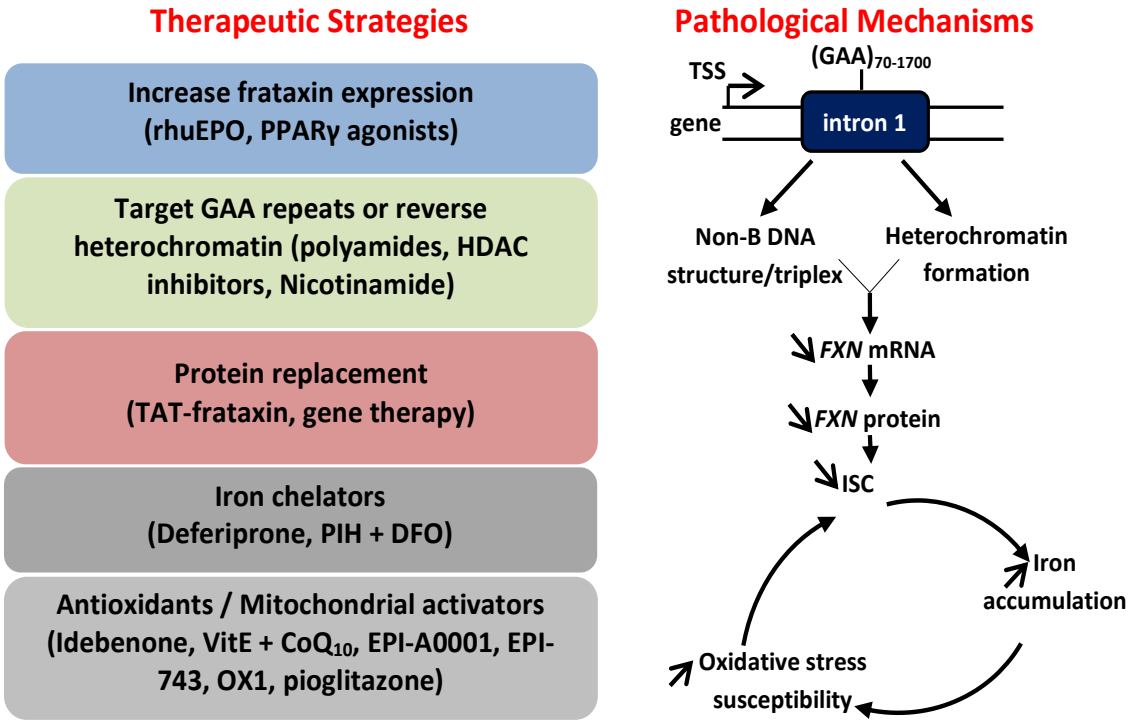

Fig. 1.9 Pathological mechanisms involved in FRDA and associated therapeutic strategy. FRDA is caused by a GAA expansion mutation within the first intron of frataxin gene. The mutation, through either a triplex-helix or a heterochromatin formation, impairs transcription and causes a severe decrease of frataxin mRNA expression and protein level. Physiological consequences of frataxin deficiency are specific ISC enzyme deficits, an intramitochondrial iron accumulation and a higher sensitivity to oxidative stress. In the left panel, the different therapeutic strategies currently under investigation to counteract defects observed in patients and to develop future treatments are presented. rhuEPO, recombinant human erythropoietin; PPAR, peroxisome proliferator-activated receptor; HDAC, histone deacetylase; PIH, pyridoxal isonicotinoyl hydrazone; DFO, desferrioxamine; VitE, vitamin E; CoQ_{10}, coenzyme Q_{10} [95].

As stated before in section 1.11.2, the second characteristic of expanded GAA repeats that results in decreased frataxin is heterochromatin formation, or gene silencing, Fig. 1.10. A promising therapeutic strategy is to directly target the heterochromatin state of the GAA repeat expansion with histone deacetylase inhibitors (HDACi) to restore frataxin levels [96]. HDACi prevents the deacetylation of histones and may revert silent heterochromatin to an active conformation that is conducive for gene expression [130].

FRDA cells treated with the highly active HDACi compound 4b [N1-(2-aminophenyl)-N7- phenylheptanediamide] resulted in a significant increase in frataxin, accompanied by increased histone H3 acetylation near the GAA repeat [132]. This result is consistent

with GAA knock-in mice treated with a novel HDACi compound 106 [N1-(2-aminophenyl)-N7-p-tolylheptanediamide] [52]. Recent studies suggested the potential

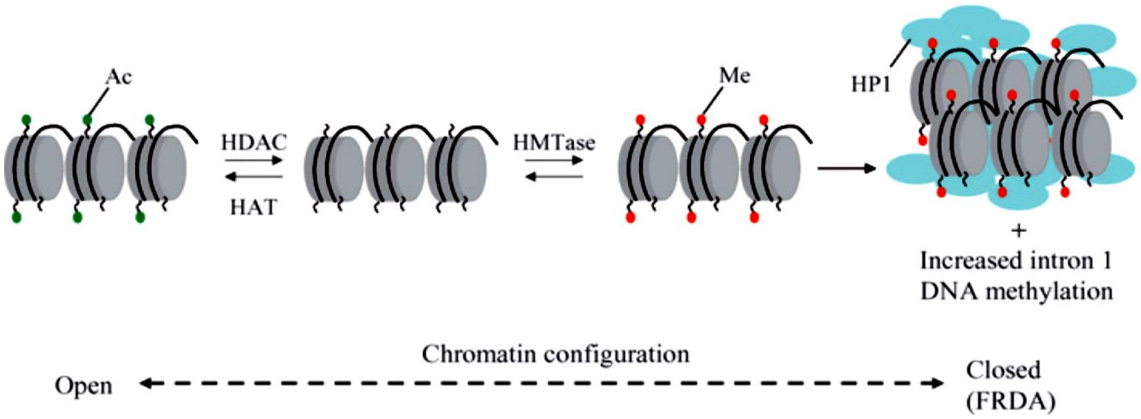

Fig. 1.10 A model for heterochromatin formation in FRDA. Normal FRDA alleles contain open chromatin with acetylated histones (Ac, green). Non B-DNA structures, as a consequence of expanded GAA repeats, may induce histone deacetylase (HDAC) activity that, along with histone methyltransferases (HMTase), generate methylated histones (Me, red). The methylation of lysine 9 on histone H3 is a hallmark of heterochromatin and has been found in FRDA patient cells. Further chromatin compaction may be aided by the binding of HP1 and increased DNA methylation. Agents designed to increase histone acetyltransferase (HAT) activity or inhibit HDAC activity would be expected to increase frataxin levels. Indeed, some HDAC inhibitors have been found to increase frataxin expression [131].

therapeutic effects of class III HDACi compounds such as sirtinol, splitomicin and nicotinamide (vitamin B3) in the treatment of trinucleotide repeat disorders [133-135]. Festenstein *et al.* have shown that nicotinamide, a class III HDACi, can reverse the downregulation of *FXN* in different FRDA models [135]. In addition to the aforementioned molecules which directly target the GAA repeat, a number of other molecules have also been reported to increase frataxin mRNA or protein levels whereby recombinant human erythropoietin (rhuEPO) has been established to increase frataxin protein in lymphocytes from FRDA patients [121].

Since there are many similarities between FRDA and fragile X syndrome (both contain non-translated repeats that induce CpG hypermethylation and histone deacetylation), a common therapeutic procedure can be designed and implemented for both cases. Fragile X lymphoblasts treatment with 5´-azadeoxycytidine, a DNA-demethylating agent, has been reported to increase FMR1 message and protein level [136]. Although 5´-azadeoxycytidine is not clinically suitable due to toxicity effects, it can be used in combination with other drugs such as HDAC inhibitors in FRDA treatment [136].

Furthermore, HDAC inhibitors have been shown to marginally increase message levels in fragile X lymphoblasts [136]. Herman *et al.* tested several different classes of HDAC inhibitors on an FRDA lymphoblastoid cell line to examine the effect of such inhibitors on the level of frataxin in FRDA. However, BML-210 was reported as the only inhibitor which resulted in a significant increase in frataxin message levels, Fig. 1.11 [132].

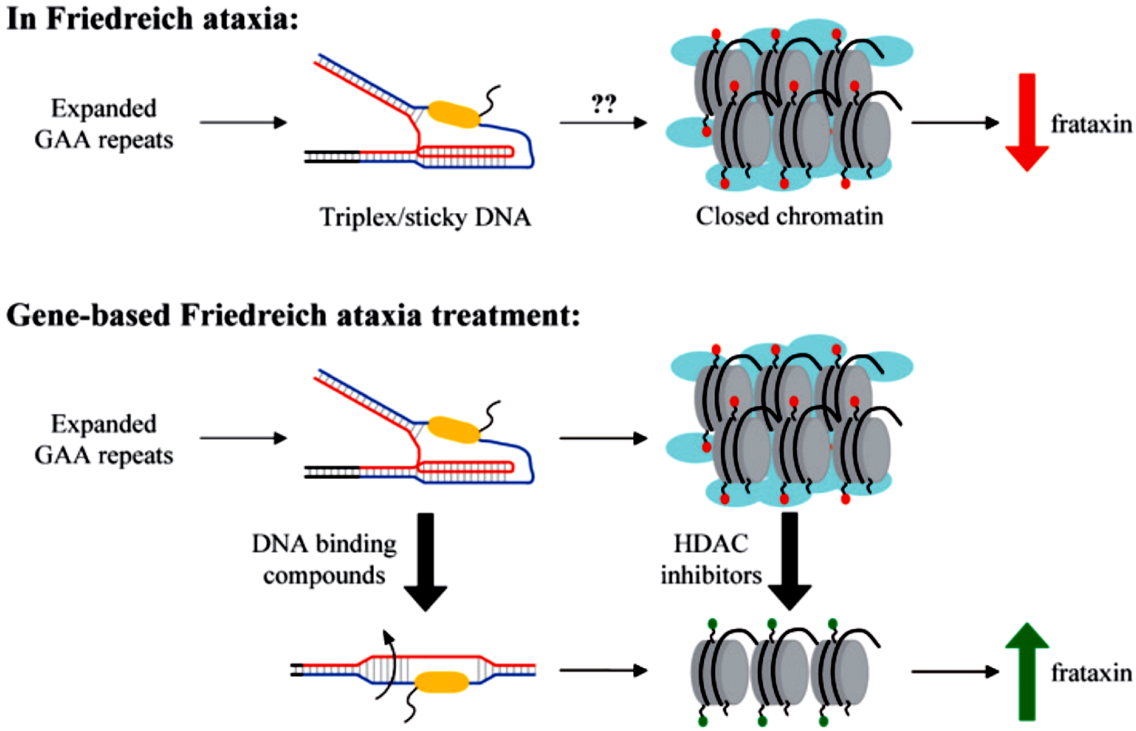

Fig. 1.11 Gene-based strategy to obtain FRDA therapeutics. In FRDA, non B-form DNA structures and heterochromatin both contribute to reduce FRDA transcription and result in pathogenically low levels of frataxin. The mechanism by which this takes place is unknown (??). An ideal gene-based treatment would overcome both obstacles (non B-form DNA and heterochromatin) to increase frataxin production. Such a therapy might include specific DNA-binding compounds that stabilise B form DNA and HDAC inhibitors that facilitate chromatin decondensation [137].

1.14 Mouse Models for FRDA

To further investigate the FRDA mechanism and to validate the potential FRDA therapeutics procedures, several mouse models have been generated [31, 106].

1.14.1 Knock-out Models

Cossee *et al.* generated Frda knockout mice by targeting exon 4 of *Fxn* that appeared normal as heterozygotes, but homozygous deletion of *Fxn* caused embryonic lethality a few days after implantation, demonstrating a crucial role for frataxin during early

embryonic development. This result suggested that the milder phenotype in human is due to residual frataxin expression associated with the expansion mutations [138].

Puccio *et al.* generated two different conditional knockout models in which *Fxn* was deleted, specifically in skeletal and cardiac muscle. Both models were viable and reproduced some morphological and biochemical features of FRDA, providing an important resource for pathophysiological studies and testing of new treatments [139].

1.14.2 Knock-in Model

To develop systems for studying both germ-line and somatic repeat instability in trinucleotide- repeat disorders, a GAA-repeat-based mouse model of FRDA would be of great value [140-146]. However, instability is only apparent when the repeat sequence is introduced within the appropriate genomic context, such as a large human genomic transgene or knock-in at the endogenous mouse locus [109, 141-143, 147, 148]. Since FRDA is caused by an unstable GAA repeat sequence and the *Fxn* intron 1 region of the mouse does not normally contain a GAA repeat sequence, insertion of GAA repeats into the *Fxn* intron 1 region of mice would be an effective way to study the dynamics of trinucleotide repeats and their relation to the disease. Miranda *et al.* inserted a $(GAA)_{230}$ repeat into the appropriate site of *Fxn* intron 1, the results showed decreased frataxin production. However no motor coordination abnormality, iron metabolism, response to iron binding, or death due to frataxin reduction was observed [106].

1.14.3 *FXN* YAC Transgenic Mouse Models

The mouse model developed by Pook *et al.* provided an essential resource to assess potential FRDA therapies that target the mutated, GAA expanded, *FXN* gene [149]. In an initial effort to assess whether human frataxin could function in a mouse background and substitute for loss of endogenous murine frataxin, they generated a human wild-type FRDA yeast artificial chromosome (YAC) transgenic mouse line, Fig. 1.12, and crossbred this with heterozygous *Fxn* exon 4 deletion knockout mice [149]. They obtained phenotypically normal homozygous *Fxn* knockout offspring that expressed only human frataxin in the appropriate tissue and corrected mitochondrial subcellular localisation. This result confirmed that 370-kb *FXN* YAC transgenic construct, 37FA12, was functional and could express frataxin during development [149]. Additionally, the generation of rescued mice through re-introduction of human frataxin into a mouse null

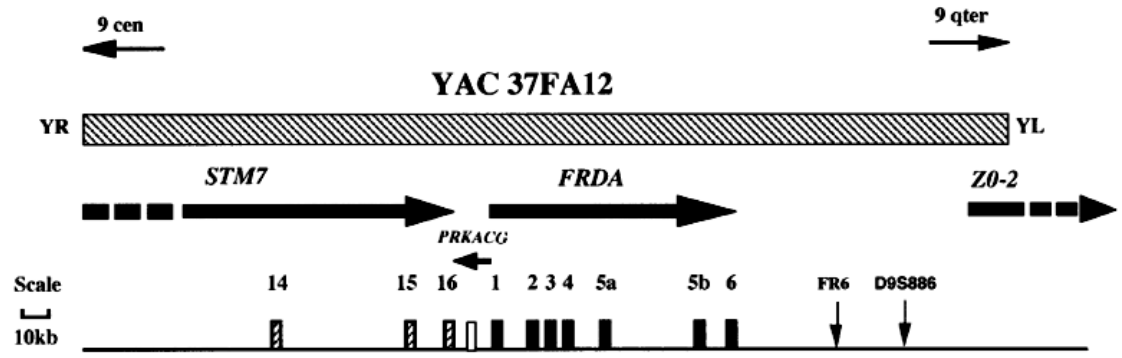

Fig. 1.12 Characterisation of YAC 37FA12 and the Y47 transgenic line. The position of YAC 37FA12 with respect to the FRDA locus at 9q13. Genes are represented as solid arrows, which indicate the direction of transcription; and the broken lines represent incomplete gene sequence. Individual exons are numbered and are shown below the relevant gene. STS markers used in the analysis are shown as downward pointing arrows [149].

background would be an effective method for future gene therapy studies to correct the defect in FRDA patients [138, 149].

They finally proceeded to generate two lines of human FRDA YAC transgenic mice,

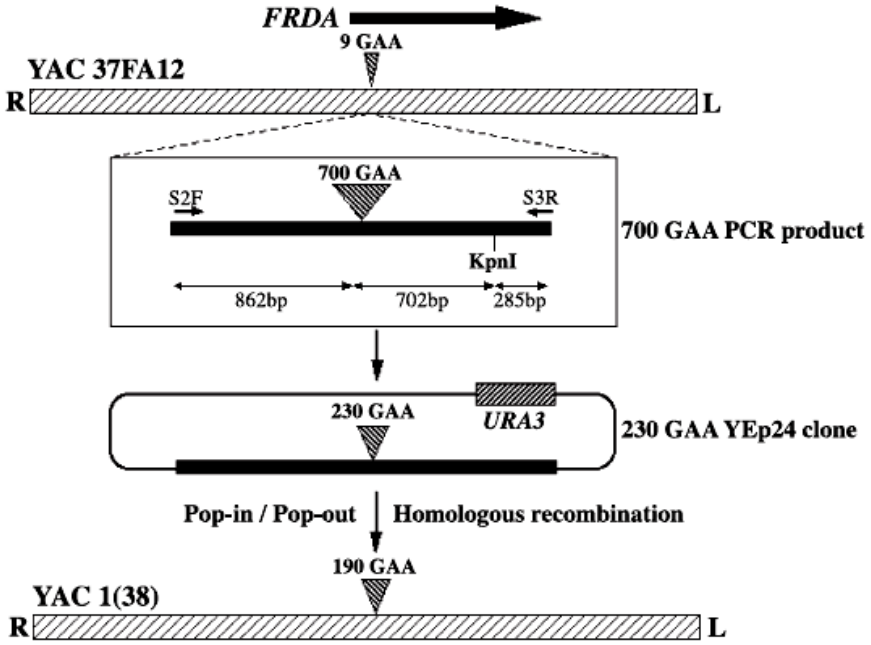

Fig. 1.13 GAA repeat modification of YAC 37FA12. The position and orientation of the normal FRDA gene (9 GAA repeats) within the human YAC clone 37FA12 are indicated by the arrow. L and R indicate left and right arms of the YAC. A 700-GAA PCR product was amplified from FRDA patient DNA using primers S2F and S3R. The PCR product was first cloned into pCR2.1 (not shown) and then into YEp24, which contains a selectable URA3 gene, with resultant contraction to 230 GAA repeats. Pop-in/pop-out homologous recombination between Yep24 and YAC 37FA12 FRDA sequences produced the 190-GAArepeat YAC clone 1(38), which was subsequently used to generate transgenic mice [103].

designated as YG8 and YG22 by using a yeast pop-in/pop-out homologous recombination strategy, Fig. 1.13 [103, 150].

Both lines of transgenic YAC mice contained transgene sequences spanning the whole 370-kb human YAC clone, including the left and right arms of the YAC and the entire FRDA gene together with GAA repeat expansions. YG8 contained two GAA sequences of 90 and 190 repeats, while YG22 contained a single 190 GAA repeat sequence [103]. FRDA transgenic mice showed age-related somatic instability in the GAA repeat sequence, particularly in the cerebellum, in a manner resembling the human FRDA condition [103]. Therefore, these mice will be useful for further detailed studies of FRDA GAA-repeat mechanisms.

1.15 Decreased Frataxin mRNA and Protein Expression in *FXN* YAC Mouse Models

Pook *et al.* investigated the viability of each GAA *FXN* transgene by crossbreeding both

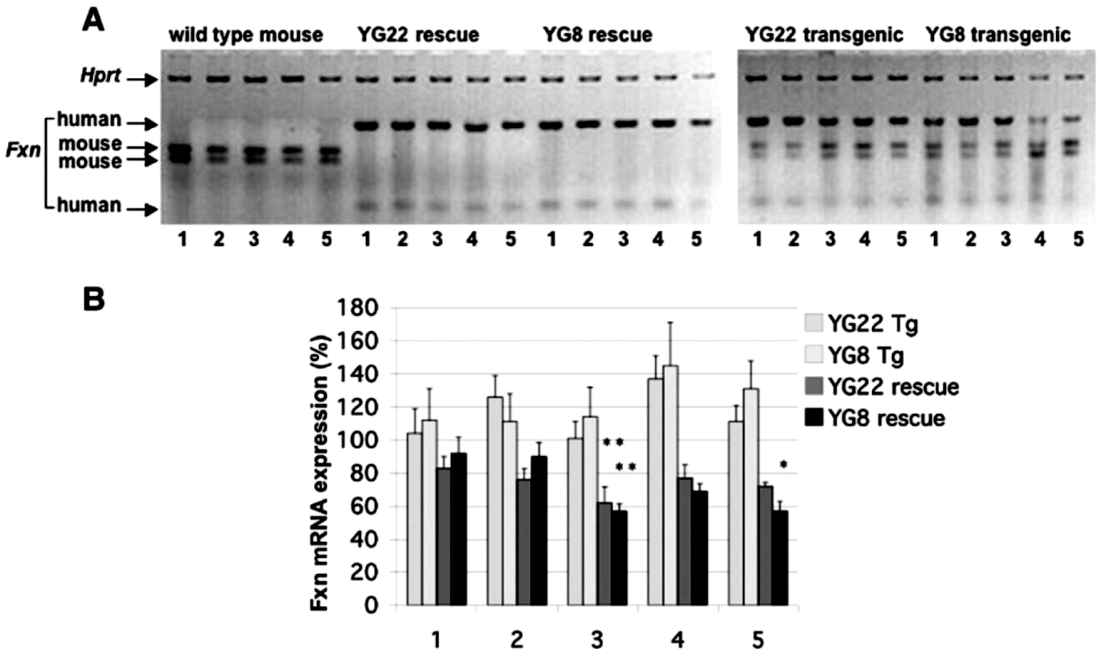

Fig. 1.14 mRNA expression analysis. **A)** A representative RT-PCR image showing restriction-digested human frataxin products (112 and 29 bp) and mouse frataxin products (75 and 64 bp), together with mouse *Hprt* controls. mRNA samples were isolated from tissues of wild-type, YG22 rescue, YG8 rescue, YG22 transgenic, and YG8 transgenic mice (lanes 1, cerebrum; 2, brain stem; 3, cerebellum; 4, heart; 5, skeletal muscle). **B)** Levels of frataxin mRNA expression as a percentage value of wild-type mouse expression. Values were generated by determining the means of six different RT-PCR experiments, each normalized to Hprt. Error bars indicate SEM. $^{*}p<0.05$, $^{**}p<0.01$ [31].

the YG22 or YG8 mice (*FXN*+, *Fxn*+/+) with heterozygous *Fxn* knockout mice (*Fxn*+/−) and further breeding the *FXN*+, *Fxn*+/− offspring from these crosses with *Fxn*+/−. The resultant rescue mice from both lines showed a normal life span up to at least 2 years of age, indicating functional frataxin derived from both GAA repeat-containing transgenes. To determine the levels of frataxin mRNA expression in YG22 and YG8 rescue and transgenic mice, semiquantitative RT-PCR was performed using primers that were capable of recognising both human and mouse frataxin cDNA. The results confirmed the presence of human-only frataxin mRNA transcripts in both YG22 and YG8 rescue mice, Fig. 1.14A. In addition, both YG8 and YG22 rescue mice exhibited comparatively decreased levels of human frataxin mRNA in all tissues (most in the cerebellum of both YG22 (62%) and YG8 (57%), together with the skeletal muscle of YG8 rescues (57%)) in comparison to endogenous mouse levels, Fig. 1.14B [31].

1.16 Histopathology

The differentially reduced levels of frataxin in the *FXN* YAC GAA mouse models are sufficient to cause a FRDA-like pathological phenotype. To detect possible neuronal abnormalities in these mouse models, neuronal histopathology studies were performed by hematoxylin-and-eosin staining and anti-calbindin immunohistology in brain, spinal cord and DRG of YG8 and YG22 mouse models. The results revealed prominent giant vacuoles in the large sensory neuronal cell bodies of the DRG in both YG8 and YG22

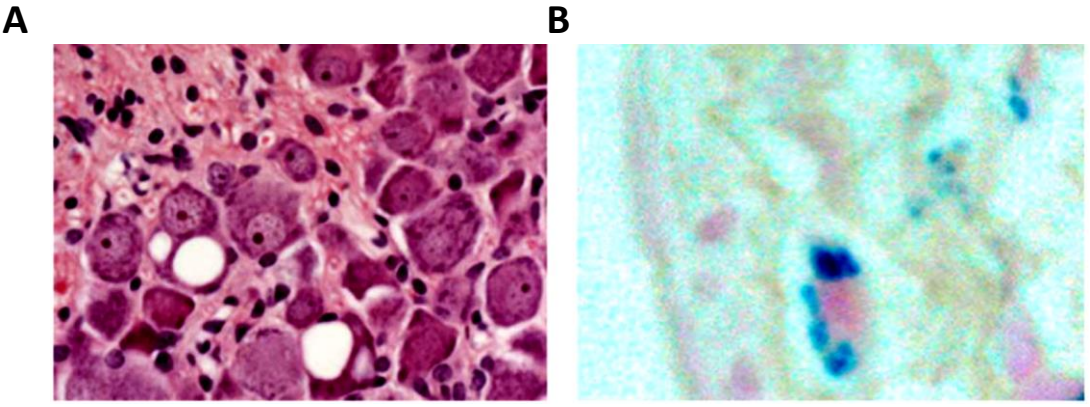

Fig. 1.15 Neuronal and cardiac histopathology. **A)** H&E-stained section of lumbar DRG from a representative YG22 rescue mouse over 1 year of age, showing two neurons containing large vacuoles. Original magnification 400×. **B)** Perl's staining of a heart section from a representative YG22 rescue mouse over 1 year of age, showing characteristic blue staining indicating iron deposition. Original magnification 600× [31].

rescue mice while such a pathological change was not observed in wild type controls, Fig. 1.15A. The occurrence of DRG vacuoles showed a progressive position dependent profile from affected distal lumbar regions at only 6 months of age to more proximal cervical regions at 13-15 months. This profile resembles the distal-to-proximal "dying-back" phenomenon of neurodegeneration that is observed in FRDA patients [31].

To determine potential hypertrophic cardiomyopathy, histopathology analysis of heart was performed by H&E, trichrome Masson and Perl's staining in YG8 and YG22 rescue mice. The results showed iron deposition in cardiomyocytes after 1 year of age, Fig. 1.15B. These were the first GAA repeat expansion-based FRDA mouse models that exhibited progressive FRDA-like pathology [31].

1.17 GAA Repeat Expansion Induces Epigenetic Changes in FRDA

Previous studies have implicated that the mutation may induce epigenetic changes and heterochromatin formation, thereby hampering gene transcription. In support of this hypothesis, studies using FRDA patient blood and lymphoblastoid cell lines have shown

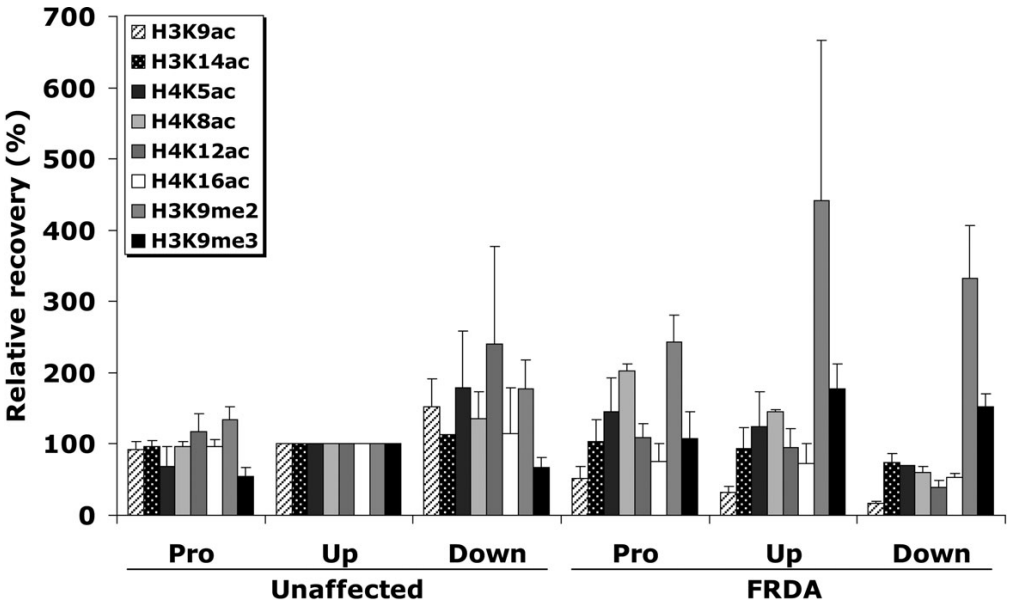

Fig. 1.16 Analysis of histone modifications in human brain tissue. ChIP quantitative PCR results for the *FXN* promoter/exon1 (Pro), upstream GAA (Up) and downstream GAA (Down) amplified regions are represented as the relative amount of immunoprecipitated DNA compared with input DNA, having taken negligible 2Ab control values into account. *FXN* values were normalized with human GAPDH and all values have been adjusted so that all of the Upstream GAA mean values from the unaffected individuals are 100%. In each case two individual ChIP samples from two FRDA patients and two unaffected controls were analysed in triplicate. The means and SEMs of these values are shown [67].

increased DNA methylation of specific CpG sites upstream of the expanded GAA repeat sequence and histone modifications in regions flanking the GAA repeat that are both consistent with transcription inhibition, Fig. 1.16.

These changes include deacetylation of histone H3 and H4 lysine residues and increased dimethylation and trimethylation of H3K9. Bisulfite sequencing and chromatin immunoprecipitation (ChIP) analysis of the *FXN* flanking GAA regions have confirmed the DNA methylation changes with hypermethylation in the upstream GAA region and hypomethylation in the downstream GAA region [67].

In order to determine whether such epigenetic changes are actually present in the most clinically relevant FRDA tissues, chromatin immunoprecipitation analysis indicated an overall decreased histone H3K9 acetylation together with increased H3K9 methylation of FRDA brain tissue. Further studies of brain, cerebellum and heart tissues from GAA repeat expansion-containing FRDA YAC transgenic mice (YG8, Y47 and YG22) exhibited comparable epigenetic changes to those detected in FRDA patient tissue. Therefore, these are excellent FRDA mouse models for the investigation of the therapeutic studies targeting epigenetic modifications of the *FXN* gene to increase frataxin expression [67].

1.18 Overview of Telomeres

The genome is susceptible to double-strand breaks (DSBs) through exposure to several factors including reactive oxygen species (ROS) and ionizing radiation (IR). However, DSBs can also be artificially created during antibody production and meiosis. It is important to note that unrepaired DSBs are highly detrimental to cell function [151].

Natural chromosomes contain telomeres at their physical ends which resemble DSBs, yet telomeres are immune from inappropriate engagement into repair reactions, Fig. 1.17 [151]. This is mainly attributed to the formation of a higher order structure which circumvents DNA damage surveillance mechanisms. However, telomeres are established as one of the major sites affected through the process of DNA damage provided that their respective higher order structure is altered [152]. Consequently, dysfunctional telomeres are incorporated into end-to-end chromosome fusions resulting in genome instability. Several telomere binding and DNA damage proteins are involved in the protective structure and maintenance of telomeres, however, the function of these

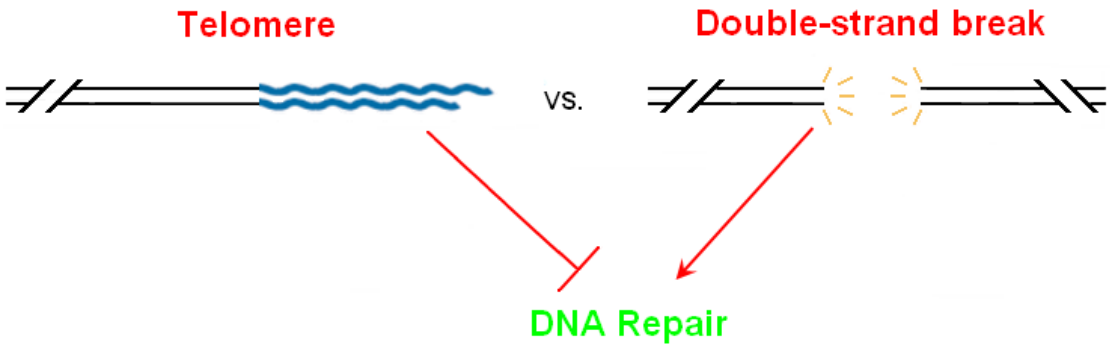

Fig. 1.17 DNA repair model. A double-strand break (denoted by radiating lines) is recruited into an end-joining reaction whereas a telomere (blue wavy lines) is stable and refractory to be detected as DNA damage. Black lines designate non-telomeric sequence [151].

proteins is yet to be fully established. Consequently, investigation of the dynamic interaction between telomeres, telomere binding proteins and proteins of the DNA damage response (DDR) is a major focus of the telomere field and cancer research [151].

1.19 The End Replication Problem

Telomeres form a protective nucleoprotein cap at the end of the chromosome to protect the chromosome terminus from numerous deleterious activities such as degradation by nucleases, recognition as a DNA break by DNA damage repair machinery, and inappropriate recombination. While the new DNA is synthesised in the 5′ to 3′ direction, the 3′ to 5′ leading strand is copied to completion in the forward direction, Fig. 1.18A. However, the 5′ to 3′ lagging strand is synthesised in fragments utilising an RNA primer at the 3′ end of the lagging strand to assist DNA synthesis in fragments in the 5′ to 3′ direction, Fig. 1.18B. Once the DNA fragments of the lagging strand are synthesised, they are joined by DNA polymerase I and ligase to construct single continuous strand of DNA, Fig. 1.18C. The final segment of 5′ to 3′ DNA (where the RNA primer was bound) is not completely replicated and a 3′ single strand overhang is formed, Fig. 1.18D. The process of terminal chromosomal lost in DNA replication is termed “the end-replication problem” [153, 154].

1.20 Telomere Structure and Function

To prevent DNA sequences from continual erosion at their physical ends due to end-replication problem, chromosomes are capped by telomeres which consist of hexameric sequences of repeated nucleotides [155]. Telomeres can be defined as discrete, tandem

arrays of simple DNA repeats that contain the ends of linear chromosomes, capable of providing chromosome end protection through circumventing the end-replication problem. Telomere erosion occurs during each round of DNA replication due to the end replication problem; however it can also be accelerated by exposure to oxidative stress [156]. Telomeres initiate replicative senescence once they reach a critical length due to shortening.

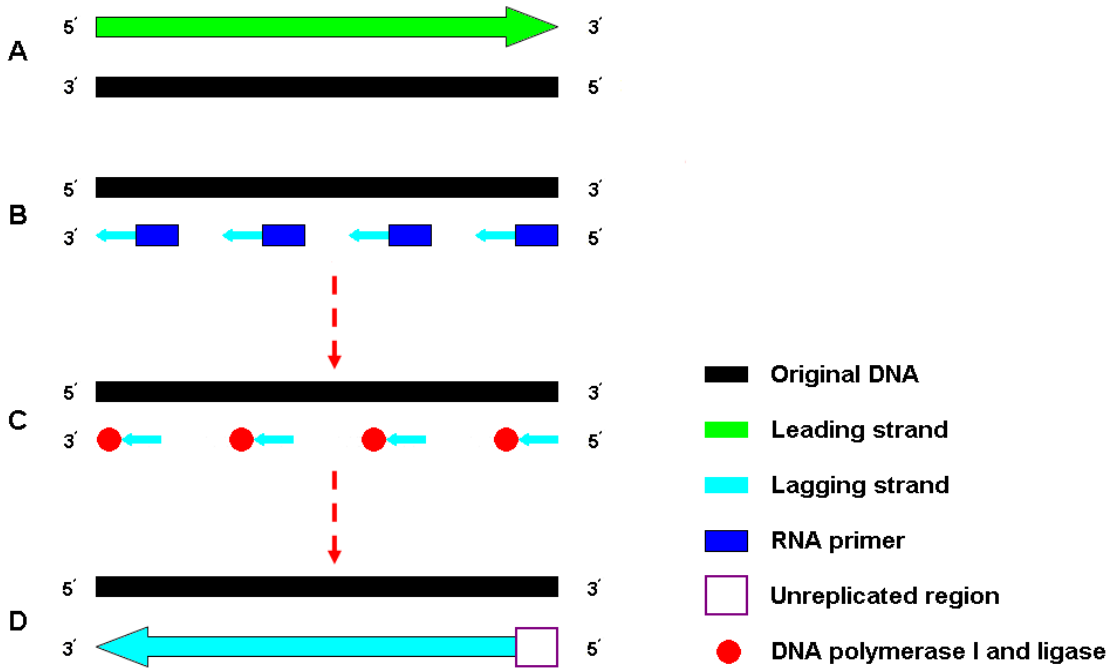

Fig. 1.18 The end replication problem. **A)** New DNA is synthesised in the 5´ to 3´ direction, the 3´ to 5´ leading strand is copied to completion during the replication. **B)** The 5´ to 3´ lagging strand is synthesised in segments in the 5´ to 3´ direction utilising an RNA primer. **C)** The fragments are then joined by DNA polymerase I and DNA ligase to form a constant strand of DNA. **D)** The ending portion of the lagging strand, where the RNA primer binds, remains unreplicated, and a 3´ single strand overhang is formed [154].

1.20.1 Structure of Telomeres

Both the sequence and length of telomeres vary between species. Telomeric DNA is composed of tandem arrays of short, G-rich repeats. In humans, the repeat is TTAGGG and in most plants is TTTAGGGG [157]. Although the number of telomere repeats is variable, a telomere requires a certain minimum number of repeats to be functional. Human telomeres range from 10 to 15kb whereas the telomeres of the mouse, *Mus musculus*, are typically longer than 25kb [158, 159].

1.20.2 G-overhangs

The common and essential feature of all telomeres is the existence of a G-rich strand running in the 5´ to 3´ direction relative to the terminus in a short single-stranded (ss) 3´ overhang. This guanine-rich strand is longer than the complementary c-rich strand, forming a 3´ single strand protrusion known as the G-overhang. The first evidence for the presence of G-overhangs originated from the ciliates *Oxytricha nova* and *Euplotes crassus* in which the overhang was only 14 nucleotide (nt) long [160]. Subsequently, ss TG1-3 tails were found in *Saccharomyces cerevisiae* by non-denaturing Southern blotting [161]. In plants, at least half of the telomeric ends possess the overhang, approximately 20-30 nt long [162]. G-overhangs have also been detected in humans, approximately 150 nt long [163].

The length of G-overhang varies among different species; however it is proportional to the length of bulk telomere tracts. Longer G-overhangs are detected in organisms sheltering longer telomere tracts. For instance, in vertebrates the G-overhang is approximately 250 nt long [163], while in *Tetrahymena* G-overhangs are only14-21 nt long [162].

The exact mechanism of G-overhang generation is yet to be discovered. G-overhangs are naturally produced during the lagging strand synthesis, when the most 3´ RNA primer is removed as depicted in Fig. 1.19. Although, the G-overhang provides a substrate for telomerase elongation and the leading strand replication mechanism produces a blunt end DNA product, Fig. 1.19, G-overhangs are present on both chromosome ends due to the replication of either the leading or lagging strand mechanisms. Therefore, an alternative mechanism for G-overhang generation must be present to construct a symmetrical terminus [163, 164]. The presence of asymmetric G-overhangs in mammalian cells indicates that G-overhangs on the leading and lagging strands are generated by different mechanisms. It is presumed that G-overhangs are formed through a combination of telomerase action and nucleolytic resection of the C-strand, Fig. 1.19 [165]. Moreover, it has been reported that the absence of Mre11, a nuclease involved in telomere length maintenance and DNA double-strand break repair, results in G-overhang signal reduction [165] and telomere dysfunction due to improper telomere function. The G-overhang is an essential structural and functional feature of

the chromosome which protects telomeres from end-to-end chromosome fusions during telomere replication *in vivo* [165].

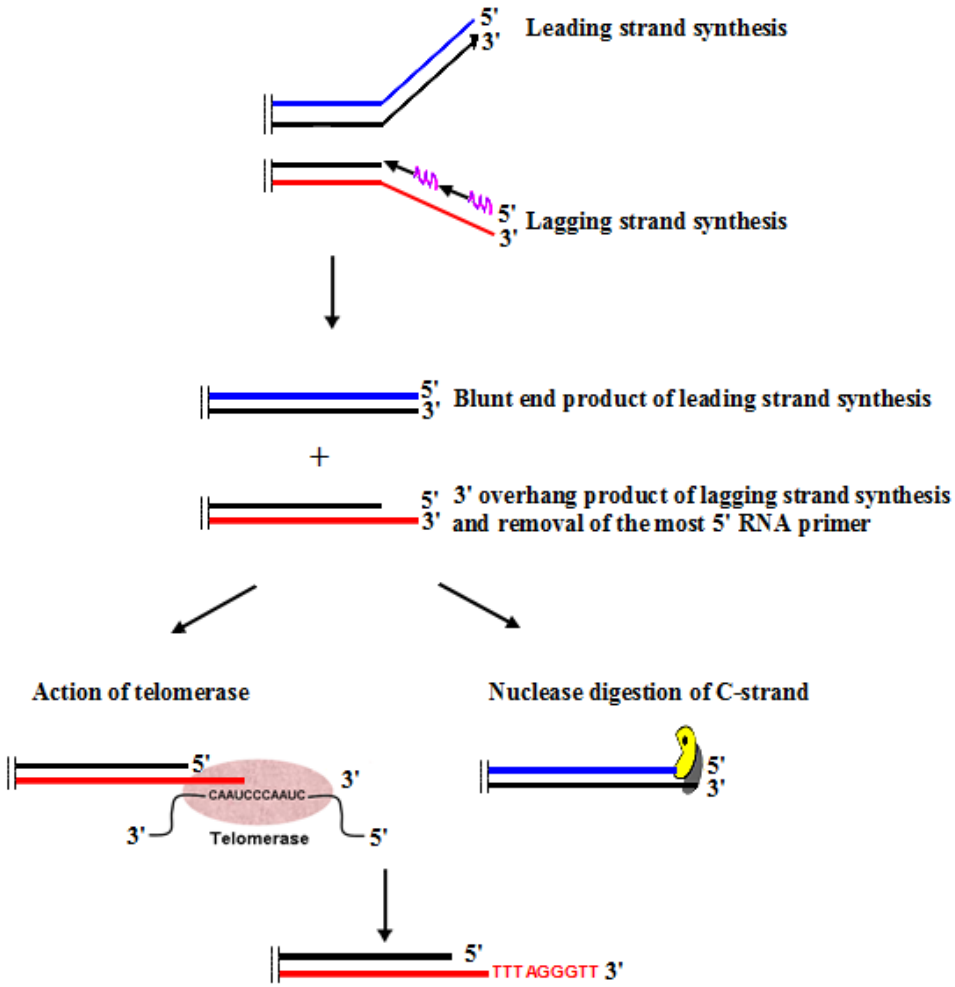

Fig. 1.19 Telomere replication. The G-rich and C-rich strands are produced by the leading and lagging strand synthesis respectively. The newly replicated strands are represented in black while the last RNA primer is illustrated in purple. Removal of the last RNA primer leads to the generation of G-overhang on the 3´ end of the lagging strand. Nuclease digestion of the 5´ to 3´ C-strand is presumed to occur on telomeres replicated by the leading strand synthesis to create a G-overhang. Telomerase extends the 3´ overhang through reverse transcription. The RNA subunit binds the 3´ overhang. Telomerase is represented by the pink oval. Newly added telomere repeats are shown in red [166].

1.20.3 T-loop

Jack Griffith detected lariat-like molecules in enriched telomeric restriction fragments *in vitro* by electron microscopy of Psoralen/UV cross-linked DNA [167]. G-overhangs are involved in the formation of the protective structure known as the t-loop, in which they fold back and invade the duplex telomeric repeats, creating a displacement loop (D-

loop) consisting of ss G-rich repeats. T-loop was found *in vitro* in many evolutionary distant species, including plants and animals [167-169]. However, t-loops have not been found in budding yeast even though their telomere repeats are highly irregular. This may be due to the limited base-pairing between the G-overhang and a C-rich strand of duplex DNA, preventing t-loop formation in *S. cerevisiae* [170]. Although the exact function of the t-loop *in vivo* is not known, it is presumed to be involved in chromosome end protection via sequestering the G-overhang and the telomeres from deleterious manners [171]. The t-loop is thought to unfold during the S-phase to make telomeres accessible for telomere repeat addition via telomerase as shown in Fig. 1.20.

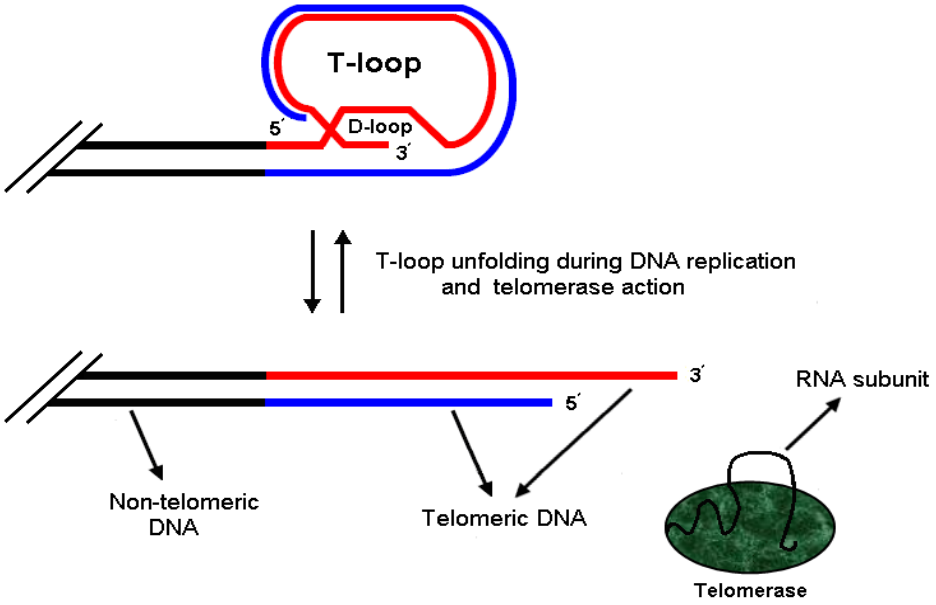

Fig. 1.20 Proposed structure for telomeres. The 3´ G-rich telomere overhang invades and displaces duplex telomeric DNA, forming a t-loop. During DNA replication and telomerase action, the t-loop unfolds during the S phase.

1.20.4 Telomere Function

As previously stated, the higher order structure of telomeres allows them to act as a protective measure at chromosome ends. Telomeres circumvent end-to-end chromosome fusions, preventing the formation of dicentric chromosomes. Additionally, the protective structure of telomeres prevents the loss of genetic information from sub-telomeric regions which may occur via stochastic processes. Furthermore, telomeres have an important role in distinguishing chromosome ends from DNA DSBs and preventing DNA damage signalling [172].

Chromosome instability due to end-to-end fusion takes place when telomeres reach a critical length and cells bypass replicative apoptosis [173]. The function of enzyme telomerase is to add repetitive telomere sequence to chromosome ends in order to maintain or elongate the telomeres. Telomere erosion in cells with mutation within shelterin protein is abnormally rapid due to unprotected telomeres recruiting DNA damage response factors, resulting in either apoptosis or senescence [173].

1.21 Hayflick's Limit and Telomere Length

Hayflick's limit, discovered by Leonard Hayflick in 1961, is referred to as a clock or timing mechanism, representing the replicative limit of normal cells undergoing a specific number of population doublings (PD). This is presumably due to the telomeres reaching a critical length. This phenomenon can cause cell senescence due to cell division blockage when the Hayflick's limit is reached in telomeres of human cells. This mechanism appears to be directly related to ageing, genomic stability and the development of cancer [174, 175].

1.22 Telomere Length Dynamics

Several studies have reported that telomere length varies in human tissues and between individuals. Mean telomere length was found to be similar between different tissues of a single foetus, although it significantly varied between individuals [176]. Particularly, the telomere length of haematopoietic stem cells (HSC) usually varies between 8.5kb and 13kb at birth [177]. The factors that determine the telomere length variations at birth are not fully understood, yet it is thought to be genetically determined. For instance, the telomere length variability of peripheral blood lymphocytes (PBL) is less in monozygotic twins than in dizygotic twins [178, 179]. Consequently, variations in the proliferative potential of HSCs of different individuals could be justified by substantial variations in the mean telomere length between individuals.

Telomeres are dynamic structures that can shorten or lengthen. A balance between telomere shortening and lengthening activities in each cell leads to the formation of species-specific length of the telomere tract [180]. Moreover, the rate of telomere loss differs among different cell types. For example, the rate of telomere loss *in vitro* cultured endothelial cells is approximately 190bp/PD while it is approximately 50bp/PD in fibroblasts [181].

Telomere shortening is primarily due to incomplete replication of the DNA ends which is attributed to the semiconservative nature of the DNA replication process. The shortening process involves the removal of the last RNA primer from the extreme 5´ terminus of the daughter strand during the lagging strand synthesis where this single-stranded region cannot be filled in by the DNA replication mechanism. This DNA amplification failure is referred to as the end replication problem [154, 182]. However, the shortening process could occur through other active mechanisms including telomere rapid deletion (TRD) of exceptionally long telomeres and telomere attrition caused by deficiency in key regulators of telomere length [182].

1.23 Telomere Length Maintenance Mechanisms

Telomere maintenance mechanism is crucial for immortalisation. However, the majority of normal human somatic cells do not employ such a mechanism, with the exception of HSCs, Endothelial Progenitor Cells (EPCs) and germ cells [183, 184]. Telomere maintenance in human cells may be due to the enzyme telomerase or an alternative lengthening of telomeres (ALT) mechanism. In the absence of enzyme telomerase or ALT mechanism, telomeres become critically short and may result in DNA degradation, telomere fusions, activation of DNA damage pathways and ultimately senescence or cell death [184].

1.23.1 Telomerase

As previously stated, telomeres shorten with each cell division due to the end-replication problem. Consequently, once telomeres reach a critical length, after a finite number of cell division, the protective cap can no longer be produced and chromosome ends are recognised as a DSB [152]. Telomere loss can be counteracted by the action of a specialised enzyme called telomerase. Telomerase is a ribonucleoprotein reverse transcriptase, capable of telomere elongation using the G-overhang as a substrate. The human telomerase enzyme consists of three components: the reverse transcriptase catalytic unit hTERT, the RNA template hTR or hTERC and the nucleolar phosphoprotein dyskerin [185, 186].

Extension of G-rich telomeric DNA by telomerase involves several steps including alignment, nucleotide addition and translocation, Fig. 1.21. The RNA subunit of telomerase contains a sequence complementary to the G-rich telomeric repeat. In

humans, this sequence is 5´ CUAACCCUAAC 3´, which is employed as a template for extending the 3´ G-overhang of the telomere through reverse transcriptase subunit (hTERT), Fig. 1.21. Subsequently, endogenous DNA polymerases extend the 5´ lagging strand. The human telomerase RNA component (hTR) is constitutively expressed in human cells. TERC characteristics at the nucleotide level differ amongst various tissues except the template region. Nevertheless, TERCs share a common highly conserved secondary structure that comprises of a pseudoknot, template, template boundary regions and an H/ACA domain, which is important for pre ribonucleo proteins (RNP) formation and nucleolar localisation of the telomerase RNP itself. Dyskerin is necessary for the stability of hTR and the entire telomerase complex. Dyskeratosis congenita, a pathology which results in bone marrow failure due to progressive telomere shortening, occurs as a result of mutation in Dyskerin [187, 188].

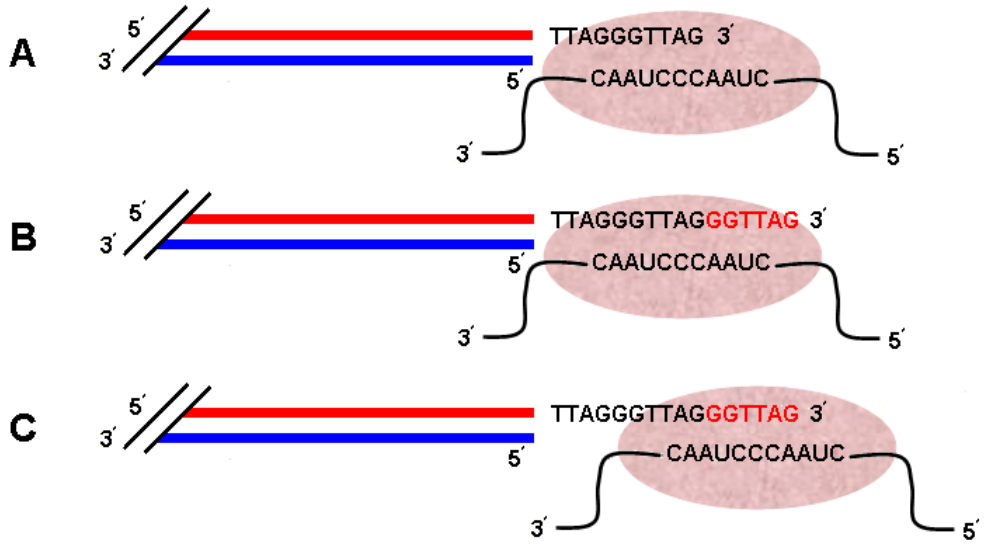

Fig. 1.21 The mechanism of telomere extension by human telomerase. **A)** Alignment. Telomerase is orient by Watson-Crick base pairing between the RNA template and the 3´ terminus of the G-overhang. **B)** Extension of the G-overhang. Six nucleotides are added (shown in red). **C)** Translocation of telomerase. Once the 5´ boundary in the RNA is reached, telomerase translocates so that the RNA template is repositioned for the next round of synthesis. Pink oval and curved black lines represent TERT and TERC respectively.

hTERT is the limiting component of telomerase activity, since telomerase activity is reconstituted through ectopic expression of hTERT. The TERT subunit of telomerase is a reverse transcriptase (RT) that varies in size, ranging from 148 nt in ciliates to 400-600 nt in vertebrates and to approximately 1300 nt in yeast [189]. The TERT contains all seven canonical RT motifs (1, 2, A, B, C, D, E) which are conserved in other RTs. In

addition, TERT consists of a large N-terminal extension and a small C-terminal extension, both of which are required for telomerase activity. TERT is a unique RT as it stably associates with the intrinsic TERC component. Another feature that distinguishes TERT from other RTs is the capability to processively add short repeats. There are various mechanisms regulating TERT expression and telomerase activity. hTERT is presumed to be positively and negatively regulated by phosphorylation and ubiquitination respectively. Telomerase expression is repressed by several genes implicated in tumorigenesis, including the Menin, Mad/Myc pathway and TGFβ target Sip1 [190].

The telomerase activity *in vivo* has been extensively investigated using knockout mice that did not express either RNA template (mTR or mTERC) or catalytic reverse transcriptase subunit (mTERT) [191, 192]. These investigations revealed that mTR and mTERT were not essential for survival since the knockout mice were fertile and viable for at least four generations. However, these knockout mice showed greater rate of telomere shortening with no detectable telomerase activity. Despite the absence of telomerase activity, HSCs isolated from the mTR or mTERT knockout mice successfully engrafted lethally irradiated mice [193]. Nevertheless, the number of times the HSCs derived from the control mice could be serially transplanted was twice that of the knockout mice. These findings indicated that telomerase may contribute in limiting the telomere shortening during serial transplantation, thus extending the lifespan of HSCs.

In humans, telomerase is expressed in actively dividing tissues such as germline and cancer cells but not in most somatic cells. Telomerase activity can be accessed *in vitro* using a single-stranded telomeric DNA primer, radio labelled nucleotides and the telomere repeat amplification protocol (TRAP) assay. However, the TRAP assay is more accurate since it utilises PCR for telomerase detection [194]. Telomerase has a general affinity for G-rich oligonucleotide sequences where it preferentially binds to telomeric sequence primers over non-telomeric sequences. Nevertheless, many telomeric-like sequences can be extended through the enzyme [195].

1.23.2 ALT Mechanism

Recent developments in telomerase detection techniques demonstrated that around 10% of human tumours and 25% of tumour cell lines did not express telomerase activity

[196]. The results indicated that the cells lacking telomerase activity appeared to have long, heterogeneous telomeres, ranging in length from 10 to 50kb. Further analysis indicated that the telomeres in such cells were maintained through an alternative lengthening of telomeres (ALT) mechanism which involves recombination of telomeric ends, Fig. 1.22 [196]. However, the exact mechanism involved in such a process is yet to be determined. Although the ALT mechanism is commonly associated with tumour cells, it may maintain telomeres in normal murine tissues [197].

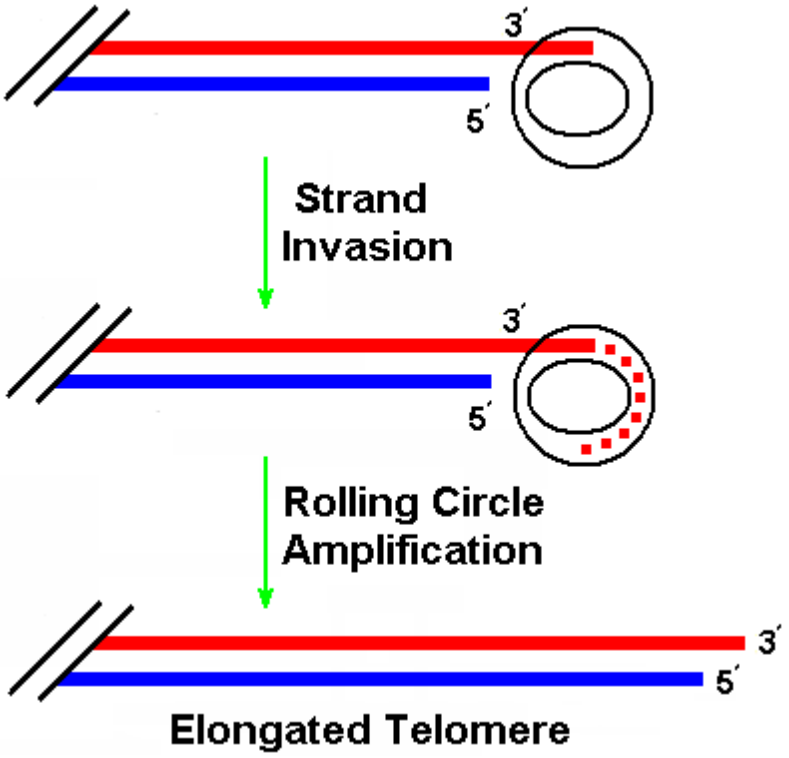

Fig. 1.22 ALT mechanism. In the absence of telomerase, telomere elongates via rolling circle amplification.

There are several unique features that characterise ALT cell lines, including heterogeneous telomere length, presence of extra-chromosomal linear and circular telomeric DNA (ECTR), high frequency of telomere-sister chromatid exchanges (T-SCE) and ALT associated promyelocytic leukemia bodies (APBs) [155, 198].

Telomere length in ALT cells is highly variable. Analysis of ALT cells using terminal restriction fragment (TRF), Q-FISH and single telomere length analysis revealed that these cells included long and heterogeneous telomeres ranging from 2 to greater than 20 kb within an individual cell [199-201]. This heterogeneity is generated by a combination of gradual telomere attrition and rapid lengthening or shortening events.

The former is due to the shortening of telomeres at a rate similar to that reported for telomeres of somatic cells without telomerase, mainly due to incomplete replication, while the later can be explained by homologous recombination (HR) with unequal T-SCE.

ECTR DNA molecules are also present in ALT cells which take many forms including predominantly double-stranded telomeric circles (t-circles), partially single-stranded circles and linear double-stranded DNA [202]. However, very limited information is available regarding the ECTR molecules other than that they are commonly, but not exclusively, associated with the ALT-associated promyelocytic leukemia bodies (APBs) [203].

ALT cells also contain unique large specialised ALT-associated promyelocytic leukemia (PML) nuclear bodies (APBs) ranging in size from 0.1 to 1μm. PML nuclear bodies are nuclear matrix-associated structures of unknown function that contain PML protein and have been implicated in a wide variety of cellular processes including oncogenesis, apoptosis and DNA damage responses. PML in APBs is also accompanied by SP100 protein. In addition, PML protein co-localises with telomeric DNA, telomere binding proteins and several proteins involved in DNA replication, recombination and repair [204, 205]. Although, the exact role of APBs in the ALT mechanism is still unknown, there is a clear association between the presence of APBs and the utilisation of ALT in telomere maintenance [198].

Another characteristic of ALT cells is the occurrence of T-SCEs with higher frequency than telomerase-positive cells or normal cells. The molecular explanation of T-SCEs is yet to be fully established; nevertheless, several studies have shown that the activation of ALT results in the recruitment of proteins required for SCE at telomeres. In addition, it has been previously reported that telomeric DNA in ALT cells contains nicks and gaps which may lead to structural impediment to DNA replication and therefore result in T-SCEs. Moreover, SCEs may also originate from the DNA damage since telomeres are vulnerable to breakage and SCEs are involved in the repair of double-strand breaks [206, 207]. The previous findings [208, 209] has led to the hypothesis that unequal T-SCEs in ALT cells can result in one daughter cell with an elongated telomere (prolonged proliferative capacity) and another daughter cell with a shortened telomere (decreased proliferative capacity). Therefore, this could lead to unlimited proliferation

of the cell population, provided there exists a mechanism with which elongated telomeres can be segregated into one daughter and shortened telomeres into the other [202, 208].

1.24 Telomeres and Ageing

Telomeres shorten stochastically and also during each cell division. Progressive telomere loss, due to cell division, is an important timing mechanism linked to replicative senescence, which is characteristic of "ageing" both in cell culture and *in vivo* [210]. The hypothesis of ageing in telomeres is based on the detection of shorter telomeres in somatic tissues of older individuals compared to the younger ones. This trend holds true when comparing somatic and germline cells whereby telomeres in the former cells are shorter. Telomeres of cells obtained from young individuals progressively shortened when grown in cell culture. In contrast, elongating telomeres *in vitro* by telomerase expression extended the proliferative capacity of the cultured human cells [210]. Furthermore, examination of children diagnosed with progeria revealed the existence of shorter telomeres in some somatic tissues than the age-matched controls [211]. Although further investigation is necessary to determine the impact of cellular senescence due to telomere loss on biological ageing, recent findings indicate the contribution of impaired telomere maintenance to both accelerated and normal ageing [212].

1.25 Telomere Length and FRDA

Telomeres at the ends of chromosomes become shorter as cells divide in the process of ageing. Telomere length has been considered as a biological marker of age. In humans, telomere length shortening is associated with pathogenesis of diseases, including cancers, dementia, hypertension, diabetes mellitus, cardiovascular diseases, dyskeratosis congenita, ulcerative colitis, atherosclerosis and metabolic syndrome. Telomere shortening has also been found in age-related neurodegenerative diseases such as Alzheimer's disease (AD), Parkinson's disease (PD), Huntington's disease [213]. FRDA is a neurodegenerative disorder caused by a reduction in frataxin expression, resulting in mitochondrial dysfunction and oxidative damage. Oxidative-induced telomere DNA damage is an important determinant of telomere shortening since it accelerates the rate of telomere attrition and chromosomal instability [156]. Although recent research demonstrated a significant telomere shortening in human FRDA

peripheral blood leukocytes [214], there is very limited information available regarding the status of telomere length in FRDA cells. Therefore, the hypothesis has been made that oxidative-mediated telomere shortening may contribute to FRDA pathogenesis.

1.26 Aims of the Project

FRDA is a progressive neurodegenerative disorder with no effective therapy. The Ataxia Research Group at Brunel University established a GAA repeat expansion-based *FXN* yeast artificial chromosome (YAC) transgenic mouse model in a *Fxn*-null background. Copy number variation (CNV) frequency difference between the cases and control subjects at specific loci is necessary to determine whether a given CNV plays a role in the progression of a disease or impacts the expression of a clinical trait. Therefore, the first aim of this research project was to investigate the copy number and integration sites of the *FXN* gene in different mouse models and to determine the distribution of the *FXN* transgenes among the mouse chromosome, chapter II.

On the other hand, FRDA mouse models are likely to have impaired function of the human transgene-derived frataxin with potential functional deficiencies in motor coordination ability and changes in physical status that are consistent with the FRDA disease [31]. In addition, 10-30% of the FRDA patients develop overt diabetes and 30% have impaired glucose tolerance [215]. Therefore, the effects of *FXN* deficiencies on function of FRDA mouse models were investigated using different tests of motor coordination, balance and strength. Subsequently, glucose and insulin tolerance tests were carried out to investigate the possibility of diabetes in the FRDA mouse models, chapter III.

Furthermore, the frataxin mRNA and protein levels as well as the somatic GAA repeat instability were examined in the FRDA mouse models to identify their correlation with FRDA-like pathological phenotype, chapter IV.

Moreover, it has been demonstrated that the FRDA cells are more sensitive to ionising radiation than the control cells, suggesting that FRDA is a DNA repair-deficient disorder [216]. In addition, oxidative stress has been reported to accelerate the rate of telomere attrition and chromosomal instability [156]. Therefore, it was hypothesised that telomere length may be shortened due to oxidative damage in the FRDA patients. Consequently, the telomere length and rate of telomere shortening in the FRDA cells were measured, chapter V.

CHAPTER II

DETERMINATION OF AMPLIFICATION OF THE *FXN* GENE USING TAQMAN COPY NUMBER AND FLUORESCENCE *IN SITU* HYBRIDISATION ASSAYS

2.1 Introduction

Copy number variation (CNV) is an important polymorphism associated with genetic diseases such as cancer, immune diseases and neurological disorders. It can influence the expression of genes within and/or close to the rearranged region(s). CNV can be caused by genomic rearrangements such as deletion, duplication, inversions and translocations, allowing transcription levels to be higher or lower than those that can be achieved by controlling the transcription of a single copy. They form at a faster rate in comparison to other types of mutation and can arise both meiotically and somatically [217-219]. Therefore, copy number variation frequency difference between cases and control subjects at specific loci is necessary to determine whether a given CNV plays a role in disease or impacts the expression of a clinical trait.

Copy number variations in the genome can be detected using different techniques such as array comparative genomic hybridisation (aCGH), SNP arrays from GWAS (Genome Wide Association Studies) [220], CNV-seq [221], TaqMan copy number and fluorescence *in situ* hybridisation (FISH) assays. In this chapter two different techniques, TaqMan copy number and FISH assays, were performed to investigate the copy number and integration site of the *FXN* transgene. The former is one of the most sophisticated techniques designed for the detection and measurement of CNV in the human genome. This technique is quantitative and robust with high reproducibility, accuracy, specificity and sample throughput. The latter is widely used for the analysis of genes and chromosomes.

2.2 Hypothesis and Research Objectives

2.2.1 Hypothesis

As previously described in section 1.14 (chapter I), the Ataxia Research Group at Brunel University established GAA repeat expansion-based *FXN* YAC transgenic mouse models in a null background, YG8R and YG22R, containing 190+90 and 190 GAA repeat sequence respectively. This was achieved by crossbreeding human genomic YAC transgenic mice that contained the entire *FXN* gene and expanded GAA repeats with heterozygous *Fxn* knockout mice. A new YG8sR (YG8R with a small GAA band) line was recently generated by crossbreeding YG8R with Y47R (control transgenic mice contained the same human *FXN* YAC transgene but with normal-sized GAA repeats) containing a contraction of GAA repeat sequence to a single band with

120 GAA repeat units. It was hypothesised that the number of integral copies of the *FXN* gene can vary between different lines due to duplication, either within intron 1 or other segments, or deletion of the *FXN* gene, originating from unequal crossing-over between homologous chromosomes, Fig. 2.1.

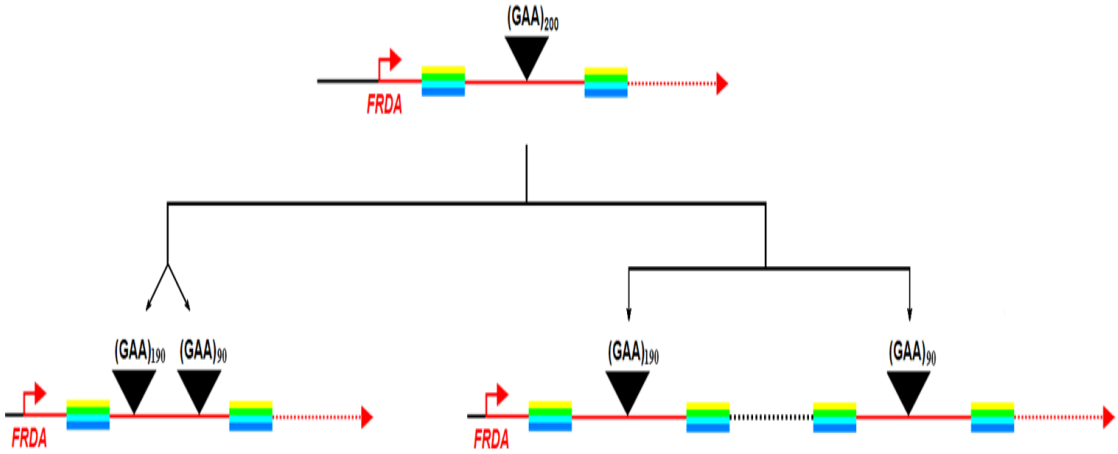

Fig. 2.1 Copy number variation by homologous recombination. The duplication of the *FXN* gene containing GAA repeats may undergo two paths, within intron1 (left) or within other segments (right). The same mechanism can result in deletion.

2.2.2 Research Objectives

- To investigate the copy number variation of the *FXN* gene in YG8, YG22, YG8s and Y47 Lines using TaqMan copy number assay
- Investigation of homozygous and hemizygous YG8 copy number using TaqMan copy number assay
- Comparison of the *FXN* gene copy number of YG8, YG22, YG8s and Y47 lines within different generations using TaqMan copy number assay
- To verify the results obtained from copy number assay and to determine the integration site of the *FXN* transgene using fluorescence *in situ* hybridisation assay

2.3 Materials and Methods

2.3.1 TaqMan® Copy Number Assay

2.3.1.1 Genomic DNA Extraction

Genomic DNA (gDNA) was isolated from mouse-tails using phenol/chloroform method. Tails, 5mm in length, were collected in 1.5ml tubes (Eppendorf) and digested

by adding 400µl of digestion buffer (100mM Tris-HCl pH 8.0 (hydroxymethyl aminomethane-HCl), 5mM EDTA, 200mM NaCl, and 0.2% SDS and 10µl of 50mg/ml proteinase K (BDH). The samples were subsequently mixed and incubated in a 55˚C waterbath overnight. The next day, the incubated samples were vortexed and 400µl of phenol, equilibrated with Tris-HCl pH 8.0, was added. Samples were vortexed (Whirlimixer) for 15 seconds and centrifuged (Eppendorf Micro Centrifuge Model 5415 R) at 16100 rcf for 5 minutes. The supernatant containing the DNA was removed and

Table 2.1 Sample reading from DNA extraction

Sample name	$A_{260/280nm}$ ratio	$A_{260/230nm}$ ratio	DNA concentration (ng/µl)
WT(8J.38)	1.92	2.83	172.4
YG8(8.2286)	1.67	2.27	112.9
YG8(8.196)	1.94	2.30	533.7
YG8(8.230)	1.89	2.30	550.6
YG8(8.1973)	1.84	1.50	37.9
YG8(8.1070)	1.91	1.25	49.9
YG22(1450)	1.93	2.98	139.9
YG22(PMS2.602)	1.93	2.22	454.1
YG22(PMS2.608)	1.92	2.19	450.0
YG22(PMS2.609)	1.92	2.34	289.7
YG8s(8.2329)	1.92	2.12	247.5
YG8s(8.2330)	1.89	2.17	283.9
Y47(Y.30)	1.87	2.76	144.6
Y47(Y.1)	1.86	2.21	194.3
Y47(Y.2)	1.87	1.94	145.2
Y47(Y47.15)	1.85	1.56	58.9
Y47/43	1.89	2.29	568.0
Y47/15/6/3	2.01	1.45	289.1

transferred to a clean 1.5ml microcentrifuge tube containing 500µl of chloroform/ isoamyl alcohol (24:1, v/v) and gently mixed by inverting tubes and centrifuged again at 16100 rcf for 5 minutes. Next, 350µl of the resulting supernatant was removed to a fresh microcentrifuge tube containing 800µl of absolute ethanol and 30µl of 3M Na-acetate (pH 5.2). Samples were mixed well by inverting tubes several times and subsequently placed at -80˚C for 10-15 minutes. Genomic DNA was precipitated following this step and formed a visible mass. The DNA was pelleted by centrifugation at 16100 rcf for 30 minutes at 4˚C. After removing the supernatant; the DNA was washed with 1ml of 70% ethanol and centrifuged at 16100 rcf for 20 minutes at 4˚C. The ethanol was discarded and the DNA pellets were air-dried for 10-15 minutes at RT. The dried pellets were resuspended in 50µl T.E. (10mM Tris, 1mM EDTA, pH 8.0) buffer and stored at 4˚C. The concentration of DNA was read on the ND1000 spectrophotometer at 260 and 280nm wavelengths using 1µl of DNA. Table 2.1 illustrates the DNA readings extracted from the mouse-tails utilised in this experiment.

2.3.1.2 GAA PCR

A GAA polymerase chain reaction (PCR) was performed on mouse genomic DNA samples to detect the genotype. The primers listed in Table 2.2 were utilised.

Table 2.2 Primer Sequences for GAA PCR

Primer	Sequence (5´➔3´)	Product size (bp)
GAA Forward	GGGATTGGTTGCCAGTGCTTAAAAGTTAG	421
GAA Reverse	GATCTAAGGACCATCATGGCCACACTTGCC	

1µl of DNA was used for amplification in PCR. The following reagents were added to the DNA in a 0.2ml tube:

- 12.5µl of 2× Qiagen Master Mix (Qiagen) containing $MgCl_2$, Taq DNA polymerase and dNTPs)
- 5µl of Q buffer
- 1µl of 50µM GAA reverse primer
- 1µl of 50µM GAA forward primer
- Nuclease free water to 25µl

The samples were mixed and the reactions were carried out in a PTC-225 Pelter Thermal Cycler (MJ Research) using the following program, Table 2.3.

Table 2.3 GAA PCR program

Steps	Temperature	Duration	Cycles
Denaturation	94˚C	2 mins	1
Denaturation	94˚C	10 sec	
Annealing	60˚C	30 sec	10
Elongation	68˚C	45 sec	
Denaturation	94˚C	10 sec	
Annealing	60˚C	30 sec	20
Elongation	68˚C	1 min, with 20 sec increments	
Extension	68˚C	10 mins	1

To visualise the amplicons, a 1% agarose gel made with 100ml 1× TBE (89mM Tris-borate, 2mM EDTA, pH 8.3) buffer was prepared. 1µl of 10mg/ml of ethidium bromide (EtBr) was added per 100ml of agarose gel before pouring the gel into a Flowgen agarose gel electrophoresis tank. Once the agarose gel was set, 300ml of 1× TBE buffer was added and each PCR sample was loaded into appropriate wells in the gel. 5µl of 1kb plus DNA ladder (Invitrogen, UK) was used to accurately size the PCR product. The gel was run at 70V for 30-60 minutes until the PCR products were run three quarters of the way into the gel. The PCR products were then visualised using a UVP GDAS (Gel Documentation Analysis System) 1200 under the ultraviolet light. Three

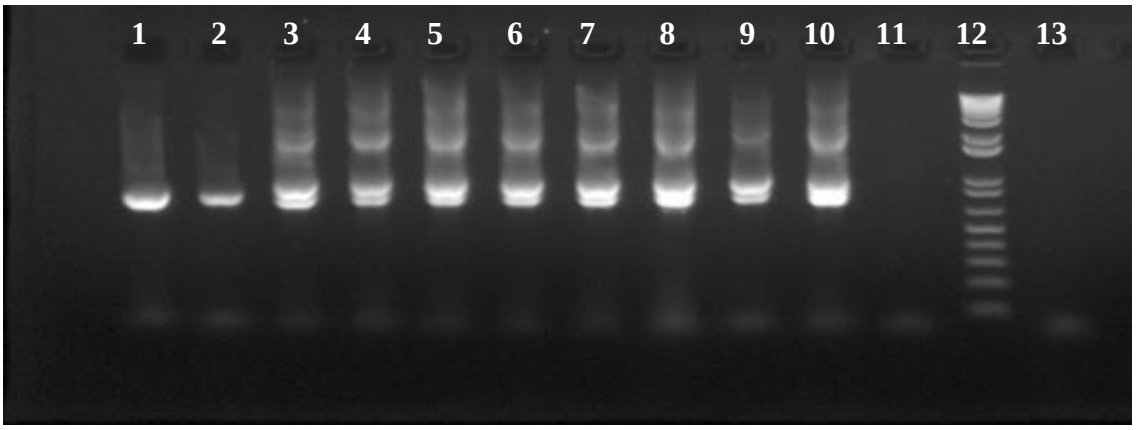

Fig. 2.2 Agarose gel electrophoresis of GAA PCR reaction products from FRDA transgenic mouse tissues. Lanes 1 to 9 are templates. Lane 10, 11 and 13 are positive, negative and dH_2O negative controls respectively. A $1kb^+$ DNA Ladder was used for size evaluation.

controls (positive, negative and blank (water) controls) were used. A single band should be seen in a positive lane, and no band should be seen in a negative control lane. The size of the PCR products must match the expected product size, Fig. 2.2.

2.3.1.3 *Fxn* KO PCR

This PCR was performed to identify the wild type or knockout *Fxn* alleles. The primers listed in Table 2.4 were used.

Table 2.4 Primer Sequences for KO PCR

Primer	Sequence (5´➔3´)	Product size (bp)
WJ5	CTGTTTACCATGGCTGAGATCTC	Wild-type allele (WJ5-WN39)=**520**
WN39	CCAAGGATATAACAGACACCATT	
WC76	CGCCTCCCCTACCCGGTAGAATTC	Mutant allele (WJ5-WC76)=**245**

1µl of DNA was used for amplification in PCR. The following reagents were added to the DNA in a 0.2ml tube:

- 12.5µl of 2× Kapa Master Mix (Kapa Biosystem, UK) containing $MgCl_2$, Taq DNA polymerase and dNTPs)
- 0.5µl of 50µM WJ5 primer
- 0.5µl of 50µM WN39 primer
- 0.1µl of 50µM WC76 primer
- Nuclease free water to 25µl

The samples were mixed and the reactions were carried out in a PTC-225 Pelter Thermal Cycler (MJ Research) using the following program, Table 2.5.

Table 2.5 KO PCR program

Steps	Temperature	Duration	Cycles
Denaturation	94ºC	1 min	1
Denaturation	94 ºC	20 sec	30
Annealing	54 ºC	20 sec	
Elongation	72 ºC	20 sec	
Extension	72ºC	10 mins	1

The amplicons were analysed by agarose gel electrophoresis in 1× TBE buffer as previously described in Section 2.3.1.2. The PCR products were then visualised using a

UVP GDAS 1200 under the ultraviolet light. Four controls (wild-type, heterozygous, rescue and blank (negative) controls) were used. The size of the PCR products must match the expected product size, Fig. 2.3.

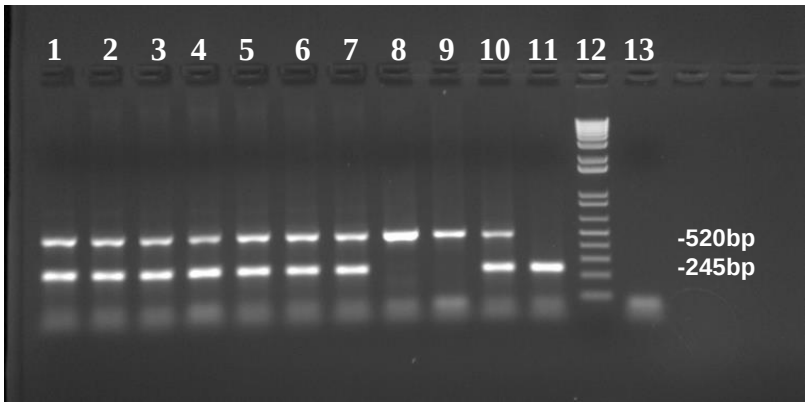

Fig. 2.3 Agarose gel electrophoresis of KO PCR reaction products from FRDA transgenic mouse tissues. Lanes 1 to 8 are templates. Lanes 9, 10 and 11 are wild-type, heterozygous, rescue positive controls respectively. Lanes 12 and 13 are $1kb^{+}$ DNA and negative control (dH_2O) respectively.

2.3.1.4 Preparation of Genomic DNA Samples

Genomic DNA (gDNA) was quantified using the UV absorbance (A_{260}/A_{280}) measurement, ensuring A_{260}/A_{280} ratio greater than 1.7, and diluted to 5ng/µl using 1× TE (Tris-EDTA) buffer (pH 8.0) to make a 5× stock solution.

2.3.1.5 TaqMan® Copy Number Assays

TaqMan® copy number assays are run simultaneously with a TaqMan® copy number reference assay in a duplex real-time polymerase chain reaction (PCR). The copy number assay amplifies the target gene or genomic sequence of interest and the reference assay amplifies a sequence that is known to exist in two copies in a diploid genome. A TaqMan® copy number reference assay (Applied Biosystems), containing mouse-specific Tert (Telomerase Reverse Transcriptase) forward and reverse primers and a TaqMan TAMRA™ probe, and two predesigned TaqMan® copy number assays (Applied Biosystems), containing human-specific *FXN* forward and reverse primers and a TaqMan MGB probe, were used in this experiment, Table 2.6. The location of the TaqMan® copy number assays is shown in Fig. 2.4. The TaqMan MGB probe includes a FAM™ reporter dye attached to the 5´ end, a nonfluorescent quencher (NFQ) and a minor groove binder (MGB) attached to the 3´ end (MGBs increase the melting temperature (T_m) without increasing the probe length, allowing the design of shorter

probes). The TaqMan TAMRA™ probe includes VIC® reporter dye attached to the 5´ end and TAMRA™ quencher attached to the 3´ end.

Table 2.6 TaqMan® Copy Number Human-specific *FXN* Assays

Assays	Chr	Reporter Dye	Context Sequence (5´➔3´)	Location on Transcript or Gene	Product size (bp)
Hs05092416-cn	9	FAM	CTCCAGCAGAGCTAAGCATCAAGTA	Within Intron3	106
Hs02407730-cn	9	FAM	TTCGAACCAACGTGGCCTCAACCAG	Intron1- Exon2	80

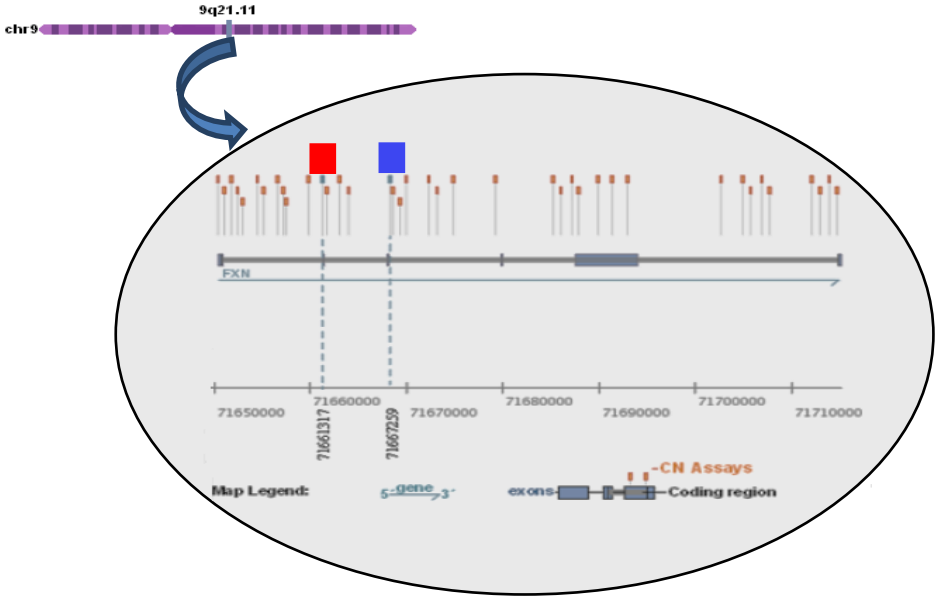

Fig. 2.4 Schematic representation of the TaqMan®copy number assays located on the *FXN* gene, cytoband 9q21.11c, the blue and green squares indicate the location of the Hs05092416-cn and Hs02407730-cn assays respectively.

2.3.1.6 Preparation of the Reactions

The master mixes listed in Table 2.7 were prepared for an extra 2 reactions in 1.5ml

Table 2.7 Reaction mixture component and volumes

Reaction mixture component	Volume per well (µl) 96-well plate
2× TaqMan® Universal Master Mix (Applied Biosystems) containing Ampli*Taq*®GoldDNA polymerase, ultra-pure and dNTPs	10.0
TaqMan® Copy Number Assay, 20× working stock	1.0
TaqMan® Copy Number Reference Assay, 20×	1.0
Nuclease-free water	4.0
Total Volume	**16.0**

centrifuge tube based on the reaction volume and the number of reactions (using four replicates of each sample).

The following samples were run on each plate using four replicates for each gDNA sample:

- **Samples or Unknowns:** gDNA samples in which the copy number of the target is unknown.
- **No Template Controls (NTC):** A sample that does not contain a DNA template, used for the detection of contamination and background fluorescence.
- **Calibrator sample:** A DNA sample with a known copy number for the target of interest.

16µl of the reaction mixture was added into each well of a MicroAmp® *Fast* Optical 96-well Reaction Plate (Applied Biosystems) using a p20 pipette (Gilson). The diluted gDNA samples were mixed and spun (Microcentrifuge 5415 C, Eppendorf) briefly before pipetting to the plate. 4µl of gDNA (5ng/µl) was added to the wells containing the reaction mixture. The reaction plate was sealed with MicroAmp® Optical Adhesive Film (Applied Biosystems) and centrifuged for 10 seconds at 101 rcf. The reaction plate was loaded into a ABI Prism® 7900 HT real-time PCR instrument (Applied Biosystems) using the following program:

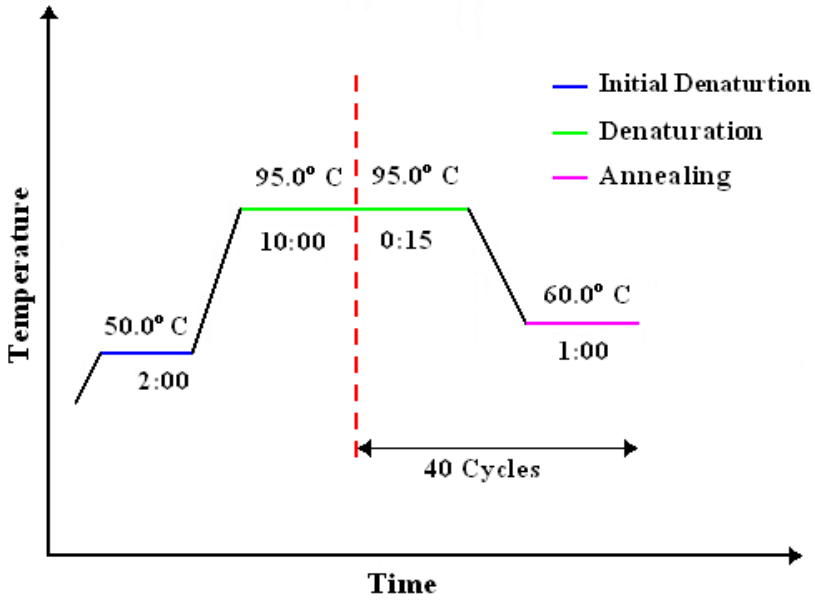

Fig. 2.5 Schematic diagram of qPCR program

During PCR, the gDNA template is denatured and each set of assay primers anneals to its specific target sequences. Each TaqMan probe anneals specifically to its

complementary sequence between forward and reverse primer binding sites. When each oligonucleotide probe is intact, the proximity of the quencher dye to the reporter dye causes the reporter dye signal to be quenched. During each round of PCR, the target and reference sequences are simultaneously amplified by Ampli*Taq*®Gold DNA polymerase. This enzyme has a 5´ nuclease activity that cleaves probes that are hybridized to each amplicon sequence. When an oligonucleotide probe is cleaved by the Ampli*Taq*®Gold DNA polymerase 5´ nuclease activity, the quencher is separated from the reporter dye increasing the fluorescence of the reporter. Accumulation of PCR products can be detected in real time by monitoring the increase in fluorescence of each reporter dye at each PCR cycle, Fig. 2.6.

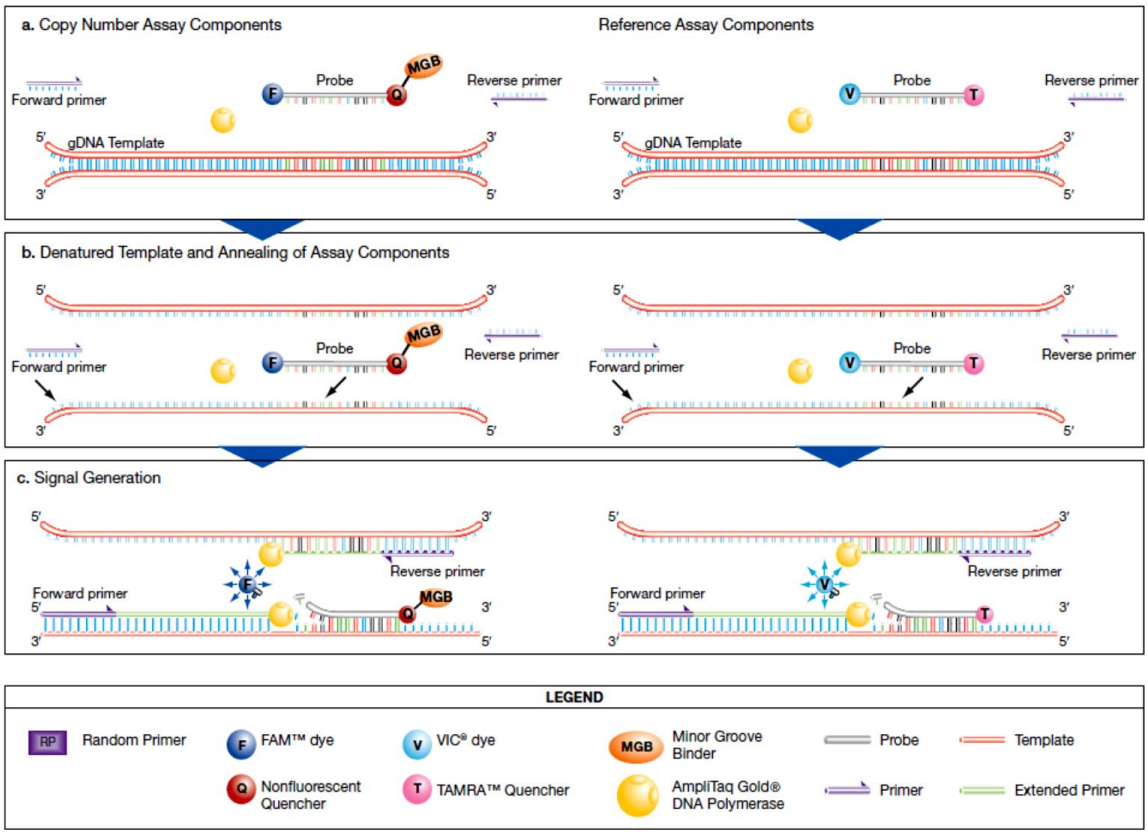

Fig. 2.6 PCR and detection of target and reference gDNA sequences in a duplex reaction [222]

The number of copies of the target sequence in each genomic DNA sample was determined by relative quantitation (RQ) normalized to the known copy number of the reference sequence using the comparative Ct (ΔΔCt) method and the Ct data were subsequently compared to a calibrator sample known to have two copies of the target sequence, analysed by Applied Biosystems CopyCaller™ Software v.2.0. The predicted

copy number values were calculated by rounding up the actual copy number values (for example, calculated values of 0.4 and 0.5 corresponded to predicted values of 0 and 1 respectively).

2.3.1.7 Statistical Analysis

All statistical analysis (standard deviation) was performed using CopyCaller® Software v.2.0 (Applied Biosystems).

2.3.2 Fluorescence *in situ* Hybridisation Assay

2.3.2.1 Cell Culture

Fibroblast cell lines were studied for the detection of human *FXN* gene by fluorescence *in situ* hybridisation. The cell cultures consisted of four mouse fibroblastic cell lines developed from four different FRDA transgenic mice (YG8R, YG22R, YG8sR and Y47R). Mouse fibroblasts were established from kidney of FRDA transgenic mice using the method described by Gomes-Pereira and Monckton [223]. The mouse was dissected on a clean bench and the kidney was collected aseptically in 50ml 1× sterile ice-cold PBS. The kidney was transferred to a laminar-flow hood to avoid contamination and placed on a 10cm tissue culture dish with 10ml of ice-cold sterile PBS and washed briefly to remove blood cells and fat tissues. The tissue was minced into approximately $1mm^3$ cubes and transferred into a sterile 15ml conical tube containing 10ml sterile ice-cold PBS. These tissue pieces were allowed to settle down over a period of 2 minutes after which the PBS was aspirated. Subsequently, they were washed twice with 10ml sterile PBS. Then 5ml of prewarmed 0.25% trypsin/EDTA solution was added and the culture dish was incubated in a humidified 5% CO_2 incubator at 37˚C for 30 minutes by gently inverting the tube after every 5 minutes. The plunger was removed from a 5ml syringe and the pieces of tissue and enzymatic solution were transferred into the syringe. The plunger was placed back in syringe and the contents of the syringe were squirted into a $25cm^2$ tissue culture flask, through a sterile 18-gauge needle. The tissue culture flask was placed in the incubator for an additional 15 minutes. The contents of the flask were transferred into a 15ml conical tube, the pieces of cellular debris were allowed to settle down over a period of 2 minutes and then the supernatant was transferred into a fresh 15ml conical tube for centrifugation at 389 rcf for 5 minutes. The supernatant was removed and the cell pellet

was cultivated in a 25cm^2 tissue culture flask containing 5ml of DMEM culture medium (Gibco) supplemented with 10% fetal bovine serum (Gibco) and 2% Pen-Strep (Gibco). The primary cultures were incubated at 37˚C in a 5% CO_2 humidified incubator. The primary fibroblasts were ready in 5-7 days in culture.

2.3.2.1.1 Mycoplasma PCR Testing

Mycoplasma PCR was carried out using Mycosensor™ PCR Assay Kit (Stratagene). Briefly, 100µl of supernatant was taken carefully from a culture flask into a sterile 1.5ml Eppendorf tube and incubated for 5 minutes at 95˚C in a water bath. 10µl of strataClean was added to the tube and mixed well by flicking the tube followed by the centrifugation at 15700 rcf for 1 minute. 20µl of supernatant was transferred to a fresh 0.5ml PCR tube and placed on ice until required to use. 5µl of supernatant was used for amplification in PCR. The following reagents were added to the samples in a 0.25ml tube:

- 5µl 10× PCR buffer (Qiagen)
- 2.5µl Q buffer (Qiagen)
- 1µl 25mM $MgCl_2$
- 1µl 10mM dNTP mix
- 2µl primer mix
- 0.5µl *Taq*DNA polymerase (5U/µl)
- 4µl internal control template
- 29µl dH_2O

The samples were mixed and the reactions were carried out in a PTC-225 Pelter Thermal Cycler (MJ Research) using the following program, Table 2.8.

Table 2.8 Mycoplasma PCR program

Steps	Temperature	Duration	Cycles
Denaturation	94ºC	30 sec	1
Denaturation	94ºC	30 sec	
Annealing	55ºC	1 min	35
Elongation	72ºC	1 min	
Extension	72ºC	10 mins	1

To visualise the results, 10-15µl of PCR products were separated in 2% agarose TBE mini-gels along with a 1kb$^+$ DNA ladder (Invitrogen) at 75V for ~30 minutes, Fig. 2.7.

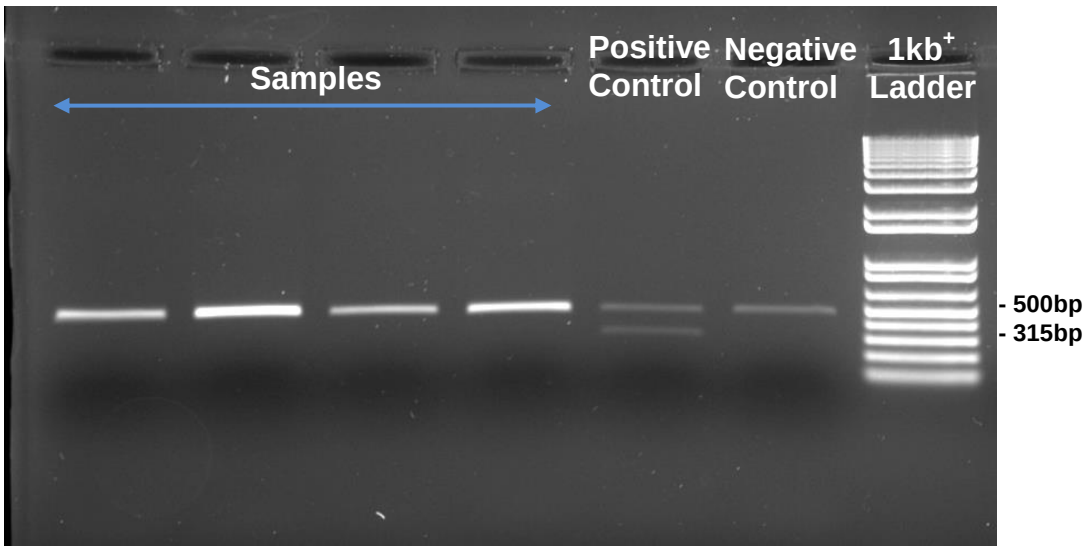

Fig. 2.7 Agarose gel electrophoresis of mycoplasma PCR reaction products from FRDA transgenic mouse fibroblast cell lines. Lanes 1 to 4 are templates. Lane 5 and 6 are positive and negative controls respectively. A 1kb$^+$ DNA Ladder was used for size evaluation.

2.3.2.1.2 Harvesting of Cultures and Preparation of Slides

Culture medium, PBS and Trypsin/EDTA solutions were prewarmed to 37˚C in a water bath. Before harvesting, cells were treated with 0.1µg/ml colcemid (Sigma) for 1 hour. The medium was removed by vacuum suction and cells were washed gently with sterile PBS. Adherent fibroblasts were digested with trypsin/EDTA for 5 minutes at 37˚C in the CO_2 incubator to bring them into suspension. The trypsin/EDTA solution was neutralized by adding 10ml of DMEM culture medium. Cells were collected by centrifugation at 389 rcf for 5 minutes and treated with 10ml of hypotonic solution (0.075M KCl) for 15 minutes at 37˚C and fixed with methanol:acetic acid (3:1). The process of fixation was repeated two more times for 10 and 30 minutes at RT respectively and each time 1ml of fresh fixative was added drop wise, followed by the addition of 2ml of extra fixative solution. Subsequently, the cell pellets were resuspended in fresh fixative solution and 15µl of cell suspension was spread on a wet slide which was then air-dried.

2.3.2.2 Preparation of DNA Probes

2.3.2.2.1 Bacterial Artificial Chromosomes (BACs)

The BACs, 265B8 and 876N18, used in this study were a kind gift from Dr. Joseph Sarsero (Murdoch Children's Research Institute, Melbourne, Australia) [224]. Bacterial cells containing the probe were first grown as streaks on an agar plate containing luria Bertani LB medium (1% (w/v) NaCl, 1% (w/v) Bactotryptone, 0.5% (w/v) yeast extract, 1.5% (w/v) Agar and 12.5µg/ml chloramphenicol. Plates were incubated overnight at 37˚C and the positive colonies were then taken from the culture and cultivated again in 10ml of fluid LB-broth culture medium supplemented with 12.5µg/ml chloramphenicol overnight with vigorous shaking at 37˚C. 500µl of an overnight bacterial culture was mixed with 500µl of glycerol (80% in LB medium) and stored at -20˚C or at -80˚C for long term storage. 4ml of the overnight culture was centrifuged for 10 minutes at 800 rcf and the supernatant was discarded. The pellet was resuspended in 300µl of P1 buffer containing 15mM Tris-HCl (pH 8.0), 10mM EDTA and 100µg/ml RNase A (sigma-Aldrich) and the cells were lysed by adding 300µl of P2 lysis buffer containing 0.2M NaOH and 1% SDS followed by gentle mixing and 5 minutes incubation at RT. The lysate was then neutralised by adding 300µl of buffer P3 containing 3M Potassium Acetate, gently mixed and incubated on ice for 10 minutes. The reaction was centrifuged at 9300 rcf for 10 minutes at 4˚C and the supernatant containing the DNA was transferred to a fresh 2ml tube. The DNA was precipitated by adding 800µl of ice-cold isopropanol, mixing and incubating overnight at -20˚C. After overnight incubation the tubes were centrifuged at 9300 rcf for 15 minutes at 4˚C. The DNA pellet was washed with 500µl of ice-cold 70% ethanol, centrifuged at 9300 rcf for 10 minutes at 4˚C, air-dried and dissolved in 40µl of ddH_2O. The DNA was stored at -20˚C.

2.3.2.2.2 Confirmation of Probe Amplification Region Using PCR

In order to verify the inserts and amplification regions, the probe DNAs were subjected to PCR amplification with primers for FRDA exon 1-5b, STM7 exon 14 and FR6 [225], Table 2.9. As represented in Fig. 2.8, a 188kb BAC clone 265B8 contained exon 1 to 5b of the human *FXN* locus and PIP5K1B (STM7) gene upstream of the FRDA locus, whereas 876N18 clone contained the entire human *FXN* locus following FR6 gene downstream of exon 5.

Table 2.9 PCR Primers for Amplification of *FXN* (X25) Exons

Exon	Forward Primer (5´➔3´)	Reverse Primer (5´➔3´)	Size (bp)	Annealing Temp.
PIP5K14	TAAAGCTGCATTTATTCTTGAG	CTGATGTTGATGTGGTAACAG	254	50
***FXN*1**	AGTAGCCGGCCTCCTGG	GTGGGGCCAACTCTGCC	83	60
***FXN*2**	AGTAACGTACTTCTTAACTTTGGC	AGAGGAAGATACCTATCACGTG	166	50
***FXN*3**	AAAATGGAAGCATTTGGTAATCA	AGTGAACTAAAATTCTTAGAGGG	227	55
***FXN*4**	AAGCAATGATGACAAAGTGCTAA	TGGTCCACAATGTCACATTTCGG	241	55
***FXN*5a**	CTGAAGGGCTGTGCTGTGGA	TGTCCTTAAAACGGGGCT	222	55
***FXN*5b**	CCCATGCTCAAGACATACTCC	ACAGTAAGGAAAAAACAAACAGCC	224	55
FR6	CCTTTCCTGGATGCATTGTGT	TCATGAGGGTGGGACTCTCA	157	58

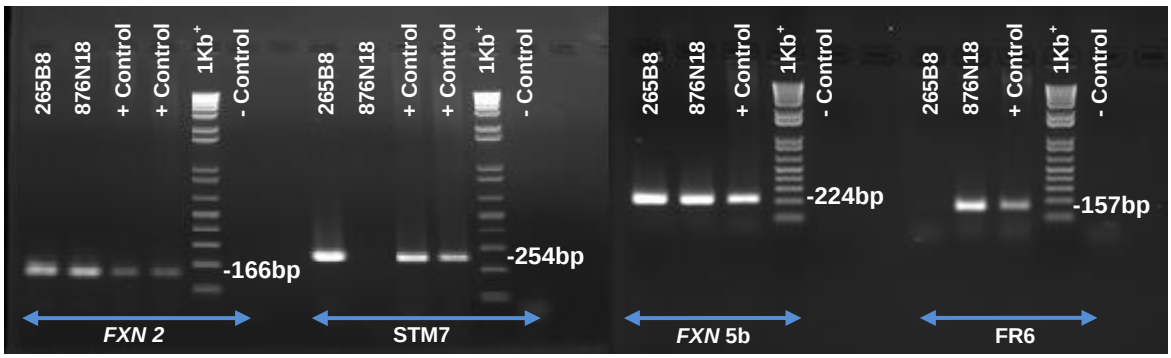

Fig. 2.8 PCR screen for amplification regions of 265B8 and 876N18 clones using 1% agarose gel. 265B8 contained exon 1 to 5b of the human *FXN* locus and PIP5K14 (STM7-exon 14) gene upstream of the FRDA locus, whereas 876N18 clone contained the entire human *FXN* locus following FR6 gene downstream of exon 5. −, negative control (dH2O); +, positive controls (Mp.42 and 62341B) were used as controls. A $1kb^{+}$ DNA Ladder (Invitrogen) was used for size evaluation.

2.3.2.2.3 Measurement of DNA Concentration

DNA concentration was measured with a Nanodrop spectrophotometer (Nanodrop 2000C, Thermo Scientific, UK) using 1µl of the DNA sample, Table 2.10. The purity of the sample was determined by the OD_{260}/OD_{280} ratio. For pure DNA sample this ratio should be between 1.7 and 2.0.

Table 2.10 Quality Check of the DNA Probes

BACs	DNA Concentration ng/µl	Ratio 260/280
RP11-265B8	693.2	1.84
RP11-876N18	486.2	1.79

2.3.2.2.4 Labelling of DNA Probes

In order to detect human *FXN* sequences on FRDA transgenic mouse chromosomes, the corresponding 265B8 and 876N18 probes were labelled with biotin and digoxigenin respectively and detected immunologically with the antibodies coupled to fluorescent fluorochromes. The nick translation method is based on the ability of the DNase I to introduce randomly distributed breaks of a single strand, or nicks, into DNA. The nicks are then filled by DNA-polymerase I, which replaces the removed nucleotides with digoxigenin- or biotin-labelled ones. Labelling by nick translation was performed with DIG-Nick Translation (Roche) and Biotin-Nick Translation kits (Roche) as follows:

- 5µl dNTP Mix (minus dTTP)
- 1µl dUTP conjugated with biotin or digoxigenin
- 1µg of probe DNA
- ddH_2O up to a volume of 45µl

5µl of PolI/DNaseI mix was added to the reaction and mixed gently followed by incubation for 2 hours at 16˚C.

2.3.2.2.5 Gel Electrophoresis

Because the actual size of the probe after labelling reaction plays an important role in maximising specific hybridisation and decreasing background, the fragments of the probe broken by nick translation should be between 200 to 500bp in length. In order to check that the probe DNA has reached a suitable size, 5µl of the labelled probes were loaded onto a 2% agarose gel and proceeded with electrophoresis. A XIII DNA size Ladder (Peq GOLD) was used for size evaluation.

2.3.2.2.6 Purification of Labelled Probes

In order to remove un-incorporated labelled nucleotides, the FISH probes were run through illustra Microspin G50 columns (GE Healthcare, UK). After purification, 5µl of salmon sperm DNA (11.0mg/ml, Invitrogen), 10µl 3M NaAC and 2.25V of ice-cold 100% ethanol were added to the DNA suspension. The DNA was then precipitated overnight at -20˚C and centrifuged at 15700 rcf for 30 minutes at 4˚C. The pellet was washed with 200µl of ice-cold 70% ethanol and centrifuged at 15700 rcf for 15 minutes

at 4˚C. After air drying, the DNA pellet was resuspended in 20µl ddH_2O and stored at -20˚C until use.

2.3.2.3 Dual Colour Fluorescence *in situ* Hybridisation Assay

2.3.2.3.1 Slide Denaturation

Slides were washed three times for 5 minutes with 2× SSC in a Coplin jar on a shaking platform followed by dehydration in 70%, 90% and 100% ethanol for 3 minutes and air-drying. The chromosomal DNA on the glass slides were then denatured in 70% formamide in 2× SSC under the fume hood at 70˚C for 5 minutes. The slides were moved quickly to a coplin jar containing ice-cold 2× SSC for 5 minutes on a shaking platform to stop the denaturing of the DNA and wash the non specific binding. Subsequently, the slides were dehydrated in 70%, 90% and 100% ethanol for 3 minutes and air-dried.

2.3.2.3.2 Probe Denaturation

Before hybridisation, dual colour FISH probes were prepared. 5µl of Cot-1 human DNA (Roche) was added to 5µl of competitor DNAs (Biotin-labelled and digoxigenin-labelled probes) to reduce non-specific background hybridisation signals. The pellets were dried in a vacuum desiccator for 15 minutes and resuspended in 10µl of hybridisation buffer (Sigma). The probe mix was denatured by incubating at 65˚C for 10 minutes, followed by preannealing at 37˚C for 10 minutes.

2.3.2.3.3 Hybridisation

10µl of the probe mix was applied for each slide, covered with a 22×22mm^2 coverslip and sealed with bicycle glue. The slides were subjected to hybridisation at 37˚C overnight using a humid-chamber in a water bath.

2.3.2.3.4 Post-Hybridisation Washes and Detection of Labelled Probes

After hybridisation, the slides were washed in 2× SSC for 5 minutes on a shaking platform to remove the coverslips. Subsequently, slides were placed in a prewarmed coplin jar containing 0.4× SSC for 5 minutes at 70˚C followed by washing in 2× SSC for 5 minutes at RT. The slides were then incubated in freshly prepared blocking

solution (1.8g (3% w/v) of bovine serum albumin (BSA) (Acrose Organic) in 60ml of 4× SSC/Tween®20) for 1 hour at 37˚C to stop non-specific bindings.

Biotin-labelled and digoxygenin- labelled probes were detected with Cy3-conjugated streptavidin and fluorescein isothiocyanate (FITC)-conjugated anti-digoxigenin antibody respectively as follows:

- 1.5µl of Avidin D-Texas Red (final concentration of 2µg/ml) (Vector Laboratories) and 1.5µl of mouse anti- digoxigenin (final dilution of 1:666) (Sigma-Aldrich) were diluted in 1ml of blocking solution. 75µl of this solution was added onto each slide, covered with parafilm and incubated in humid chamber at 37˚C for 20 minutes. Slides were washed three times in 4× SSC/Tween®20 for 5 minutes on a shaking platform in the dark.
- 10µl of biotinylated anti-Avidin D (final concentration of 5µg/ml) (Vector Laboratories) and 1µl of rabbit anti- mouse-FITC (final dilution of 1:1000) (Sigma-Aldrich) were diluted in 1ml of blocking solution. 75µl of this solution was added onto each slide, covered with parafilm and incubated in humid chamber at 37˚C for 20 minutes. Slides were washed three times in 4× SSC/Tween®20 for 5 minutes on a shaking platform in the dark.
- 1.5µl of Avidin D-Texas Red (final concentration of 2µg/ml) and 10µl of monoclonal anti- rabbit-FITC (final dilution of 1:100) (Sigma-Aldrich) were diluted in 1ml of blocking solution. 75µl of this solution was added onto each slide, covered with parafilm and incubated in humid chamber at 37˚C for 20 minutes. Slides were washed three times in 4× SSC/Tween®20 for 5 minutes on a shaking platform in the dark followed by an additional wash in 1× phosphate buffered saline (PBS) (Sigma-Aldrich) for 5 minutes on a shaking platform at RT.
- The slides were mounted with DAPI counterstain (4´,6-diamidino-2-phenylindole dihydrochloride)/Antifade (0.1µg/ml, MP Biochemicals), covered with a 22×40mm^2 coverslip and sealed with bicycle glue.

2.3.2.3.5 Microscope Analysis and Imaging

The slides were visualised through an Olympus BX41 Fluorescence microscope (Zeiss) equipped with a Sensys cooled CCD camera under 100× immersion oil objective.

SmartCapture3 sofware (Digital Scientific) was used for acquisition and storage of FISH analysis. 50 cells were quantified for each sample.

2.3.3 Confirmation of The Presence of *FXN* Exons in YG8s Lines Using PCR

In order to verify the presence of *FXN* exons in YG8s rescue mice, two different YG8s lines (8.2330 and 8.2329) were screened for deletion mutations using PCR. The same primers as those previously described in Table 2.9, Section 2.3.2.2.2 were utilised for FRDA exons 1-5b. The PCR reaction was performed in a total volume of 25µl using 200ng/µl of genomic DNA, 50µM of each primers and 12.5µl of 2× Kapa Master Mix (for exon 1 PCR 12.5µl of 2× Qiagen Multiplex PCR Master Mix and 5µl of Q buffer were used). PCR amplification was performed on a MJ Research PTC-225 thermal cycler using the following parameters: initial denaturation 94˚C, 1 minute, 35 cycles of denaturation 94˚C, 20 seconds, annealing (˚C represented in Table 2.9) 20 seconds, and extension 72˚C, 20 seconds, followed by a final extension of 10 minutes, 72˚C.

2.3.3.1 Optimisation of *FXN* Exon 1 Annealing Temperature Using Gradient PCR

In order to determine the optimal annealing temperature for exon 1 primers, gradient PCR was performed using the gradient function of the universal block set from a gradient of 53˚C to 59.7˚C. The PCR reaction was performed in a total volume of 25µl

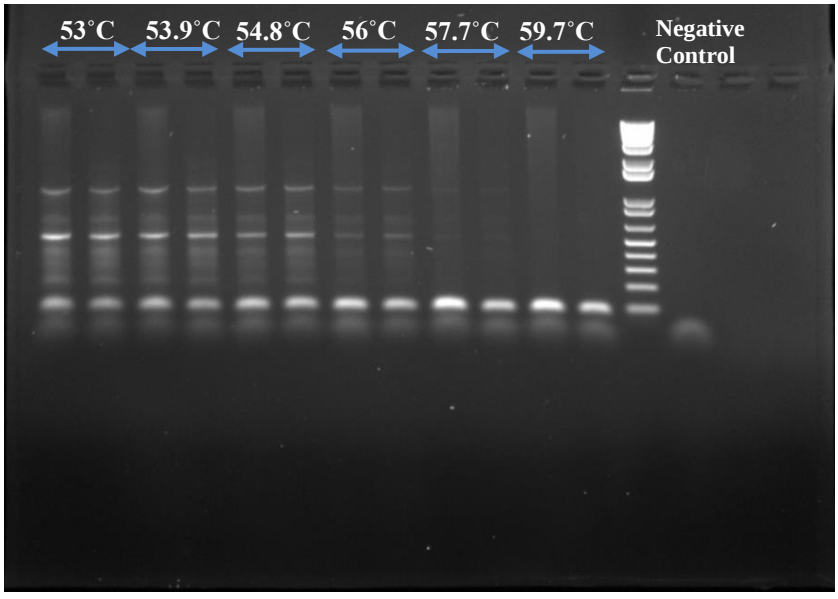

Fig. 2.9 Determination of optimal annealing temperature for *FXN* exon 1 Primers using gradient PCR. The calculated primer annealing temperature was 53˚C; the actual annealing temperature was 59.7˚C.

using 200ng/µl of genomic DNA, 50µM of each forward and reverse *FXN* exon 1 primers, 12.5µl of 2× Qiagen Multiplex PCR Master Mix and 5µl of Q buffer. PCR amplification was performed on a MJ Research PTC-225 thermal cycler using the following test parameters: initial denaturation 94˚C, 2 minutes, 30 cycles of denaturation 94˚C, 30 seconds, annealing 53˚C to 59.7˚C, 30 seconds and elongation 72˚C, 1 minute followed by a final extension of 5 minutes, 72˚C. As shown in Fig. 2.9, best conditions were found in well 10 and 11 of the cycler where the temperature was 59.7˚C.

2.4 Results

2.4.1 Investigation of CNV in FRDA Mouse Models Using TaqMan® Copy Number Assay

2.4.1.1 Detection of CNV of the *FXN* Gene in YG8, YG22, YG8s and Y47 Lines

To detect and measure CNV in the human genome, YG8, YG22, YG8s, Y47 and WT lines were investigated using real-time PCR and unquenching of fluorescent probes for the target sequence. As previously described in Section 2.3.1.5, two sets of TaqMan® copy number assays were applied in this experiment. Hs05092416-cn assay, represented in blue, was designed to amplify a 106bp fragment of *FXN* within intron 3 while Hs02407730-cn assay, represented in red, was designed to amplify an 80bp fragment of *FXN* within intron 1 and exon 2. A TaqMan® copy number reference assay containing mouse-specific Tert was used as the reference which was known to have two copies in a diploid genome. Wild type (WT) line served as a negative control with no copy number to verify the specificity of the primers. The preliminary results indicated that YG22 and Y47 lines had a single copy of the *FXN* gene whereas the YG8 line showed two copies of the target gene, further confirming the duplication hypothesis, Fig. 2.10. YG8s line showed less than one copy of the target gene (CN=0.33) presumed to indicate the deletion of the *FXN* gene, Fig. 2.10. The YG8 (8.2286) line was used as a calibrator. The copy number of the calibrator was assessed using a sample (Y47.15) with two copy number which was previously calculated by competitive copy number PCR analysis [149].

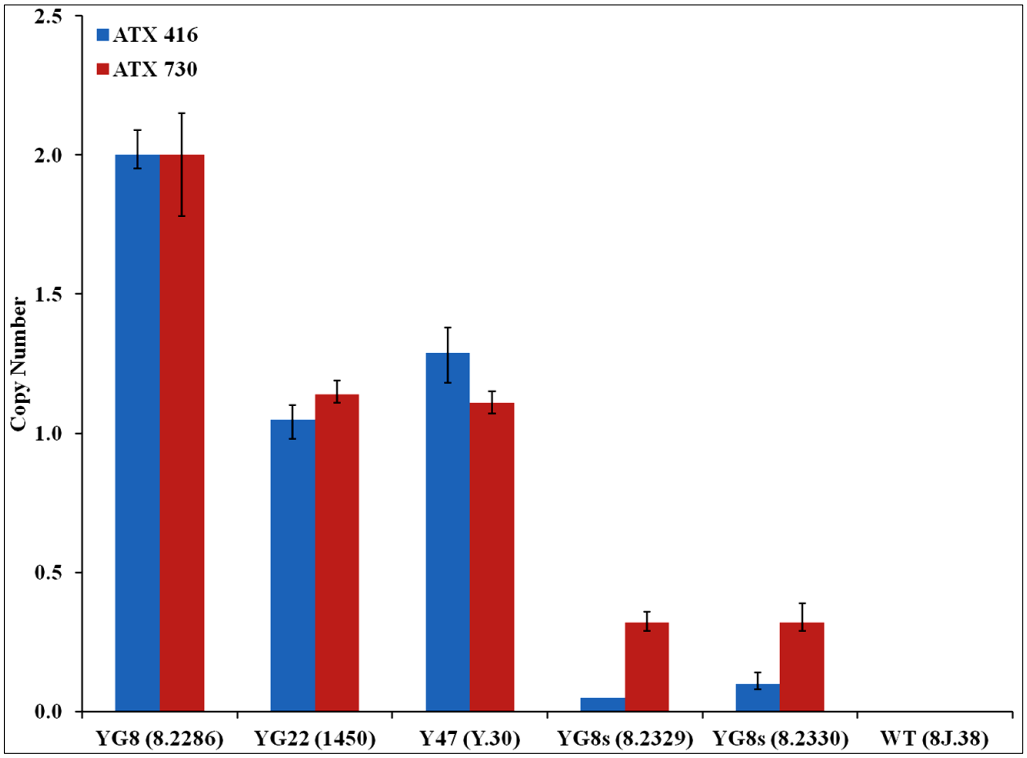

Fig. 2.10 Copy number variation in YG8, YG22, YG8s and Y47 lines. Two TaqMan copy number assays were applied; Hs05092416-cn assay, represented in blue, was designed to amplify a 106bp fragment of *FXN* within intron 3 and Hs02407730-cn assay, represented in red, was designed to amplify an 80bp fragment of *FXN* within intron 1 and exon 2. Wild type (WT) served as a negative control with no copy number while YG8 (8.2286) line was used as a calibrator. Error bars indicate standard deviation.

2.4.1.2 Investigation of Homozygous YG8 Copy Number

As part of this investigation the copy number of homozygous YG8 lines was also measured. Based on the hemizygous results, Fig. 2.10, homozygous YG8 lines were expected to have 4 copies which were confirmed with the TaqMan copy number assay within intron 1 and exon 2, Fig. 2.11. However, the results with the TaqMan copy number assay within intron 3 showed up to 6 copies, confirming the presence of duplication, Fig. 2.11.

2.4.1.3 CNV within Different Generations in Y47, YG8 and YG22 Lines

The relative copy number of YG22 and Y47 lines was studied within different generations. The results indicated an increase in copy number of different YG22 lines which further confirmed the variation in *FXN* copy number within different generations of this line. The increased *FXN* copy number in YG22 ($PMS2^{-/-}$.602, $PMS2^{+/-}$.608 and $PMS2^{-/-}$.609) confirmed the presence of duplication, Fig. 2.12. Although, previously

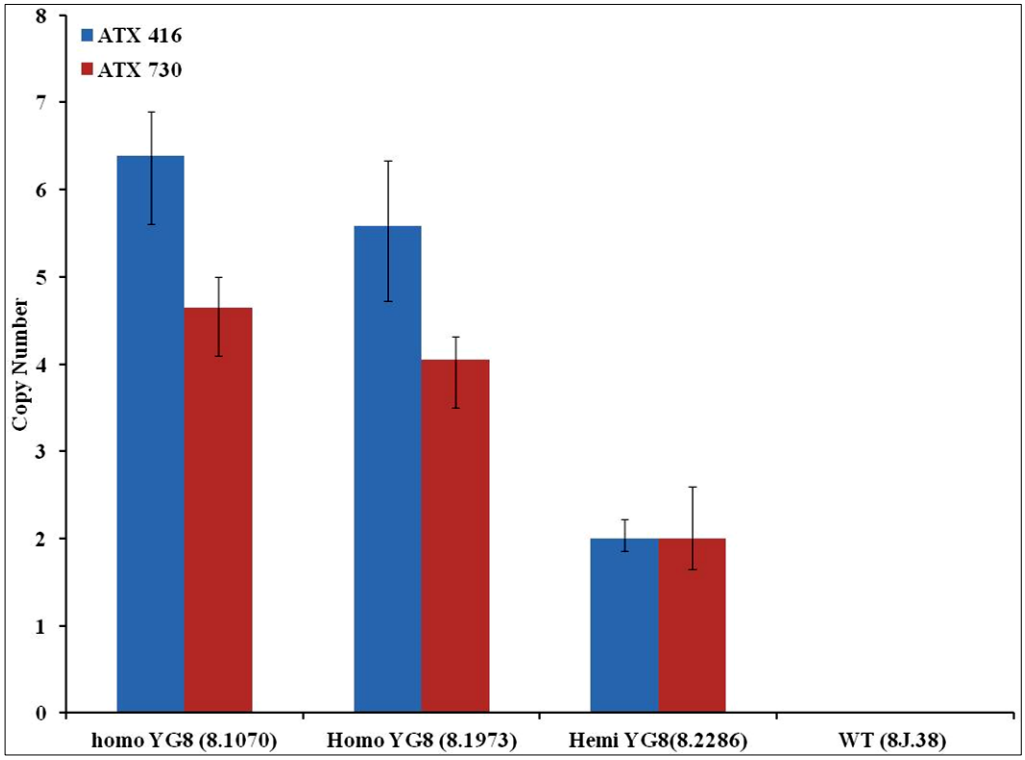

Fig. 2.11 Copy number variation in homozygous YG8 lines. Two TaqMan copy number assays were applied; Hs05092416-cn assay, represented in blue, was designed to amplify a 106bp fragment of *FXN* within intron 3 and Hs02407730-cn assay, represented in red, was designed to amplify an 80bp fragment of *FXN* within intron 1 and exon 2. Wild type (WT) served as a negative control with no copy number, YG8 (8.2286) line used as a calibrator. Error bars indicate standard deviation.

generated Y47 lines, Y47/43, a sibling of first generation (Y47.15); and Y47/15/6/3, third generation, had two copies of the *FXN* gene [149], no difference was detected in the copy number of recently generated Y47 lines (Y.1, Y.2 and Y.30), Fig. 2.13. The apparent discrepancy can be explained by the difference between the C57BL6/J background of the former and the later lines. No difference was identified in *FXN* copy number of all studied hemizygous YG8 lines (data not shown).

2.4.2 Investigation of CNV in FRDA Mouse Models Using Fluorescence *in situ* Hybridisation Assay

Fluorescence *in situ* hybridisation (FISH) using dual colour probes containing the entire RP11-265B8 and RP11-876N18 sequences was performed on both metaphase and interphase spreads of YG8, YG22, YG8s and Y47 cell lines. RP11-265B8 and RP11-876N18 probes were detected with Cy3-conjugated streptoavidin and fluorescein isothiocyanate (FITC)-conjugated anti-digoxigenin antibody respectively to determine

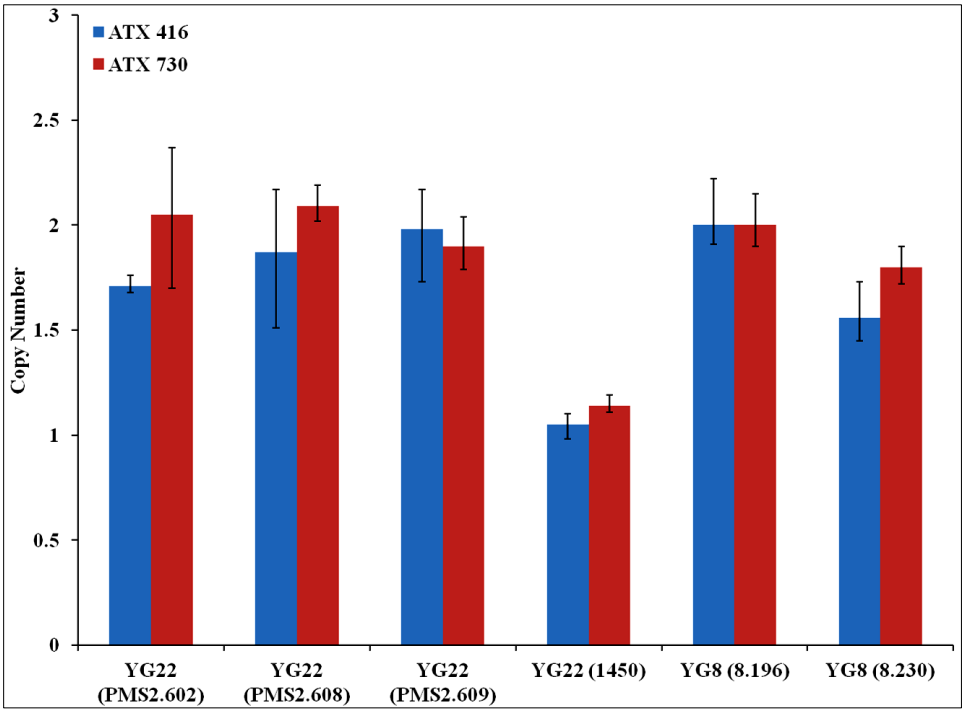

Fig. 2.12 Copy number variation in YG22 lines within different generations. Two TaqMan copy number assays were applied; Hs05092416-cn assay, represented in blue, was designed to amplify a 106bp fragment of *FXN* within intron 3 and Hs02407730-cn assay, represented in red, was designed to amplify an 80bp fragment of *FXN* within intron 1 and exon 2. YG8 (8.196) line with copy numbers of two used as a calibrator.

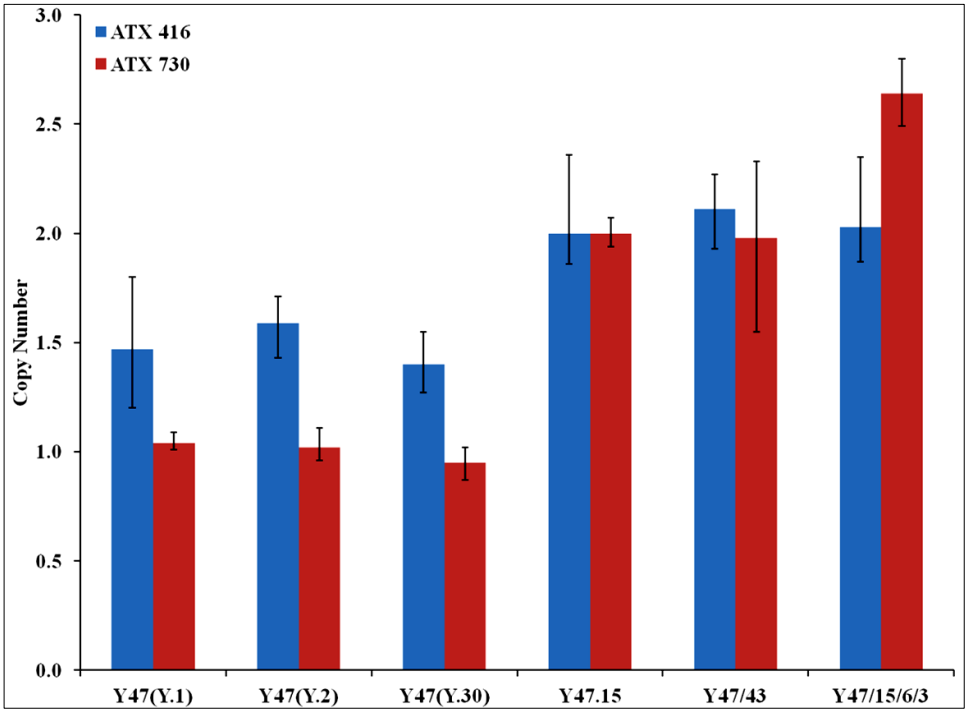

Fig. 2.13 Copy number variation in Y47 lines within different generations. Two TaqMan copy number assays were applied; Hs05092416-cn assay, represented in blue, was designed to amplify a 106bp fragment of *FXN* within intron 3 and Hs02407730-cn assay, represented in red, was designed to amplify an 80bp fragment of *FXN* within intron 1 and exon2. Y47 (Y47.15) line with copy numbers of two used as a calibrator.

the integration site of the transgenic *FXN* gene in YG8 (8.234), YG22 (1107), YG8s (MEF-M3) and Y47 (478.18) cell lines. All four cell lines were found to have a single integration site by analysis of metaphase chromosomes (Fig. 2.14; Metaphase). YG8 showed three hybridisation signals indicating the presence of a single integration site containing multiple copies of the transgenic *FXN* gene (Fig. 2.14; YG8 Interphase), whereas YG22 and Y47 showed one signal indicating one copy of the *FXN* transgene (Fig. 2.14; YG22 and Y47 Interphase). At least 25% of the YG8s cells had no signals (Fig. 2.15), while 75% of those showed one signal corresponded to the transgenic *FXN* gene (Fig. 2.14; YG8s Interphase). This discrepancy can be explained by somatic mosaicism of the YG8s in which one copy of the transgene is indeed present, but in only 75% of the total number of cells. It is important to note that only 5% of the control cells had no signals.

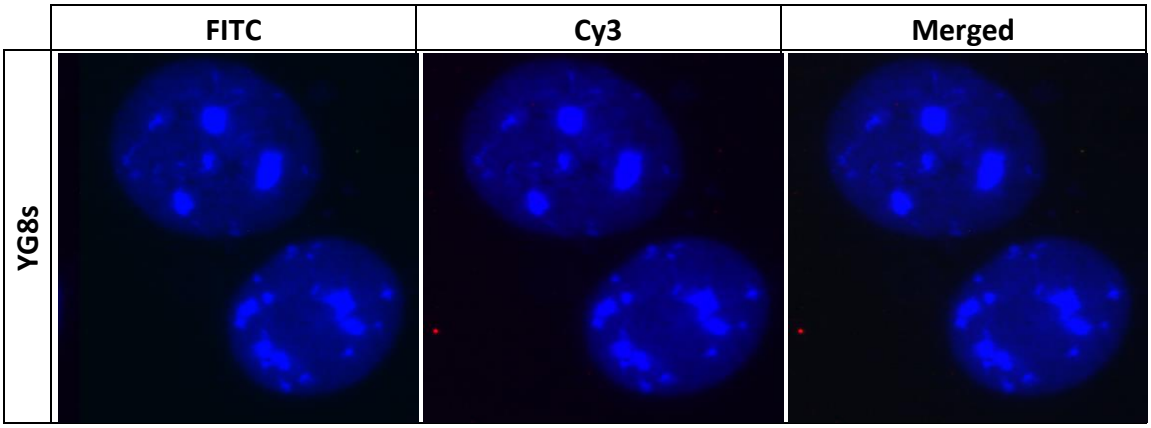

Fig. 2.15 Detection of mosaicism in YG8s transgenic mice. At least 25% of the YG8s cells had no signal, indicating mosaicism in YG8s lines.

2.4.3 Detection of *FXN* Exons in YG8s Rescue Mice

As previously discussed in sections 2.4.1.1 and 2.4.2, the identities of the cloned *FXN* fragment in YG8s lines were investigated by FISH and copy number assays. The copy number results showed less than one copy of the *FXN* gene (CN=0.33) in YG8s lines presumed to indicate the deletion of the *FXN* gene. In contrast the results from the FISH assay indicated the authenticity of the cloned fragment. In order to further examine the presence of *FXN* exons in YG8s rescue mice, two different YG8s lines (8.2330 and 8.2329) were screened for deletion mutations by PCR which allowed for a relatively rapid analysis of the exon sequences. The presence of all *FXN* exons was confirmed using human *FXN*-exon specific primers, Fig. 2.16.

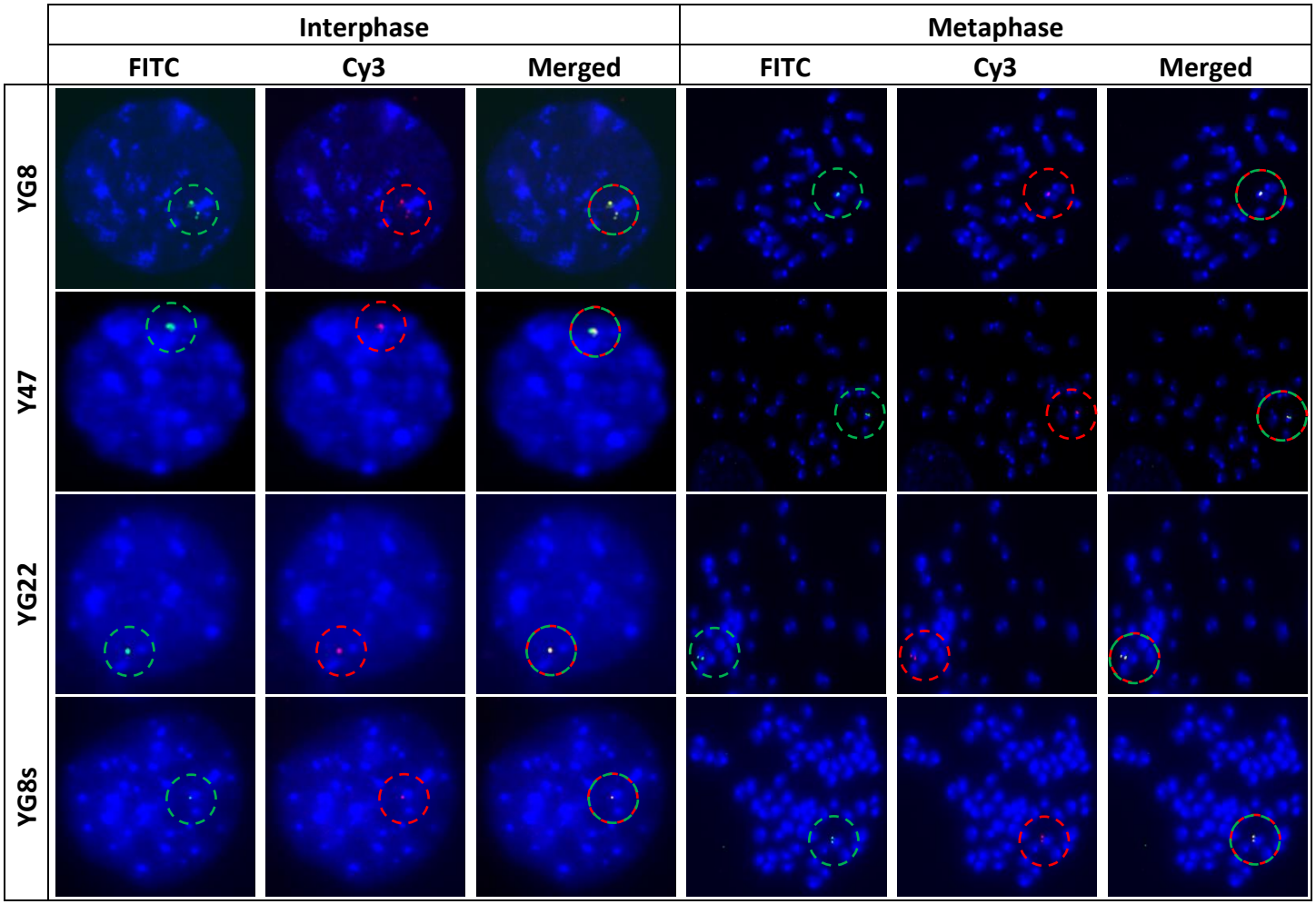

Fig. 2.14 Determination of the integration site of the transgenic *FXN* gene by FISH. Biotin-labelled RP11-265B8 and digoxigenin- labelled RP11-876N18 probes were hybridised onto interphase and metaphase chromosomes (DAPI stained) of YG8 (8.234), YG22 (1107), YG8s (MEF-M3) and Y47 (478.18) cells. **YG8, Y47, YG22 and YG8s Metaphase:** all four cell lines showed a single integration site of the *FXN* transgene by metaphase analysis. **YG8 Interphase:** YG8 showed three hybridisation signals corresponded to the transgenic *FXN*, **Y47 and YG22 Interphase:** whereas YG22 and Y47 showed one signal indicating one copy of the *FXN* transgene. **YG8s Interphase:** 75% of the YG8s cells showed one signal indicating one copy of the target gene.

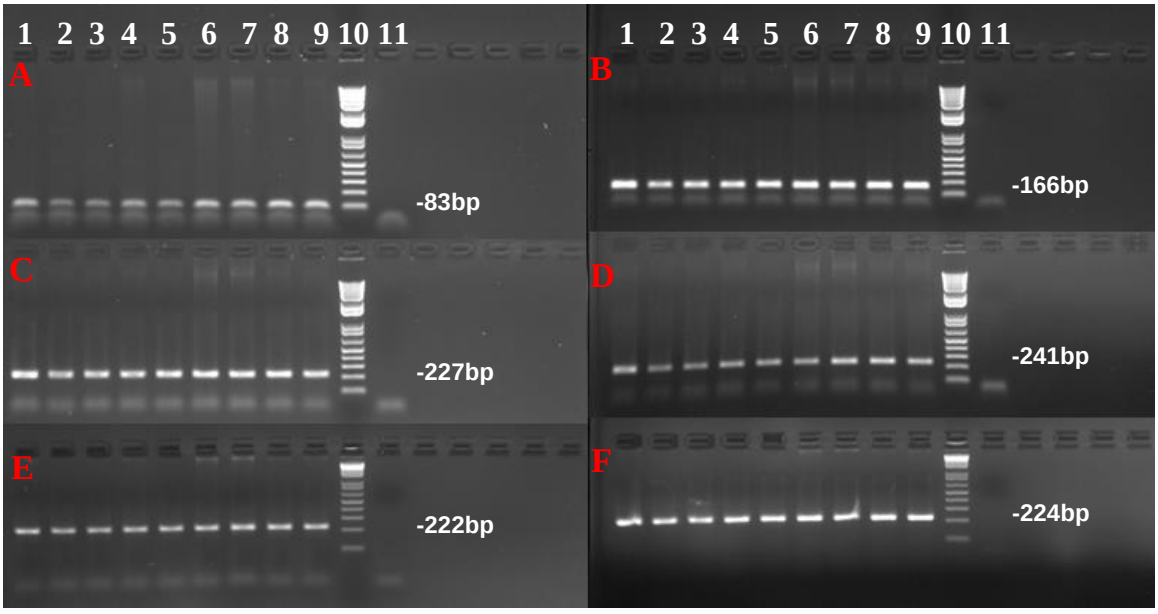

Fig. 2.16 Validation of the presence of *FXN* exons in YG8s rescue mice by PCR. Agarose gel is showing PCR products of A) exon 1, B) exon 2, C) exon 3, D) exon 4, E) exon 5a and F) exon 5b. Lane 1 and 2 are 8.2329 (YG8s) and 8.2330 (YG8s) respectively. Lane 3 to 9 are 8E47.1 (Y47R), 8E47.2 (YG8ER), 8E47.6 (YG8ER), D.147 (YG8ER) and 8J47.144 (Y47R) used as positive controls respectively. Lane 10 and 11 are 1kb^{+} DNA ladder and negative control respectively.

2.4 Discussion

In order to investigate the difference in the *FXN* gene copy number in different samples, two assays corresponding to the gene of interest and the reference gene were adopted to simultaneously quantitate both genes in the same DNA samples using real-time PCR. A single copy gene should have a relative copy number of 1, therefore, a relative copy number greater than 1 indicates the presence of duplication of the target gene while a number smaller than 1 implies deletion of such gene. When duplication occurs, multiple copies of a gene may be closely linked on the same chromosome or may be separated from each other by a large genomic distance. In order to identify the copy number of the *FXN* gene, three different experiments were performed. Firstly, the copy numbers of YG8, YG22, YG8s and Y47 lines were measured. The results indicated that the YG22 and Y47 lines had a single copy of the *FRDA* gene while the YG8 line was shown to have two copies of the *FRDA* gene. These results were in good agreement with those previously reported [103, 149]. The YG8s lines showed less than one copy of the target gene (CN=0.33) presumed to indicate the deletion of the *FXN* gene. Secondly, the copy number of homozygous YG8 lines was measured using the TaqMan copy number assay. The results showed that the YG8 lines had relative copy number of four within intron 1

and exon 2 and up to 6 copies within intron 3. The former was in good agreement with the theoretical expectations based on the hemizygous results while the later confirmed the duplication hypothesis. Finally, the copy number of hemizygous YG22, YG8 and Y47 lines was investigated within different generations. The results indicated an increase in copy number of YG22 lines from 1 to 2, confirming the variation in *FXN* copy number within different generations of this line. However, no difference was detected in the copy number of recently generated Y47 lines even though the previously generated Y47 lines were shown to have two copies of the FRDA gene. These findings were in good agreement with those previously reported [149]. Such discrepancy can be associated with the differences in the C57BL6/J background of the former and the later lines. No difference was detected in *FXN* copy number of all the studied hemizygous YG8 lines.

To further investigate the copy number and integration site of the *FXN* gene, FISH assay was performed on both metaphase and interphase spreads of YG8, YG22, YG8s and Y47 cell lines. Metaphase analysis of YG8, YG22, YG8s and Y47 chromosomes by dual colour FISH indicated a single integration site of the transgenic *FXN* gene in all cell lines. YG8 showed three hybridisation signals indicating the presence of a single integration site containing multiple copies of the transgenic *FXN* gene, whereas YG22 and Y47 showed one signal indicating one copy of the *FXN* transgene. In YG8s lines, at least 25% of the YG8s cells had no signals, while the remaining cells showed one signal corresponding to the transgenic *FXN* gene.

In addition, the analysis of *FXN* exons in YG8s rescue mice by PCR confirmed the presence of all *FXN* exons in these lines. These results suggested the incidence of somatic mosaicism in YG8sR cells indicating that the *FXN* gene is missing in some cells but not in all of YG8sR cells. However, according to the copy number results, the copy number of FRDA gene in YG8sR mice was not exactly 0 when compared with WT negative line. These results suggested the presence of the *FXN* gene in this line since the complete deletion of the FRDA gene would lead to embryonic lethality. Furthermore, the observed copy number in YG8sR line is unlikely to be due to the contamination in the samples since two different samples were used and PCR analysis of all exons were positive for these lines. Consequently, the somatic chromosomal mosaicism observed in YG8sR mouse jeopardised the accuracy of the *FXN* copy number measurement using the TaqMan copy number assay. In contrast, fluorescence *in situ* hybridisation technique is the most effective method for the detection of somatic mosaicism since a large number of cells can

be individually examined for the presence or absence of a specific deletion [226]. Further investigation of the somatic mosaicism in YG8sR mice could be carried out in the future studies using the BAC probes together with mouse centromere- and/or telomeres specific probe [227, 228] to confirm the incidence of mosaicism in this line.

As previously discussed, the FISH and copy number results indicated that YG8R lines have multiple, rather than single, copies of the *FXN* transgene integrated into a single chromosomal site. In addition, results from the Jackson Laboratory using single nucleotide polymorphism (SNP) assay showed that the transgenes are localised on Chr 16 of the YG8R mouse chromosomes. Accordingly, it was of particular interest to determine how the *FXN* transgenes in the YG8R line have become distributed among the mouse chromosome. However, both TaqMan copy number and FISH assays were not capable of providing such information, therefore other techniques such as Fibre FISH should be utilised in future investigations in order to characterise the FRDA transgenes in different mouse models.

In conclusion, TaqMan copy number assay allowed for the detection of the copy number variations of the *FXN* gene between different lines and generations in both hemizygous and homozygous transgenes. FISH assay further confirmed the *FXN* copy number variation and also detected the somatic chromosome mosaicism in YG8sR line which could not be identified with TaqMan copy number assay. Due to the limitation of TaqMan copy number assay in identifying mosaicism, the combination of FISH and TaqMan copy number assay could provide the most accurate results for chromosomal investigations with the additional benefit of retaining information at the single-cell level.

CHAPTER III

FUNCTIONAL STUDIES OF FRDA MOUSE MODELS

3.1 Introduction

As previously discussed in section 1.14 (chapter I), the Ataxia Research Group at Brunel University established GAA repeat expansion mutation-based mouse models of FRDA, YG8R and YG22R, containing 190+90 and 190 GAA repeat sequences respectively. However, a new YG8sR (YG8R with a small GAA band) line, containing a contraction of GAA repeat sequence to a single band with 120 GAA repeat units, was recently generated from YG8R breeding. YG8R, YG8sR and YG22R mice are likely to have impaired function of the human transgene-derived frataxin with potential functional deficiencies in motor coordination ability and changes in physical status that are consistent with FRDA disease. In addition, 10-30% of FRDA patients develop overt diabetes and 30% have impaired glucose tolerance which can result from lack of insulin secretion by the insulin-producing ß cells in the pancreas, insulin resistance in muscle, liver and fat, or from a combination of both [215]. Frataxin is involved in iron metabolism, thus, depletion of frataxin leads to increased levels of ROS within pancreatic islets. This could potentially lead to both hyperglycemia and impaired insulin secretion [229]. Recent studies have revealed that FRDA patients exhibit some degree of insulin resistance, suggesting the possibility of an additional role for frataxin in mediating insulin signalling and insulin secretion [215]. Therefore, it is of great importance to further investigate the insulin and glucose tolerance responses in the FRDA mouse models. The aim of this chapter was to characterise the effects of *FXN* deficiencies on function of FRDA mouse models using different tests of motor coordination, balance and strength. In addition, glucose and insulin tolerance tests were carried out to investigate the possibility of diabetes in FRDA mouse models.

3.2 Materials and Methods

To assess the functional outcome of FRDA mice and the effects of mutant *FXN* gene on their functional capacity, the accelerating rotarod analysis together with locomotor activity test, body weight measurement, beam-walk, hang wire, grip strength and foot print tests were conducted. Furthermore, the effect of deficient frataxin on glucose and insulin tolerance was assessed. Detailed explanation of the experimental procedures is outlined below.

3.2.1 Body Weight Analysis

Mouse body weights were recorded once a month from 4-12 months of age using a Mettler Toledo balance (Mettler Toledo PB1501, UK), Fig. 3.1. 10 mice including 5 males and 5 females from each group (C57BL/6J (B6), Y47R, YG22R, YG8R and YG8sR) were assessed.

Fig. 3.1 Body weight analysis of the mice

3.2.2 Rotarod Test

The motor deficits associated with FRDA were assessed using a Ugo-Basille 7650 accelerating rotarod treadmill apparatus, designated for testing the balance and coordination aspects of general motor function, Fig. 3.2. The rotarod device consisted of a rotating rod, driven by an electric motor, upon which the animals were placed. Mutant and control littermate mice (n=10 including 5 males and 5 females used for each group) were placed on the rods and four trials were performed with the speed of the rotation gradually increasing from 4 to 40 rpm. Each trial lasted approximately 3 to 5 minutes, separated by a rest period of 200 seconds between each trial. The time score where the mouse completes the task (by staying on the rotarod for 400s) or falls from the apparatus was recorded. Mice were assessed monthly for an 8 month period from 4-12 months of age (i.e. 9 time points).

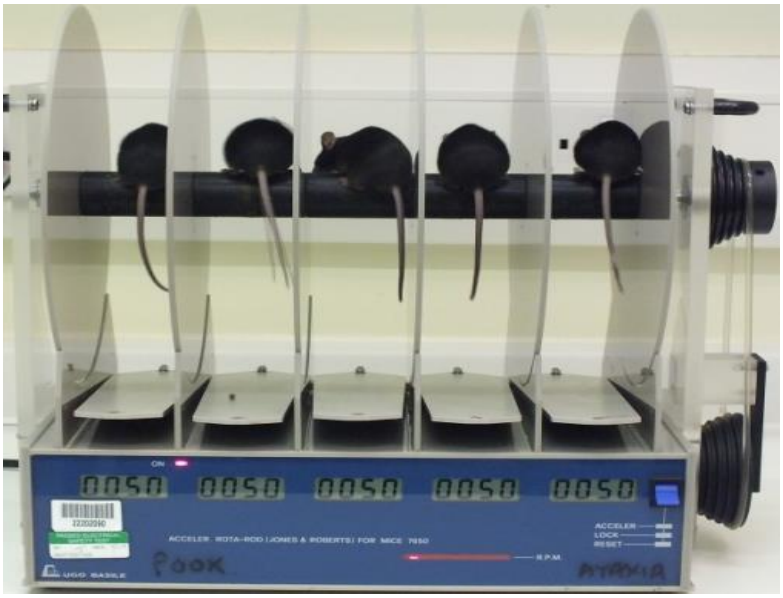

Fig. 3.2 Rotarod apparatus

3.2.3 Beam-breaker Test

Average velocity, ambulatory distance, vertical and jump count and time were measured over a 2 minute period and repeated four times for each mouse using a beam-breaker activity monitor (MED-OFA-510 activity chamber, Med Associates), Fig.3.3. The system consisted of 2 subject containment environment (chamber) and infrared (I/R) transmitters connected to the computer with data acquisition/analysis software (SOF-811), Fig.3.4. Locomotor activity of the mice (*n*=10 including 5 males and 5 females used for each group) was assessed monthly over an 8 month period from 4-12 months of age. Data analysis and manipulation was performed using Microsoft Excel.

Fig. 3.3 Beam-breaker activity monitor chambers

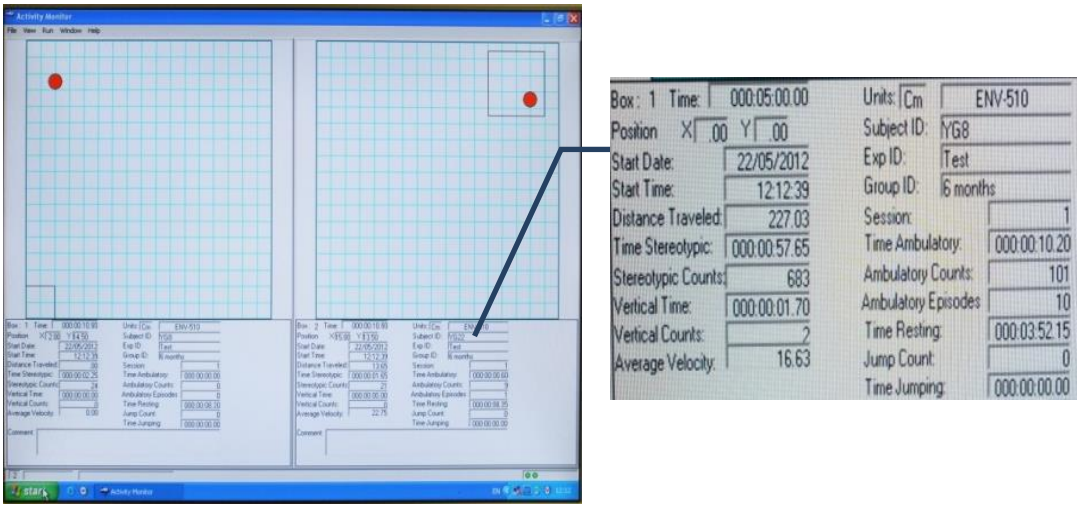

Fig. 3.4 Beam-breaker activity monitor software

3.2.4 Beam-walk Test

Beam-walk test was performed to compare the motor coordination and balance capabilities of FRDA transgenic and control mice. The test was carried out with two wooden beams of 90cm long, one with an external diameter of 12mm and the other 22mm. The beams were placed horizontally 50cm above the bench surface with one end mounted on a narrow support with a 60W lamp while a darkend escape box was located at the other end of the beam as illustrated in Fig. 3.5. Motor function was assessed by measuring the time taken for the mouse to cross the beam and enter the escape box. Mutant and control littermate mice listed in Table 3.1 received two trainings and were assessed four times on the wider and narrower beams respectively with a rest period of 5 minutes between each trial.

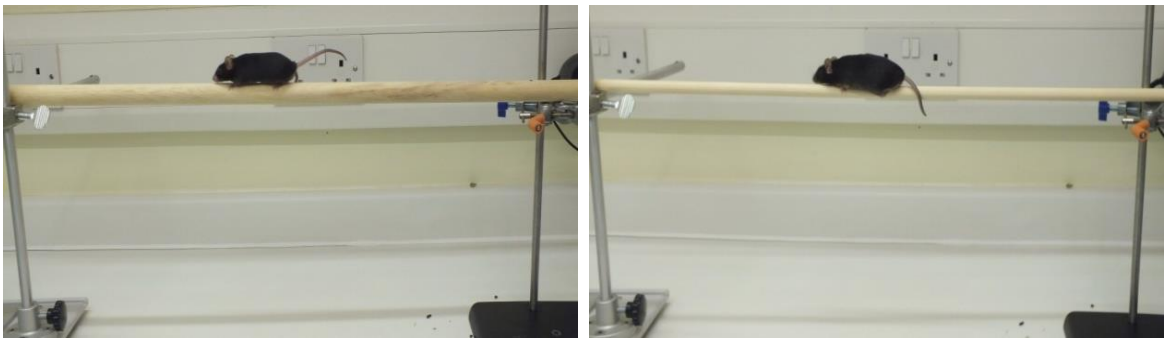

Fig. 3.5 Beam-walk device. Motor function of the mice was measured using 22×900mm (left) and 12×900mm (right) beams.

Table 3.1 The details of FRDA/control mice used for functional studies

Mouse	Genotype	Gender	Total Number	Number of Male & Female	Average Weight (g)	Weight (g)	Average Age (month)
B6	C57BL6/J Control	Male	10	5	32.5	34.8	14.8
		Female		5		30.2	13.6
Y47R	Transgenic Control	Male	10	5	43.1	52.7	16.2
		Female		5		34.4	15.6
YG22R	FRDA YG22 Rescue	Male	10	5	38.2	41.1	14.0
		Female		5		35.2	16.0
YG8R	FRDA YG8 Rescue	Male	10	5	36.0	40.7	13.9
		Female		5		31.3	15.8
YG8s R	FRDA YG8 Small Rescue	Male	10	5	38.1	44.4	13.0
		Female		5		31.8	12.0

3.2.5 Hang Wire Test

The hang wire test was performed to assess the grip strength of the mouse models. The mutant and control littermate mice used in this study are listed in Table 3.1. The mice were hung from a horizontally positioned wire (2mm in diameter and 30cm long) with each end affixed to a vertical stand, Fig. 3.6. Bedding material was placed underneath the wire to break the fall. The test commenced shortly after the mouse held onto the wire and the length of time before the fall was recorded. Four trials were performed with a rest period of 5 minutes between each trial.

Fig. 3.6 Hang wire test

3.2.6 Grip Strength Test

The grip strength meter (Salter Brecknell Model 12 Spring Balance) was used to assess the forelimb grip strength, Fig. 3.7. The mice were held by the scruff of the neck with one hand and the base of the tail with the other hand. They were then free to grasp a metal grid attached to a meter as they were moved along the axis of the grid. The peak force with which mice pulled the grid was measured in four trials with a rest period of 5 minutes between each trial. The mutant and control littermate mice used in this study are listed in Table 3.1.

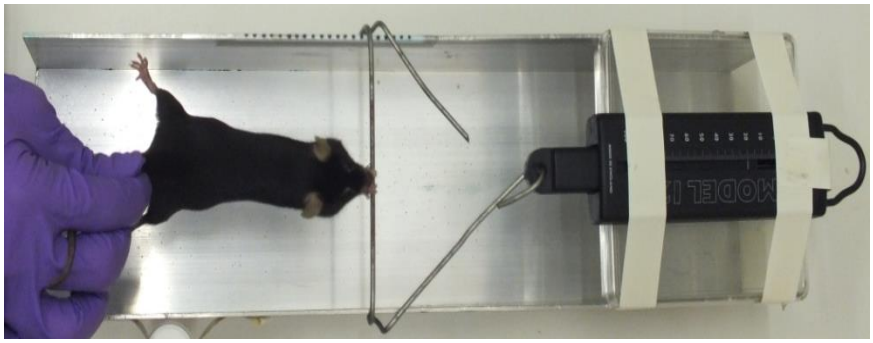

Fig. 3.7 Grip strength test

3.2.7 Foot Print Test

To obtain the footprints, mouse paws were dipped in nontoxic water-based food dye (forepaws in black and hindpaws in blue colour). The mice were allowed to walk along a

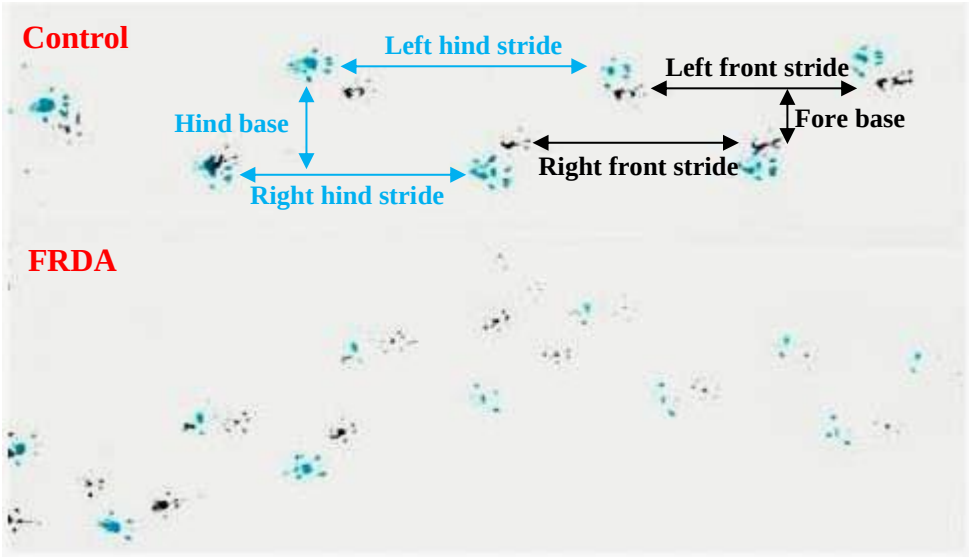

Fig. 3.8 Footprint analysis. Footprint patterns were quantitatively assessed for six parameters including left hind and front stride length, right hind and front stride length, fore base width and hind base width as shown on footprint patterns of a control (top panel) and FRDA mouse (bottom panel).

38.5cm long, 9.5cm wide gangway (with 7cm high side walls) with white paper lining the floor. All mice had one training run and were then given three trials. Three steps from the middle portion of each run with a total number of nine steps for each mouse were measured for left hind and front stride length, right hind and front stride length, fore base width (the width between the right and left forelimbs) and hind base width (the width between the right and left hindlimbs), Fig. 3.8. The mutant and control littermate mice used in this study are listed in Table 3.1.

3.2.8 Glucose Tolerance Test

In order to determine the blood glucose readings, 1mg/g glucose solution (D-Glucose, Sigma Aldrich) was injected intraperitoneally into the mice after a 16 hour fasting period. Blood glucose was measured from the tail vein immediately prior to glucose administration and after 20, 40 and 60 minutes with a glucometer (ACCU-CHEK® Aviva blood glucose meter, Roche). The mutant and control littermate mice used in this study are listed in Table 3.1.

3.2.9 Insulin Tolerance Test

For intraperitoneal insulin-tolerance test, the mice listed in Table 3.2 were fasted for 16 hours. Blood glucose was measured from the tail vein and the mice received an intraperitoneal injection of insulin (0.75U/kg, Sigma Aldrich) and blood glucose was measured again at time points of 20, 50 and 80 minutes after injection.

Table 3.2 The details of the mice used for insulin tolerance test

Mouse	Genotype	Gender	Total Number	Number of Male &	Average Weight (g)	Weight (g)	Average Age (month)
B6	C57BL6/J Control	Male	8	2	29.6	37.5	3.8
		Female		6		26.9	3.7
Y47R	Transgenic Control	Male	10	5	22.6	22.4	4.5
		Female		5		22.7	4.5
YG22R	FRDA YG22 Rescue	Male	9	5	44.3	49.4	11.2
		Female		4		38.1	13.1
YG8JR	FRDA YG8 Rescue	Male	10	5	20.5	22.1	1.4
		Female		5		18.9	1.5
YG8s R	FRDA YG8 Small Rescue	Male	9	4	35.3	41.2	13.5
		Female		5		30.5	12.6

3.2.10 Statistical Analysis

Functional measurements were statistically analysed by two way analysis of variance (ANOVA) and/or Student's *t* test. The level of significance used throughout was $P \leq 0.05$.

3.3 Results

3.3.1 Investigation of Motor Deficits in FRDA Mice Using Rotarod Test

Motor coordination was assessed on a rotarod treadmill at monthly time points from 4-12 months of age in YG8R and YG22R and YG8sR FRDA mice. C57BL/6J (B6) and Y47R (containing the human *FXN* YAC transgene with normal-sized GAA repeats) mice were used as the controls. 10 mice were assessed for each group, 5 males and 5 females. As evident in Fig. 3.9, the coordination ability of the YG22R, YG8R and YG8sR mice was significantly reduced when compared to B6 and Y47R controls, Table 3.3. This trend held true when both male and female values were taken together, Fig. 3.9A, or when male and female values were considered alone, Fig. 3.9B and Fig. 3.9C. However, the results from Student's *t* test at 12 months indicated a considerable decrease in rotarod performance of all FRDA mice in comparison to B6 when males and females were taken together or when males were considered alone, Table 3.4. In contrast, detailed analysis of the female-only values showed no statistically significant difference at 12 months, although a declining trend in rotarod performance was observed, Table 3.4. A possible explanation for such a trend may be due to the differences in body weight of males and females.

Table 3.3 Two-way ANOVA analysis of rotarod performance in FRDA mice

Mouse	Genotype	Gender	Versus B6	Versus B6 (Male & Female)	Versus Y47R	Versus Y47R (Male & Female)
YG22R	FRDA YG22 Rescue	Male	P=2.03E-29	P=8.89E-10	P=4.84E-09	P=0.03
		Female	P=0.001		P=0.01	
YG8R	FRDA YG8 Rescue	Male	P=9.48E-36	P=3.25E-34	P=7.09E-13	P=3.77E-16
		Female	P=9.88E-06		P=1.51E-06	
YG8s R	FRDA YG8 Small Rescue	Male	P=1.27E-11	P=2.32E-12	P=0.76	P=5.59E-06
		Female	P=1.26E-14		P=4.01E-12	

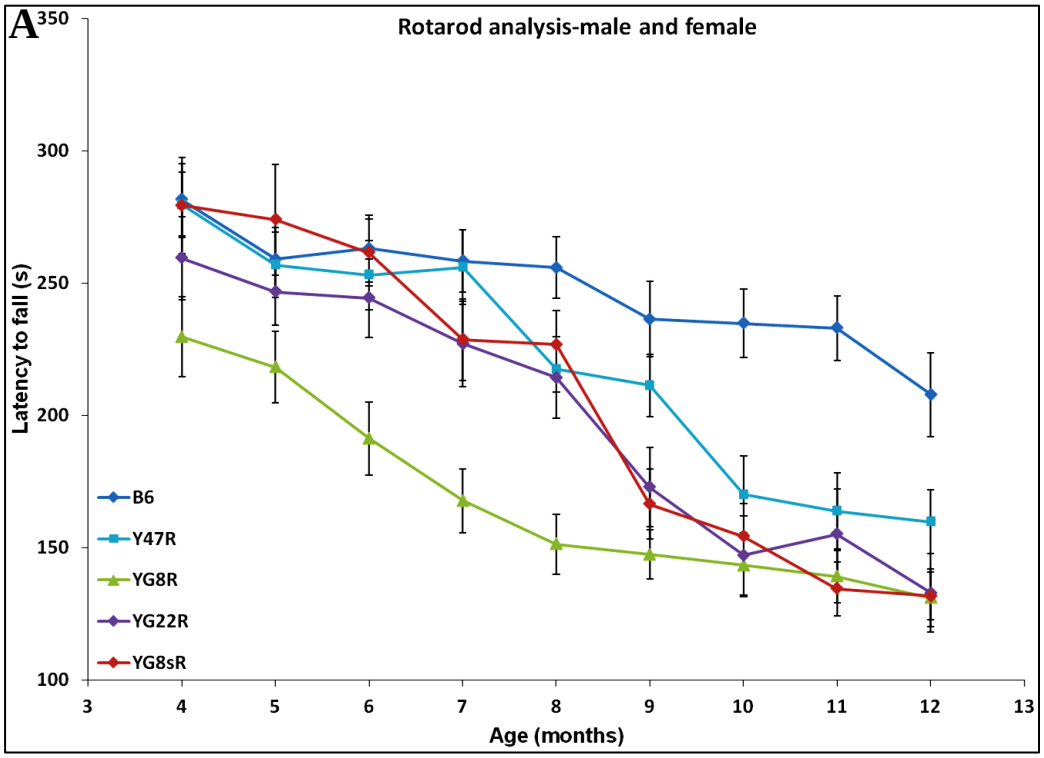
A
Rotarod analysis-male and female
Latency to fall (s)
350
300
250
200
150
100
3
4
5
6
7
8
9
10
11
12
13
Age (months)
B6
Y47R
YG8R
YG22R
YG8sR

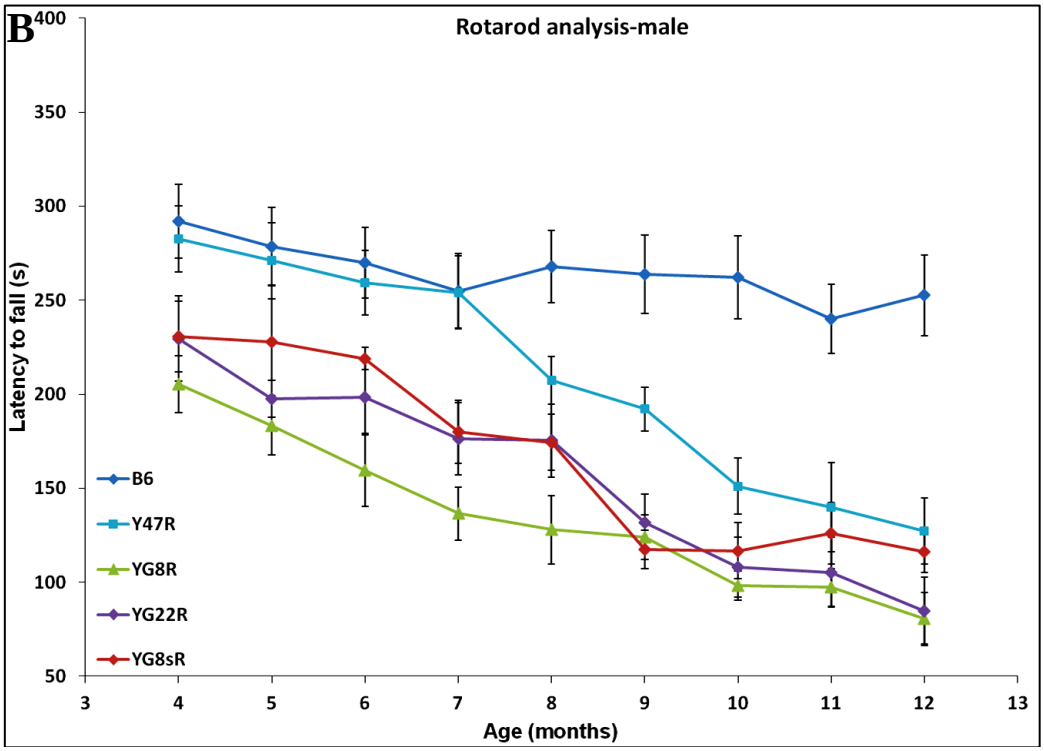
B
Rotarod analysis-male
Latency to fall (s)
400
350
300
250
200
150
100
50
3
4
5
6
7
8
9
10
11
12
13
Age (months)
B6
Y47R
YG8R
YG22R
YG8sR

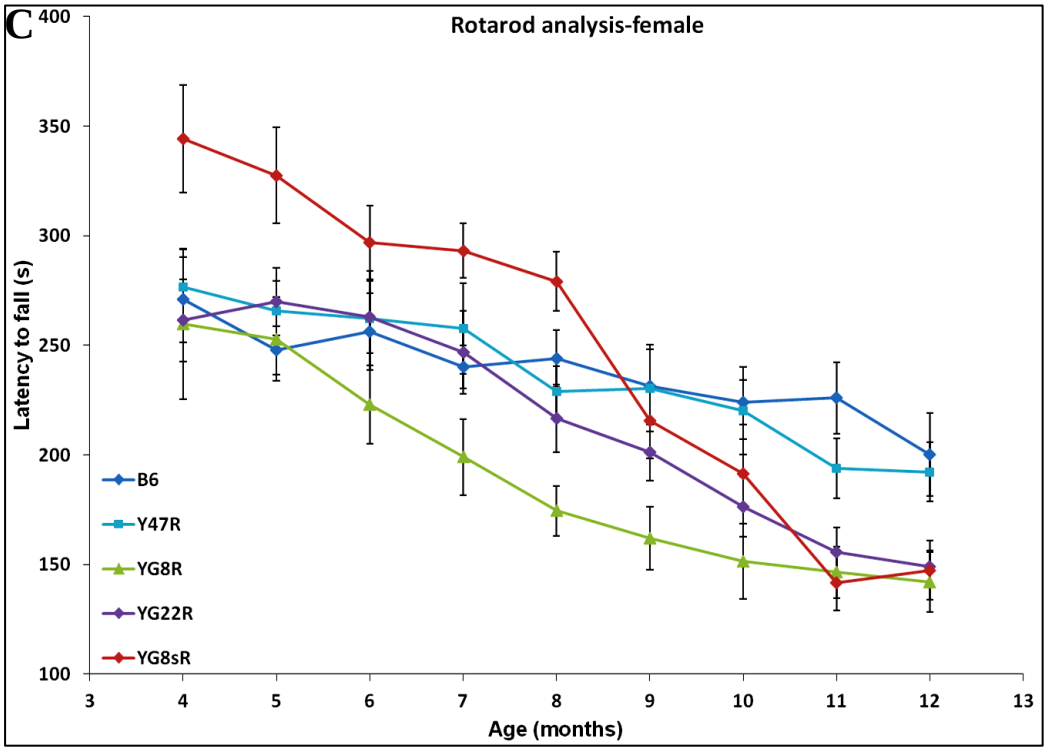

Fig. 3.9 Rotarod analysis of YG22, YG8 and YG8s rescue mice. Rotarod analysis of YG22R, YG8R and YG8sR compared to B6 and Y47R controls shows a coordination deficit in all three rescue mice when **A)** both male and female values were taken together (*n*=10 mice per genotype) or **B)** male alone (*n*=5 mice per genotype) or **C)** female alone (*n*=5 mice per genotype). Error bars indicate SEM and values represent mean ± SEM.

The body weight from selected littermates was also recorded monthly from 4-12 months of age. YG22R, YG8R and YG8sR mice demonstrated a significant increase in weight compared to B6 control when both male and female values were taken together, Fig. 3.10A. A similar trend was also observed when male and female values were considered alone, Fig. 3.10B and Fig. 3.10C. The statistical significance of the differences was evaluated by two-way ANOVA, Table 3.5. The increase in weight may be attributed to the observed decreased locomotor activity of the mice. However, unlike B6, Y47R showed a considerable increase in weight in comparison to all the tested mice. This in turn may have affected their rotarod performance as evident in Fig. 3.9 and Fig. 3.10. In addition, the greater rotarod performance of the females in comparison to the males may be due to their lower body weight. Since body weight influences the rotarod performance, the rotarod values were corrected for body weight. As represented in Fig. S.1, the difference in the rotarod performance of B6 and Y47R controls was small in magnitude when normalised by the weight factor. Although the decline in the rotarod performance of Y47R was attributed to the increase in the body weight, other genetic factors may play a part in the observed trend since Y47R mice are transgenic. The statistical significance of

the differences was evaluated by two-way ANOVA and Student's *t* test as depicted in Table S.1 and Table S.2 respectively.

Table 3.4 Student's *t* test analysis of rotarod performance in FRDA mice from 4 to 12 months

Mouse	Male and Female	4m	5m	6m	7m	8m	9m	10m	11m	12m
YG22R	Vs B6	0.28	0.37	0.34	0.73	0.03	0.004	2.95E-05	0.0003	0.0008
	Vs Y47R	0.31	0.56	0.66	0.17	0.17	0.04	0.2	0.79	0.16
YG8R	Vs B6	4.35E-05	0.49	0.0002	0.0002	7.39E-09	4.44E-06	1.7E-06	7.92E-08	0.0001
	Vs Y47R	2.83E-05	0.03	0.001	9.31E-06	0.01	6.74E-05	0.15	0.55	0.08
YG8sR	Vs B6	0.92	0.08	0.92	0.79	0.09	0.001	3.07E-05	3.58E-08	8.95E-05
	Vs Y47R	0.99	0.48	0.64	0.19	0.02	0.01	0.40	0.39	0.06
Mouse	**Male**	**4m**	**5m**	**6m**	**7m**	**8m**	**9m**	**10m**	**11m**	**12m**
YG22R	Vs B6	0.04	0.01	0.01	0.007	0.001	1.1E-06	1.23E-07	8.49E-06	5.67E-07
	Vs Y47R	0.07	0.002	0.02	0.007	0.72	0.0001	0.08	0.55	0.09
YG8R	Vs B6	0.001	0.009	0.0001	2.47E-05	5.24E-06	1.11E-05	3.47E-07	8.89E-05	5.91E-06
	Vs Y47R	0.001	0.001	0.0003	2.2E-05	0.02	0.002	0.22	0.74	0.48
YG8sR	Vs B6	0.03	0.50	0.01	0.007	0.003	8.87E-07	5.64E-06	5.69E-05	4.35E-06
	Vs Y47R	0.05	0.23	0.03	0.006	0.66	3E-05	0.87	0.90	0.59
Mouse	**Female**	**4m**	**5m**	**6m**	**7m**	**8m**	**9m**	**10m**	**11m**	**12m**
YG22R	Vs B6	0.51	0.0006	0.18	0.01	0.70	0.21	0.99	0.46	0.50
	Vs Y47R	0.63	0.02	0.11	0.50	0.02	0.92	0.64	0.32	0.61
YG8R	Vs B6	0.01	0.09	0.19	0.53	0.0002	0.05	0.32	0.0003	0.62
	Vs Y47R	0.005	0.67	0.38	0.03	0.31	0.005	0.21	0.13	0.04
YG8sR	Vs B6	0.02	0.0002	0.10	0.0001	0.07	0.57	0.40	0.0002	0.50
	Vs Y47R	0.03	0.004	0.06	0.15	0.0002	0.57	0.26	0.09	0.02

Table 3.5 Two-way ANOVA analysis of body weight in FRDA mice

Mouse	Genotype	Gender	Versus B6	Versus B6 (Male & Female)	Versus Y47R	Versus Y47R (Male & Female)
YG22R	FRDA YG22 Rescue	Male	P=1.26E-05	P=2.34E-05	P=6.43E-10	P=0.0006
		Female	P=0.01		P=0.54	
YG8R	FRDA YG8 Rescue	Male	P=9.04E-06	P=0.009	P=1.83E-07	P=0.0001
		Female	P=0.93		P=0.05	
YG8s R	FRDA YG8 Small Rescue	Male	P=1.06E-07	P=6.31E-05	P=0.001	P=0.01
		Female	P=0.51		P=0.006	

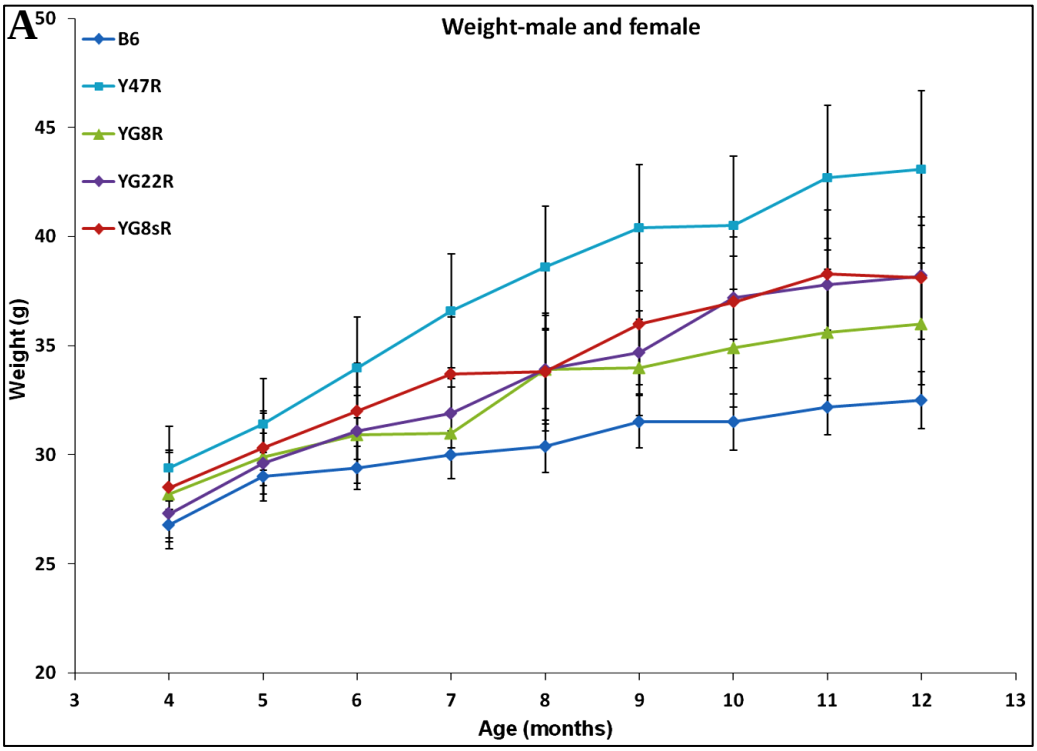
A
Weight-male and female
B6
Y47R
YG8R
YG22R
YG8sR
Weight (g)
Age (months)
50
45
40
35
30
25
20
3
4
5
6
7
8
9
10
11
12
13

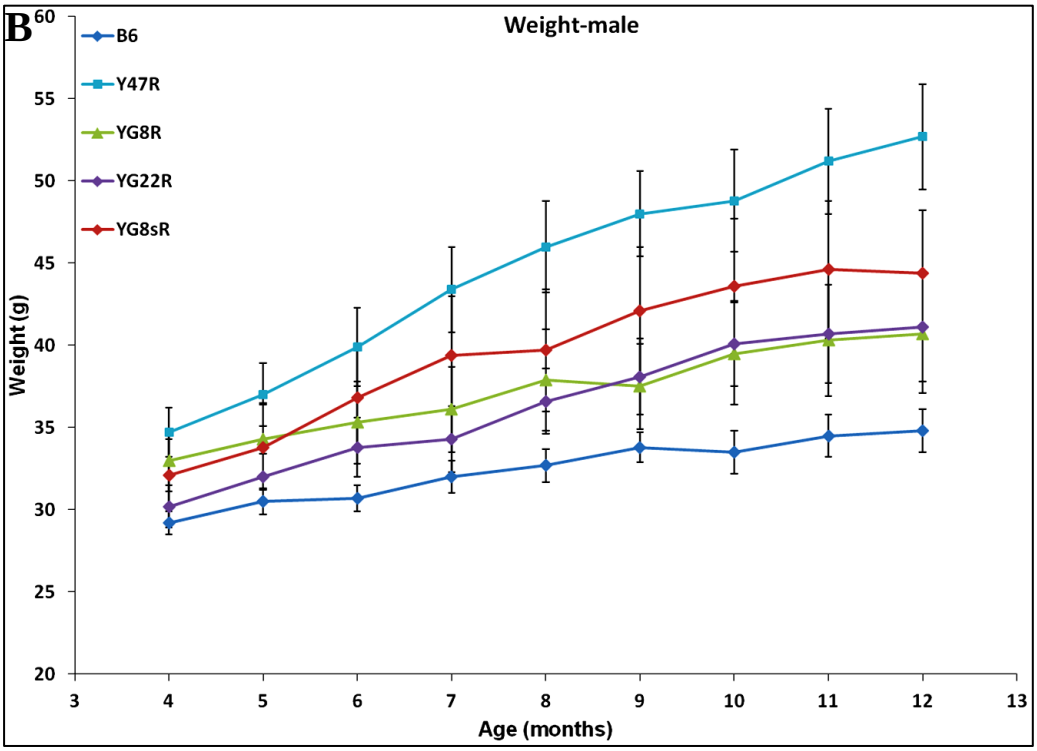
B
Weight-male
B6
Y47R
YG8R
YG22R
YG8sR
Weight (g)
Age (months)
60
55
50
45
40
35
30
25
20
3
4
5
6
7
8
9
10
11
12
13

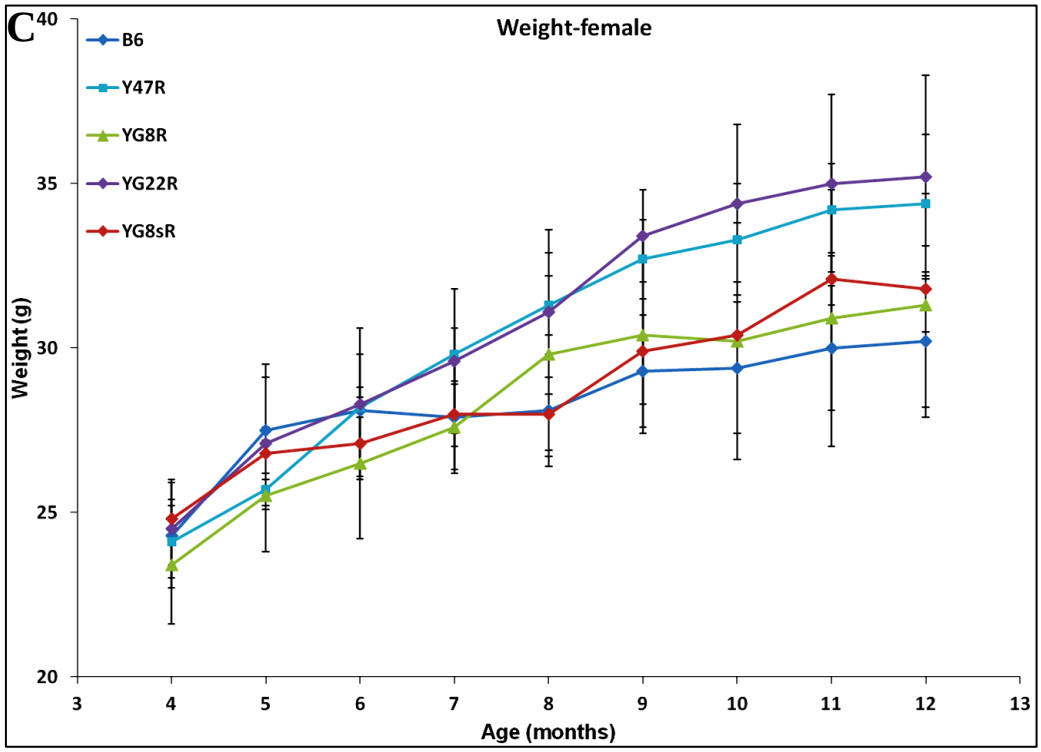

Fig. 3.10 Body weight analysis of mice. **A)** Weight analysis of YG22R, YG8R and YG8sR compared to B6 and Y47R controls when both male and female values were taken together (*n*=10 mice per genotype). The results indicated a significant increase in weight of all FRDA mice in comparison to B6 control. A similar tendency was seen when **B)** male and **C)** female values were analysed separately (*n*=5 mice per genotype). Error bars indicate SEM and values represent mean ± SEM.

3.3.2 Investigation of Motor Deficits in FRDA Mice Using Beam-breaker Test

Locomotor activity of the mice, including average velocity, ambulatory distance, vertical count and time, jump count and time were measured over a 2 minute period and repeated four times for each mouse using a beam-breaker activity. 10 mice including 5 males and 5 females were assessed monthly for each group over an 8 month period from 4-12 months of age. Statistical analysis was performed by two-way ANOVA method for all the experimental results, Table 3.6. As shown in Fig. 3.11, YG8R, YG22R and YG8sR mice exhibited significantly lower average velocity (total distance covered divided by the total time elapsed) compared to B6 and Y47R controls. A similar trend was observed when male and female were taken together, Fig. 3.11A, or analysed separately, Fig. 3.11B and Fig. 3.11C respectively.

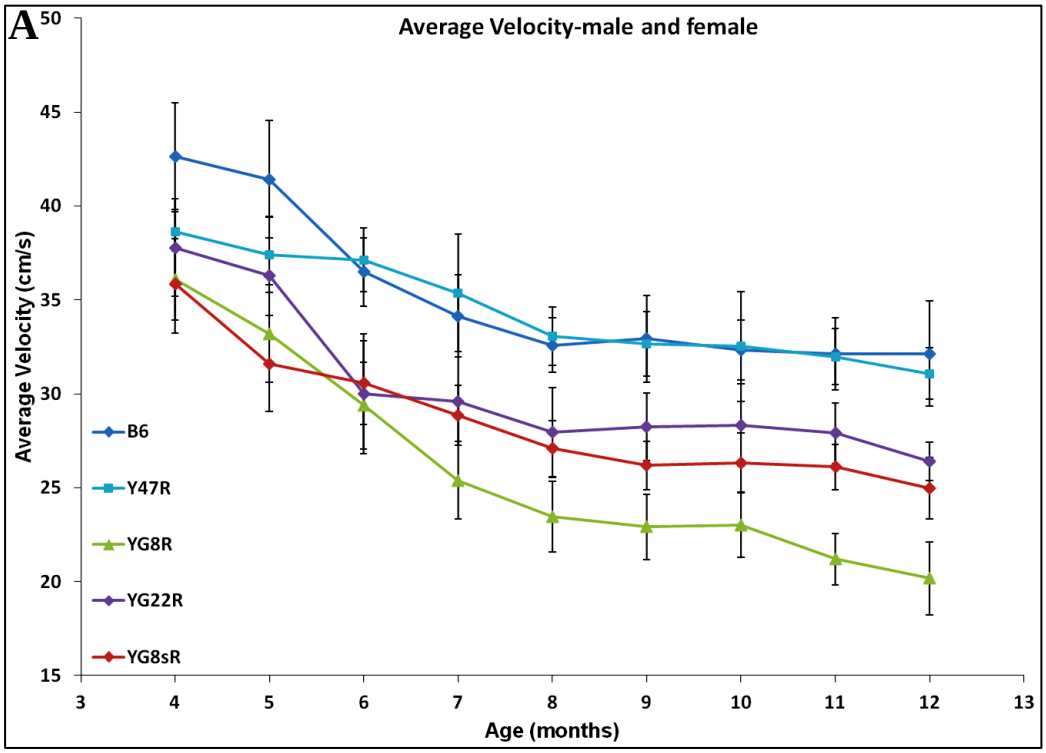
A
Average Velocity-male and female
Average Velocity (cm/s)
50
45
40
35
30
25
20
15
3
4
5
6
7
8
9
10
11
12
13
Age (months)
B6
Y47R
YG8R
YG22R
YG8sR

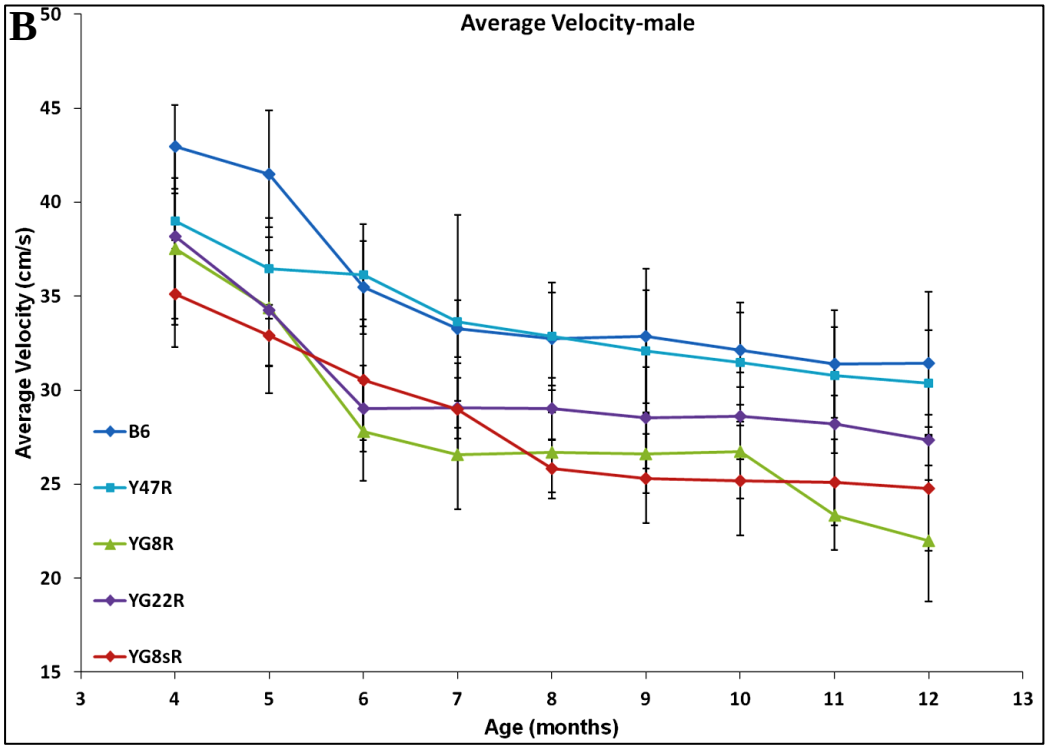
B
Average Velocity-male
Average Velocity (cm/s)
50
45
40
35
30
25
20
15
3
4
5
6
7
8
9
10
11
12
13
Age (months)
B6
Y47R
YG8R
YG22R
YG8sR

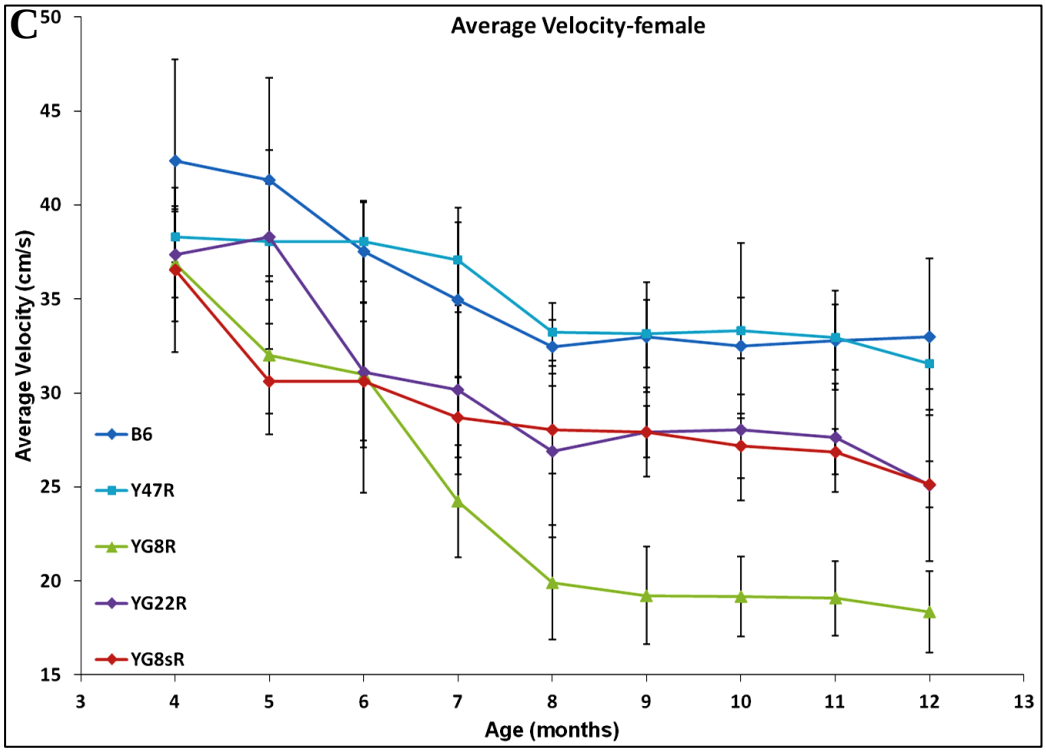

Fig. 3.11 Average velocity of mice. **A)** YG8R, YG22R and YG8sR displayed significantly decreased average velocity compared to B6 and Y47R controls when both male and female values were taken together (*n*=10 mice per genotype). Analysis of **A)** males and **B)** females separately (*n*=5 mice per genotype) revealed that all three deficient genotypes had decreased average velocity compared to the controls. Error bars indicate SEM and values represent mean ± SEM.

Ambulatory distance (total distance covered by the mice within a specific time) traveled by FRDA mice were significantly less than the controls when male and female were taken together, Fig. 3.12A. The same trend held true when males, Fig. 3.12B, and females, Fig. 3.12C, were analysed separately except in the case of YG8sR female where higher ambulatory values were observed; possibly due to their lower body weight.

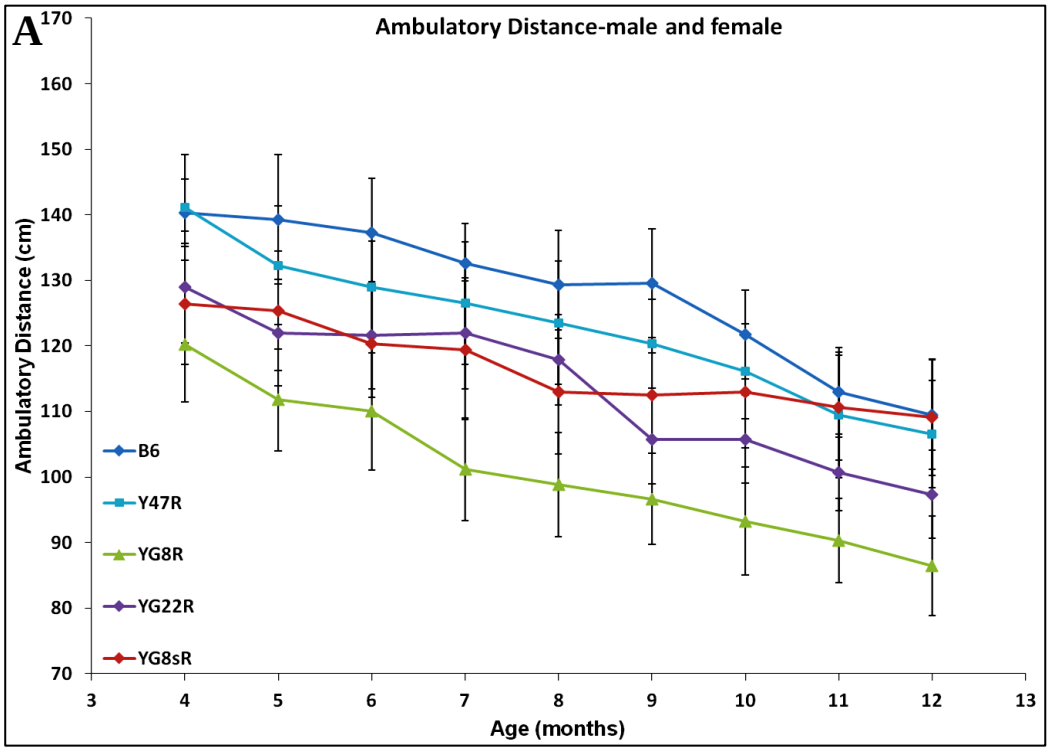
A
Ambulatory Distance-male and female
Ambulatory Distance (cm)
170
160
150
140
130
120
110
100
90
80
70
3
4
5
6
7
8
9
10
11
12
13
Age (months)
B6
Y47R
YG8R
YG22R
YG8sR

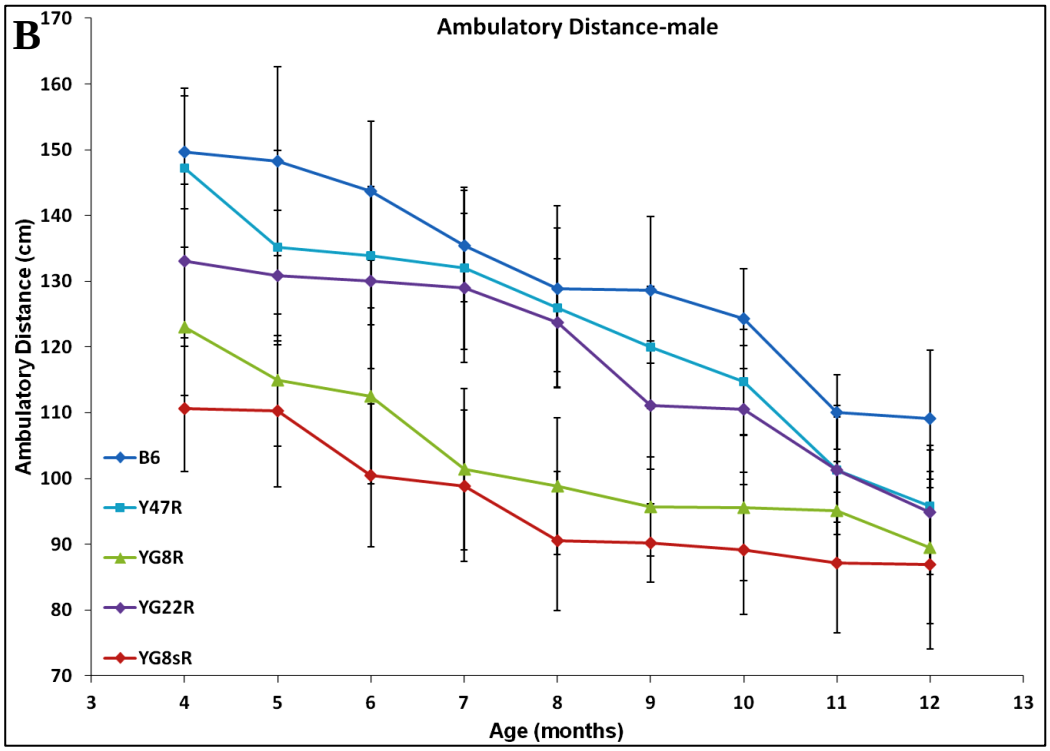
B
Ambulatory Distance-male
Ambulatory Distance (cm)
170
160
150
140
130
120
110
100
90
80
70
3
4
5
6
7
8
9
10
11
12
13
Age (months)
B6
Y47R
YG8R
YG22R
YG8sR

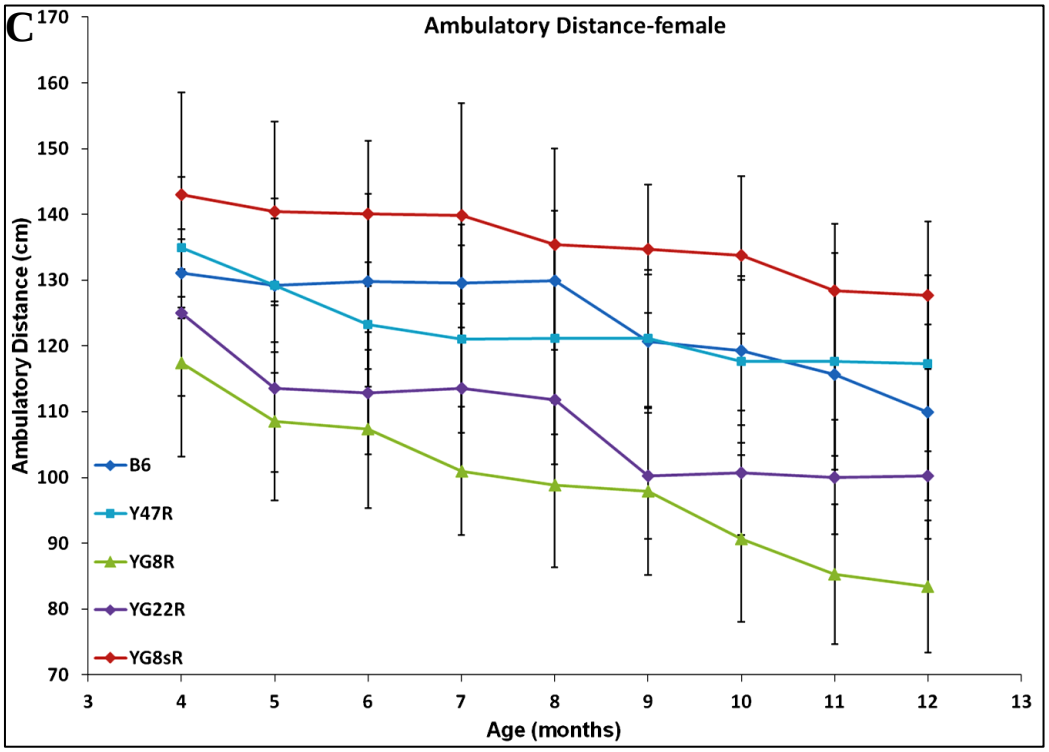

Fig. 3.12 Ambulatory distance of mice. **A)** YG8R, YG22R and YG8sR displayed significantly decreased ambulatory distance compared to B6 and Y47R controls when both male and female values were taken together (*n*=10 mice per genotype). Analysis of **B)** males and **C)** females separately (*n*=5 mice per genotype) revealed the same pattern, except YG8sR female which had greater ambulatory distance. Error bars indicate SEM and values represent mean ± SEM.

The vertical count and time (total number and time when the mouse stands with the hind legs) were also measured. As evident in Fig. 3.13, a significant decrease in the vertical count and time was detected in the FRDA mice compared to the controls when analysing males and females together and separately.

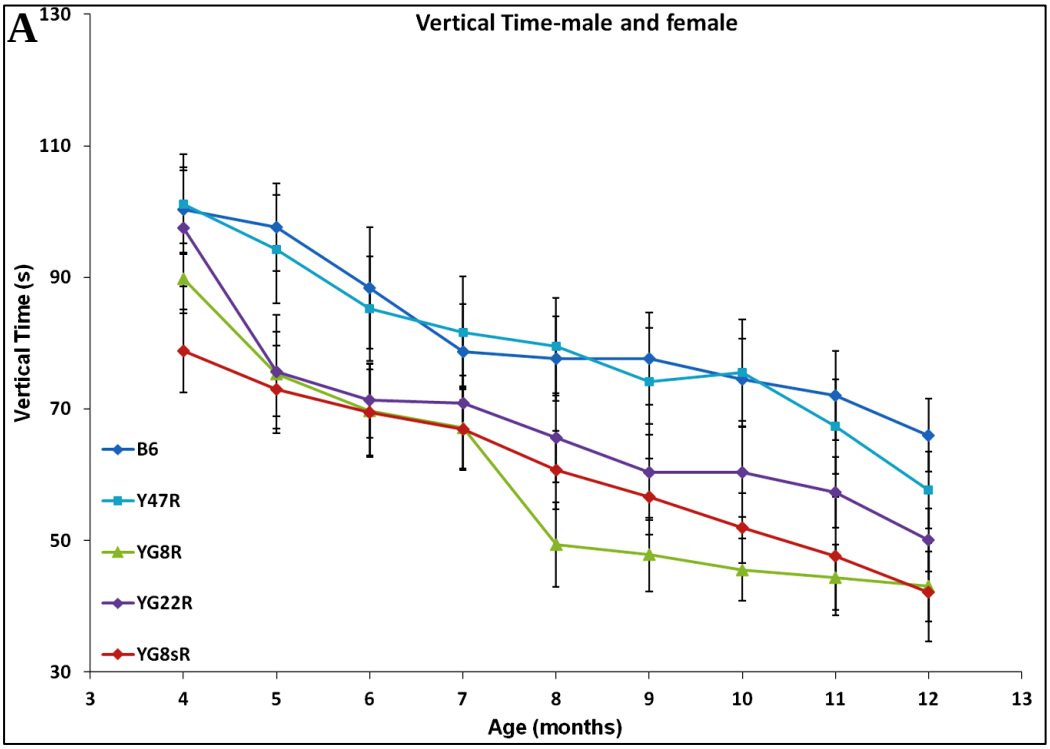
A
Vertical Time-male and female
Vertical Time (s)
130
110
90
70
50
30
3
4
5
6
7
8
9
10
11
12
13
Age (months)
B6
Y47R
YG8R
YG22R
YG8sR

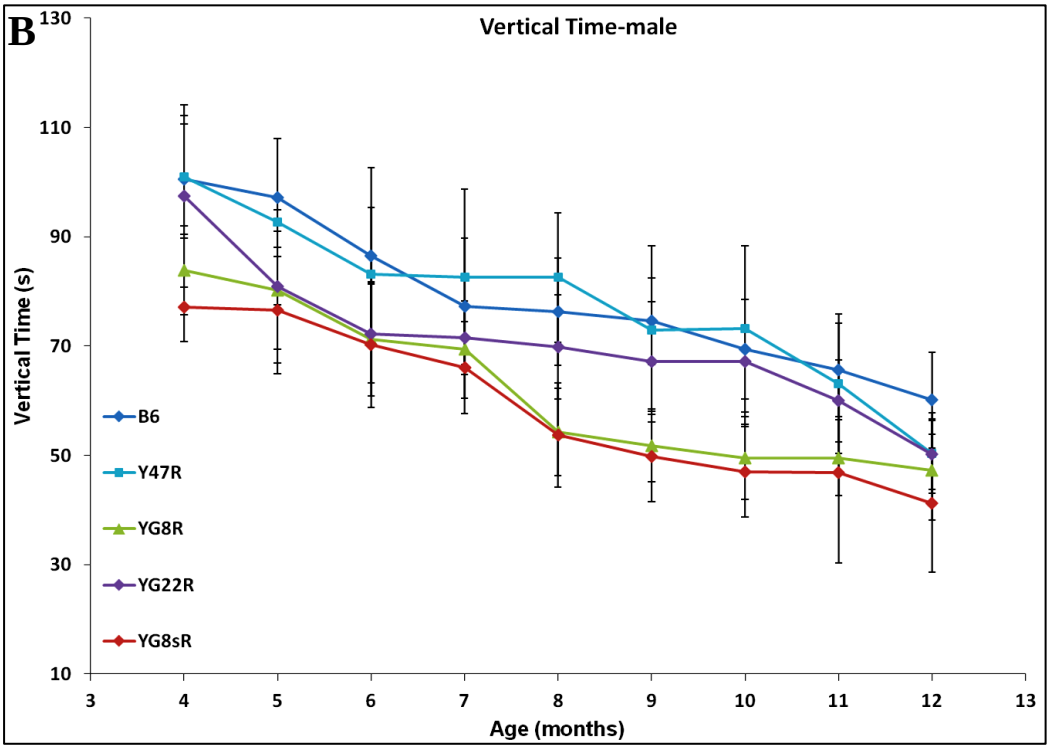
B
Vertical Time-male
Vertical Time (s)
130
110
90
70
50
30
10
3
4
5
6
7
8
9
10
11
12
13
Age (months)
B6
Y47R
YG8R
YG22R
YG8sR

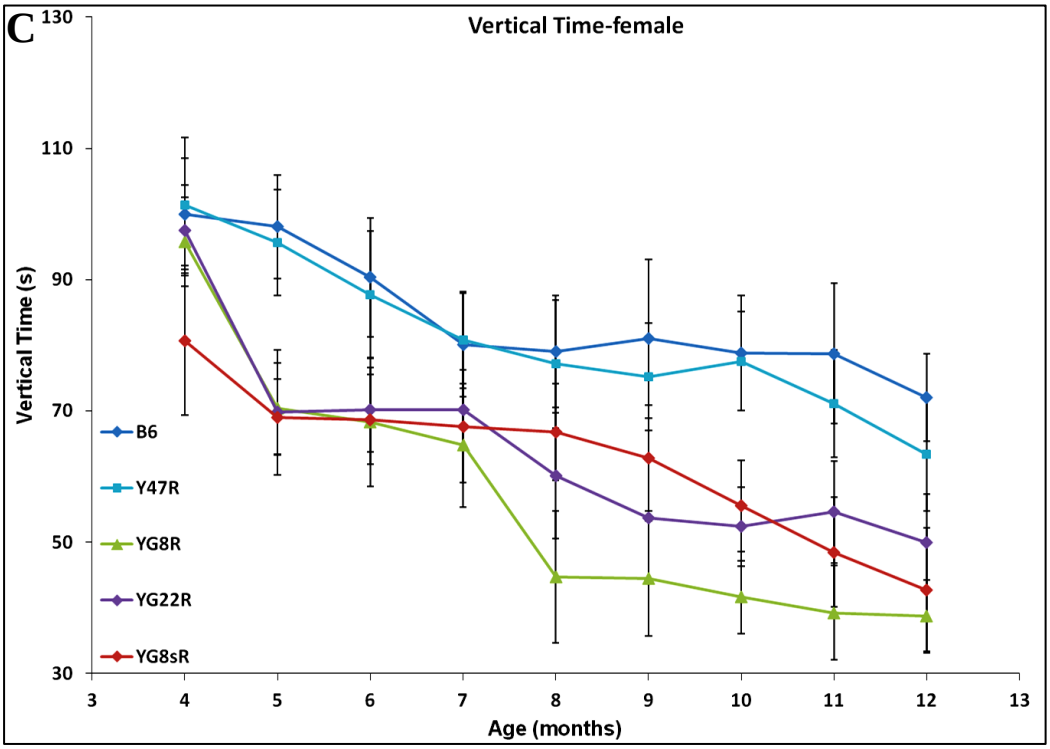
C
Vertical Time-female
Vertical Time (s)
130
110
90
70
50
30
3
4
5
6
7
8
9
10
11
12
13
Age (months)
B6
Y47R
YG8R
YG22R
YG8sR

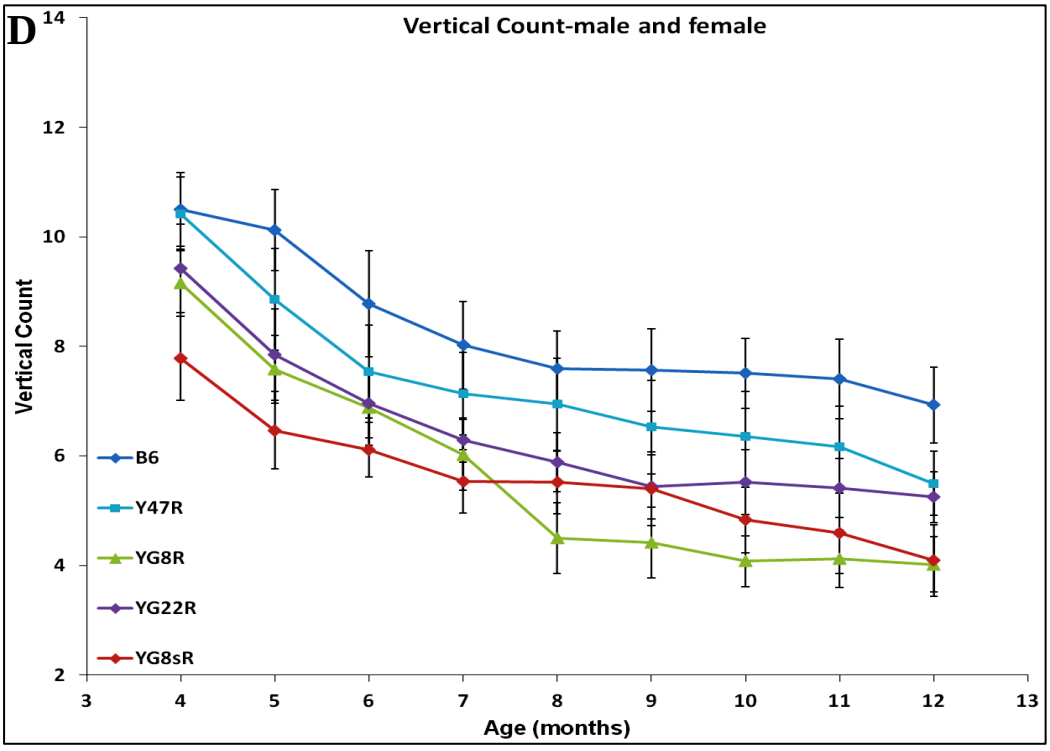
D
Vertical Count-male and female
Vertical Count
14
12
10
8
6
4
2
3
4
5
6
7
8
9
10
11
12
13
Age (months)
B6
Y47R
YG8R
YG22R
YG8sR

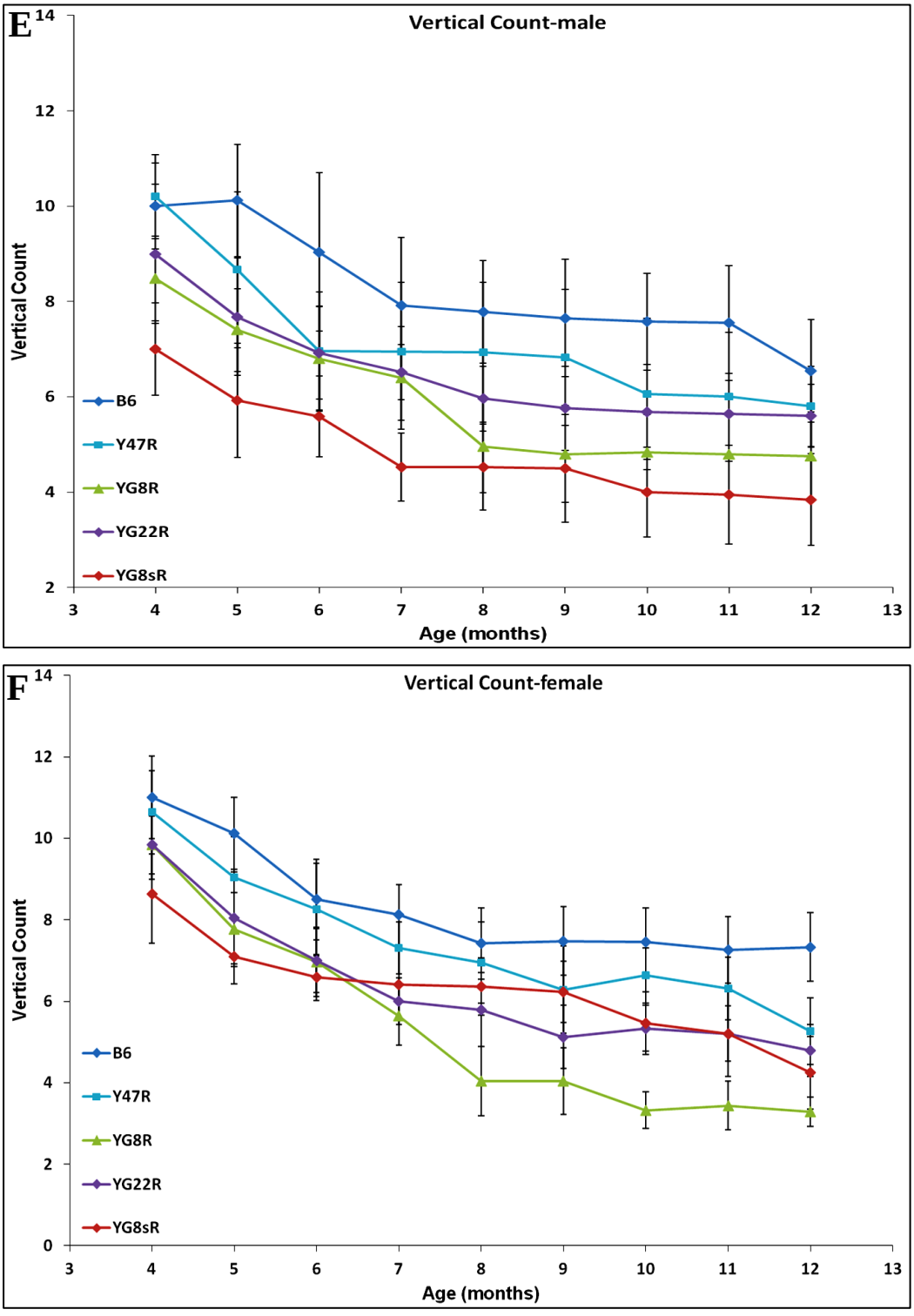

Fig. 3.13 Vertical time and count of mice. **A)** Vertical time and **D)** count were significantly decreased in YG8R, YG22R and YG8sR compared to B6 and Y47R controls when both male and female values were analysed together (*n*=10 mice per genotype). Analysis of **B, E)** males and **C, F)** females separately (*n*=5 mice per genotype) revealed the same pattern. Error bars indicate SEM and values represent mean ± SEM.

Subsequently, the Jump count and time (total number and time that the mouse jumps) were recorded. As evident in Fig. 3.14, a significant decrease in jump count and time was detected in the FRDA mice compared to the controls when analysing males and females together and separately.

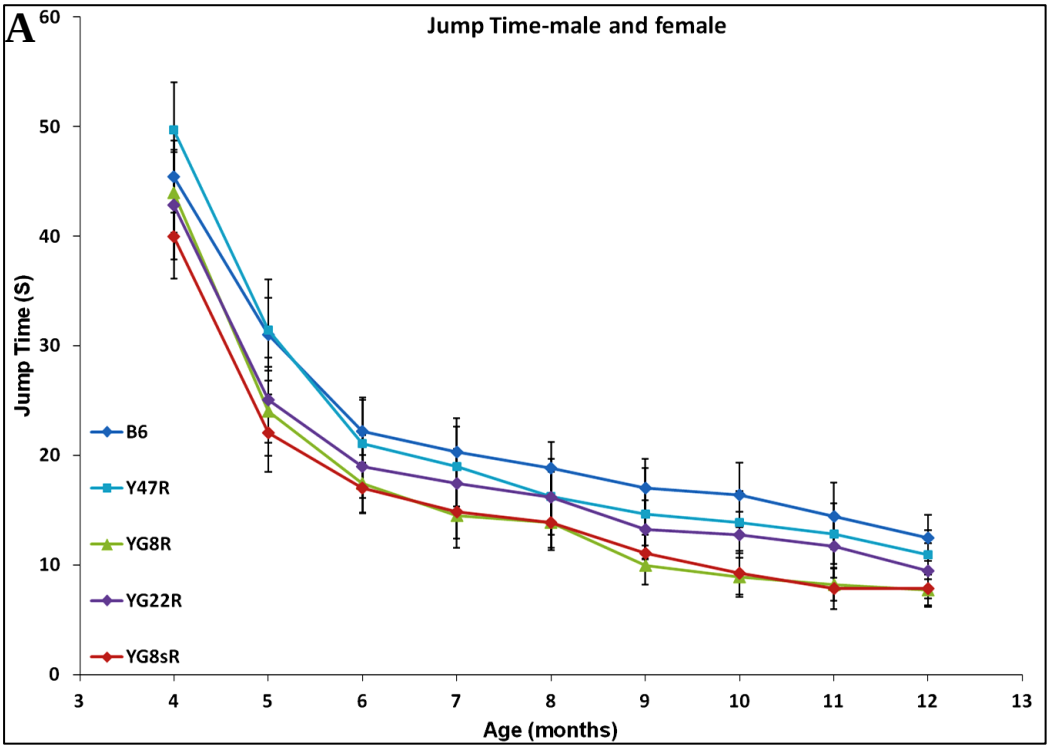

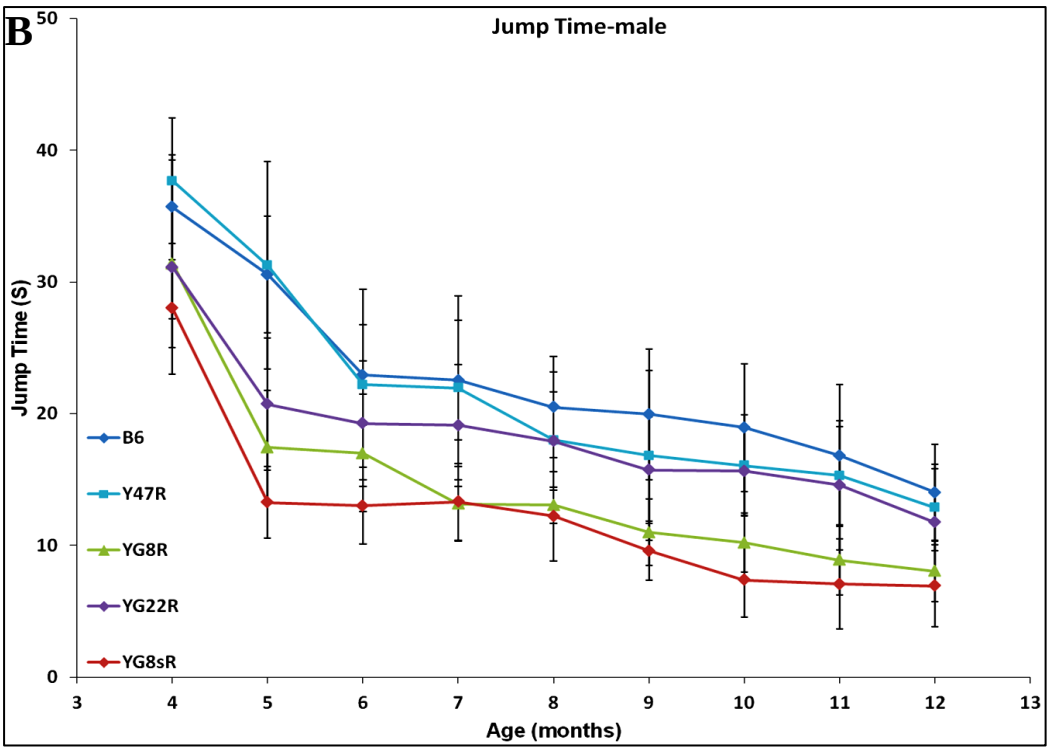

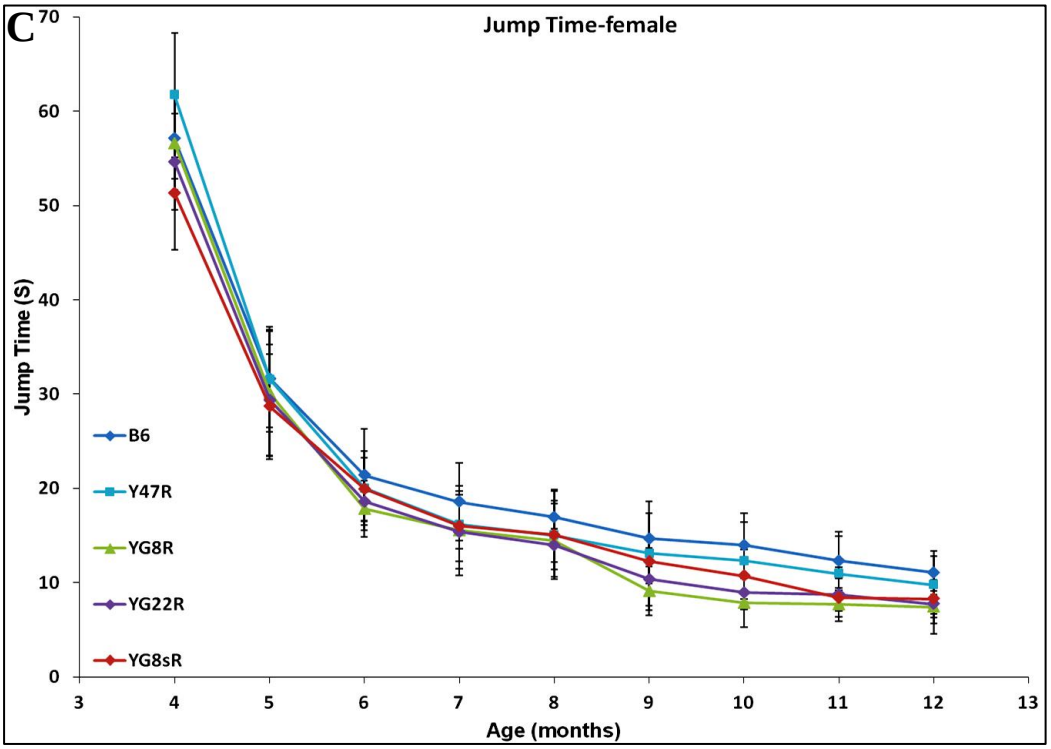
C
Jump Time-female
Jump Time (S)
Age (months)
B6
Y47R
YG8R
YG22R
YG8sR

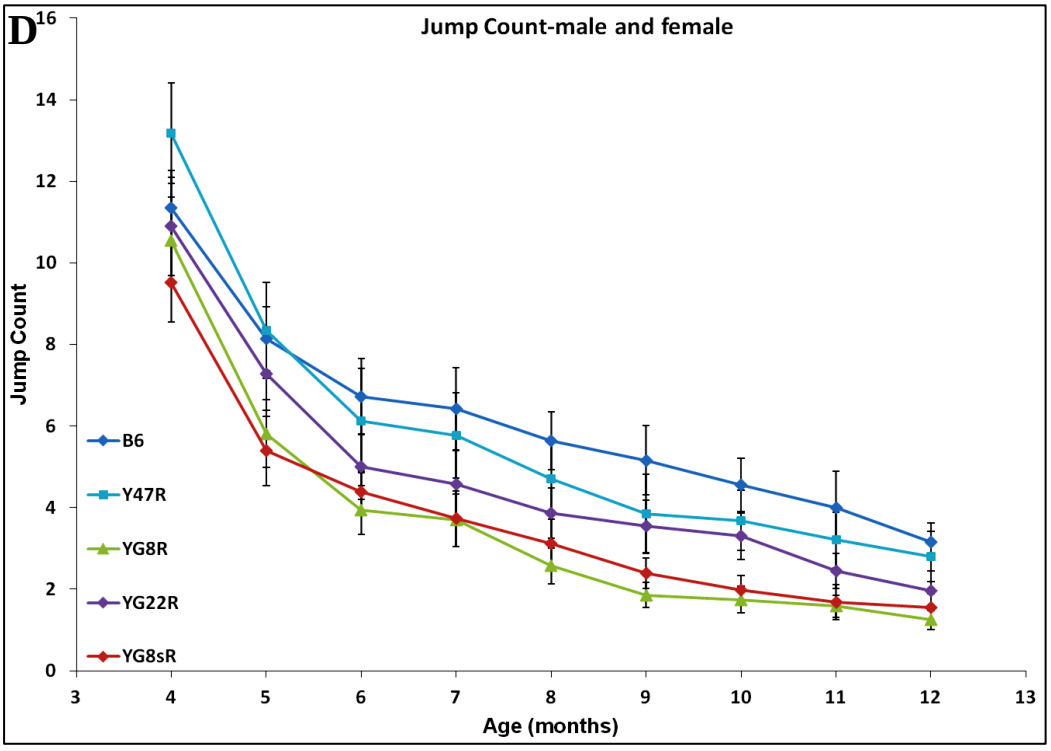
D
Jump Count-male and female
Jump Count
Age (months)
B6
Y47R
YG8R
YG22R
YG8sR

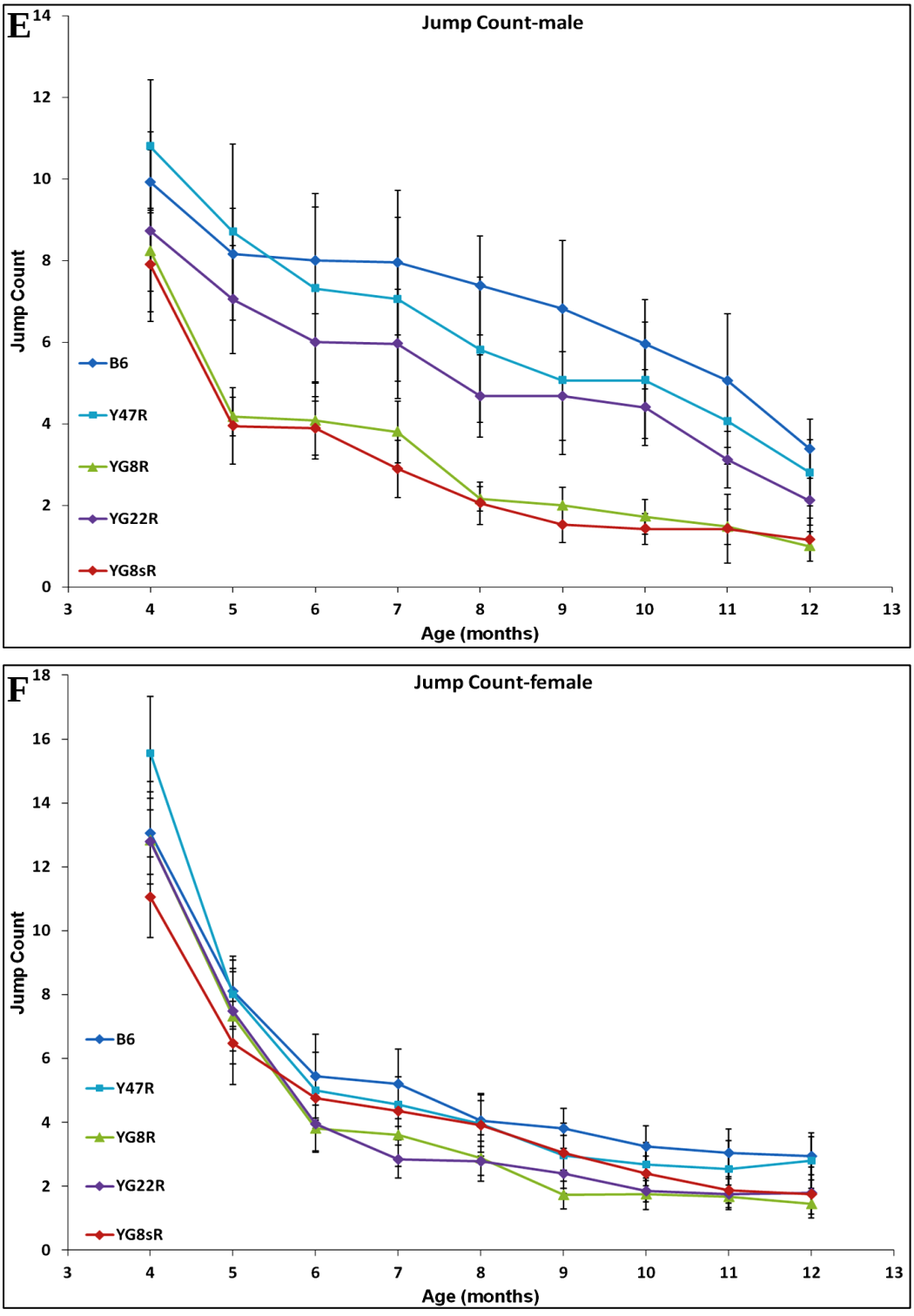

Fig. 3.14 Jump time and count of mice. **A)** Jump time and **D)** count were significantly decreased in YG8R, YG22R and YG8sR compared to B6 and Y47R controls when both male and female values were taken together (*n*=10 mice per genotype). Analysis of **B, E)** males and **C, F)** females separately (*n*=5 mice per genotype) revealed the same pattern. Error bars indicate SEM and values represent mean ± SEM.

Table 3.6 Two-way ANOVA analysis of locomotor activity in FRDA mice

Locomotor Activity	Mouse	Gender	Versus B6	Versus B6 (Male & Female)	Versus Y47R	Versus Y47R (Male & Female)
Average Velocity	YG22R	Male	P=0.007	P=0.002	P=0.008	P=0.4
		Female	P=0.08		P=0.1	
	YG8R	Male	P=1.91E-05	P=7.26E-12	P=0.2	P=0.004
		Female	P=9.79E-08		P=2.95E-08	
	YG8s R	Male	P=7.87E-12	P=1.74E-12	P=0.1	P=0.001
		Female	P=0.001		P=0.002	
Ambulatory distance	YG22R	Male	P=0.007	P=0.0001	P=0.3	P=0.01
		Female	P=0.006		P=0.01	
	YG8R	Male	P=5.01E-08	P=1.22E-12	P=0.0001	P=1.04E-08
		Female	P=3.18E-06		P=1.61E-05	
	YG8s R	Male	P=1.28E-14	P=0.004	P=2.39E-09	P=0.1
		Female	P=0.004		P=0.004	
Vertical Time	YG22R	Male	P=0.6	P=0.0006	P=0.1	P=0.5
		Female	P=1.95E-06		P=0.002	
	YG8R	Male	P=0.008	P=1.87E-07	P=0.8	P=0.03
		Female	P=1.47E-06		P=0.001	
	YG8s R	Male	P=4.42E-07	P=1.88E-12	P=0.01	P=5.62E-05
		Female	P=1.07E-06		P=0.001	
Vertical Count	YG22R	Male	P=0.02	P=2.71E-06	P=0.07	P=0.8
		Female	P=1.89E-06		P=0.06	
	YG8R	Male	P=0.0007	P=1.48E-09	P=0.5	P=0.2
		Female	P=4.86E-08		P=0.01	
	YG8s R	Male	P=2.26E-12	P=1.05E-16	P=0.001	P=0.0004
		Female	P=7.08E-06		P=0.09	
Jump Time	YG22R	Male	P=0.6	P=0.5	P=0.4	P=0.7
		Female	P=0.5		P=0.1	
	YG8R	Male	P=0.0001	P=0.01	P=0.04	P=0.06
		Female	P=0.9		P=0.4	
	YG8s R	Male	P=7.84E-10	P=4.67E-05	P=5.17E-05	P=0.0008
		Female	P=0.9		P=0.3	
Jump Count	YG22R	Male	P=0.1	P=0.05	P=0.8	P=0.2
		Female	P=0.1		P=0.03	
	YG8R	Male	P=1.3E-09	P=6.42E-07	P=0.0002	P=0.0001
		Female	P=0.3		P=0.09	
	YG8s R	Male	P=8.34E-14	P=2.37E-09	P=5.05E-07	P=2.41E-06
		Female	P=0.4		P=0.1	

3.3.3 Investigation of Motor Deficits in FRDA Mice Using Beam-walk Test

Beam-walk performance was assessed for the investigation of motor deficiencies in YG8R and YG22R and YG8sR FRDA mice while B6 and Y47R were used as the controls. 10 mice, 5 males and 5 females, were assessed for each group and the average latency of 4 trials on 22×900mm and 12×900mm beams was recorded. As evident in Fig. 3.15A, the FRDA mice took significantly longer to cross both 22mm and 12mm beams compared to the controls when analysing males and females together. However, no significant difference was detected in the beam-walk performance of YG22R on the 12mm beam compared to Y47R control. This may be due to the higher body weight of YG22R mice, affecting their balance and performance on the narrower beam. The same trend was observed when female values were considered alone, Fig. 3.15C. All three female deficient genotypes took significantly longer than B6 and Y47R to cross the 22mm and 12mm beams except YG22R on the latter beam. The significance of these observations was confirmed by Student's *t* test which indicated a significant effect of genotype on the latency between mutant and control mice when traversing both beams. The analysis of YG8R, YG22R, and YG8sR males also showed a coordination deficit on both 22mm and 12mm beams when compared to B6 controls, Fig. 3.15B. However, detailed analysis of the male values on the 12mm beam indicated no significant difference in comparison to Y47R due to their higher weight. These results suggest that although the beam-walk is an effective model to assess severity of the FRDA disease, other factors such as body weight and age might have an impact on the experimental results.

In order to assess the effect of body weight on animals' performance, the beam-walk values were normalised by the body weight. As shown in Fig. S.2, body weight did not change the pattern of significance when both males and females were considered together or females alone. However, the difference between the FRDA and Y47R male mice was significant when the values were normalised.

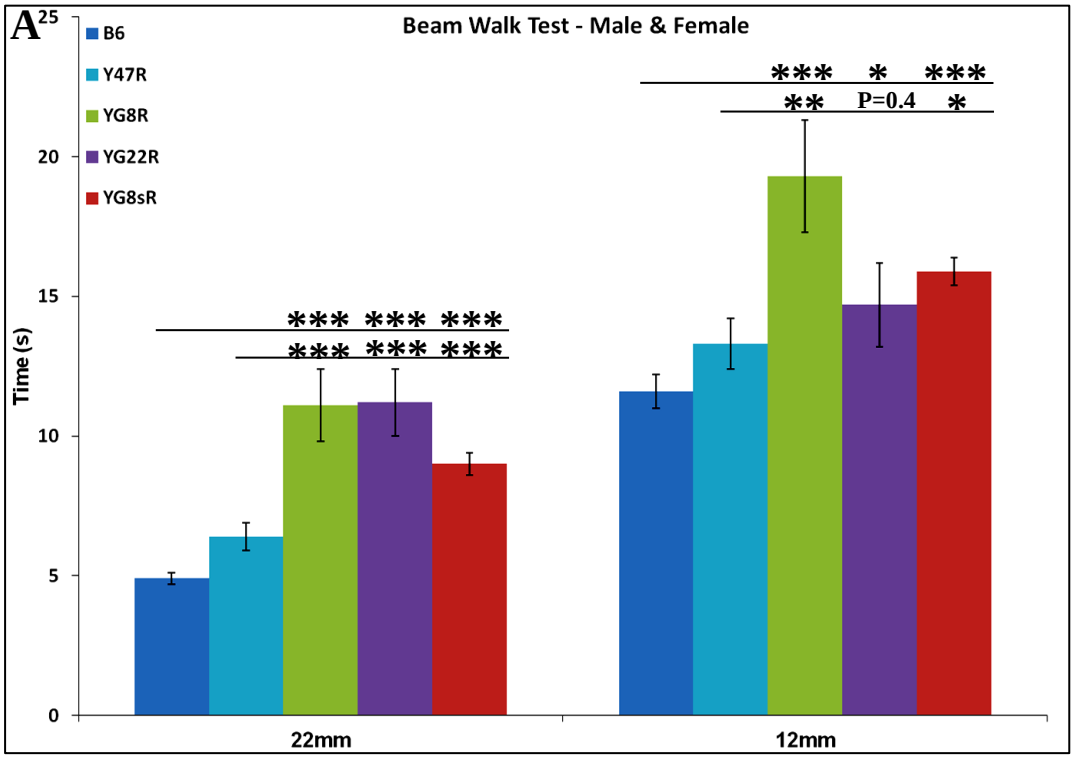
A
Beam Walk Test - Male & Female
B6
Y47R
YG8R
YG22R
YG8sR
Time (s)
25
20
15
10
5
0
*** *** ***
*** *** ***
*** * ***
** P=0.4 *
22mm
12mm

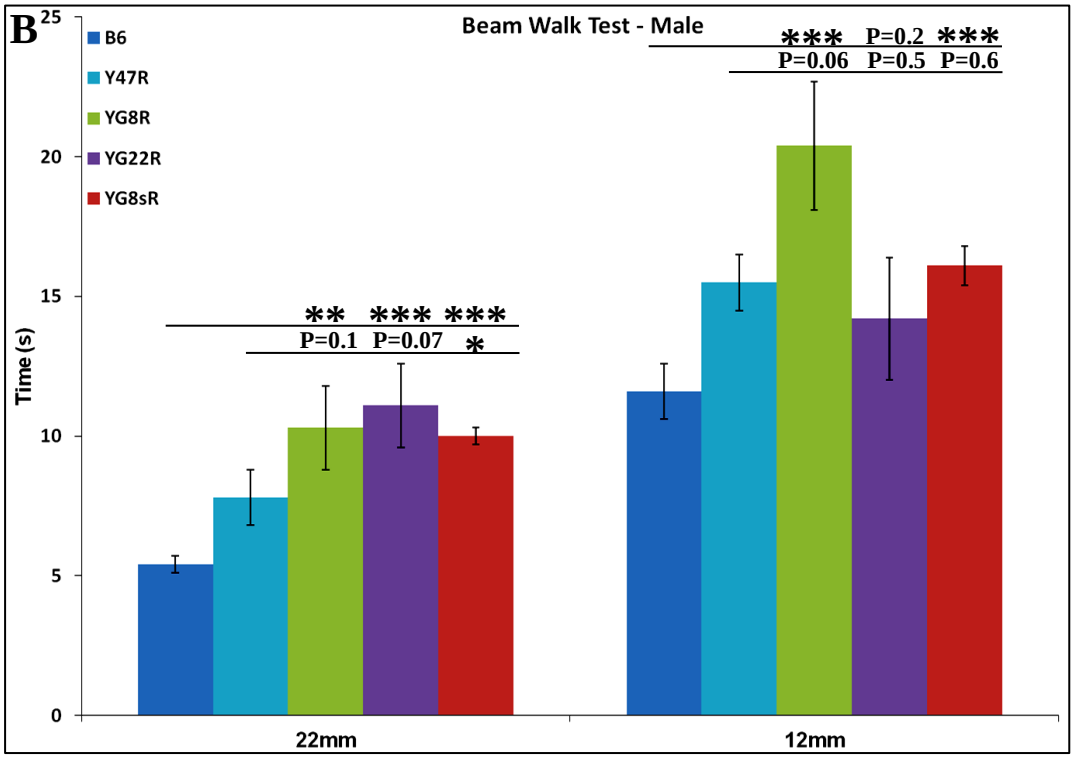
B
Beam Walk Test - Male
B6
Y47R
YG8R
YG22R
YG8sR
Time (s)
25
20
15
10
5
0
** *** ***
P=0.1 P=0.07 *
*** P=0.2 ***
P=0.06 P=0.5 P=0.6
22mm
12mm

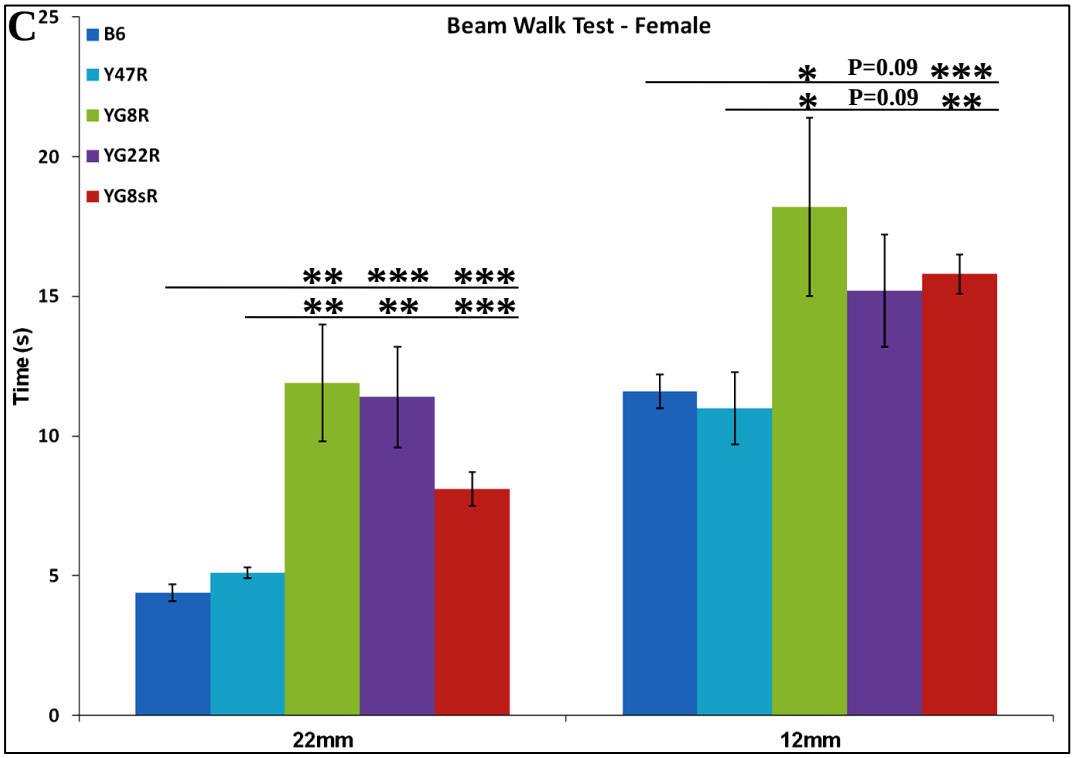

Fig. 3.15 Beam-walk analysis of mice. **A)** Analysis of YG8R, YG22R and YG8sR compared to B6 and Y47R controls showed a coordination deficit on both 22mm and 12mm beams in all rescue mice (*n*=10 mice per genotype) when both male and female values were taken together. However, no significant difference in beam-walk of YG22R on the 12mm beam was observed in comparison to Y47R control. **B)** Beam-walk analysis of YG8R, YG22R, and YG8sR male mice compared to B6 control (*n*=5 mice per genotype) revealed that all three deficient genotypes required significantly more time to cross the 22mm and 12mm beams, however there was no significant difference between these mice and Y47R control. **C)** Analysis of female littermates of both YG8R and YG8sR (*n*=5 mice per genotype) showed that these mice took significantly longer than B6 and Y47R to cross both 22mm and 12mm beams. Although YG22R followed a similar performance trend as that of YG8R and YG8sR on the 22mm and 12mm beams compared to B6 and Y47R controls, the difference in beam-walk on 12mm beam was not significant. Error bars indicate SEM and values represent mean ± SEM. Asterisks indicate significant differences between mutant and control mice (*P<0.05, **P<0.01 and ***P<0.001). Statistical differences between mutant and B6 control mice are indicated by the top line drawn over the bars while the bottom line indicates the differences between mutant and Y47R control mice.

3.3.4 Investigation of Motor Deficits in FRDA Mice Using Hang Wire Test

To further assess the neurological consequences of frataxin depletion, mutant mice were analysed by hang wire test. The mice were hung from a horizontally positioned wire with each end affixed to a vertical stand and the length of time the mouse held onto the wire was recorded. 10 mice were assessed for each group including 5 males and 5 females. As represented in Fig. 3.16, the YG8R, YG22R and YG8sR mice fell off the hang wire

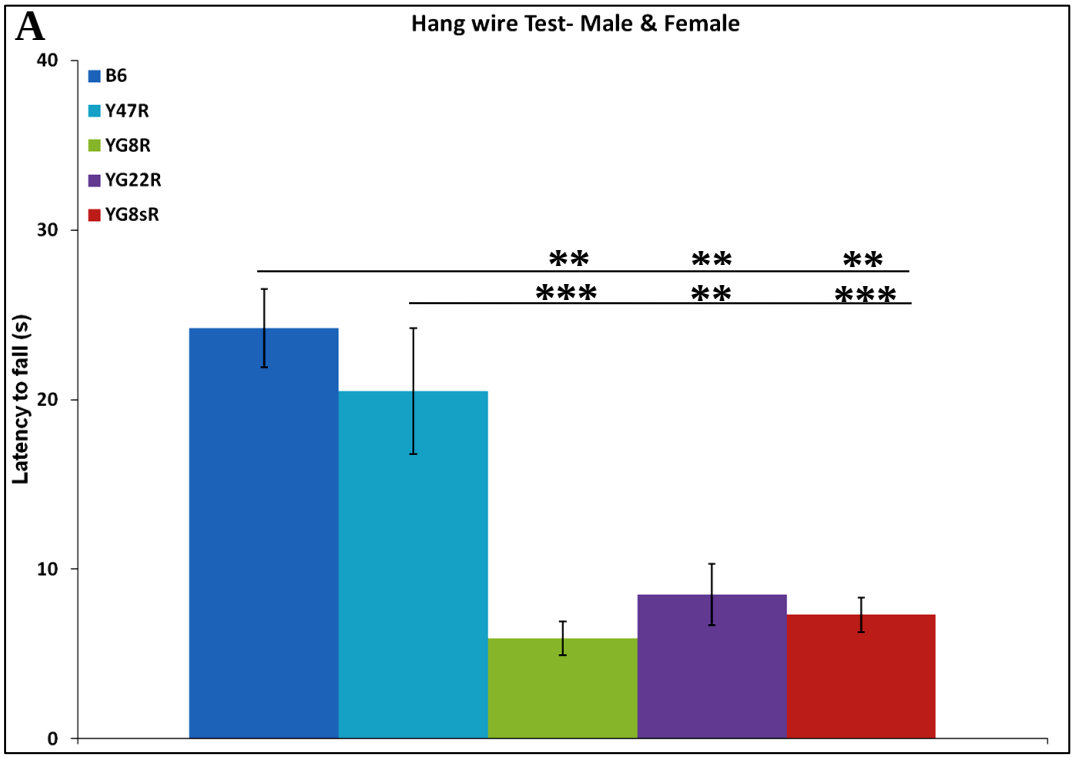
A
Hang wire Test- Male & Female
B6
Y47R
YG8R
YG22R
YG8sR
Latency to fall (s)
40
30
20
10
0
**
***
**
**
**
***

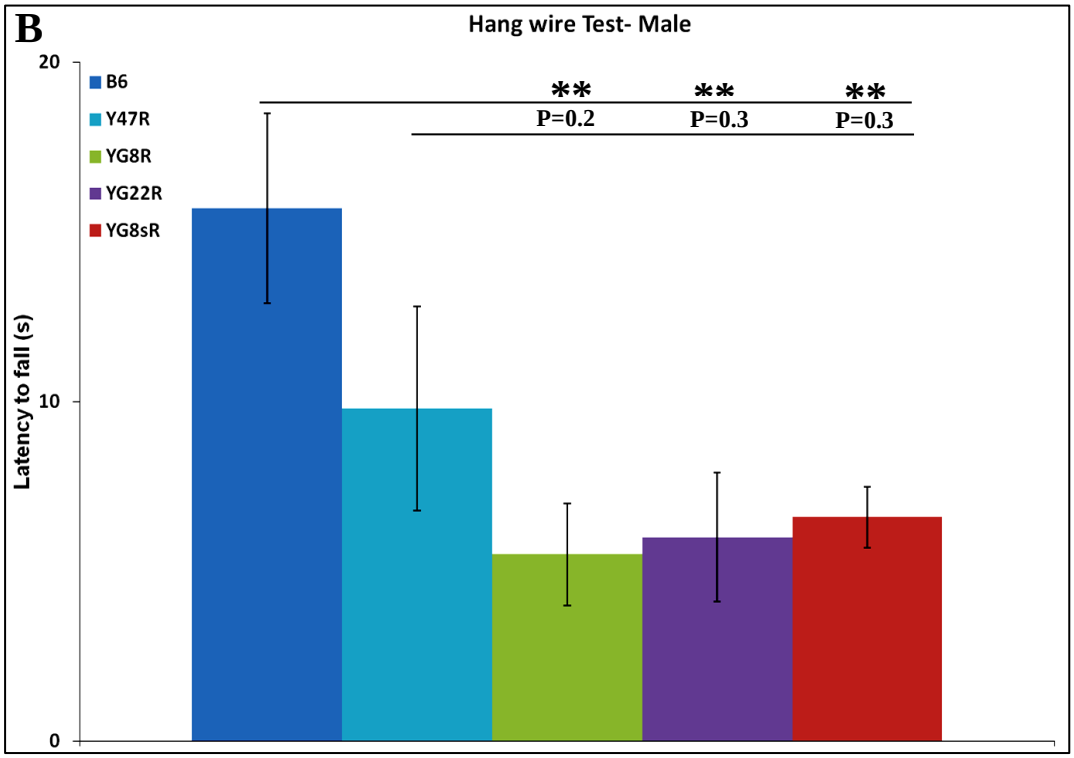
B
Hang wire Test- Male
B6
Y47R
YG8R
YG22R
YG8sR
Latency to fall (s)
20
10
0
**
P=0.2
**
P=0.3
**
P=0.3

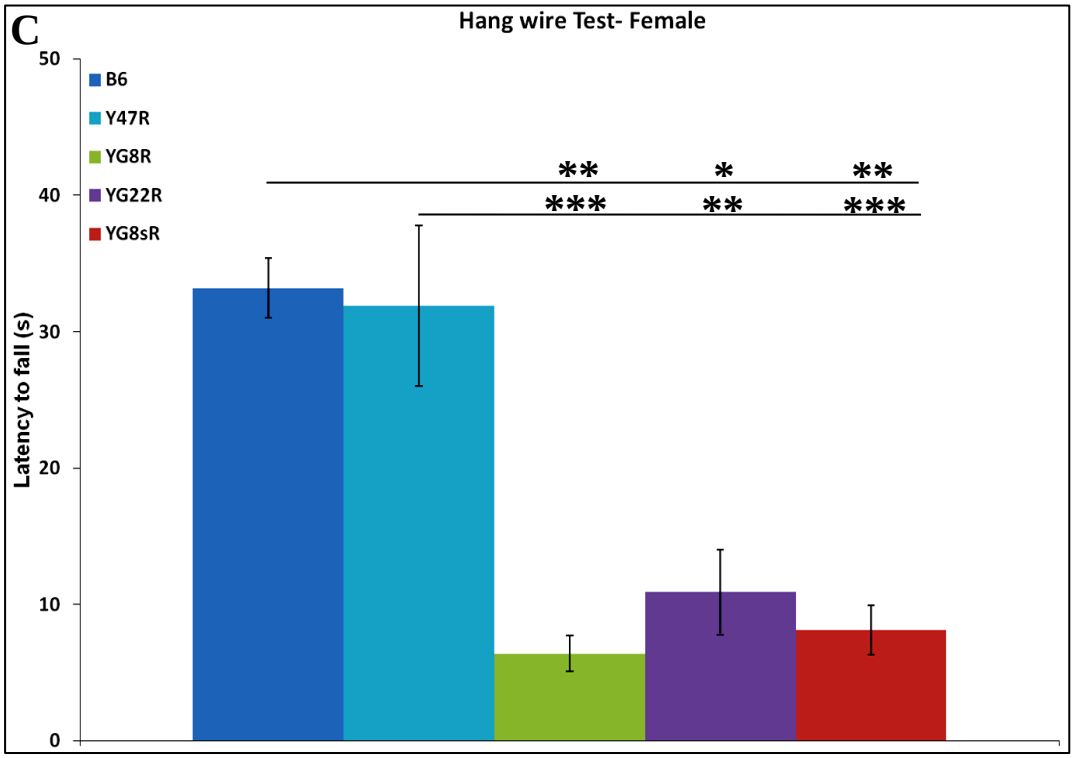

Fig. 3.16 Hang wire analysis of mice. **A)** Analysis of YG8R, YG22R and YG8sR revealed impaired neuromuscular strength and lack of coordinated motor control compared to B6 and Y47R controls when both male and female values were taken together (*n*=10 mice per genotype). Analysis of YG8R, YG22R and YG8sR **B)** males and **C)** females separately (*n*=5 mice per genotype) revealed the same pattern compared to B6 and Y47R controls. However, there was no significant different between all male mutant and Y47R control mice. Error bars indicate SEM and values represent mean ± SEM. Asterisks indicate significant differences between mutant and control mice (*P<0.05, **P<0.01 and ***P<0.001). Statistical differences between mutant and B6 control mice are indicated by the top line drawn over the bars while the bottom line indicates the differences between mutant and Y47R control mice.

quicker when compared to Y47R and B6 controls, suggesting a reduced strength. This trend held true when male and female values were taken together, Fig. 3.16A, or when male and female values were considered separately (for comparison with B6), Fig. 3.16B and Fig. 3.16C respectively. Significant differences between the performances of mutant and control mice were confirmed by the Student's *t* test. A significant difference was also seen between female mutant and Y47R control mice, Fig. 3.16B. However, no significant difference was observed between male mutant and Y47R control mice, Fig. 3.16C. This may be attributed to the heavier weight of Y47R male mice, preventing them from clinging to the wire for any extended period of time.

3.3.5 Investigation of Motor Deficits in FRDA Mice Using Grip Strength Test

To further assess forelimb grip strength, a grip strength meter was used to measure the peak force with which mice pulled a wire. 10 mice were assessed for each group, 5 males and 5 females, to identify the correlation between the hang wire and grip strength performance of the FRDA mice. The results showed a significant decrease in grip strength of all YG8R, YG22R and YG8sR mice compared to Y47R and B6 controls. This trend held true when both male and female values were taken together, Fig. 3.17A, or when male and female values were considered alone, Fig. 3.17B and Fig. 3.17C respectively. The significance of the difference between the groups was confirmed by Student's *t* test, indicating the significance of the difference between the performance of mutant and control mice.

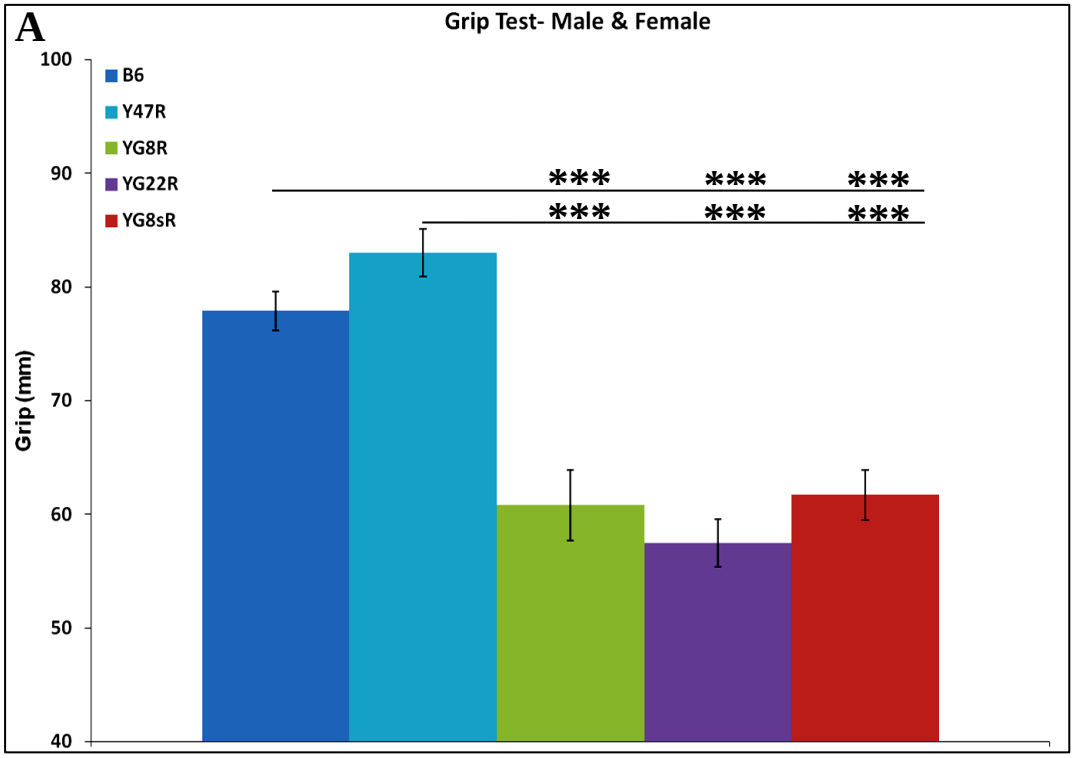

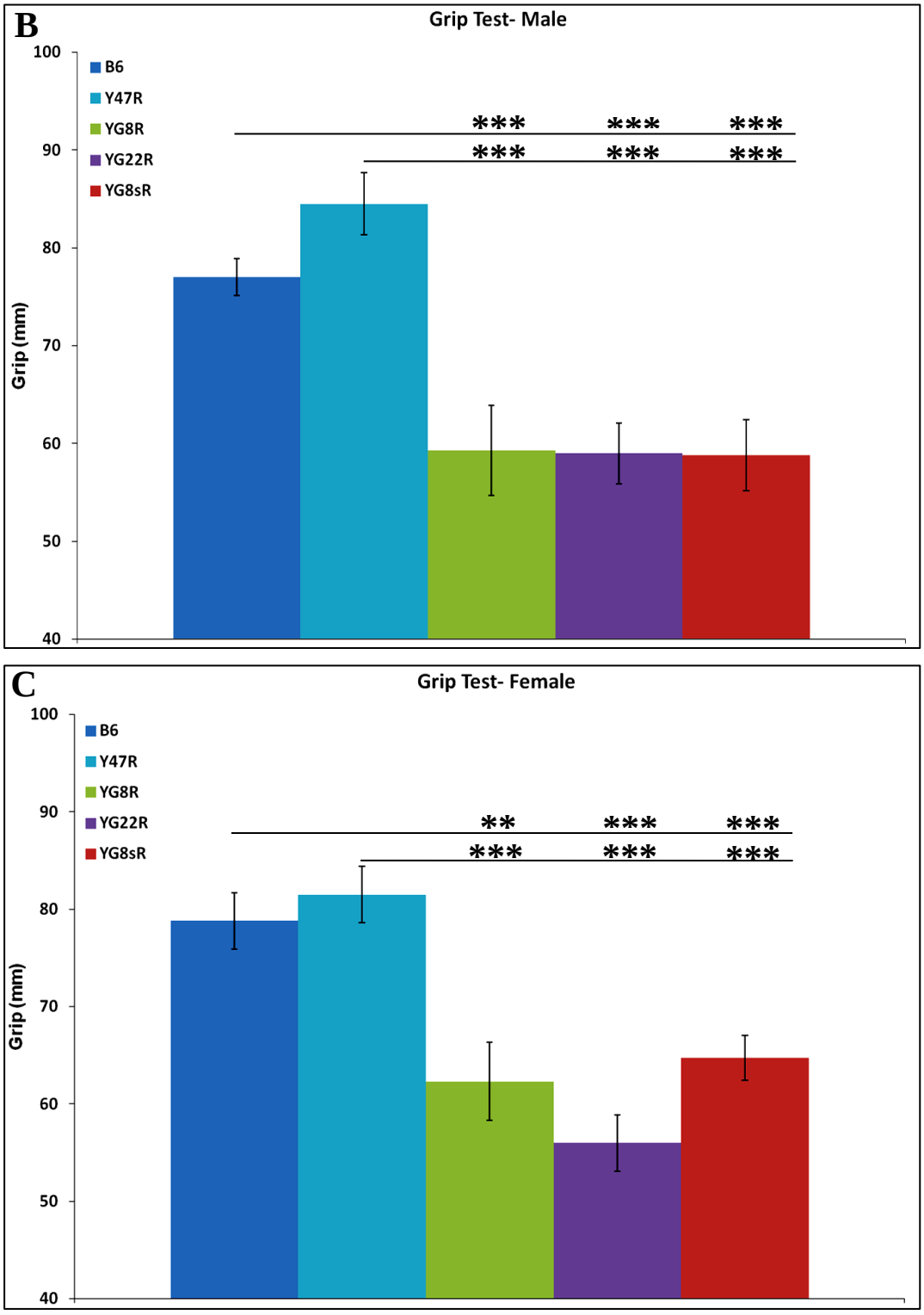

Fig. 3.17 Grip strength analysis of mice. **A)** Analysis of YG8R, YG22R and YG8sR revealed significantly reduced grip strength compared to B6 and Y47R controls when both males and females were analysed together (*n*=10 mice per genotype). Analysis of **B)** males and **C)** females separately (*n*=5 mice per genotype) revealed a significant decrease in grip strength of all mutant mice compared to the controls. Error bars indicate SEM and values represent mean ± SEM. Asterisks indicate significant differences between mutant and control mice ($^{*}P<0.05$, $^{**}P<0.01$ and $^{***}P<0.001$). Statistical differences between mutant and B6 control mice are indicated by the top line drawn over the bars while the bottom line indicates the differences between mutant and Y47R control mice.

3.3.6 Investigation of Gait Deficits in FRDA Mice Using a Foot Print Test

To characterise the motor behavioural phenotype of FRDA mice, gait abnormalities were assessed by analysing the footprint pattern of mutant and control mice while they walked along a narrow gangway. As evident in Fig. 3.8, the control mice walked in a straight line with a regular and even alternating stride, whereas YG8R, YG22R and YG8sR mice progressively moved from side to side while walking along the gangway, demonstrating an overall loss of control of fine movement. Moreover, further analysis of the footprints indicated that both hind and front stride length decreased in YG8R, YG22R and YG8sR FRDA mice compared to Y47R and B6 controls, Fig. 3.18. This trend held true when both male and female values were taken together (*n*=10 mice per genotype), Fig. 3.18A, or when female values were considered alone (*n*=5 mice per genotype), Fig. 3.18B. Although, FRDA male mice exhibited the same pattern in stride length in comparison to the controls (*n*=5 mice per genotype), Fig. 3.18C, only stride length in left hindlimb and right forelimb of YG8sR, and left forelimb and right forelimb of YG22R were significantly different compared to those of the controls. There was also a significant decrease in right hindlimb of YG8sR mice compared to Y47R control.

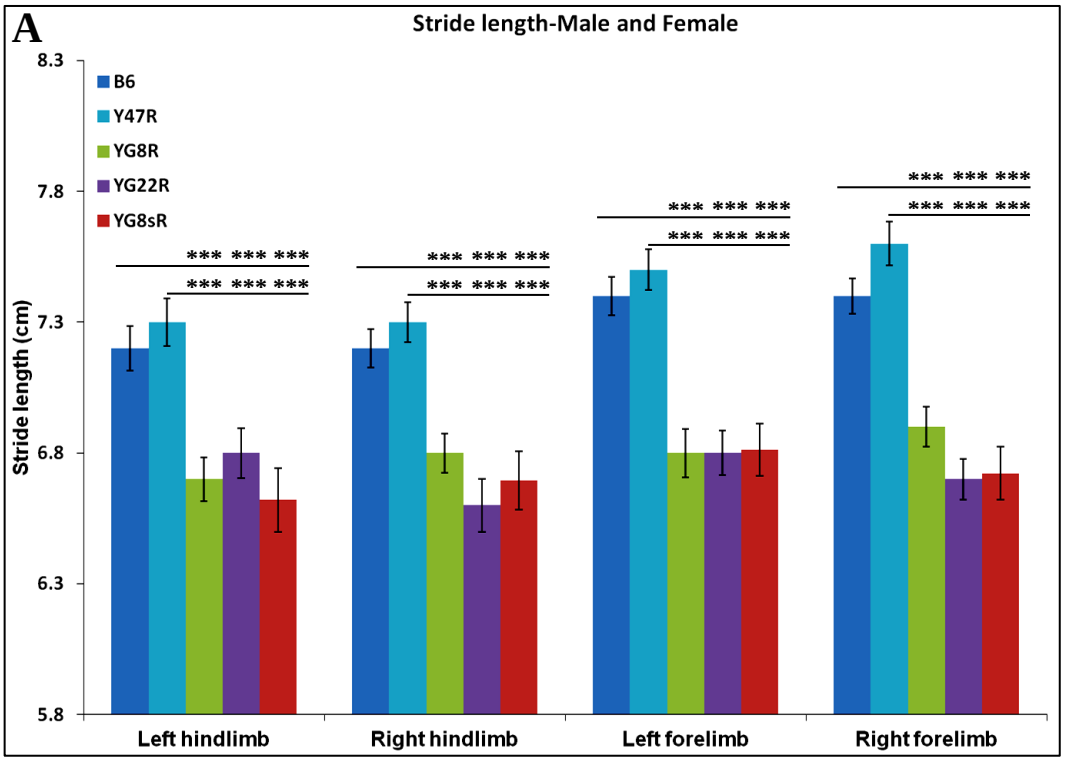

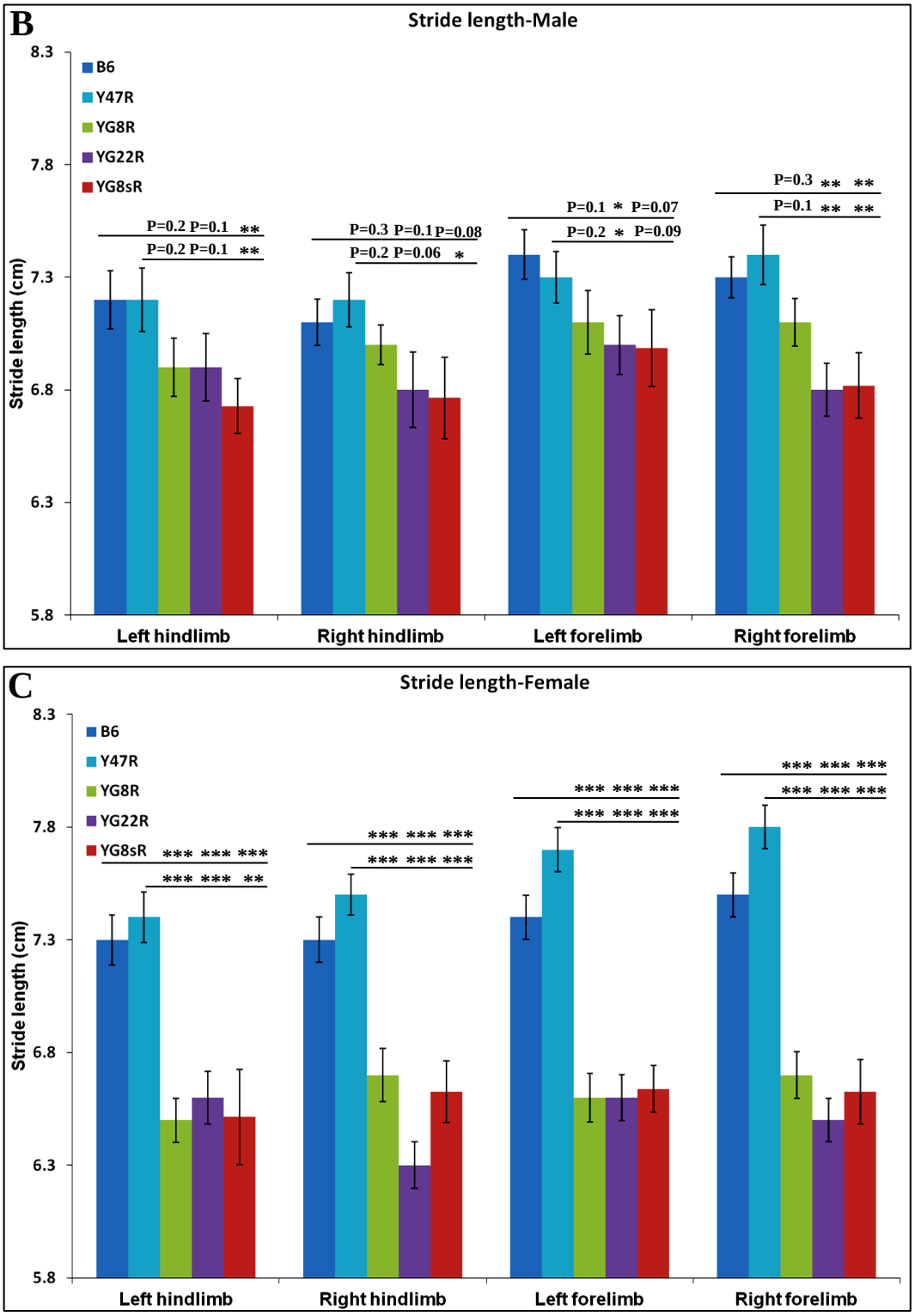

Fig. 3.18 Stride length analysis of mice. **A)** Analysis of YG8R, YG22R and YG8sR revealed significantly reduced stride length compared to B6 and Y47R controls when both male and female values were taken together (*n*=10 mice per genotype). Analysis of **B)** males and **C)** females separately (*n*=5 mice per genotype). Error bars indicate SEM and values represent mean ± SEM. Asterisks indicate significant differences between mutant and control mice (*P<0.05, **P<0.01 and ***P<0.001). Statistical differences between mutant and B6 control mice are indicated by the top line drawn over the bars while the bottom line indicates the differences between mutant and Y47R control mice.

FRDA mice were also analysed for hind base and fore base width. The results indicated significantly shorter base width of both hind and forepaws, Fig. 3.19. This trend held true when both male and female values were analysed together (*n*=10 mice per genotype), Fig. 3.19A, or when male and female values were considered alone (*n*=5 mice per genotype), Fig. 3.19B and Fig. 3.19C respectively. However, there was no significant difference in hind base width of YG8R male mice compared to B6 male control.

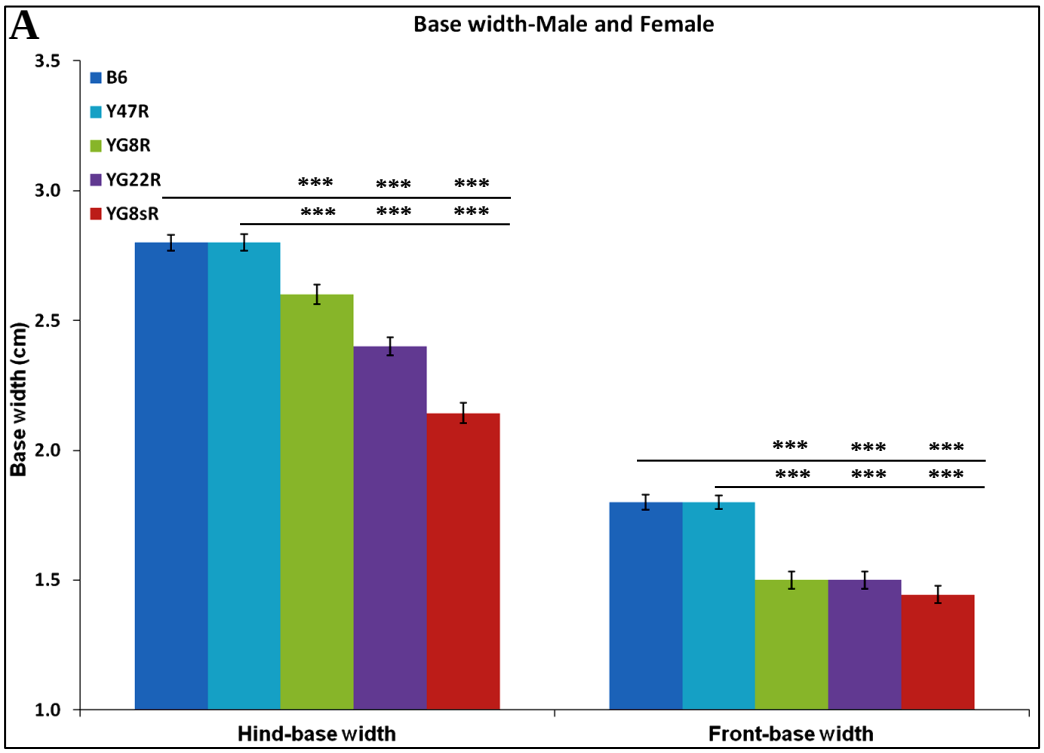

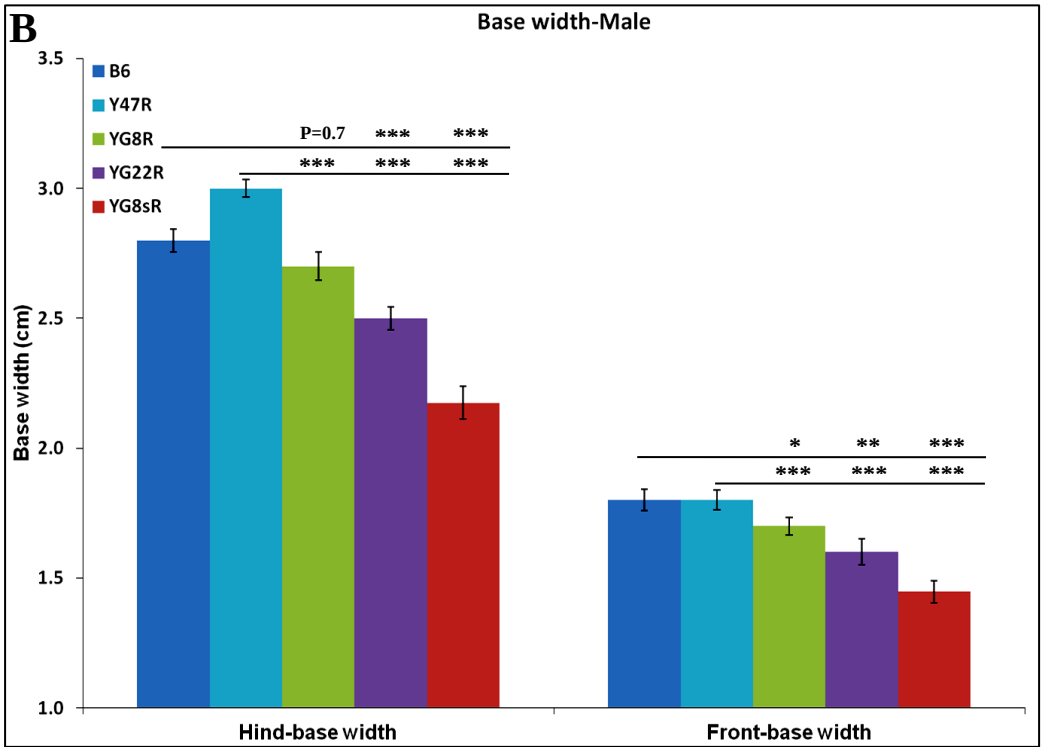

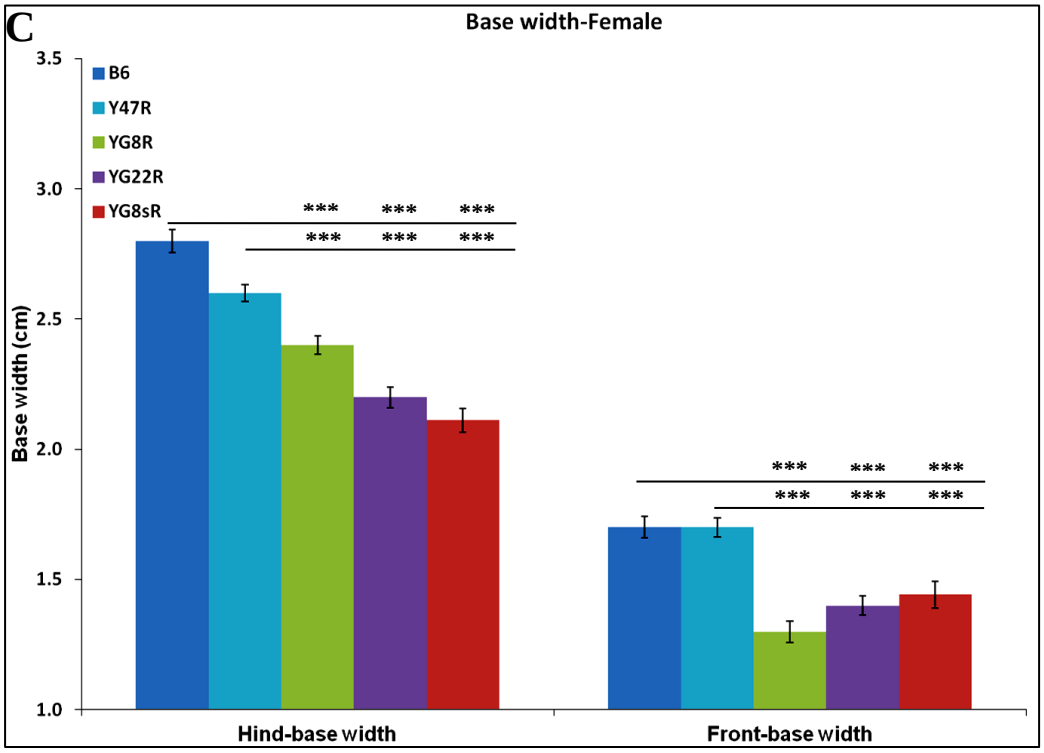

Fig. 3.19 Base width analysis of mice. **A)** Analysis of YG8R, YG22R and YG8sR revealed significantly shorter base width of both fore and hindpaws compared to B6 and Y47R controls when both male and female values were taken together (*n*=10 mice per genotype). Analysis of **B)** males and **C)** females separately (*n*=5 mice per genotype) showed a significant decrease in both fore and hind base width in all mutant mice compared to the controls. Error bars indicate SEM and values represent mean ± SEM. Asterisks indicate significant differences between mutant and control mice (*P<0.05, **P<0.01 and ***P<0.001). Statistical differences between mutant and B6 control mice are indicated by the top line drawn over the bars while the bottom line indicates the differences between mutant and Y47R control mice.

In addition, the average stride length (left/right hindlimb and left/right forelimb), Fig. S.3, and the average base width (hind and fore base width), Fig. S.4, followed the same pattern as those previously observed in Fig. 3.19. The significance of the difference between the groups was confirmed by Student's *t* test. The results highlighted the non-uniformity in step alteration and lack of coordination in FRDA mouse models, also inherent in FRDA patients.

3.3.7 Glucose Tolerance Response in FRDA Mouse Models

To determine the prevalence of abnormalities in glucose handling in FRDA mice, a glucose tolerance test was performed in three FRDA mouse models (YG8R, YG22R and YG8sR) and two controls (Y47R and B6) after a 16h fasting period. 1mg/g glucose was administered intraperitoneally and blood glucose concentration was measured prior to

glucose administration and after 20, 40 and 60 minutes using a glucometer. 10 mice, 5 males and 5 females, were assessed for each group. As evident in Fig. 3.20A, blood glucose concentration was higher in all three FRDA mouse models compared to Y47R and B6 controls when both male and female values were analysed together, suggesting glucose intolerance response in these mice. However due to large individual variations, the differences did not reach the statistical significance analysed by Student's *t* test, except YG8sR which had a significant glucose intolerance response at 40 and 60 minute time points compared to Y47R and B6 controls respectively ($P<0.05$), Fig. 3.20A. A similar tendency was observed when male values were considered alone. A significant difference was identified in YG22R at 40 minute time point and in YG22R and YG8sR mice at 60 time point compared to Y47R and B6 controls ($P<0.05$), Fig. 3.20B. Surprisingly, female mice responded differently to the glucose tolerance test. The excursions in glucose indicated no difference in female YG22R, YG8sR and control mice, except YG8R which had a higher glucose concentration after 40 minutes, Fig. 3.20C. The basal glucose concentrations of FRDA and control mice were similar, however between the genders, female mice displayed a lower basal glucose level than their male counterparts. This might be due to the lower body weight of the female mice and thus higher insulin sensitivity, Fig. 3.20D. Fold change analysis did not provide additional information regarding the glucose tolerance test, Fig. S.5. For all time points, statistical analysis using two-way ANOVA was performed for all the groups, Table 3.7.

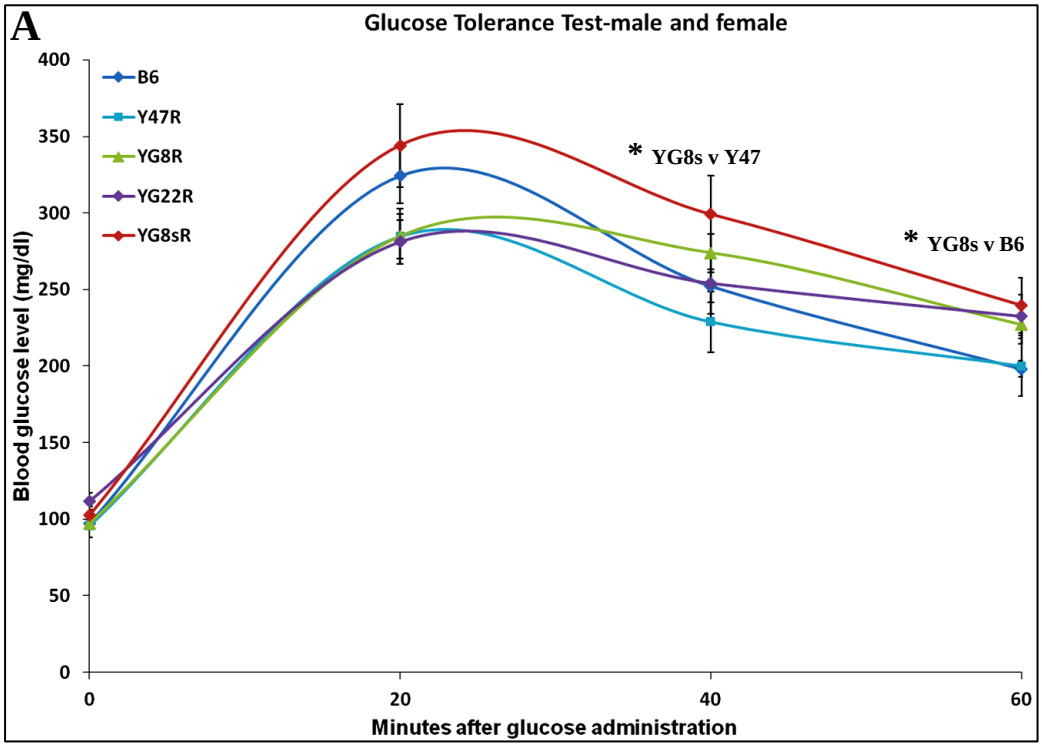

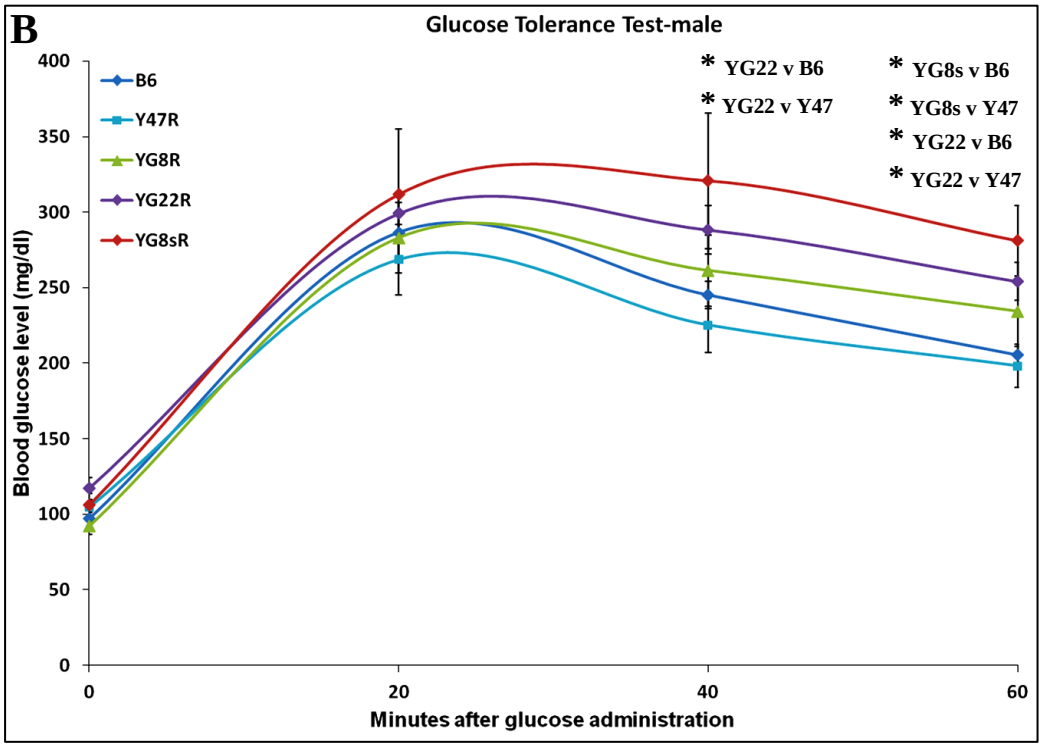
B
Glucose Tolerance Test-male
B6
Y47R
YG8R
YG22R
YG8sR
* YG22 v B6
* YG22 v Y47
* YG8s v B6
* YG8s v Y47
* YG22 v B6
* YG22 v Y47
Blood glucose level (mg/dl)
Minutes after glucose administration

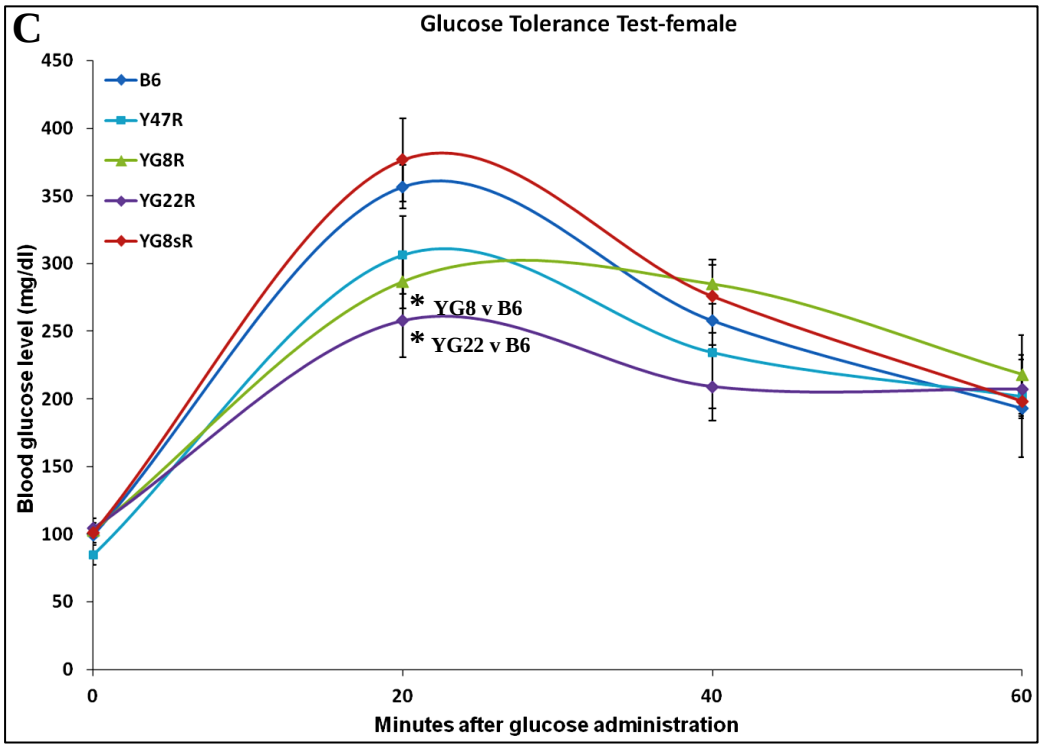
C
Glucose Tolerance Test-female
B6
Y47R
YG8R
YG22R
YG8sR
* YG8 v B6
* YG22 v B6
Blood glucose level (mg/dl)
Minutes after glucose administration

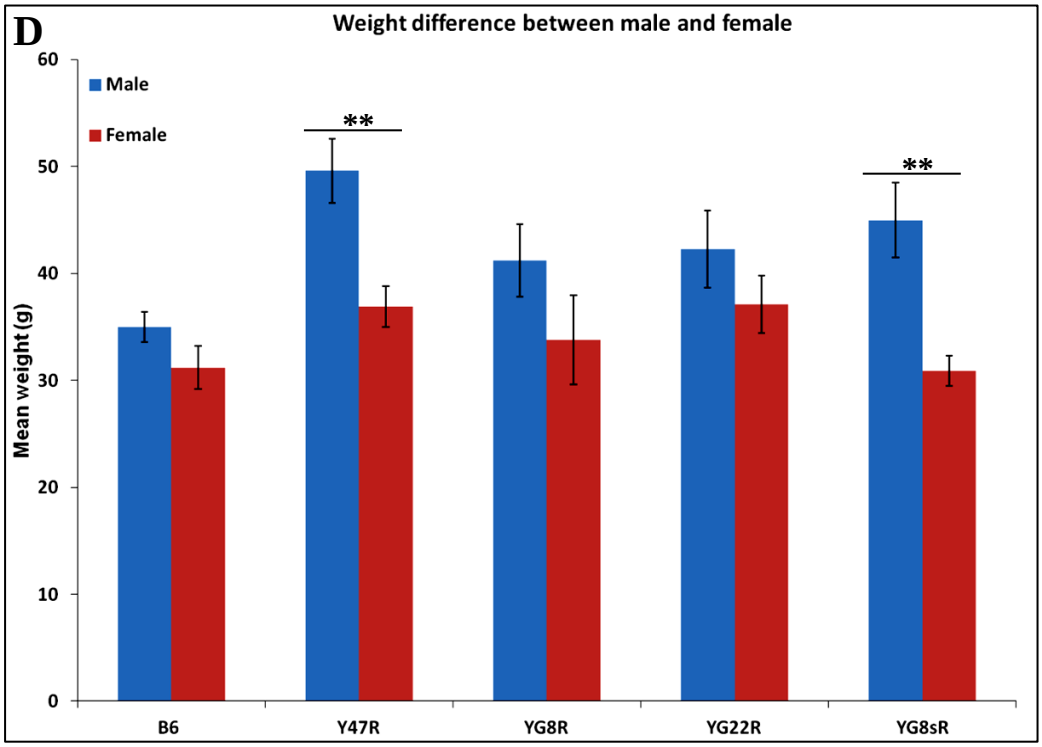

Fig. 3.20 Glucose tolerance test of mice. **A)** Glucose concentration was higher in YG8R, YG22R and YG8sR compared to B6 and Y47R controls when both male and female values were taken together (*n*=10 mice per genotype). **B)** Similar results were obtained when male values were considered alone (*n*=5 mice per genotype). **C)** Analysis of female mice showed no difference between the FRDA and control mice (*n*=5 mice per genotype). **D)** The disparity in body weight of males and females. Error bars indicate SEM and values represent mean ± SEM. Asterisks indicate significant differences between mutant and control mice (*P<0.05, **P<0.01 and ***P<0.001), analysed by Student's *t* test.

Table 3.7 Two-way ANOVA analysis of glucose tolerance in FRDA mouse models

Mouse	Genotype	Gender	Versus B6	Versus B6 (Male & Female)	Versus Y47R	Versus Y47R (Male & Female)
YG22R	FRDA YG22 Rescue	Male	P=0.001	P=0.8	P=0.0009	P=0.2
		Female	P=0.09		P=0.4	
YG8R	FRDA YG8 Rescue	Male	P=0.07	P=0.1	P=0.1	P=0.02
		Female	P=0.001		P=0.7	
YG8s R	FRDA YG8 Small Rescue	Male	P=0.003	P=0.004	P=0.005	P=0.0003
		Female	P=0.3		P=0.02	

3.3.8 Insulin Tolerance Response in FRDA Mouse Models

To determine insulin sensitivity in FRDA mice, an insulin tolerance test was performed in three FRDA mouse models (YG8R, YG22R and YG8sR) and two controls (Y47R and B6) after a 16h fasting period. 0.75U/kg insulin was administered intraperitoneally and

blood glucose concentration was measured prior to insulin administration and after 20, 50 and 80 minutes using a glucometer. 10 YG8R (5 males and 5 females), 9 YG22R (5 males and 4 females), 9 YG8sR (4males and 5 females), 8 B6 (2 males and 6 females) and 10 Y47R (5 males and 5 females) were assessed. As evident in Fig. 3.21A, control mice did not show any apparent lowering of blood glucose. In contrast; FRDA mice, except YG8R, showed lower blood glucose levels after 50 minute time point, indicating a relative increase in insulin sensitivity with respect to control littermates, Fig. 3.21A. The results from the male littermates indicated that although the blood glucose concentration was normalised after 50 minutes, FRDA male mice exhibited a more rapid glucose lowering after insulin injection, Fig. 3.21B. Female FRDA mice had a greater reduction in blood glucose concentration after 50 minutes, suggesting insulin hypersensitivity, Fig. 3.21C. However, YG8R had smaller changes in blood glucose after insulin injection; this may be due to their lower body weight, Fig. 3.21D. Fold change analysis also revealed the difference in glucose concentration between the mutant and control mice, Fig. S.6. The significance of the difference between the groups was confirmed by Student's *t* test.

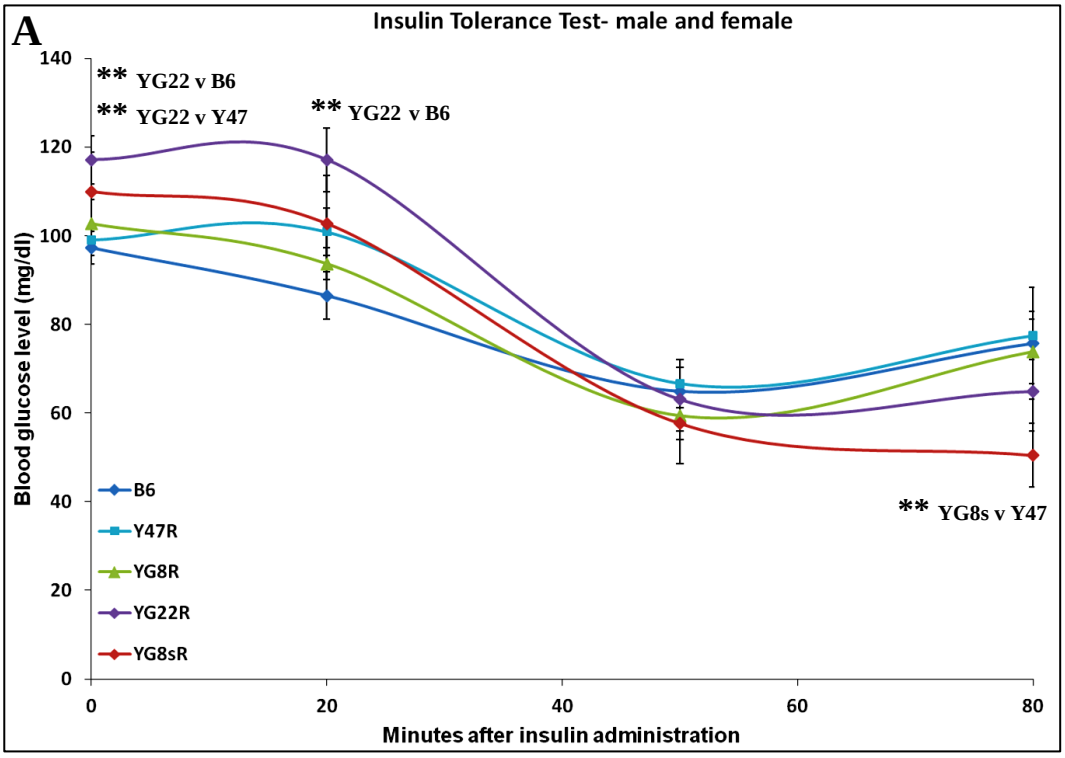

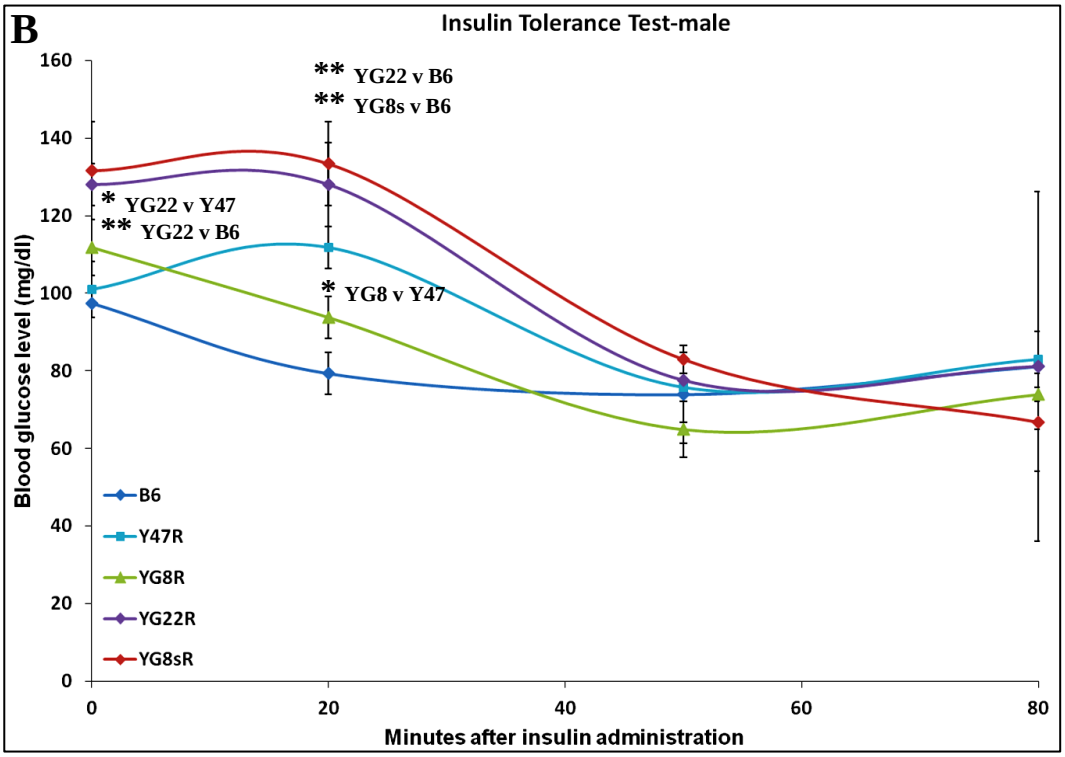
B
Insulin Tolerance Test-male
** YG22 v B6
** YG8s v B6
* YG22 v Y47
** YG22 v B6
* YG8 v Y47
Blood glucose level (mg/dl)
Minutes after insulin administration
B6
Y47R
YG8R
YG22R
YG8sR
0
20
40
60
80
100
120
140
160

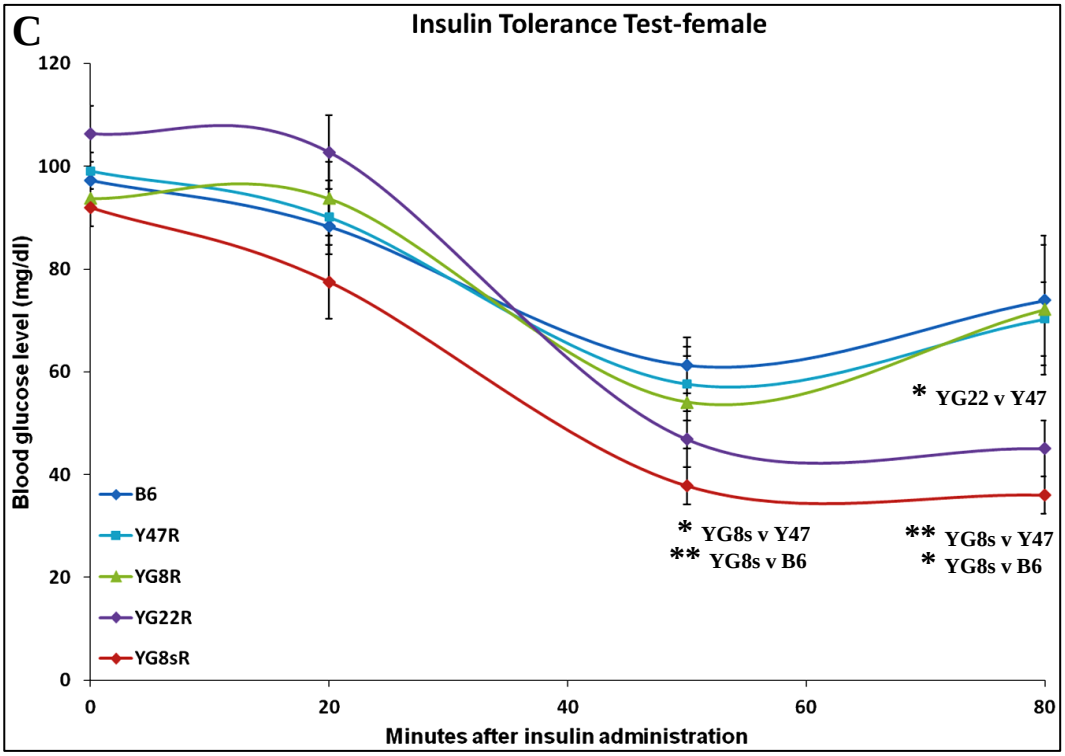
C
Insulin Tolerance Test-female
* YG22 v Y47
* YG8s v Y47
** YG8s v B6
** YG8s v Y47
* YG8s v B6
Blood glucose level (mg/dl)
Minutes after insulin administration
B6
Y47R
YG8R
YG22R
YG8sR
0
20
40
60
80
100
120

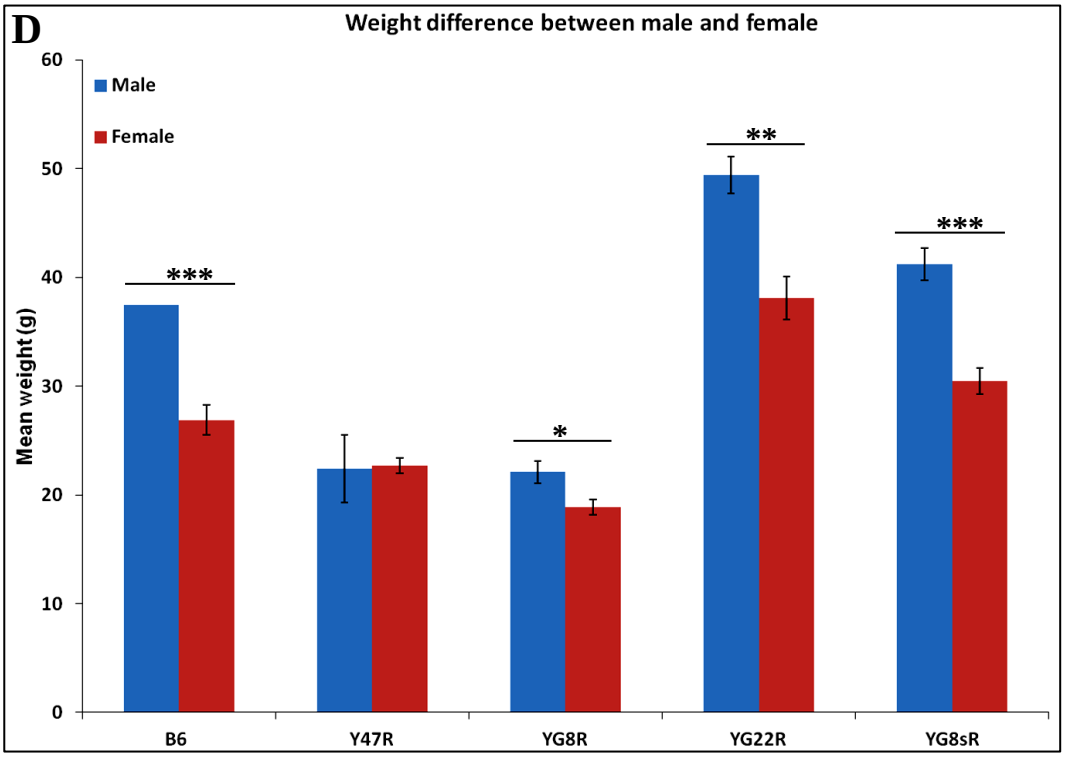

Fig. 3.21 Insulin tolerance test of mice. **A)** YG8R, YG22R and YG8sR showed lower blood glucose level after insulin injection compared to B6 and Y47R controls when both male and female values were considered. **B)** Although the blood glucose concentration was normalised after 50 minutes, FRDA male mice exhibited a more rapid glucose lowering after insulin injection. **C)** Female mice showed a greater reduction in blood glucose concentration after 50 minutes. **D)** The disparity in body weight of males and females. Error bars indicate SEM and values represent mean ± SEM. Asterisks indicate significant differences between mutant and control mice ($^{*}P<0.05$, $^{**}P<0.01$ and $^{***}P<0.001$).

3.5 Discussion

Previous studies demonstrated that both YG22R and YG8R FRDA mice expressed comparatively decreased levels of human frataxin in comparison to the endogenous mouse levels [31]. However, the results indicated that YG8R exhibited slightly less frataxin expression in comparison to YG22R. Therefore, it was hypothesised that the 190 and 190 + 90 GAA repeat expansion mutation sizes within YG22 and YG8 may induce the FRDA-like pathological phenotype and functional deficits. To determine the effect of reduced frataxin level on FRDA-like pathological phenotype and functional deficits, coordination ability of YG8R, YG22R and recently generated YG8sR was assessed using an accelerating rotarod apparatus over an 8 month period from 4 to 12 months of age. B6 and Y47R (containing the human *FXN* YAC transgene with normal-sized GAA repeats) were used as the controls. The YG8R, YG22R and YG8sR showed a significant decline

in their motor function compared to B6 and Y47R controls, though, the degree of impairment was more significant in YG8R mice. However, Y47R littermate controls exhibited significantly reduced rotarod performance after 7 months of age which was not expected. A possible explanation for such performance irregularity may be due to the higher initial weight of Y47R. On the other hand, analysis of the male and female values alone indicated that the former are more affected than the latter. This may be due to several factors. Firstly, lower body weight of the females may have contributed to the improved function of these mice. Secondly, females may be more capable of adapting to the experimental environment and conditions compared to the male mice. Moreover, body weight analysis of YG22R, YG8R and YG8sR demonstrated an increase in weight compared to B6. The increase in weight may be attributed to the observed decreased locomotor activity of the mice. However, unlike B6, Y47R showed a considerable increase in weight in comparison to all the tested mice. In order to reduce the effect of body weight on rotarod performance, the results were normalised by the body weight factor. The normalised results indicated small difference in the rotarod performance of B6 and Y47R controls. However, the decline in the rotarod performance of Y47R may not have been solely due to the body weight since Y47R were transgenic and other genetic factors may have contributed. Therefore, it is suggested to use B6 as the control in the future studies. The coordination deficiency in YG8R and YG22R was previously assessed by rotarod analysis and open field assay using WT control [31]. The results obtained as part of this investigation were in good agreement with those previously reported [31], further supporting the notion that the additional 90 GAA repeats in the YG8 line may be responsible for an even more pronounced functional deficiency.

The locomotor activity analysis using beam-breaker apparatus showed a significant decrease in average velocity, ambulatory distance, vertical time and count, jump time and count of the mutant mice compared to B6 and Y47R controls which were consistent with those previously reported [31]. However, YG8sR females showed greater ambulatory distance which was not expected. A possible explanation for such performance irregularity may be due to the lower body weight of these mice, suggesting gender dependent differences in body weight and functional activity of the FRDA mouse models. To further assess the motor behaviour and balance in the FRDA mice, beam-walk test was utilised using two different beam sizes, 12mm and 22mm. The results indicated that the FRDA mice took significantly longer to cross both beams in comparison to the controls.

However the difference was more significant when compared to the B6 control. This may be due to the higher body weight of Y47R mice, affecting their balance and performance. Muscle strength, assessed by forelimb grip strength and hang wire tests, was significantly decreased in all the FRDA mice compared to B6 and Y47R controls. Gait parameters (stride length and base width) of the mutant and control mice were also evaluated by footprint analysis. The results showed a non-uniform gait pattern with significantly decreased stride length and base width in the FRDA mice compared to B6 and Y47R controls. These results were in good agreement with those previously reported [230]. The identified functional deficits in the FRDA mouse models may be due to the reduced levels of frataxin, inducing an FRDA-like phenotype. If so, then these functional tests provide an experimental approach capable of detecting the phenotypic consequences of the reduced level of frataxin in the FRDA mice, making them amenable to novel therapeutic strategies.

Another symptom of FRDA disease is susceptibility to diabetes. FRDA patients are at risk of getting increased blood sugar levels or glucose intolerance, with approximately 20% progressing to overt diabetes as well as neurological problems. Therefore, glucose and insulin tolerance tests were performed in the FRDA mouse models to determine the prevalence of abnormalities in glucose handling and insulin sensitivity. The glucose tolerance results indicated that the FRDA mice were glucose intolerant. However, males and females responded differently, the excursions in glucose were similar in the female FRDA and the controls. This might be due to the lower body weight of the females, thus higher insulin sensitivity. Basal blood glucose level did not change amongst the tested mouse models. Taken together, these results indicated that insulin secretion following a glucose injection was delayed in the FRDA mice. This delay was more paramount in the males, suggesting increased body weight contributed to insulin resistance. Furthermore, the glucose-lowering effect of exogenous insulin was enhanced in the FRDA mouse models during insulin tolerance test, suggesting insulin hypersensitivity in these lines. Insulin hypersensitivity supports the existence of several pathways of insulin signalling, promoting glucose uptake and utilisation in peripheral tissues by either insulin-dependent or insulin-independent mechanisms. These results were consistent with those previously reported [215], suggesting mitochondrial dysfunction due to frataxin deficiency in the FRDA mouse models may contribute to pancreatic ß cell dysfunction. On this account, it is of interest to assess the relative contribution of insulin resistance and ß cell dysfunction

or deficiency in genes of the insulin receptor substrate (IRS) family in the future studies. This may provide a novel treatment strategy for the prevention of the disorder envisaged in FRDA patients.

CHAPTER IV

GAA REPEAT INSTABILITY AND *FXN* GENE AND PROTEIN EXPRESSION IN FRDA MOUSE MODELS

4.1 Introduction

As previously stated in section 1.14 (chapter I), two lines of human *FXN* YAC transgenic mice which contained GAA repeat expansions of 190 repeats and 190+90 repeats, designated YG22R and YG8R respectively, were generated by the Ataxia Research Group, Brunel University. A new YG8sR (YG8R with a small GAA band) line was recently generated from YG8R breeding. Previous studies demonstrated that both YG8R and YG22R FRDA mice expressed comparatively decreased levels of human frataxin mRNA and protein in comparison to the endogenous mouse levels [31]. Other studies also revealed YG8 and YG22 to have decreased mRNA levels in brain and heart tissues compared to Y47 [67]. Furthermore, the YG8 and YG22 exhibited an FRDA-like molecular disease phenotype that included intergenerational and somatic instability of the GAA repeat expansion mutation [41, 103] as well as progressive functional deficits compared to wild-type controls that were consistent with FRDA disease [31]. To further investigate the pathological phenotype of FRDA mouse models, different functional analysis were carried out (chapter III) which revealed functional deficits in the YG8R, YG22R and YG8sR compared to the Y47R and B6 controls. The aims of this part of the investigation were to examine the frataxin mRNA and protein levels together with the somatic GAA repeat instability in the FRDA mouse models and to identify their correlation with FRDA-like pathological phenotype. Such studies are crucial to highlight the importance of careful interpretation of the phenotypes of the mouse models in selecting the optimum mouse models capable of reproducing most of the characteristic features of the FRDA disease.

4.2 Materials and Methods

4.2.1 Collection and Preparation of Mouse Tissues

Following the completion of functional analysis, the mice were sacrificed by cervical dislocation. The Tail (Ta), Brain (B), Cerebellum (C), Liver (L), Heart (H), Kidney (K), Pancreas (P) and Dorsal Root Ganglia (DRG) were collected from the control (B6 and Y47R) and FRDA (YG8R, YG22R and YG8sR) mice. The collected tissues were snap-frozen in liquid nitrogen and stored at -80˚C. All procedures were carried out in accordance with the UK Home Office ‘Animals (Scientific Procedures) Act 1986’.

4.2.2 Genomic DNA Isolation from Tissues

Genomic DNA (gDNA) was isolated from mouse tissues using phenol/chloroform method as described in section 2.3.1.1 (chapter II). Tails of 5mm long and 50-100mg tissues (tail, brain, cerebellum, liver, heart, kidney and pancreas) were collected in 1.5ml tubes and digested by adding 400µl of digestion buffer and 10µl of 50mg/ml proteinase K. The samples were subsequently mixed and incubated in a 55˚C waterbath overnight. The following day, the incubated samples were vortexed and 400µl of phenol, equilibrated with Tris-HCl pH 8.0, was added. Samples were vortexed for 15 seconds and centrifuged at 16100 rcf for 5 minutes. The supernatant containing the DNA was removed and transferred to a clean 1.5ml microcentrifuge tube containing 500µl of chloroform/isoamyl alcohol (24:1, v/v). Subsequently, the samples were gently mixed by inverting the tubes and centrifuged at 16100 rcf for 5 minutes. Next, 350µl of the resulting supernatant was removed to a fresh microcentrifuge tube containing 800µl of absolute ethanol and 30µl of 3M Na-acetate (pH 5.2). Samples were mixed well by inverting the tubes several times and were subsequently placed at -80˚C for 10-15 minutes. Genomic DNA was precipitated following this step and formed a visible mass. The DNA was pelleted by centrifugation at 16100 rcf for 30 minutes at 4˚C. After removing the supernatant, the DNA was washed with 1ml of 70% ethanol and centrifuged at 16100 rcf for 20 minutes at 4˚C. The ethanol was discarded and the DNA pellets were air-dried for 10-15 minutes at RT. The dried pellets were resuspended in 50µl T.E. buffer and stored at 4˚C.

4.2.3 Determination of Genomic DNA Quantity and Purity

The concentration of DNA was read on the NanoDrop™ 2000c spectrophotometer (NanoDrop, Thermo Scientific) at 260 and 280nm wavelengths using 1µl of DNA.

4.2.4 Polymerase Chain Reaction (PCR)

4.2.4.1 GAA PCR

The GAA PCR was performed on mouse genomic DNA samples to detect the genotype as previously described in section 2.3.1.2 (chapter II). The PCR products were visualised on a 1% ethidium bromide stained agarose gel.

4.2.4.2 Long Gel GAA PCR

In order to estimate the GAA repeat size in different FRDA mouse models, samples were initially tested for the presence of the FRDA YAC transgene by GAA PCR. Subsequently, the samples of interest were run along with 100bp and 1kb^{+} DNA ladders overnight on a 20cm long gel made with 1.5% agarose and 1× TBE.

4.2.5 Extraction of Total RNA - Trizol® Method

Total RNA was isolated from the mouse tissues using an Invitrogen Trizol reagent following the manufacturer's instructions. To extract RNA, 30-40mg tissue samples were homogenised in 1ml of Trizol reagent by an Eppendorf homogenising rod and incubated for 10 minutes at RT. 200µl of chloroform (sigma-Aldrich) was then added per 1ml of Trizol to the samples. The samples were shaken vigorously for 15 seconds, incubated for 15 minutes at RT and then centrifuged at 16100 rcf for 15 minutes at 4˚C. The chloroform caused the Trizol to separate into a colourless aqueous phase and an organic phase containing phenol and chloroform. RNA remained exclusively in an upper aqueous phase. DNA and protein can be extracted from the organic phase by further precipitation. The upper aqueous layer (~0.5ml) was removed to a new 1.5ml microcentrifuge tube and RNA was precipitated by adding 0.5ml of isopropanol (sigma-Aldrich). The samples were incubated for 10 minutes at RT and then centrifuged at 16100 rcf for 15 minutes at 4˚C. A pellet containing RNA was visible after the centrifugation. The supernatant was removed and the RNA pellet was washed with 1ml of 75% ethanol, vortexed and centrifuged at

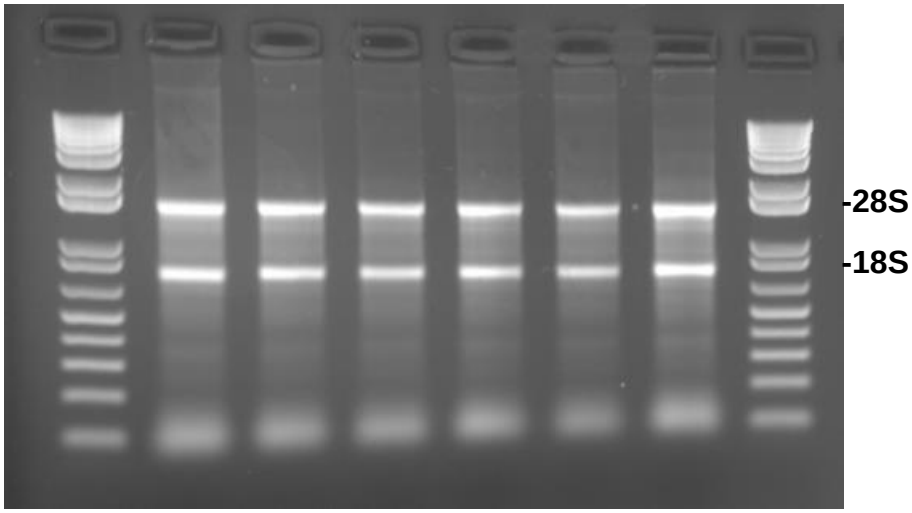

Fig. 4.1 Gel electrophoresis of the RNA samples using 1% agarose gel. Sharp, distinct bands corresponding to 28S (upper bands) and 18S (lower bands) ribosomal RNA indicate intact RNA. A 1kb^{+} DNA ladder (Invitrogen) was used for size evaluation.

5250 rcf for 5 minutes at 4˚C. The supernatant was removed and the RNA pellet was left to air dry for about 5-10 minutes at RT. The pellet was resuspended in 20µl of nuclease free water and retropipetted several times. The samples were left on ice for at least one hour and stored at -80˚C. The concentration of RNA was read at 260 and 280nm with a Nanodrop spectrophotometer (Nanodrop 2000C, Thermo Scientific, UK) using 1µl of the RNA samples. RNA concentrations were measured to ensure a ratio of >1.7, indicating the RNA is free of proteins and DNA. Total RNA was also quality checked using 1µl of the RNA samples loaded onto a 1% agarose gel, Fig. 4.1.

4.2.6 DNase I Treatment of RNA

Deoxyribonuclease I, Amplification Grade (DNase I, Amp Grade, Invitrogen) digests single and double stranded DNA to oligodeoxy-ribonucleotides containing 5´-phosphate. It is suitable for eliminating DNA during critical RNA purification procedures such as those prior to RNA-PCR amplification. DNase I, Amp Grade is purified from bovine pancreas and has a specific activity of ≥10,000U/mg.
To remove any genomic DNA and inhibit RNase enzymes, following reagents were added to 1 µg of total RNA:

- 1µl 10× DNase I reaction buffer
- 1µl DNase I, Amp Grade, 1U/µl
- Nuclease free water to 10µl

The samples were left for 15 minutes at RT. DNase I reaction was inactivated by adding 1µl of 25mM EDTA solution to the reaction mixture and heating it for 10 minutes at 65˚C. The RNA samples were subsequently used for reverse transcription.

4.2.7 Complementary DNA (cDNA) Synthesis

Cloned AMV first-strand cDNA synthesis kit (Invitrogen) was used to synthesise first strand cDNA. The following components were added to 5µl of the DNase I treated total RNA:

- 1µl of Oligo $(dT)_{20}$ Primer
- 2µl of 10mM dNTP mix (10mM each of dATP, dGTP, dCTP, dTTP at neutral pH)
- 4µl of DEPC-water

The mixtures were incubated for 5 minutes at 65˚C and then placed on ice for at least 1 minute. The contents were collected and the following mixture was added:

- 4µl of 5× cDNA synthesis buffer
- 1µl of 0.1M DTT
- 1µl of 40U/µl RNase Out
- 1µl of 15U/µl cloned AMV RT
- 1µl of DEPC-water

The samples were gently mixed by pipetting up and down and were incubated at 55˚C for 1 hour and then at 85˚C for further 5 minutes to terminate the reaction. The cDNA samples were used immediately or stored at -20˚C.

4.2.8 Reverse Transcriptase PCR (RT-PCR)

The presence or absence of genomic DNA contamination in DNase I treated total RNA and cDNA, was also confirmed by PCR before performing mRNA quantification. 1µl of the cDNA and DNase I treated total RNA was used for amplification in PCR. The following reagents were added to the cDNA and DNase I treated total RNA:

- 12.5µl of 2× Kapa Master Mix (Kapa Biosystem, UK) containing $MgCl_2$, Taq DNA polymerase and dNTPs)
- 1µl of 5µM *FXN*RT-R primer
- 1µl of 5µM *FXN*RT-F primer
- Nuclease free water to 25µl

The samples were mixed and the reactions were carried out in a thermocycler (MJ Research). The details of the primers (Sigma, UK) and the program used are represented in Tables 4.1 and 4.2 respectively.

Table 4.1 Primers used for RT-PCR and real-time PCR

Primer		Sequence (5´➔3´)	Product size (bp)
***FXN*RT-F**	*FXN* expression (Human Specific)	CAGAGGAAACGCTGGACTCT	**172**
***FXN*RT-R**		AGCCAGATTTGCTTGTTTGGC	
FRT I-F	*FXN* expression (Human and Mouse)	TTGAAGACCTTGCAGACAAG	**121**
RRT II-R		AGCCAGATTTGCTTGTTTGG	
***Gapdh*-m-F**	*Gapdh* (Mouse)	ACCCAGAAGACTGTGGATGG	**81**
***Gapdh*-m-R**		GGATGCAGGGATGATGTTCT	

Table 4.2 RT-PCR program

Steps	Temperature	Duration	Cycles
Denaturation	94ºC	1 min	1
Denaturation	94 ºC	30 sec	
Annealing	54 ºC	30 sec	30
Elongation	72 ºC	1 min	
Extension	72ºC	10 mins	1

PCR products from cDNA and DNase I treated total RNA were analysed on 2% agarose gel made up in 1× TBE buffer solution. The PCR products were then visualised using a UVP GDAS 1200 Gel Documentation Analysis System under ultraviolet light, Fig. 4.2.

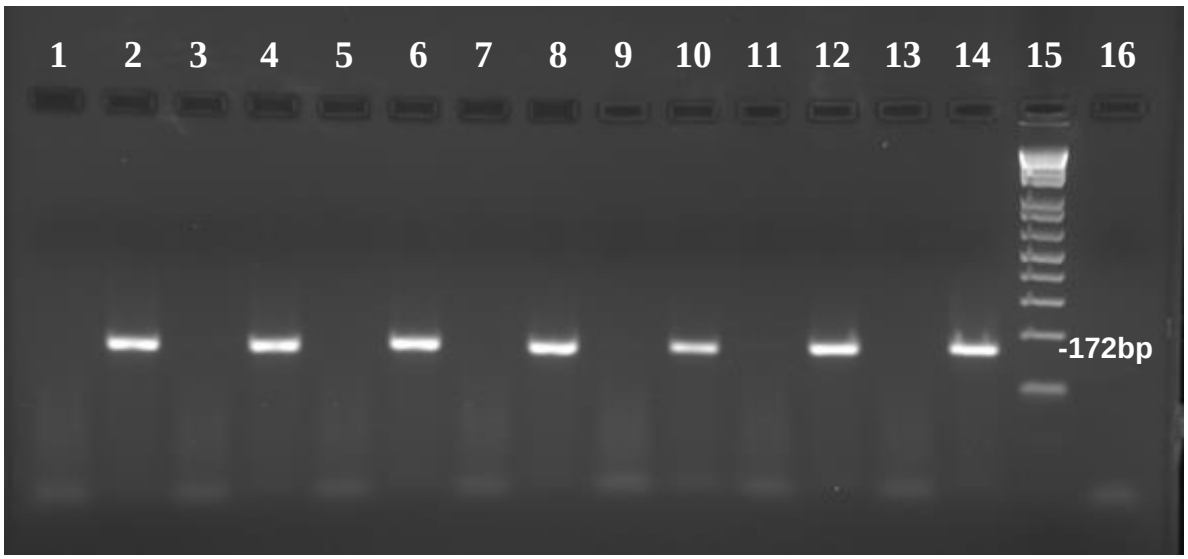

Fig. 4.2 Gel electrophoresis of human *FXN* RT-PCR analysis of the DNase I treated total RNA and cDNA using 2% agarose gel. Lanes 1, 3, 5, 7, 9, 11 and 13 are RT-PCR product from DNase I treated total RNA; Lanes 2, 4, 6, 8, 10, 12 and 14 are RT-PCR product from cDNA; Lanes 15 and 16 are 1kb^{+} DNA Ladder (Invitrogen) and negative control respectively.

4.2.9 Quantitative Real-Time RT-PCR (qRT-PCR)

The expression of genes of interest was quantitated on an ABI Prism 7900HT Sequence Detection System (Applied Biosystems) using 2× SYBR® Green PCR Master Mix (Applied Biosystems). SYBR Green dye is attached to the cDNA and produces a fluorescent signal. The signal intensity is proportional to the quantity of the cDNA present in the reaction. Consequently, in each step of the PCR reaction, the intensity of the signal increases while the amount of product increases. Each PCR-reaction was performed in triplicate on a MicroAmp optical 96-well PCR plate (Applied Biosystems),

and each reaction well contained 5µl of 5× diluted cDNA products, 0.5µl of each 50µM optimised respective forward and reverse primers (see Table 4.1 for primers used), 4.8µl of nucleare free water and 10µl of SYBR Green Master Mix (2× concentration). Target and endogenous master mixes were prepared separately and added to the plate. Subsequently, the plate was sealed with a real time plate sealer (MicroAmp, Applied Biosystems) and then centrifuged for 1 minute at 101 rcf to bring all the contents to the bottom of the well. The real time PCR reactions were run using the following programs:

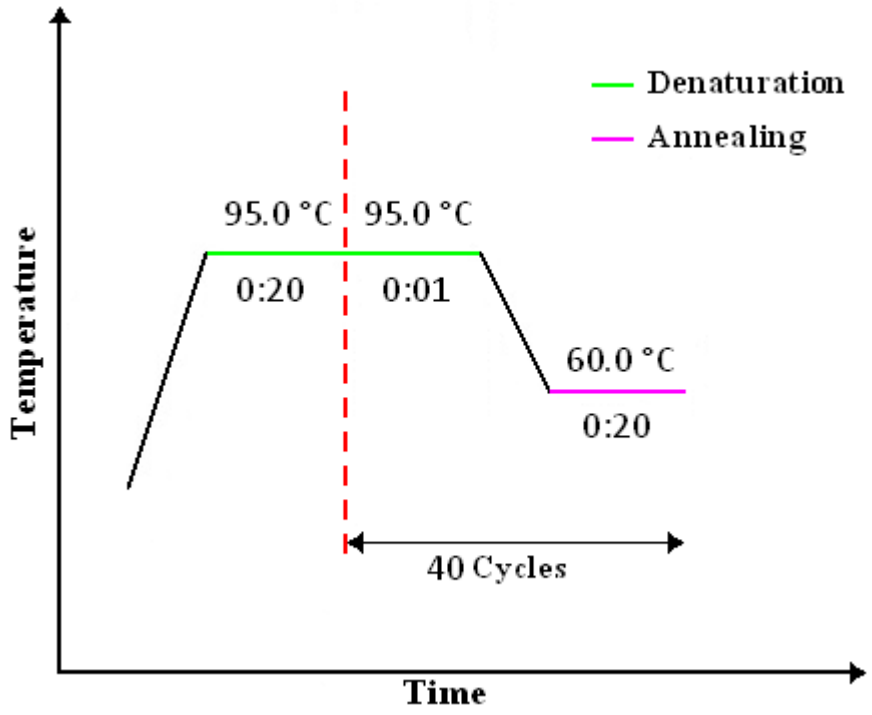

Fig. 4.3 Schematic diagram of real-time PCR program

Product specificity and efficiency was determined by SDS 2.1 software (Applied Biosystems) using dissociation curve analysis after each PCR run. The dissociation curve allows the check for primer dimer and non-specific amplification that may affect the quality of the data. Nonspecific PCR products are characterised by curves with several peaks. Best set of primers would only amplify the product of interest with no or a minimal quantity of primer dimer formation and decrease the distortion of the final fluorescence reading. Figure 4.4 represents the dissociation curve from real time PCR without primer dimer formation.

4.2.10 Protein Extraction

To extract protein, 30-40mg tissue samples were homogenised in 300µl of RIPA (RadioImmunoPrecipitation Assay) buffer (Sigma-Aldrich) and 12µl of 25× protease

inhibitor (to prevent proteolysis and maintain phosphorylation of proteins) (Thermo Scientific, UK) by an Eppendorf homogenising rod and centrifuged at 16100 rcf for 30 minutes at 4˚C. Subsequently, the total protein (supernatant) was separated from the cellular debris (pellet). The supernatant was then transferred to a clean 1.5ml microcentrifuge tube and stored at -80˚C.

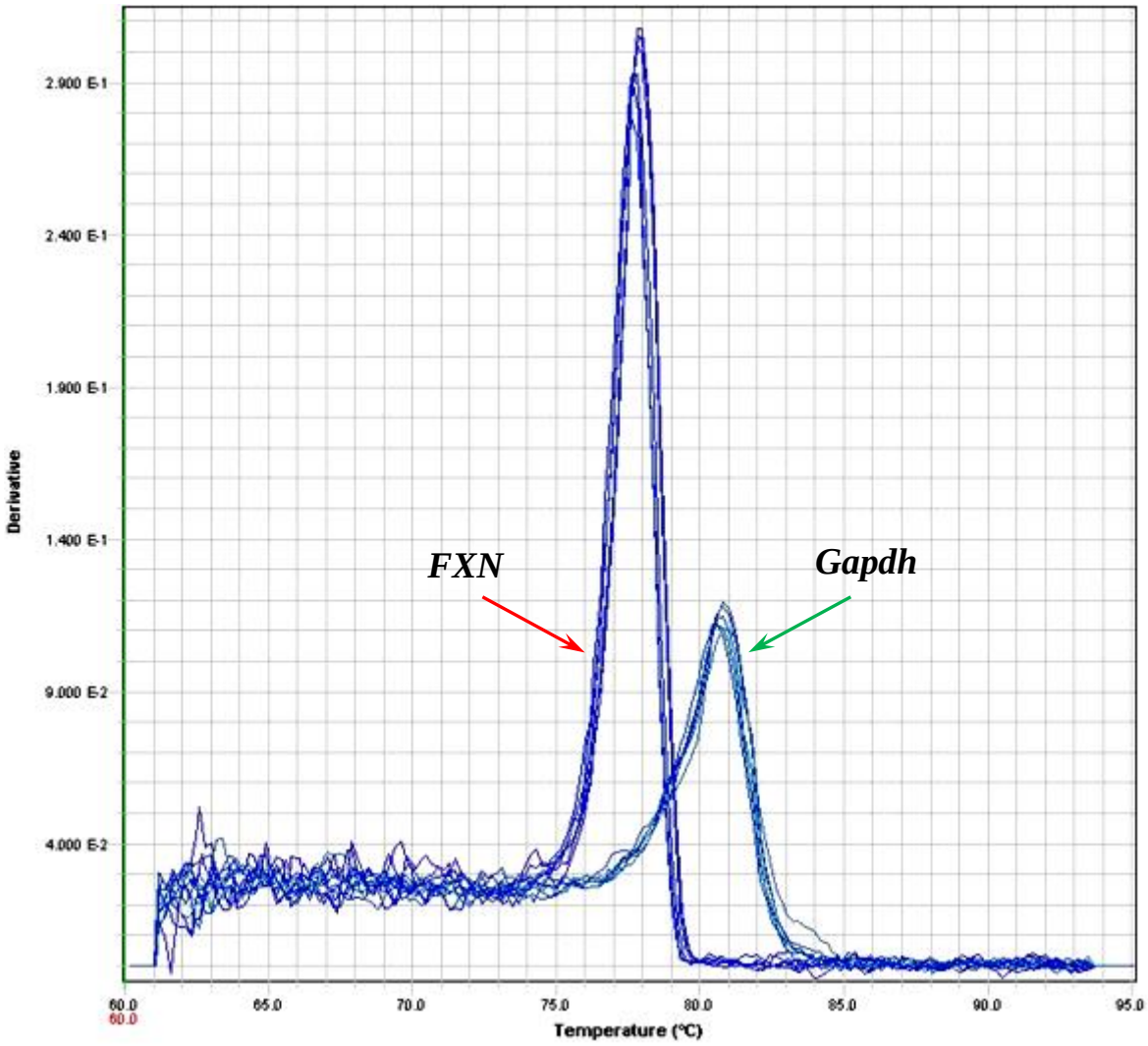

Fig. 4.4 Dissociation curve. Dissociation curve for *Gapdh* and *FXN* primers showing a clean PCR product amplified under real time conditions without any signs of primer dimmer formation or secondary products.

4.2.11 Protein Quantification Using BCA Protein Assay

Protein samples were quantified using a Pierce® BCA Protein Assay Kit (Thermo Scientific) following the manufacturer's instructions. The BCA protein assay is based on the reduction of Cu^{2+} to Cu^{1+} by protein in an alkaline medium with highly sensitive and selective colorimetric detection of the cuprous cation (Cu^{1+}) using bicinchoninic acid

(BCA). For the determination of the protein concentration, BCA protein assay reagents A and B were mixed with the ratio of 50:1 respectively. Subsequently, a serial dilution of bovine serum albumin (BSA) standard (0.025mg/ml-1.5mg/ml, Table 4.3) was made to construct a standard curve, Fig. 4.5. 10µl of BSA standards and protein samples (diluted 1:20 with dH_2O) were then added to 200µl BCA solution (A+B) and were incubated for 30 minutes at 37˚C. 200µl of each sample was placed into a 96-well plate and the protein concentration was measured using a plate reader (BP800, BioHit) at 562nm.

Table 4.3 Preparation of BSA standards for BCA analysis

Tube	Volume of dH_2O	Volume of BSA	Final Volume	Final BSA concentration
A	10 µl	30 µl	20 µl	**1500 µg/ml**
B	20 µl	20 µl	20 µl	**1000 µg/ml**
C	20 µl	20 µl of **A**	40 µl	**750 µg/ml**
D	20 µl	20 µl of **B**	20 µl	**500 µg/ml**
E	20 µl	20 µl of **D**	20 µl	**250 µg/ml**
F	20 µl	20 µl of **E**	30 µl	**125 µg/ml**
G	40 µl	10 µl of **F**	50 µl	**25 µg/ml**
H	40 µl	-	40 µl	**0 µg/ml**

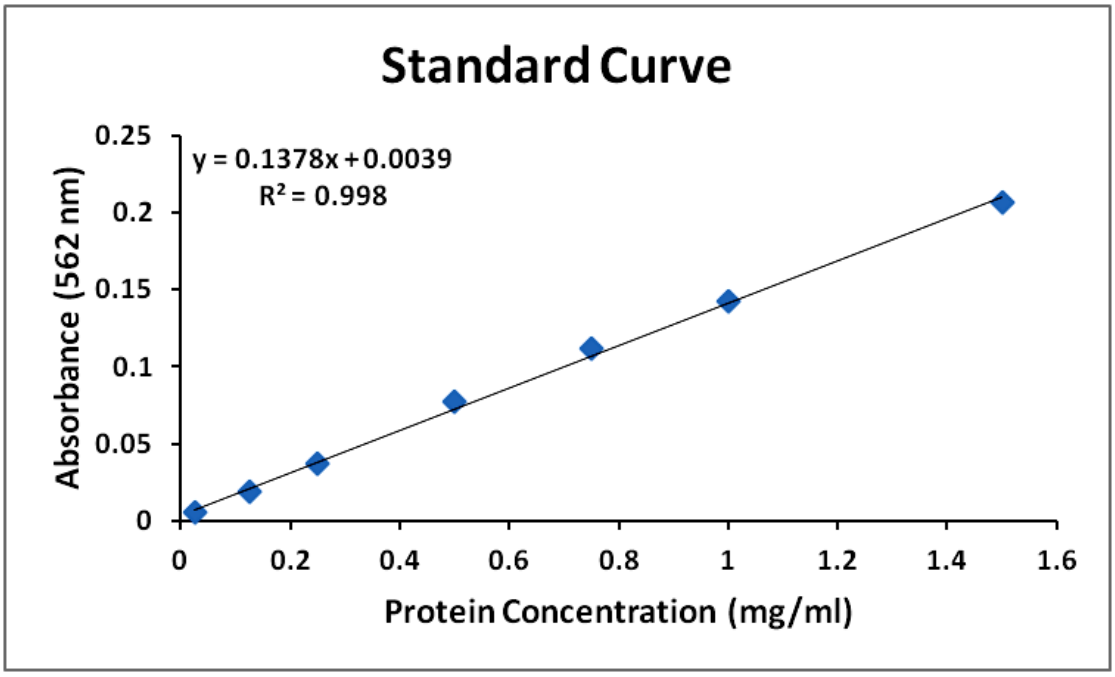

Fig. 4.5 Standard curve used for protein quantification

4.2.12 Dipstick Assay

The level of frataxin protein was measured by lateral flow immunoassay with the Frataxin Protein Quantity Dipstick Assay Kit (MitoSciences) according to the manufacturer's instructions. 2µg of protein in 25µl of extraction buffer (buffer A) was mixed with 25µl of 2× blocking buffer (buffer B) and was added to individual wells on a 96-well plate with gold-conjugated monoclonal antibody at the bottom of each well. The samples were incubated for 5 minutes, allowing the gold-conjugate to hydrate. The mixture was then resuspended gently using a pipette and dipsticks were inserted into the wells. Subsequently, frataxin within each sample was immunocaptured onto designated capture zones on the dipstick and the signal appeared 5-7mm from the bottom of the dipstick in approximately 20 minutes, Fig. 4.6. After the signal developed, the dipsticks were washed for 20 minutes with 30µl of washing buffer (buffer C) in an empty well of the microplate. The dipstick was air-dried for approximately 20 minutes and signal intensity was measured with a MS-1000 Immunochromatographic Reader (MitoSciences).

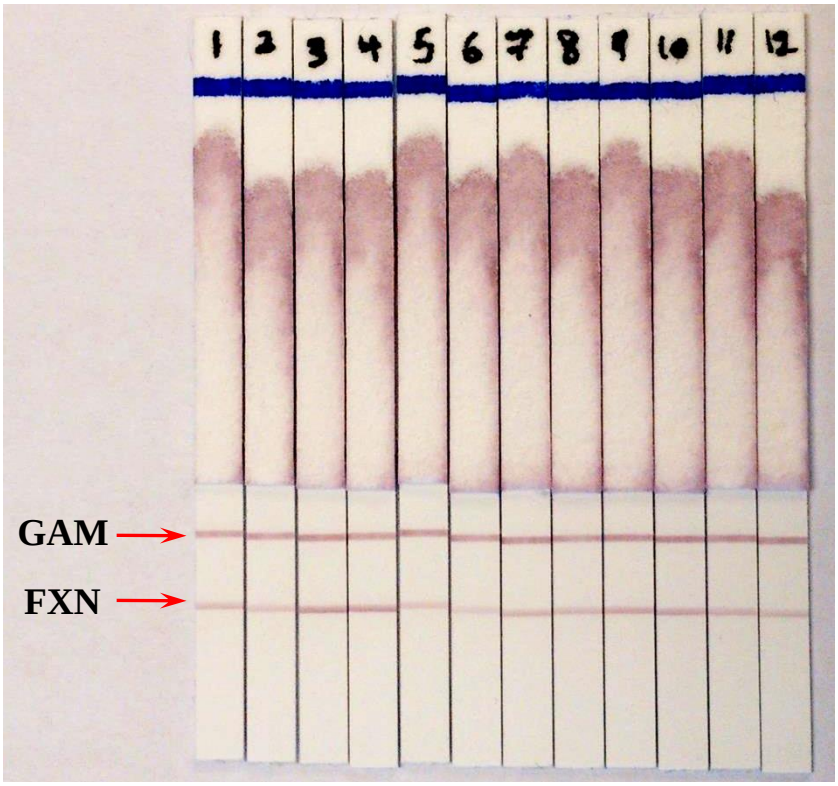

Fig. 4.6 Quantification of human FXN using dipstick immunoassay. Upper bands correspond to internal control (goat anti-mouse antibody (GAM)); lower bands correspond to human frataxin (FXN).

4.2.13 Statistical Analysis

All statistical analysis was performed using Student's *t* test and the level of significance used throughout was $P \leq 0.05$.

4.3 Results

4.3.1 Somatic GAA Repeat Instability in FRDA Mouse Models

Somatic instability of the GAA repeat was assessed in a variety of tissues (Tail (Ta), Brain (B), Cerebellum (C), Liver (L), Heart (H), Kidney (K), Pancreas (P)) from YG8R, YG22R, YG8sR and Y47R mice. As represented in Figs. 4.7 and 4.9, YG8R mice exhibited a smear of expanding GAA repeats, extending upward from 215 to 230 GAA repeats in the brain and particularly in the cerebellum tissues, and also small smeared expansion in the liver but not in any of the other tissues.

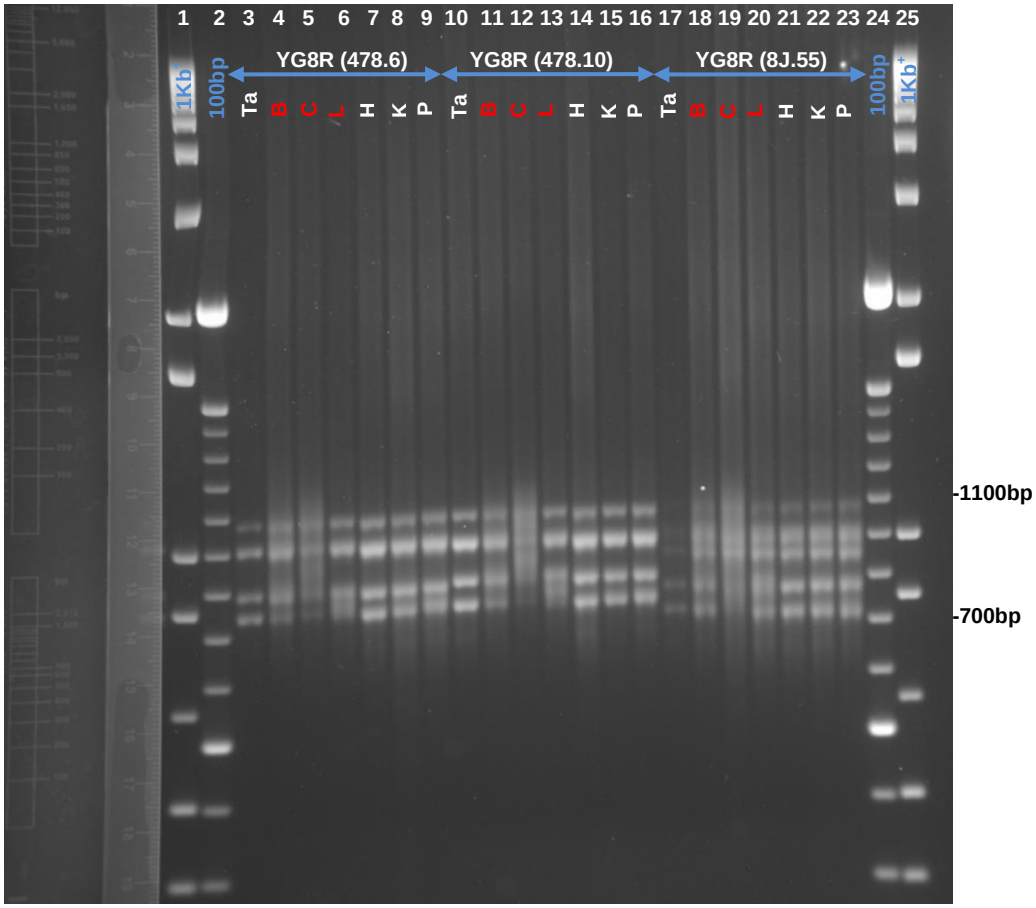

Fig. 4.7 Somatic GAA repeat instability in YG8R mice. A representative 1.5% agarose gel showing GAA PCR products from different somatic tissues (Tail (Ta), Brain (B), Cerebellum (C), Liver (L), Heart (H), Kidney (K), Pancreas (P)) of YG8R lines: 478.6 (male, Lanes 2 to 9), 478.10 (male, Lanes 10 to 16) and 8J.55 (female, Lanes 17 to 23). $1kb^{+}$ and 100bp DNA ladders were used as the molecular marker.

Size analysis of GAA sequences from YG8R lines revealed four bands of GAA repeat alleles, ranging in size from 130 to 215 repeat units in male YG8R (478.6 and 478.10) lines and five bands in female YG8R lines (8J.55 and 822.126) ranging from 125 to 215 repeats Figs. 4.7 and 4.9.

GAA repeat instability was also detected in the YG22R mice. Male YG22R (822.164 and 822.154) exhibited a smear of expanding GAA repeats in the brain, cerebellum and liver tissues from approximately 215 to 230 repeats, the smear was more pronounced in the cerebellum and liver tissues. Other tissues showed the same characteristic appearance of 150 to 215 repeats, Fig. 4.8. A similar expansion profile was also detected in YG22R females (822.118 and 822.119) with a shift of all sequences to a higher level, approximately 215 to 250 GAA repeats with smeared GAA expansions from 250 to 285 repeats in the brain and particularly in the cerebellum and liver tissues, Figs. 4.8 and 4.9.

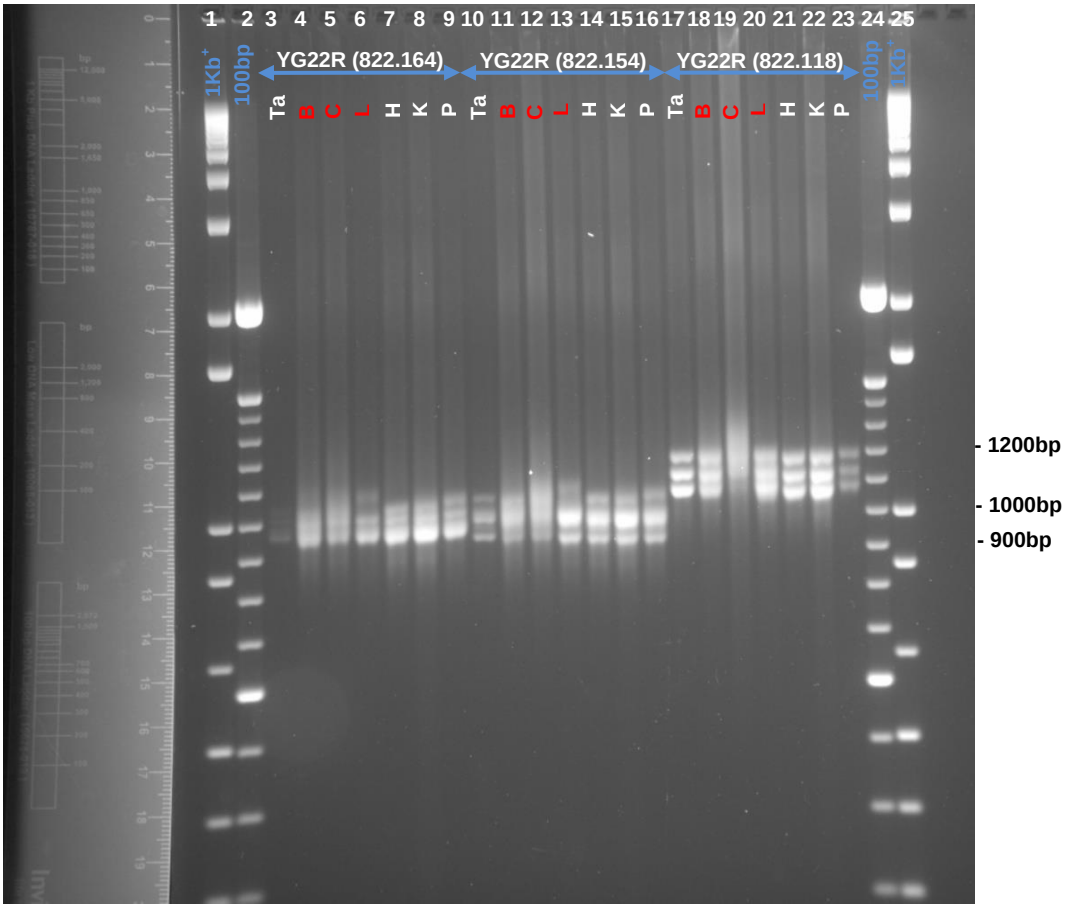

Fig. 4.8 Somatic GAA repeat instability in YG22R mice. A representative 1.5% agarose gel showing GAA PCR products from different somatic tissues (Tail (Ta), Brain (B), Cerebellum (C), Liver (L), Heart (H), Kidney (K), Pancreas (P)) of YG22R lines: 822.164 (male, Lanes 2 to 9), 822.154 (male, Lanes 10 to16) and 822.118 (female, Lanes 17 to 23). 1kb^{+} and 100bp DNA ladders were used as the molecular marker.

Y47R control line exhibited normal GAA repeat size of 9 units with no somatic instability, Fig. 4.9.

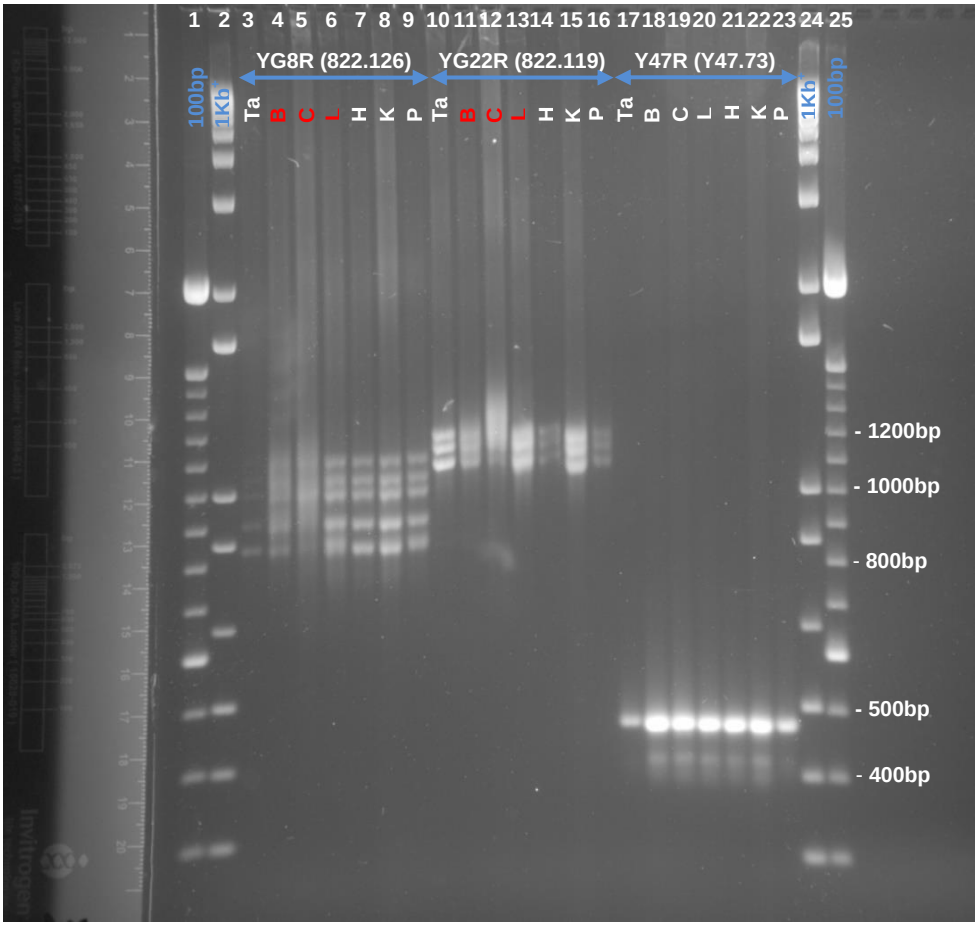

Fig. 4.9 Somatic GAA repeat instability in YG8R, YG22R and Y47R mice. A representative 1.5% agarose gel showing GAA PCR products from different somatic tissues (Tail (Ta), Brain (B), Cerebellum (C), Liver (L), Heart (H), Kidney (K), Pancreas (P)) of YG8R: 822.126 (female, Lanes 2 to 9); YG22R: 822.119 (female, Lanes 10 to 16) and Y47R: Y47.73 (female, Lanes 17 to 23) lines. $1kb^{+}$ and 100bp DNA ladders were used as the molecular marker.

YG8sR mice, established from YG8R breeding, were shown to contain a single GAA repeat sequence with approximately 120 GAA repeat units. The analysis of the GAA repeat sizes in the YG8sR male (8.2411) and female (8.2404) mice revealed a smear of expanding GAA repeats in the brain, cerebellum and liver tissues from approximately 120 to 150 repeats, the smear was greater in the brain and cerebellum, Fig. 4.10.

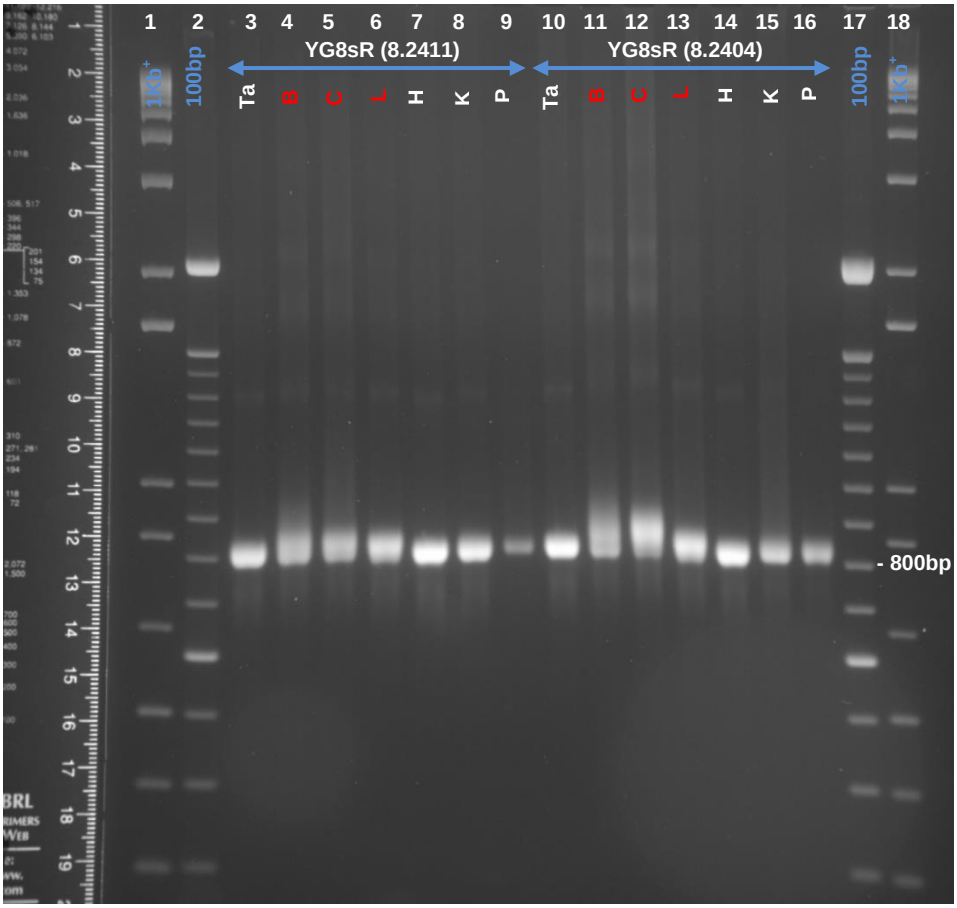

Fig. 4.10 Somatic GAA repeat instability in YG8sR mice. A representative 1.5% agarose gel showing GAA PCR products from different somatic tissues (Tail (Ta), Brain (B), Cerebellum (C), Liver (L), Heart (H), Kidney (K), Pancreas (P)) of YG8sR lines: 8.2411 (male, Lanes 2 to 9) and 8.2404 (female, Lanes 10 to 16). $1kb^{+}$ and 100bp DNA ladders were used as the molecular marker.

4.3.2 Quantification of *FXN* mRNA in Mouse Tissues

4.3.2.1 Quantification of *FXN* mRNA in Mouse Tissues Using Human Primers

In order to assess the effect of GAA repeat expansion on *FXN* expression in the studied FRDA mouse models, qRT-PCR measurements were performed using primers designed to detect human frataxin cDNA, previously described in section 4.2.9. Different endogenous control genes were previously evaluated using qRT-PCR to identify stably expressed endogenous control genes in FRDA mouse models. The results indicated that *Gapdh* was the most stably expressed endogenous control gene which can be used for accurate qRT-PCR results in *FXN* expression (C. Sandi personal communication). Therefore, the results of *FXN* expression were normalised to mouse *Gapdh* expression as the endogenous control by calculating the differences in C_t values. The cDNA samples of two mice from each studied line (one male and one female for each group) were analysed

twice for each tissue and each reaction was carried out in triplicate. The mean value of each triplet was used for further calculations using the $2^{-\Delta\Delta Ct}$ method to obtain relative quantification (RQ) values. Subsequently, the relative transcription levels of *FXN* in the FRDA and control mouse tissues were calibrated by calculating the RQ mean values, setting the Y47R brain group arbitrarily as 100%. Initial determination of *FXN* transgene expression indicated that mean mRNA levels of YG8R and YG22R decreased to 49% ($P<0.05$) and 34% ($P<0.01$) in the liver compared to Y47R, respectively. However, no significant differences were identified in other YG8R and YG22R tissues. In contrast, YG8sR mice revealed a very significant reduction of *FXN* mRNA in the brain (27%, $P<0.001$), cerebellum (18%, $P<0.01$), DRG (37%, $P<0.01$), liver (13%, $P<0.01$) and kidney (28%, $P<0.001$) compared to Y47R, Fig. 4.11A.

To illustrate the gender-specific differences in mRNA expression level, gene expression levels were compared for males and females separately. The results from males revealed significantly reduced *FXN* mRNA levels in the liver of YG8R (28%, $P<0.05$), YG22R (44%, $P<0.01$) and YG8sR (16%, $P<0.01$) and also in the brain (23%, $P<0.01$) and kidney (20%, $P<0.01$) of YG8sR, Fig. 4.11B. In contrast, analysis of female mice indicated a significant reduction of *FXN* mRNA in the liver of YG22R (27%, $P<0.05$) and in the liver (11%, $P<0.05$) and kidney (35%, $P<0.01$) of YG8sR, Fig. 4.11C. The *FXN* gene expression was also decreased in the liver of YG8R females (64%) but the difference did

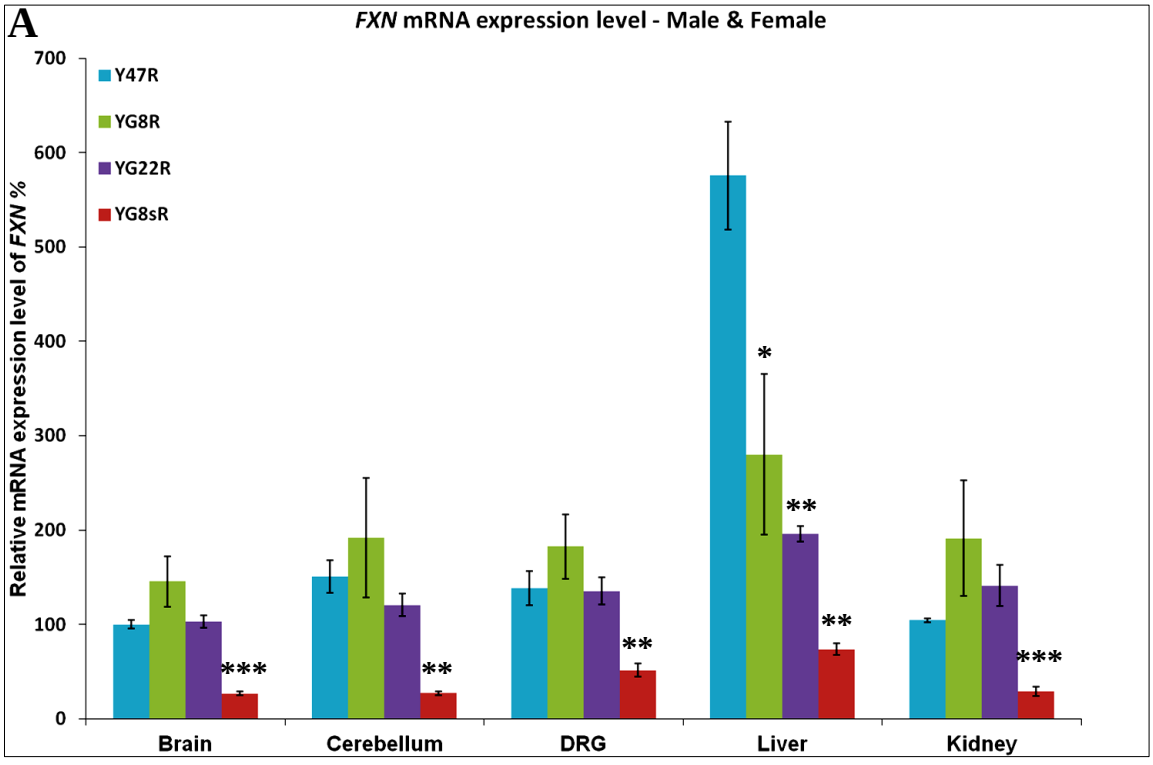

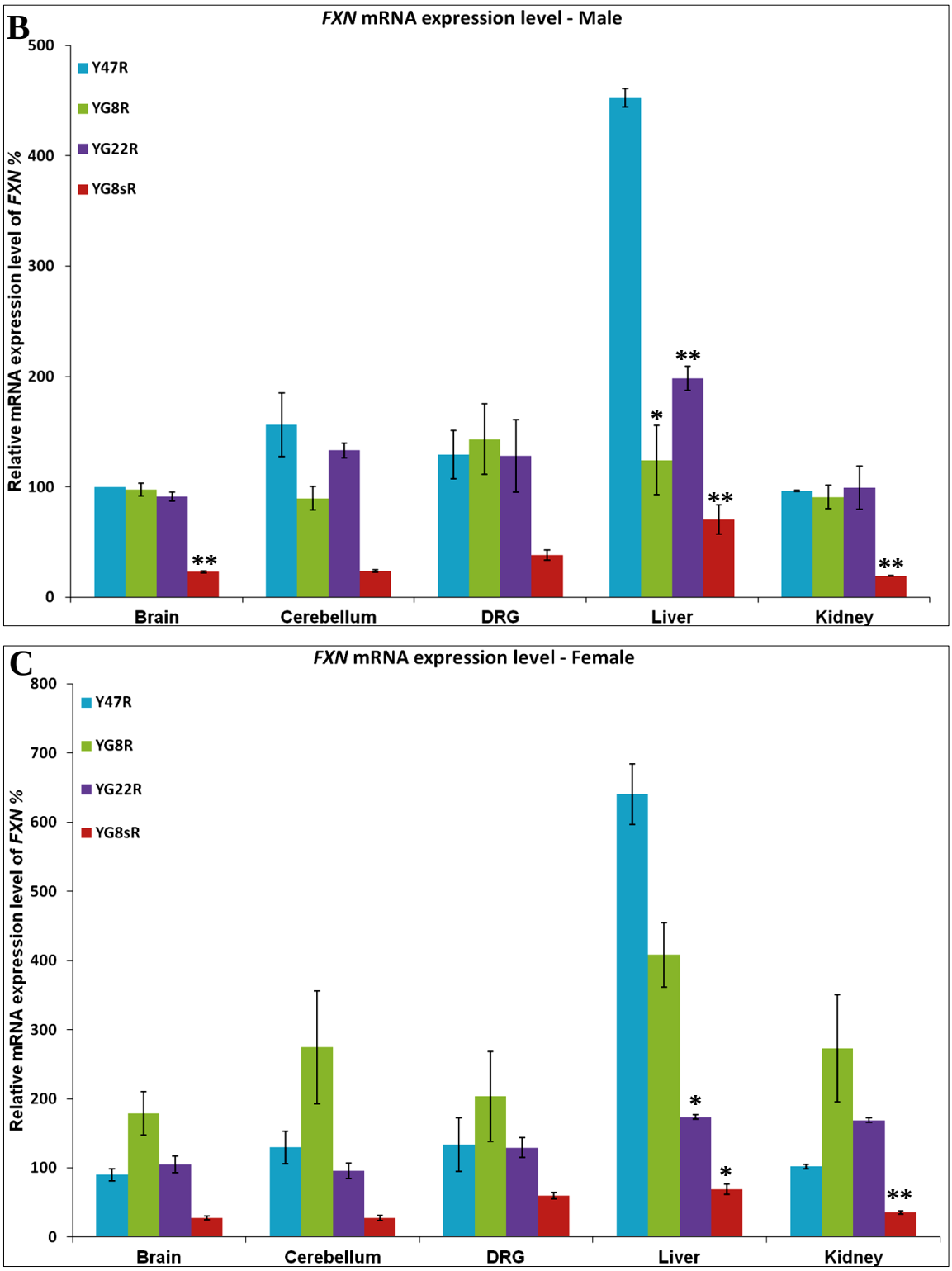

Fig. 4.11 qRT–PCR analysis of transgenic *FXN* mRNA in FRDA mice using human specific primers. **A)** Analysis of males and females together. Analysis of **B)** males and **C)** females separately. Data were normalised to the mean *FXN* mRNA level of Y47 brain samples taken as 100%. Error bars indicate SEM and values represent mean ± SEM. Asterisks indicate significant differences between the mutant and control (Y47R) mice (*P<0.05, **P<0.01 and ***P<0.001).

not reach a statistical significance (P=0.06), Fig. 4.11C. These results suggested gender-specific differences of *FXN* expression in the FRDA mouse models which might be correlated with the variation in size and pattern of the GAA repeat sequences. Furthermore, amongst all the FRDA mouse models the greatest *FXN* deficiency was detected in YG8sR.

4.3.2.2 Quantification of *FXN* mRNA in Mouse Tissues Using Mouse-Human Primers

In order to assess the *FXN* mRNA expression level in the FRDA mouse models compared to the B6 control mice, qRT-PCR measurements were performed using primers designed to detect both human and mouse frataxin cDNA, previously described in section 4.2.9. Although the results were similar to those obtained using human specific primers in comparison to the Y47R control, the slight variations in the results may be due to the lack of robustness and efficiency of the technique. Therefore, it is suggested to use large sample sizes in the future studies to improve the accuracy and repeatability of the results. Analysis of the YG22R and YG8sR compared to Y47R control revealed that *FXN* mRNA levels reduced to 53% (P<0.01) and 17% (P<0.001) in the liver, 51% (P<0.001) and 18% (P<0.001) in the cerebellum, and 77% (P=0.06) and 22% (P<0.001) in the brain tissues,

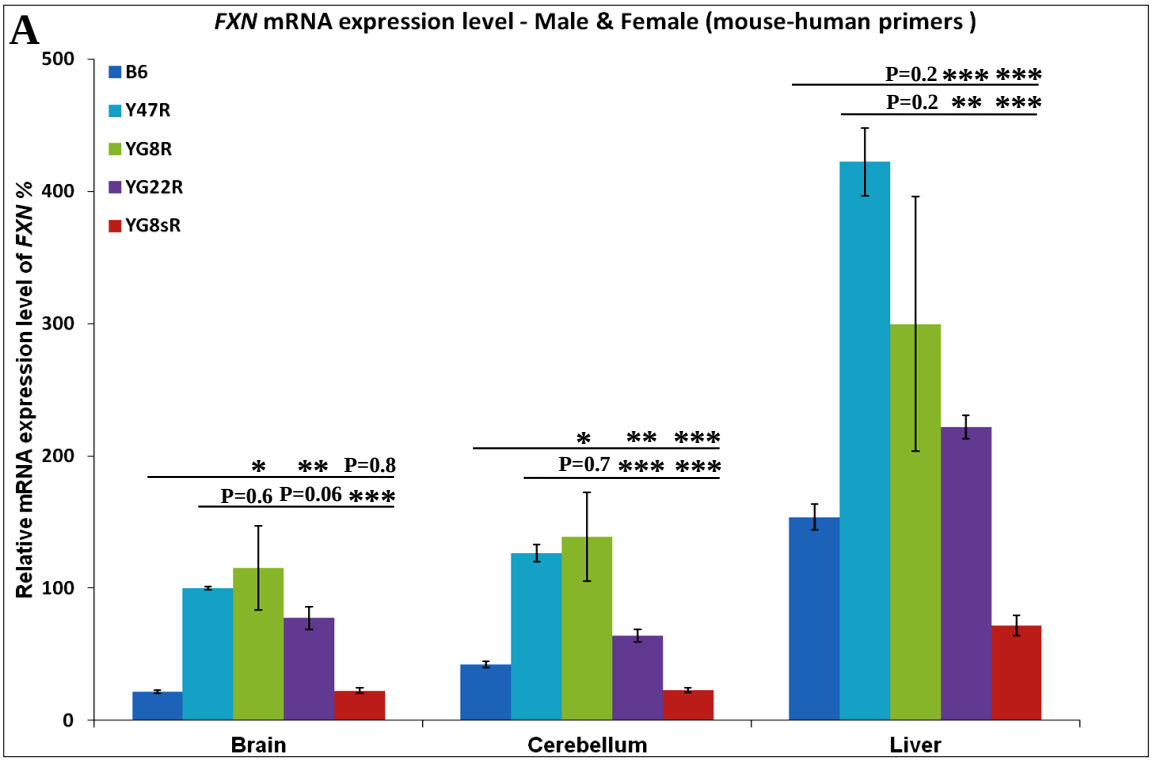

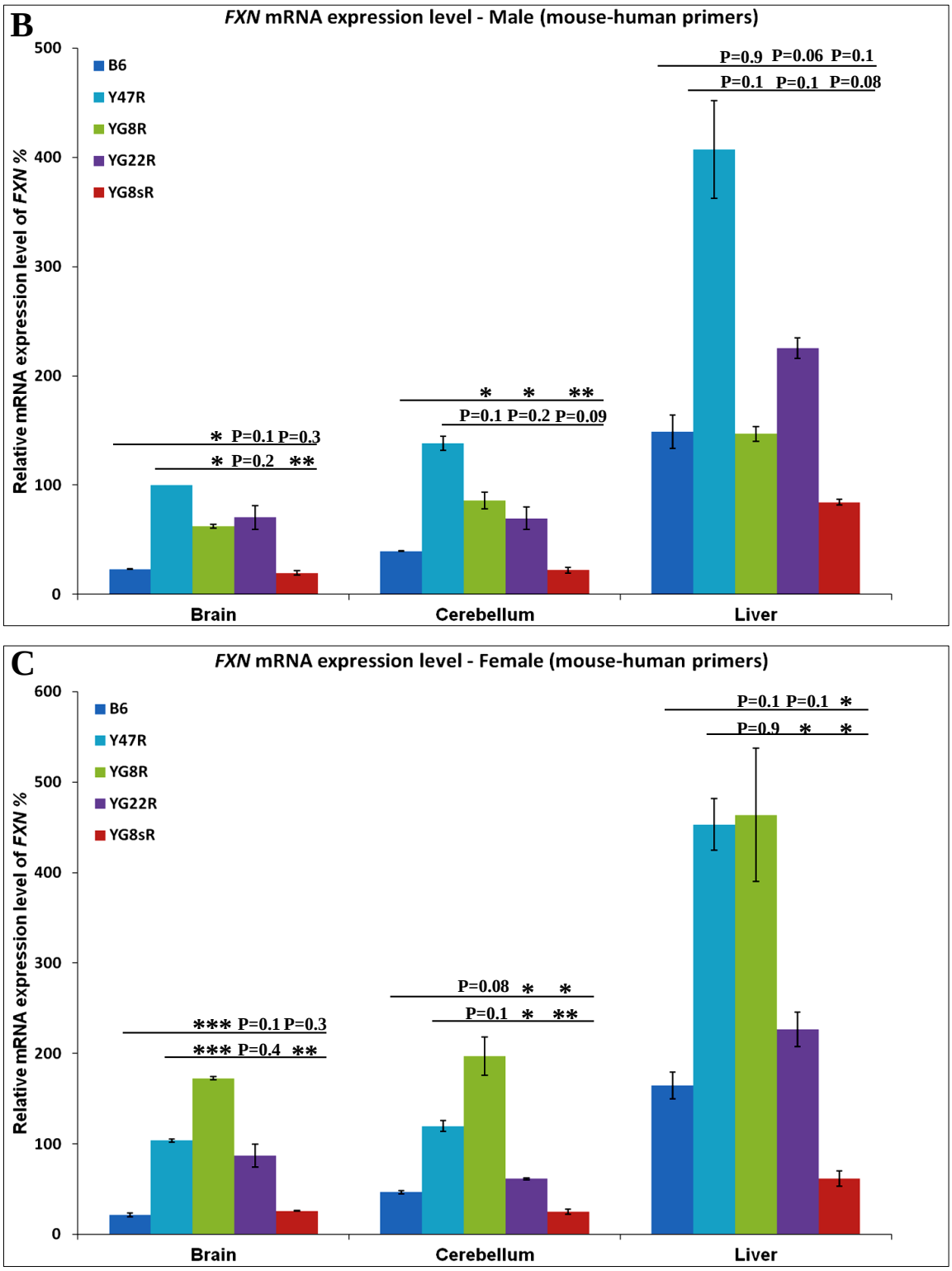

Fig. 4.12 qRT–PCR analysis of transgenic *FXN* mRNA in FRDA mice using mouse-human specific primers. **A)** Analysis of males and females together. Analysis of **B)** males and **C)** females separately. Data were normalised to the mean *FXN* mRNA level of Y47 brain samples taken as 100%. Error bars indicate SEM and values represent mean ± SEM. Asterisks indicate significant differences between the mutant and control mice (*P<0.05, **P<0.01 and ***P<0.001). Statistical differences between the mutant and B6 controls are indicated by the top line drawn over the bars while the bottom line indicates the differences between the mutant and Y47R controls.

respectively. However, no significant differences were identified in YG8R mice (29% reduction in the liver which was not significant (P=0.2)). In addition, the YG8R and YG22R did not show any marked reduction of *FXN* mRNA compared to the B6 control which was consistent with the previous findings of Ataxia Research Group, Brunel University [unpublished results]. The *FXN* mRNA expression levels were also decreased to 47% (P<0.001) in the liver and 55% (P<0.001) in the cerebellum of the YG8sR compared to the B6 control, Fig. 4.12A. On the other hand, analysis of the male YG8R, YG22R and YG8sR mice revealed reduced *FXN* mRNA levels of 62% (P<0.05), 70% (P=0.2) and 20% (P<0.01) in the brain, 62% (P<0.05), 50% (P<0.05) and 16% (P<0.01) in the cerebellum, and 36% (P=0.1), 55% (P=0.1) and 21% (P=0.08) in the liver, respectively, Fig. 4.12B. YG8sR male mice also showed to have reduced level of *FXN* mRNA expression in the brain (85%, P=0.3), cerebellum (56%, P=0.09) and liver (57%, P=0.1) compared to B6 control; however the difference was not statistically significant, Fig. 4.12B. In contrast, the levels of transgenic *FXN* mRNA expression in YG22R and YG8sR females were decreased to 84% (P=0.4) and 25% (P<0.01) in the brain, 51% (P<0.05) and 21% (P<0.01) in the cerebellum, and 50% (P<0.05) and 14% (P<0.05) in the liver tissues respectively, Fig. 4.12C. The *FXN* expression levels were also decreased in cerebellum (53%, P<0.05) and liver (38%, P<0.05) of YG8sR females compared to endogenous B6 *Fxn* mRNA, Fig. 4.12C. Therefore, YG8sR can be considered to be a suitable mouse model for the investigation of potential FRDA therapies since it was shown to have reduced level of *FXN* expression compared to both Y47R (human *FXN*) and B6 (mouse *Fxn*) controls.

4.3.3 Quantification of FXN Protein in Mouse Tissues

To determine the levels of human frataxin expression in the FRDA mouse models, frataxin protein expression levels were measured by lateral flow immunoassay with the Frataxin Protein Quantity Dipstick assay kit. Analysis of FRDA males and females together revealed that the frataxin expression was significantly decreased in the liver tissues derived from YG8R, YG22R and YG8sR mice to approximately 65% (P<0.001), 51% (P<0.001) and 24% (P<0.001) respectively compared to Y47R control, Fig 4.13A. Significant reduction in the FXN protein expression was also observed in the cerebellum of YG22R (77%, P<0.05) and YG8sR (70%, P<0.001), and in the brain of YG8sR (16%, P<0.001) compared to Y47R control, Fig 4.13A. Males and females were also analysed separately in order to determine the gender-specific differences in the FXN expression

level. The results from the males revealed a significant decrease of FXN expression in the liver of YG8R (52%, P<0.001), YG22R (47%, P<0.001) and YG8sR (22%, P<0.001) and also in the brain of YG22R (66%, P<0.001) and YG8sR (14%, P<0.001), Fig. 4.13B. The same trend was also observed in the cerebellum of YG8R (91%, P=0.2), YG22R (49%, P=0.3) and YG8sR (69%, P=0.08), and in the brain of YG8R (90%, P=0.1) males, however the differences did not reach a statistical significance, Fig. 4.13B. Analysis of the females showed a marked reduction of FXN expression in the liver of YG8R (79%, P<0.001), YG22R (55%, P<0.001) and YG8sR (25%, P<0.001), and in the brain (17%, P<0.001) and cerebellum (72%, P<0.05) of YG8sR female mice, Fig. 4.13C. The same trend was also observed in the cerebellum of YG22R females (68%, P=0.1), though the differences were not statistically significant, Fig. 4.13C. Therefore, it can be concluded that frataxin expression levels were higher in females than those in males, suggesting gender-specific differences in the FXN expression of the FRDA mice. Furthermore, amongst all FRDA mouse models the greatest FXN deficiency was detected in YG8sR compared to Y47R control. However, this approach was not applicable to compare the human frataxin levels in the FRDA rescue mice and B6 mouse frataxin levels due to the difficulties in detecting mouse Fxn protein. Consequently, YG8sR can be considered to be a suitable mouse model for the investigation of potential FRDA therapies.

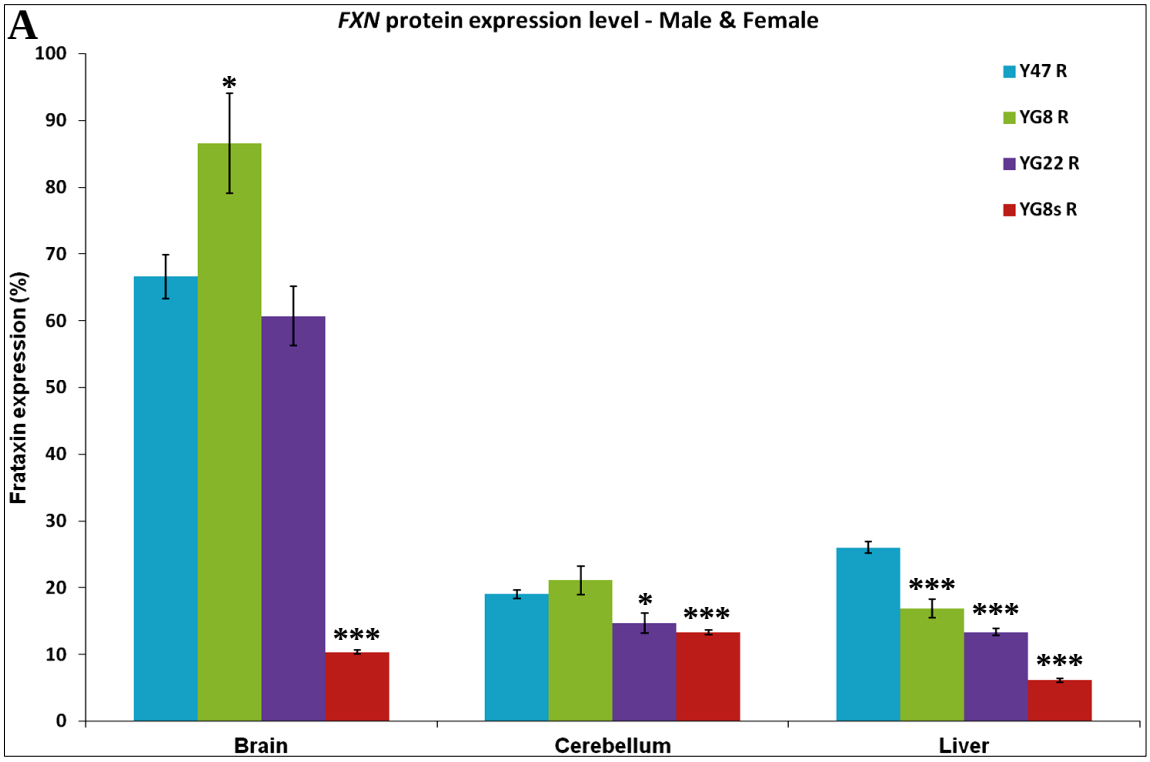

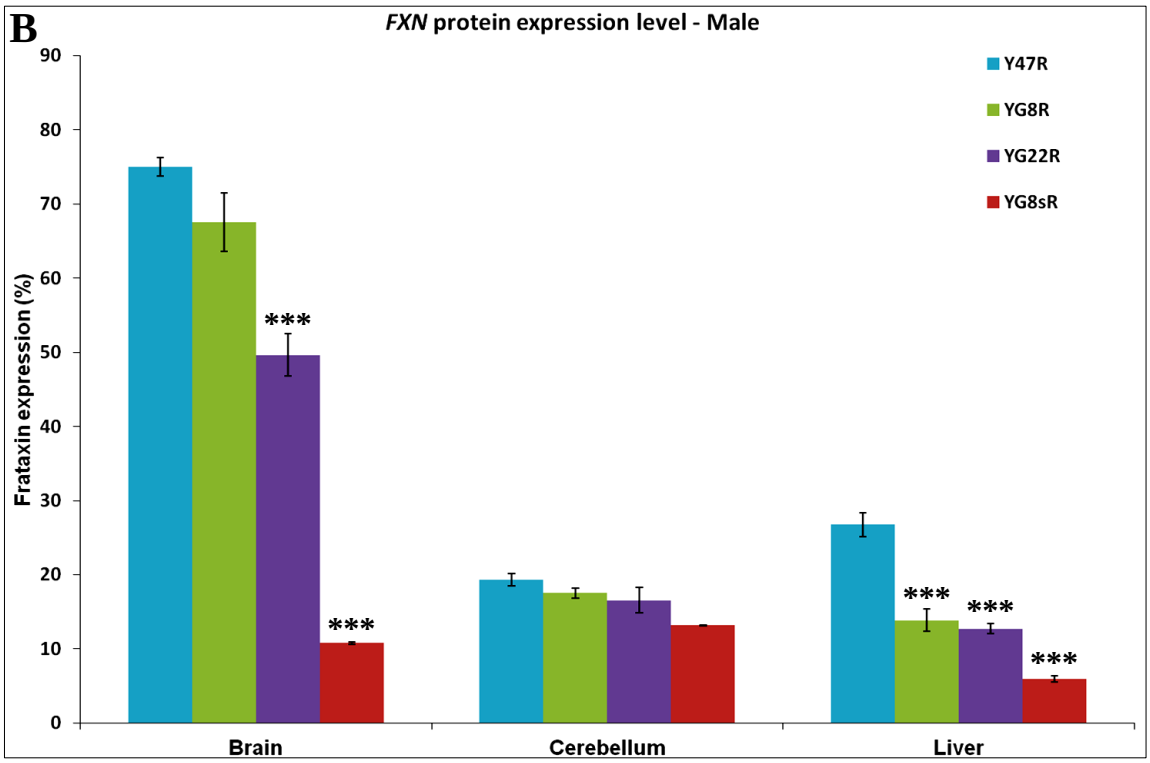

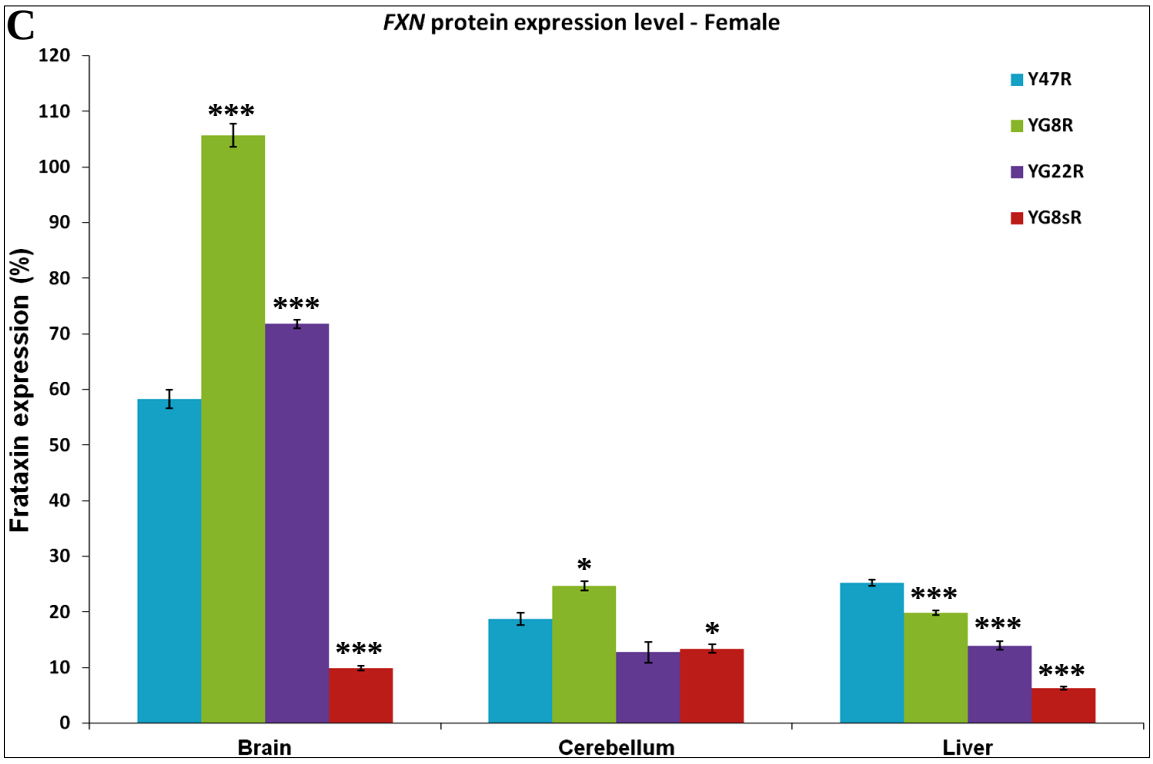

Fig. 4.13 The dipstick immunoassay of human frataxin in FRDA mice. **A)** Analysis of males and females together. Analysis of **B)** males and **C)** females separately. Error bars indicate SEM and values represent mean ± SEM. Asterisks indicate significant differences between the mutant and Y47 control (*P<0.05 and ***P<0.001).

4.4 Discussion

As discussed in chapter III, functional analysis of FRDA mouse models revealed FRDA-like pathological phenotype and functional deficits in YG8R, YG22R and YG8sR compared to Y47R (with normal sized GAA repeats) and B6 controls. To further investigate the correlation between FRDA-like pathological phenotype and frataxin deficiency in the studied mouse models, the size of the GAA repeats as well as somatic GAA instability were examined in tissues of YG8R, YG22R, YG8sR and Y47R mice. The results revealed GAA repeat somatic instability pattern in the brain, cerebellum and liver of all the FRDA mouse models. These results were in good agreement with the previous studies which also showed somatic GAA repeat instability in the brain and cerebellum of both YG22 and YG8 transgenic mice [103, 41]. However, there were differences in the pattern and size of the GAA repeats between males and females, indicative of gender-specific differences in repeat sizes which might be related to the pattern of frataxin expression. Subsequently, frataxin mRNA and protein levels were investigated. The results indicated significant reduction in the levels of the *FXN* mRNA and protein in the liver of YG8R and YG22R compared to Y47R. However, no significant differences were identified in other YG8R and YG22R tissues compared to Y47R. In addition, the YG8R and YG22R mice did not exhibit any marked reduction in the *FXN* mRNA level compared to the B6 control, this was consistent with the previous findings of Ataxia Research Group, Brunel University [unpublished results]. This might be partially due to a base pair difference between the sequence of one of the mouse and human primers, although the base pair is within the less critical 5´ region of the primer. The second possible cause may be due to the differences in the functional potential and expression profiles of the mouse and human frataxin since they may be modulated by different regulatory factors. Therefore, such differences should be considered when using mice as preclinical models of human disease.

In the case of the YG8sR line (containing a single band with approximately 120 GAA repeat units), a significant decrease in *FXN* mRNA was detected in all tissues compared to both Y47R human *FXN* and B6 mouse *Fxn* mRNA. Protein expression levels were also considerably decreased in all the tissues of the YG8sR compared to Y47R. However, this approach was not applicable to compare the human frataxin levels in the FRDA rescue mice and B6 mouse frataxin levels due to the use of a human-specific anti-FXN antibody in the dipstick assay. Of all FRDA mouse models studied, the greatest *FXN* reduction was

detected in the YG8sR tissues compared to both Y47R human *FXN* and B6 mouse *Fxn* mRNA. In addition, GAA repeat analysis identified a single GAA repeat band in YG8sR lines with no complexity compared to the other FRDA lines. Consequently, YG8sR can be considered to be a suitable mouse model for the investigation of potential FRDA therapies.

CHAPTER V

TELOMERE LENGTH ANALYSIS IN FRDA CELLS

5.1 Introduction

Maintaining genomic integrity is fundamental for the life of a cell and the survival of species. Telomeres are one of the key elements that play an essential role in the maintenance of genomic stability [231]. They are specialised nucleoprotein structures at the ends of chromosomes which consist of highly conserved hexanucleotide repeats (TTAGGG). Telomeres form a cap structure to protect the chromosome ends from exonucleolytic degradation and terminal fusions. Degradation of telomeres is caused by one of the following: an unsolved end-replication problem, exonuclease activity or DNA breakage within telomeric sequences due to oxidative damage [232, 233, 156]. Their maintenance is carried out either by the activity of a telomere specific DNA polymerase called telomerase or telomerase-independent pathway referred to as alternative lengthening of telomeres (ALT) [231]. ALT cells are characterised by recombinational events at telomeres, known as telomeric sister chromatid exchanges (T-SCE), and co-localisation of telomeres and promyelocytic leukemia protein (PML) nuclear bodies [155]. Normal human somatic cells do not have sufficient telomerase or ALT activity, thus the cell population as a whole eventually undergoes telomere-mediated senescence after a limited number of divisions due to excessive telomere degradation and short dysfunctional telomeres [234]. However, immortalised human cell lines engage the ALT mechanism to lengthen telomeres through recombination. Therefore, the telomere length is generally stable in these cells since an equilibrium exists between telomere degradation and telomere renewal [231].

As previously discussed in chapter I, Friedreich ataxia is an autosomal recessive neurodegenerative disorder caused by a reduction in frataxin expression that leads to mitochondrial dysfunction and oxidative damage. Moreover, frataxin deficiency induces a strong activation of inflammatory genes and neuronal death. Preliminary studies reported that FRDA cells were more sensitive to ionising radiation than control cells suggesting that FRDA is a DNA repair-deficient disorder [216]. In addition, oxidative stress has been reported to accelerate the rate of telomere attrition and chromosomal instability [156]. Therefore, it was hypothesised that telomere length might be shortened as a result of oxidative damage in FRDA patients. There is very limited information available regarding the status of telomere length in primary FRDA fibroblast cells. Nevertheless, the results from a recent study using human peripheral blood lymphocytes indicated a significant telomere shortening in FRDA patients compared to healthy controls [214].

The assessment of telomere dynamics is critically dependent on the technique of telomere length measurement. Several techniques are available including Southern blot analysis, quantitative fluorescence *in situ* hybridisation (Q-FISH), flow-FISH, hybridisation protection assay (HPA), single telomere length analysis (STELA) and quantitative PCR (qPCR). The aims of this part of investigation were to evaluate the length of telomeres in FRDA fibroblast cells using Q-FISH and qPCR and to measure rates of telomere shortening in these cells during replicative senescence.

5.2 Materials and Methods

5.2.1 Cell lines

Mouse fibroblast cell lines (YG8R, YG22R, Y47R and B6) established from kidney tissues, previously described in section 2.3.2.1 (chapter II), were grown in DMEM culture medium (Gibco) supplemented with 10% FBS (Gibco) and 2% Pen-Strep (Gibco) at 37˚C in a 5% CO_2 humidified incubator. Mouse lymphoma LY-R (radio-resistant) and LY-S (radio-sensitive) cells were cultured in RPMI 1640 medium (Invitrogen) supplemented with 10% FBS and 2% Pen-Strep at 37˚C in a 5% CO_2 humidified incubator. These cell lines were obtained from Dr. Predrag Slijepcevic and were used as reference for cytological testing telomeric measurements using interphase Q-FISH technique. All human fibroblast cell lines were obtained from the Coriell Cell Repository and were cultured in DMEM medium supplemented with 10-15% FBS and 2% Pen-Strep at 37˚C in a 5% CO_2 humidified incubator, Table 5.1.

Table 5.1 Details of the human primary fibroblasts

Samples	Sex	Age (Year)	Race	FBS	Number of GAA repeats
H.Normal	Male	27	Caucasian	10%	Normal
GM08399	Female	19	N/A	10%	Normal
GM04503	Female	31	Caucasian	15%	Normal
GM07492	Male	17	Caucasian	10%	Normal
GM07545	Female	22	Caucasian	15%	Normal
GM03816	Female	36	Caucasian	15%	330/380
GM04078	Male	30	Caucasian	10%	541/420
GM03665	Female	13	Caucasian	15%	445/740

The U2OS cell line (Mesenchymal adherent cells), originally derived from a 15 years old female with osteosarcoma, was grown in McCoy's culture medium (Sigma-Aldrich) supplemented with 10% FBS, 2% Pen-Strep and 2mM glutamine (Gibco) at 37˚C in a 10% CO_2 humidified incubator. The HeLa cell line (epithelial adherent cells), originally established from a 31 years old female patient with cervical carcinoma, was grown in DMEM culture medium supplemented with 10% FBS and 2% Pen-Strep at 37˚C in a 10% CO_2 humidified incubator. Both cell lines were obtained from Dr. Predrag Slijepcevic and were used as the controls.

5.2.2 Mycoplasma PCR Screening of Cell Cultures

All cell lines were subjected to mycoplasma contamination test by PCR to isolate and eliminate contamination, previously described in section 2.3.2.1.1 (chapter II).

5.2.3 Cryopreservation of Cells

The culture medium was aspirated off and the adherent cells were washed once with appropriate volume of PBS. The cells were digested with 0.05% Trypsin/EDTA (Fisher Scientific, UK) for 5 minutes at 37˚C. The detached cells in trypsin were neutralised with complete cultured medium and the cells were pelleted by centrifugation at 389 rcf for 5 minutes. The supernatant was discarded and the cells were resuspended in 1ml of culture medium supplemented with 10% (v/v) DMSO, at the desired density. Aliquots of 0.5-1.0×10^6 cells/ml were gradually frozen down using a cooling container, containing isopropanol to avoid ice crystal formation, and were subsequently transferred into liquid nitrogen.

5.2.4 Thawing of Cryopreserved Cells

Vials of cells were taken out of liquid nitrogen and swabbed with 70% IMS. Caps were loosened to release the pressure before rapidly thawing the cells in a waterbath at 37˚C. Cells were transferred into a 15ml conical tube containing 10ml of prewarmed complete culture medium and were centrifuged at 389 rcf for 5 minutes. The supernatant was discarded and the pellet was resuspended in either a $25cm^2$ or $75cm^2$ flask containing fresh culture medium. Finally, cells were incubated in a CO_2 incubator at 37˚C and 92-95% humidity.

5.2.5 Population Doubling and Growth Curve of Human FRDA Fibroblast Cells

Long term cell growth of FRDA and control fibroblasts was assessed by determining cell numbers and cumulative population doubling (CPD) levels. Cells were trypsinised with 0.05% Trypsin/EDTA at 80% confluence, pelleted and resuspended in 1ml PBS. 10µl of the cell suspension was stained by 10µl of trypan blue (Invitrogen). Subsequently, 10µl of the mixture was added on a cell counting chamber slide (Invitrogen) and was counted by a Countess^{TM} automated cell counter (Invitrogen). Trypan blue is a vital diazo dye used to colour dead cells blue. Therefore, live cells with intact cell membranes are not coloured as trypan blue is not absorbed in the viable cells while dead cells are shown as a distinctive blue colour, enabling the cell counter to distinguish the live cells from the dead. When recording the phase of a cell population, age should be expressed in terms of population doubling (PD) rather than passage number since the passage number only indicates the number of trypsinisation steps performed during the culture period. Therefore, the passage number is not adequate in describing the age of a culture as trypsinisation can be performed at different split ratios. PD at each passage was determined using the following formula:

$PD = (\text{Log } N_1 / \text{Log2}) - (\text{Log} N_o / \text{Log2})$

N_o = Number of cells at the beginning

N_1= Number of cells at the end of each cell culture period

Cumulative population doubling (CPD) level was thus the sum of population doublings:

$CPD_n = \Sigma PD_{(1, n)}$

n: Number of passages

5.2.6 Telomere Length Measurement by qPCR

Genomic DNA was extracted from the FRDA and control fibroblast cells (Table 5.1) using the phenol/chloroform method as previously described in section 2.3.1.1 (chapter II). Previously prepared lymphocyte genomic DNA was also obtained from FRDA patient and unaffected control blood samples, Table 5.2.

Table 5.2 Details of the human lymphocyte DNA samples

Samples	Type	Sex	Age of onset (Year)	Age at death (Year)	Number of GAA repeats
CA	FRDA	Male	N/A	24	750/550
MH	FRDA	Male	N/A	46	1100/450
HK	FRDA	Male	5	17	750/630
LK	FRDA	Male	7	30	730/600
CR	FRDA	Male	15	40	930/570
RS	FRDA	Female	3	35	930/600
MS	FRDA	Female	7	36	700/700
JA-T	FRDA	Male	6	25	780/780
AB	FRDA	Female	N/A	N/A	950/300
AG	FRDA	Female	N/A	N/A	900/550
BL	FRDA	Male	N/A	N/A	1060/730
BQ	FRDA	Female	N/A	N/A	950/250
BT	FRDA	Male	N/A	N/A	930/760
I CONN	FRDA	Female	N/A	N/A	950/950
LH	FRDA	Female	N/A	N/A	800/250
MB	FRDA	Female	N/A	N/A	1000/250
RB	FRDA	Male	N/A	N/A	850/750
S KEY	FRDA	Female	N/A	N/A	900/650
2803	Normal	N/A	N/A	N/A	Normal
2804	Normal	N/A	N/A	N/A	Normal
2805	Normal	N/A	N/A	N/A	Normal
2808	Normal	N/A	N/A	N/A	Normal
2809	Normal	N/A	N/A	N/A	Normal
141603	Normal	N/A	N/A	N/A	Normal
141604	Normal	N/A	N/A	N/A	Normal
141605	Normal	N/A	N/A	N/A	Normal
141607	Normal	N/A	N/A	N/A	Normal
141611	Normal	N/A	N/A	N/A	Normal
141612	Normal	N/A	N/A	N/A	Normal
141616	Normal	N/A	N/A	N/A	Normal

Telomere length was examined using a qPCR method [235]. Briefly, two master mixes of PCR reagents were prepared separately, one with telomere primer pair and the other with single copy gene primer pair (36B4), Table 5.3. The master mixes were prepared using the following reagents:

- 10µl of 2× Power SYBR® Green PCR Master Mix (Applied Biosystems) containing AmpliTaq Gold DNA polymerase, dNTPs, SYBR Green Dye, optimised buffers and passive reference dye (ROX)
- 1µl of 2µM forward primer (Telomere-F or 36B4-F) (Sigma)
- 1µl of 2µM reverse primer (Telomere-R or 36B4-R) (Sigma)
- Nuclease free water to 20µl

20µl of telomere master mix was added to each sample well (4µl of 5ng/µl DNA sample, no template control (NTC) and positive controls) and standard curve well (2µl of the telomere standard) of the first plate and 20µl of single copy gene master mix was added to each sample well (4µl of 5ng/µl DNA samples, no template control (NTC) and positive controls) and standard curve well (2µl of the single copy gene standard) of the second plate. Telomere standard curve was established by serial dilutions of telomere standard (1018400kb through to 10184kb dilution) and was used to measure the content of telomeric sequence per sample in kb, Fig. 5.2. A single copy gene (36B4), encodes the acidic ribosomal phosphoprotein PO, was used as a control for amplification of every sample performed and to determine genome copies per sample. Single copy gene standard

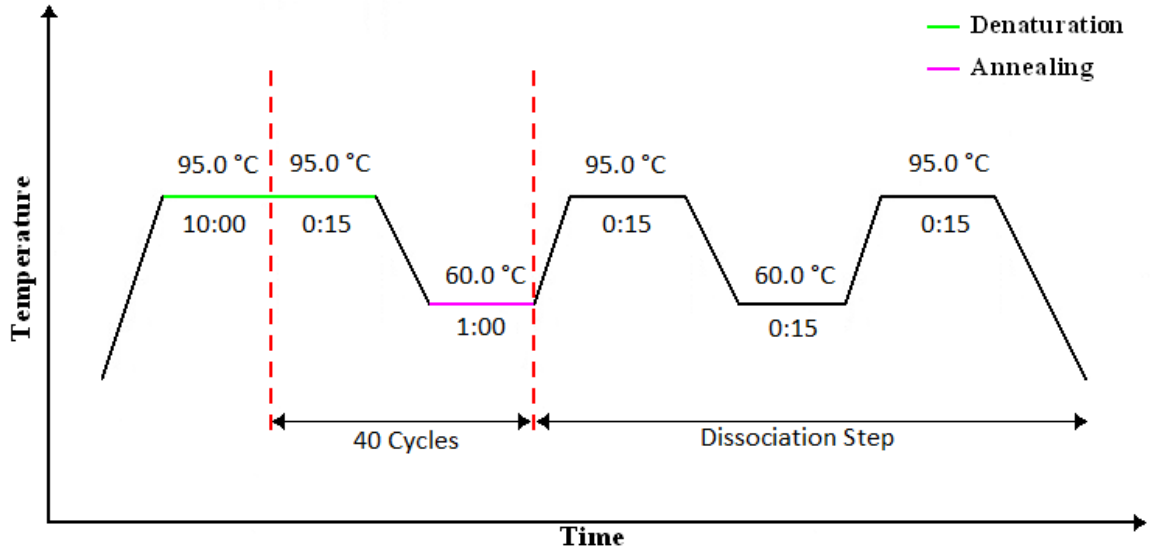

Fig. 5.1 Schematic diagram of qPCR program

curve was generated by performing serial dilutions of 36B4 standard (3062500kb through to 6.125kb dilution). Plasmid DNA (pBR322) was also added to each standard curve well to maintain a constant 20ng of total DNA per reaction tube. Subsequently, the plate was sealed and centrifuged for 1 minute at 101 rcf. The qPCR reactions were run using the programs illustrated in Fig. 5.1 for both telomere and 36B4 amplicons and their corresponding dissociation curves were analysed.

Table 5.3 Oligomers used for telomere length assay in human FRDA cells

Oligomer Name	Oligomer Sequence (5´➔3´)	Amplicon size (bp)
Telomere Standard (Human/Rodent)	$(TTAGGG)_{14}$	84
36B4 standard (Human)	CAGCAAGTGGGAAGGTGTAATCCGTCTCCACAGACAAGG CCAGGACTCGTTTGTACCCGTTGATGATAGAATGGG	75
Telo-F (Human/Rodent)	CGGTTTGTTTGGGTTTGGGTTTGGGTTTGGGTTTGGGTT	>76
Telo-R (Human/Rodent)	GGCTTGCCTTACCCTTACCCTTACCCTTACCCTTACCCT	>76
36B4-F (Human)	CAGCAAGTGGGAAGGTGTAATCC	75
36B4-R (Human)	CCCATTCTATCATCAACGGGTACAA	75

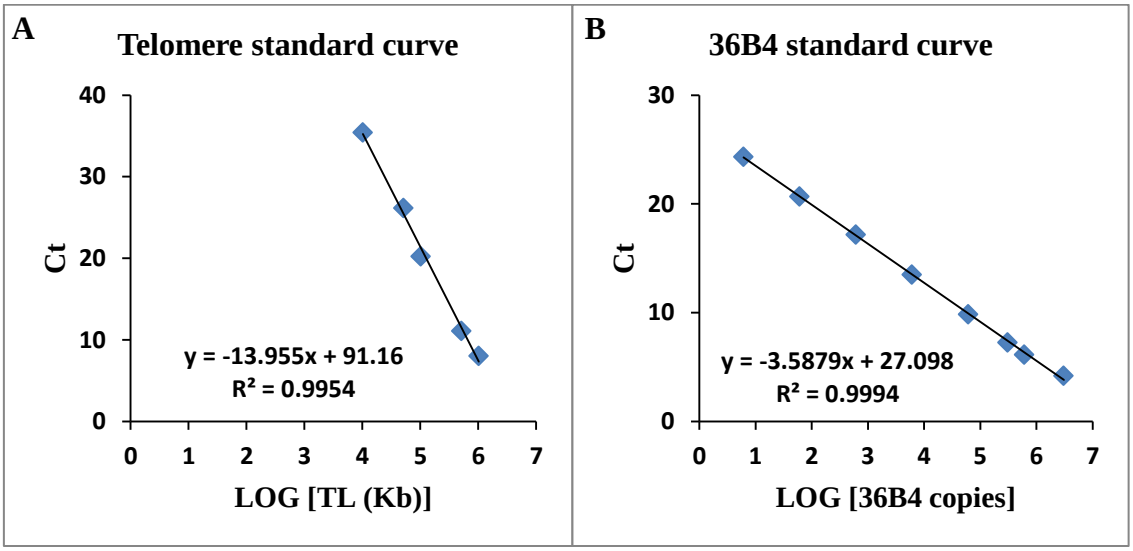

Fig. 5.2 Absolute telomere length calculation using standard curve. C_t (cycle threshold) is the number of PCR cycles for which enough SYBR green fluorescence was detected above the background. **A)** Standard curve for calculating length of telomere sequence per reaction tube: X-axis represents the amount of telomere sequence in kb per reaction with correlation coefficient of 0.995. **B)** Standard curve for calculating genome copies using 36B4 copy number: correlation coefficient 0.999.

The values (kb/reaction for telomere and genome copies/reaction for single copy gene) were exported to an excel file and were used to calculate the total telomere length in kb per human diploid genome. The telomere kb per reaction value was then divided by diploid genome copy number to give a total telomeric length in kb per human diploid genome.

5.2.7 Cytogenetic Analysis

5.2.7.1 Metaphase Preparation of Fibroblast Cell Lines

Prior to harvesting, fibroblast cells were treated with 0.1µg/ml colcemid for 2 to 4 hours. Subsequently, the cells were digested with trypsin/EDTA for 5 minutes at 37˚C in the CO_2 incubator. However, in order to maximise the number of collected mitotic cells, the culture supernatant was used to neutralise the trypsin/EDTA solution, ensuring that the suspended mitotic cells in the culture supernatant were retained and minimum metaphases were lost during the procedure. Fibroblast cells were collected by centrifugation at 249 rcf for 5 minutes and were treated with 3ml of prewarmed hypotonic solution (0.075M KCl) for 15 minutes at 37˚C and were subsequently fixed with methanol:acetic acid (3:1). The process of fixation was repeated two more times for 10 and 30 minutes at RT, respectively. During every fixation process 1ml of fresh fixative was added drop wise followed by the addition of extra 2ml of fixative solution. Subsequently, the cell pellets were resuspended in fresh fixative solution and 15µl of cell suspension was spread on a wet slide. The slides were finally air-dried and the cells were aged overnight at 54˚C on a heating block. For long term storage, slides were stored with desiccant at -20˚C.

5.2.7.2 Interphase Preparation of Fibroblast Cell Lines

For interphase analysis, samples were produced according to standard cytogenetic methods with the exception of colcemid treatment.

5.2.8 Interphase Quantitative Fluorescence *in situ* Hybridisation (I-QFISH)

5.2.8.1 Pre-Hybridisation Washes

The slides containing interphase cells were washed in PBS for 5 minutes on the shaker. The cells were then fixed in 4% formaldehyde in PBS for 2 minutes and were washed three times in PBS for 5 minutes. The cells were subsequently treated with 1mg/ml Pepsin solution (Sigma), 50ml of water acidified with 0.5ml of 1M HCl, pH 2.0, containing 10%

pepsin solution, at 37˚C for 10 minutes. The slides were then washed twice in PBS and were fixed in 4% formaldehyde in PBS for 2 minutes. Following fixation, cells were washed three times in PBS for 5 minutes and were dehydrated for 5 minutes in 70%, 90% and 100% ethanol respectively. Finally, the slides were left to air dry.

5.2.8.2 Hybridisation

Dehydrated slides were denatured and probed with 20µl of a FITC-conjugated peptide nucleic acid (PNA) telomeric oligonucleotide $(CCCTAA)_3$ probe at 70-75˚C for 2 minutes on a heating block followed by hybridisation in a dark humidified chamber for 2 hours at RT. Stock hybridisation mixture (1ml) for the telomeric probe was made up of 700µl deionised formamide, 5µl blocking reagent (10% in maleic acid), 50µl $MgCl_2$ buffer (2.5M $MgCl_2$, 9mM Na_2HPO_4, pH 7.0), 10µl Tris (1M, pH 7.2), 152µl ddH_2O and 83µl of PNA solution (6µl/ml FITC or Cy3-conjugated PNA, Applied Biosystems).

5.2.8.3 Post-Hybridisation Washes

The slides were washed twice in 70% formamide solution (70ml formamide, 10ml 2× SSC and 20ml ddH_2O) for 15 minutes and three times in PBS for 5 minutes in the dark on the shaker. Slides were then dehydrated for 5 minutes in 70%, 90% and 100% ethanol respectively. 15µl of VECTASHIELD® with fluorescence DAPI mounting medium

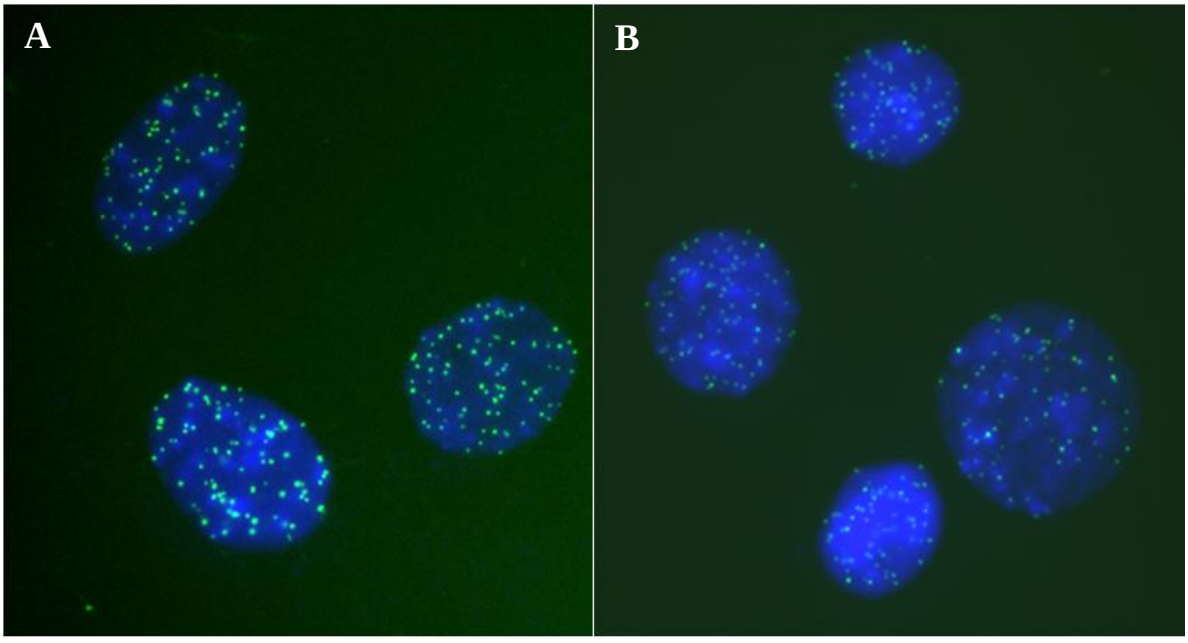

Fig. 5.3 Telomere length analysis using the Q-FISH method. Representative images of **A)** FRDA (YG8) and **B)** control (Y47) interphase cells after hybridisation with telomeric PNA oligonucleotides.

(Vector) was added to the slides and covered with a 22×50mm coverslip prior to sealing with clear nail varnish.

5.2.8.4 Image Capture and Telomere Length Analysis

Images of interphase cells were acquired on a digital fluorescence microscope (Zeiss Axioskop 2) equipped with a CCD camera (Photometrics) and Smart Capture software (Digital Scientific) using fixed exposure time of 0.5 second and magnification of 63×. Telomere fluorescence intensity per cell was analysed using IP Lab software (Digital Scientific), Fig. 5.3, and the average signal was evaluated by subtracting the background signal from the total telomeric signal intensity. 100 cells were quantified for each sample.

5.2.9 Chromosome Orientation Fluorescence *in situ* Hybridisation (CO-FISH)

The CO-FISH technique was used to measure the rate of mitotic recombination at telomeres through counting telomeric-sister chromatid exchanges (T-SCEs). Cells were grown in 3µl of 5´-bromo-2´-deoxyuridine at the concentration of 10µM BrdU/BrdC (3:1 ratio 7.5µM:2.5µM, Sigma-Aldrich) for 24 hours. During the cell cycle, BrdU is incorporated into replicating DNA strands opposite to the original parental strands. Cell-cycle progression was blocked in metaphase with colcemid and cells were fixed using standard cytogenetic techniques, previously discussed in section 5.2.7.1. The slides were aged overnight at 54˚C in order to fix the chromosomes and to make their structure resistant to the subsequent DNA denaturing.

5.2.9.1 Washing, Digestion and Fixation

The slides were washed in PBS for 15 minutes and were stained with 2.5µl of 0.5µg/ml DNA-binding fluorescent dye Hoechst 33258 in 2× SSC for 15 minutes at RT. To create nicks in the BrdU substituted strand, the slides were exposed to 365nm UV light (Stratalinker 1800 UV irradiator) for 30 minutes. The nicked BrdU-substituted DNA strands were then degraded by 100µl of Exonuclease III solution (Promega) (1.5µl Exonuclease III, 10µl buffer and 88.5µl dH_2O) at RT for 10 minutes. Subsequently, the slides were washed twice in PBS for 5 minutes on the shaker and were dehydrated for 5 minutes in 70%, 90% and 100% ethanol respectively. Finally, the slides were air-dried at RT.

5.2.9.2 Hybridisation

Dehydrated slides were denatured and probed with 20µl of a Cy3-conjugated PNA telomeric oligonucleotide $(CCCTAA)_3$ probe at 70-75˚C for 2 minutes on a heating block followed by hybridisation in a dark humidified chamber for 2 hours at RT.

5.2.9.3 Post-Hybridisation Wash

The slides were washed twice in 70% formamide solution (70ml formamide, 10ml 2× SSC and 20ml ddH_2O) for 15 minutes and three times in PBS for 5 minutes in the dark on the shaker. Slides were then dehydrated for 5 minutes in 70%, 90% and 100% ethanol respectively. 15µl of VECTASHIELD® with fluorescence DAPI mounting medium (Vector, VECTASHIELD®) was added to the slides and covered with a 22×50mm coverslip. Finally, the coverslips were sealed with clear nail varnish.

5.2.9.4 Image Analysis

Images of metaphase spreads were acquired using a Zeiss fluorescence microscope equipped with a CCD camera (Photometrics) and ISIS Capture software (in *situ* imaging system "ISIS", Meta Systems, Altlussheim, Germany). 20 metaphases were quantified for each sample.

5.2.10 Telomeric Repeat Amplification Protocol (TRAP) Assay Using TRAPEZE® Telomerase Detection Kit

Telomerase enzymatic activity was determined in human FRDA fibroblast cell lines using TRAPeze® Telomerase Detection Kit (Chemicon, Millipore). Cells were cultured in a 75 cm^2 tissue culture flask, trypsinised at 80% confluence, pelleted and resuspended in 1ml PBS. Cells were counted by a Countess™ automated cell counter. For long term storage, the supernatant was removed and the samples were stored at -80˚C.

5.2.10.1 Protein Extraction and Quantification Using CHAPS Lysis Buffer and BCA Protein Assay

Cells (10^5-10^6) were lysed in 200µl of CHAPS buffer, containing RNase inhibitor, and were incubated at 4˚C for 30 minutes. The lysate was then centrifuged at 15700 rcf for 20 minutes at 4˚C. 160µl of the supernatant was transferred to a clean 1.5ml microcentrifuge tube and was stored at -80˚C. The protein concentration was measured using a Pierce® BCA Protein Assay Kit (Thermo scientific) following the manufacturer's instructions,

previously discussed in section 4.2.11 (chapter IV). In order to obtain the final concentration of 125ng/µl, the protein concentration of the tested samples was measured from the standard curve and the samples were diluted in CHAPS lysis buffer accordingly.

5.2.10.2 Telomerase Activity Measurement Using the TRAP Assay

The TRAP assay measures enzymatic activity of telomerase. To perform the TRAP assay, serial dilutions of TSR8 were prepared with CHAPS lysis buffer and 2µl of each TSR8 dilution (20 amoles/µl, 2 amoles/µl, 0.2 amoles/µl and 0.002 amoles/µl, respectively. n.b. amole = attomole = 10^{-18} mole) was used to set up a standard calibration curve, Fig. 5.4. TSR8 is an oligonucleotide with a sequence identical to the TS primer extended with eight telomeric repeats $AG(GGTTAG)_7$ which can be used as a standard for calculating the amount of TS primers with telomeric repeats extended by telomerase in a given extract. For a valid analysis, appropriate controls were included in every assay as follows:

- Heat treated telomerase negative control: as telomerase is a heat sensitive enzyme, 10µl of the extract aliquot was heated at 85˚C for 10 minutes to inactivate telomerase
- Minus Telomerase Control (MTC): CHAPS lysis buffer was substituted for protein extract
- No Template Control (NTC): nuclease free water was substituted for protein extract
- Positive controls: telomerase-positive cell extracts provided in the kit and the human breast cancer cell line 21NT were used as positive controls

Each PCR-reaction was performed in triplicate on a MicroAmp optical 96-well PCR plate (Applied Biosystems), where each reaction well contained 5µl of 5× TRAPEZE® RT Reaction Mix (containing TS primer (5´-AAT CCG TCG AGC AGA GTT-3´), fluorescein-labelled Amplifluor® RP (reverse) primer (5´'-GCGCGG $[CTTACC]_3$CTAACC-3´) and dNTPs diluted in 10× reaction buffer S plus 10mM $MgCl_2$), 4µl of 5U/µl *Taq* Polymerase, 2µl of the samples (TSR8 dilutions, positive controls, telomerase negative, NTC, experimental samples and heat treated telomerase negative controls) and nuclease free water up to 25µl. The qPCR reactions were performed using an ABI Prism 7900HT Sequence Detection System (Applied

Biosystems). The reaction mixture was initially incubated at 30˚C for 30 minutes to allow the telomerase in the protein extracts to elongate the TS primer by adding TTAGGG repeat sequences. PCR was then started at 95˚C for 2 minutes to inactivate the telomerase followed by a 35 cycle amplification (94˚C for 15 sec, 59˚C for 60 sec and 45˚C for 10 sec). Telomerase activity in the cell lines was calculated based on the threshold cycle.

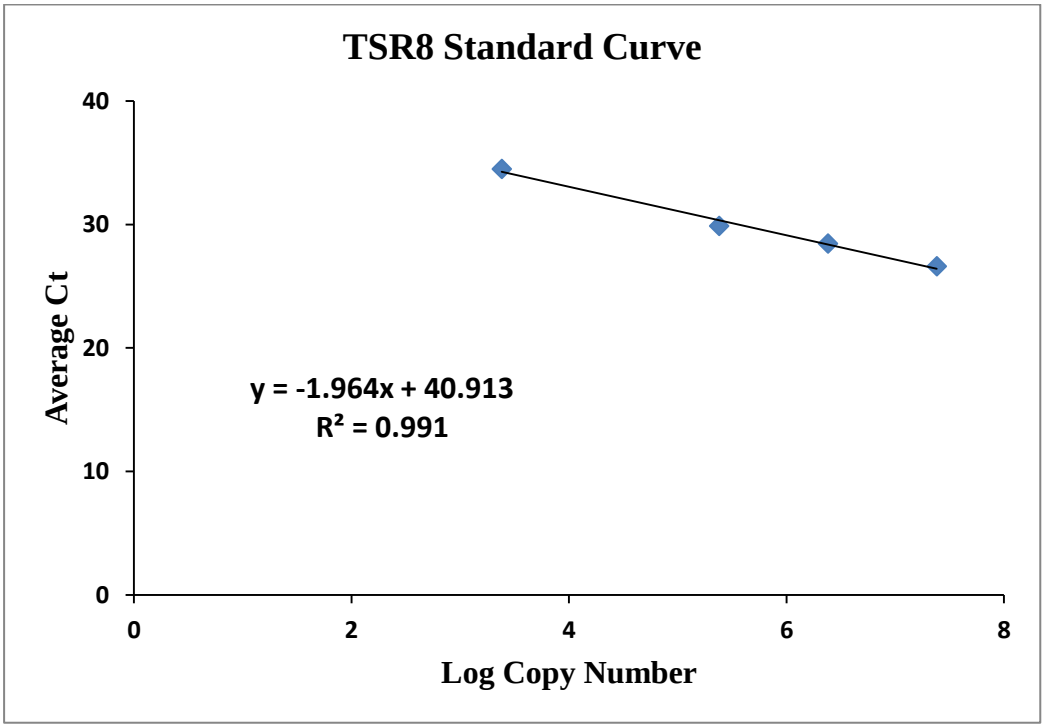

Fig. 5.4 Logarithmic plot of the TSR8 standard curve

5.2.11 Determination of hTERT Expression Levels Using qRT-PCR

5.2.11.1 Extraction of Total RNA from Human FRDA Fibroblast Cells Using Trizol®

Total RNA was extracted from 10^6 cells using the Trizol® method, previously described in section 4.2.5 (chapter IV). The cell pellet was washed with PBS and was collected by centrifugation at 389 rcf for 5 minutes. The cell pellet was loosened by gently flicking the tube and was resuspended in 1ml of Trizol®. Total RNA was extracted and the quality of the RNA was determined on agarose gel electrophoresis. RNA was quantified with spectrophotometry at 260 and 280nm. The RNA was stored at -80˚C for long term storage.

5.2.11.2 DNase I Treatment of RNA

Total RNA was treated with DNase I (DNase I, Amp Grade, Invitrogen) prior to RT-PCR using the following reagents:

- 2µg total RNA
- 2µl 10× DNase I reaction buffer
- 2µl DNase I, Amp Grade, 1U/µl
- Nuclease free water to 20µl

The samples were left for 15 minutes at RT. DNase I reaction was inactivated by adding 2µl of 25mM EDTA solution to the reaction mixture followed by heating for 10 minutes at 65˚C. The RNA samples were subsequently used for reverse transcription.

5.2.11.3 Complementary DNA (cDNA) Synthesis

Cloned AMV first-strand cDNA Synthesis Kit (Invitrogen) was used to synthesise first strand cDNA. The following components were added to the DNase I treated total RNA:

- 2µl of 250ng/µl random hexanucleotide primers
- 2µl of 10mM dNTP mix (10mM each of dATP, dGTP, dCTP, dTTP at neutral pH)

The mixtures were incubated for 5 minutes at 65˚C and were then placed on ice for at least 1 minute. The contents were collected and the following reagents were added:

- 8µl of 5× cDNA synthesis buffer
- 2µl of 0.1 M DTT
- 2µl of 40U/µl RNase Out
- 2µl of 15U/µl cloned AMV RT

The samples were gently mixed by pipetting up and down and incubated at 55˚C for 1 hour followed by 5 minute incubation at 85˚C to terminate the reaction. The cDNA samples were used immediately or stored at -20˚C.

5.2.11.4 Reverse Transcriptase PCR (RT-PCR)

The quality of the cDNA was confirmed by PCR using *FXN* human specific primers, previously described in section 4.2.8 (chapter IV).

5.2.11.5 Quantitative RT-PCR (qRT-PCR)

hTERT mRNA expression levels in FRDA human fibroblast (GM03665, GM03816 and GM04078) and two normal human fibroblast (GM07492 and GM08399) cDNA samples were quantitated by qPCR and an ABI Prism 7900HT Sequence Detection System (Applied Biosystems) was employed for this assay. Two positive controls (21MT and 21NT, human breast cancer epithelial samples) and one negative control (184, normal breast epithelial sample) were used as the controls. hTERT assay (Applied Biosystems), containing hTERT forward and reverse primers and a TaqMan TAMRA™ probe, and GAPDH assay (Assay ID: Hs99999905_m1, 124bp amplicon size, Applied Biosystems), containing GAPDH forward and reverse primers and a TaqMan MGB probe, were used in this experiment, Table 5.4. The TaqMan MGB probe included a VIC® reporter dye attached to the 5´ end, a nonfluorescent quencher (NFQ), and a minor groove binder (MGB) attached to the 3´ end (MGBs increase the melting temperature (T_m) without increasing the probe length, allowing the design of shorter probes). The TaqMan TAMRA™ probe included a FAM™ reporter dye attached to the 5´ end and TAMRA™ quencher attached to the 3´ end.

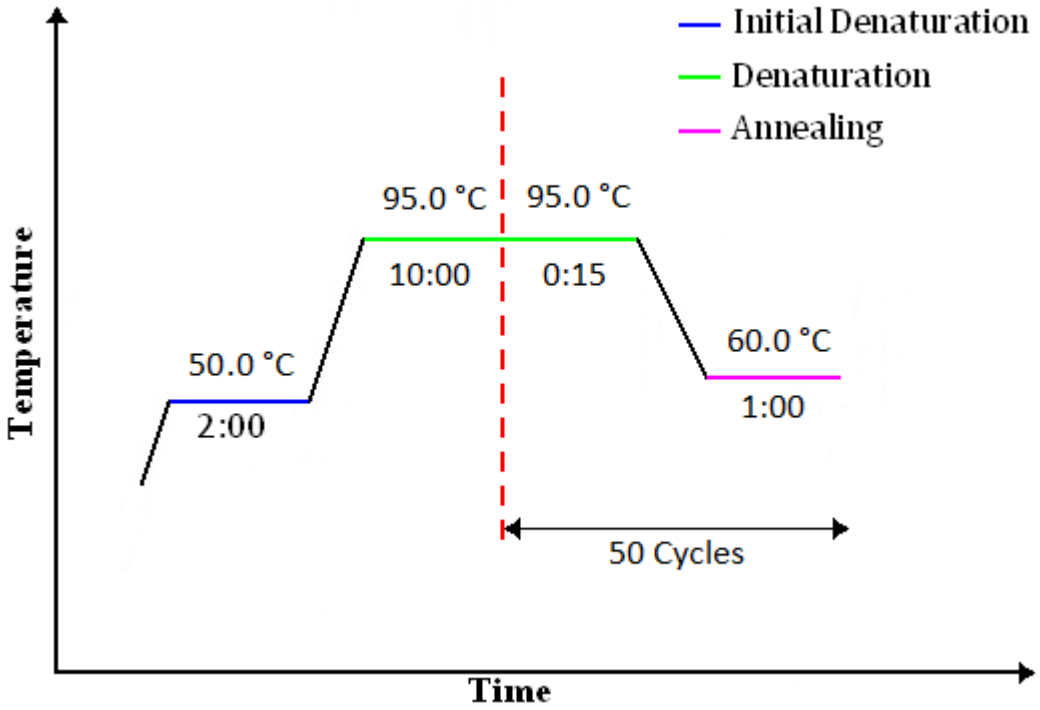

Fig. 5.5 Schematic diagram of qPCR program

Each PCR-reaction was performed in triplicate on a MicroAmp optical 96-well PCR plate (Applied Biosystems), where each reaction well contained 4µl of cDNA products, 0.3µl

of hTERT primer mix for target master mix and 1µl of GAPDH primer mix for endogenous master mix, 10µl of 2× TaqMan® Fast Universal Master Mix (Applied Biosystems) and nuclease free water to 20µl. Target and endogenous master mixes were prepared separately and were added to the plate. Subsequently, the plate was sealed with a plate sealer (MicroAmp, Applied Biosystems) and was then centrifuged for 1 minute at 101 rcf. The qPCR reactions were run using the programs depicted in Fig. 5.5.

The signal obtained for GAPDH was used as the reference housekeeping gene to normalise the amount of total RNA amplified in each reaction. Relative gene expression data were analysed using the $2^{-\Delta\Delta Ct}$ method.

Table 5.4 Synthetic oligonucleotides for qPCR

Primer	Primers and TQ probes	Reporter Dye	Sequence (5´➔3´)	Localisation Exon/Intron	Product size (bp)
hTERT	12896-F*	FAM	GAGCTGACGTGGAAGATGAGC	Exon2	260
	13156-R*		GGTGAACCTCGTAAGTTTATGCAA	Intron2	
	13095-TQ*		CACGGTGATCTCTGCCTCTGCTCTCC	Intron2	

* TQ, TaqMan probe; F, forward; R, reverse

5.2.12 ImmunoFISH Using PML Antibodies

5.2.12.1 Cell Culturing

Three FRDA human fibroblasts (GM03665, GM03816 and GM04078) and three controls (GM07492, U2OS (ALT positive) and HeLa (Telomerase positive)) were grown on poly-L-lysine-coated slides (Poly-Prep slides, Sigma-Aldrich) for 24 hours prior to immunofluorescence staining.

5.2.12.2 Immunofluorescence

The slides were fixed in ice-cold methanol-acetone (1:1) for 10 minutes and were washed three times in PBS. Cells were then blocked with 1% NCS (Newborn Calf serum) in PBS for 30 minutes and were covered with parafilm in a humid container. 75µl of promyelocytic leukemia (PML) primary antibody (Rabbit polyclonal antibody against PML, ab53773, Abcam) was added to the slides at the desired concentration (1:100 in 1% NCS/PBS) and the slides were incubated for 1 hour in a humid container covered with parafilm. The slides were washed in PBS three times for 5 minutes. 75µl of anti rabbit secondary antibody labelled with FITC (F1262-1ML, Sigma) was added to the slides at

the desired concentration (1:100 in 1% NCS/PBS) and the slides were incubated for 1 hour in a dark and humid container covered with parafilm. The slides were washed in PBS three times for 5 minutes in the dark on the shaker. 15µl of VECTASHIELD® with fluorescence DAPI mounting medium (Vector) was then added to the slides and the slides were covered with a 22×50mm coverslip prior to sealing with clear nail varnish.

5.2.12.3 Immunofluorescence and FISH (Immuno-FISH)

Cells were grown, fixed and immunostained with anti-PML antibodies, previously described in section 5.2.12.2. Subsequently, the FISH method was applied with a Cy3-conjugated PNA probe $(C_3TA_2)_3$ followed by standard formamide and SSC washes. Cells were counterstained with DAPI, covered with a 22×50mm coverslip and were sealed with clear nail varnish.

5.2.12.4 Cell Imaging and Quantification

Images of cells were obtained on a Zeiss Axioplan fluorescence microscope equipped with a CCD camera (Photometrics) and Smart Capture software (Digital Scientific) using fixed exposure time of 1 second and magnification of 1000×. The co-localisation of PML and telomere signals was analysed using ImageJ software (National Institutes of Health, Bethesda, MD). 50 cells were quantified for each sample.

5.2.13 γ-H2AX Assay

All adherent cells were grown on poly-L-lysine-coated slides (Poly-Prep slides, Sigma-Aldrich) for 24 hours prior to immunofluorescence staining. The cells were fixed in 4% formaldehyde in PBS for 15 minutes and were permeabilised with 0.2% Triton X-100 (Sigma-Aldrich) for 10 minutes at 4˚C. The cells were then blocked with 0.5% BSA in PBS for 30 minutes and were covered with parafilm in a humid container. 100µl of mouse monoclonal antiphospho-histone H2AX (Ser 139, Millipore) was added to the slides at the desired concentration (1:500 in 0.5% BSA/PBS) and the slides were incubated for 1 hour in a humid container covered with parafilm. The slides were each rinsed three times for 5 minutes in TBST (Tris-Buffered Saline with 0.1% Tween20). 100µl of secondary FITC-conjugated anti-mouse IgG antibody (Sigma) was added to the slides at the desired concentration (1:1000 in 0.5% BSA/PBS) and the slides were incubated for 1 hour in a dark and humid container covered with parafilm. The slides were each washed in TBST three times for 5 minutes in the dark on the shaker. 15µl of VECTASHIELD® with

fluorescence DAPI mounting medium (Vector) was then added to the slides and the slides were covered with a 22×50mm coverslip prior to sealing with clear nail varnish.

5.2.14 Telomere Dysfunction-Induced Foci (TIF) Assay

Cells were grown, fixed and immunostained with anti-H2AX antibodies, previously described in section 5.2.13. For telomere detection (previously discussed in section 5.2.8), the slides were dehydrated for 5 minutes in 70%, 90% and 100% ethanol respectively and were subsequently air-dried. The slides were hybridised for 2 minutes at 70-75˚C with Cy3-conjugated PNA $(C_3TA_2)_3$ probe and were incubated in a dark humidified chamber for 2 hours at RT. The slides were each washed twice in 70% formamide solution for 15 minutes and three times in TBST for 10 minutes in the dark on the shaker. Finally, the cells were counterstained with DAPI, covered with a 22×50mm coverslip, and were sealed with clear nail varnish. The slides were analysed using a Zeiss fluorescence Axioplan microscope equipped with a CCD camera and Smart Capture software. 50 cells were quantified for each sample.

5.2.15 Statistical Analysis

For statistical analysis two-tailed Student's *t* test or two-way analysis of variance (ANOVA) were used to assess the significance of the differences of the group data.

5.3 Results

5.3.1 Telomere Length Analysis by Quantitative FISH (Q-FISH)

To measure the telomere length in FRDA and normal fibroblast cells, Q-FISH was performed. A total of 100 interphase cells per cell line were captured and the mean telomere fluorescence intensity per cell was used to determine the mean difference between the FRDA and normal fibroblast cell lines.

5.3.1.1 Telomere Length Analysis in FRDA Mouse Models

Initially, telomere fluorescence intensity was analysed in mouse FRDA (YG8R and YG22R) and control (Y47R and B6) fibroblast cells. In order to quantify the results, two mouse lymphoma LY-R and LY-S cells were used as calibration standards with known telomere lengths of 49kb and 7kb respectively [236]. The results revealed that the mouse FRDA cell lines (YG8R and YG22R) had significantly increased telomeric repeat fluorescence ($P<0.001$) compared to the controls (Y47R and B6), Fig. 5.6. LY-R control

also showed to have approximately 6 times greater telomere fluorescence than LY-S control which further confirmed the accuracy of the technique. The statistical significance of the differences was evaluated by the Student's *t* test.

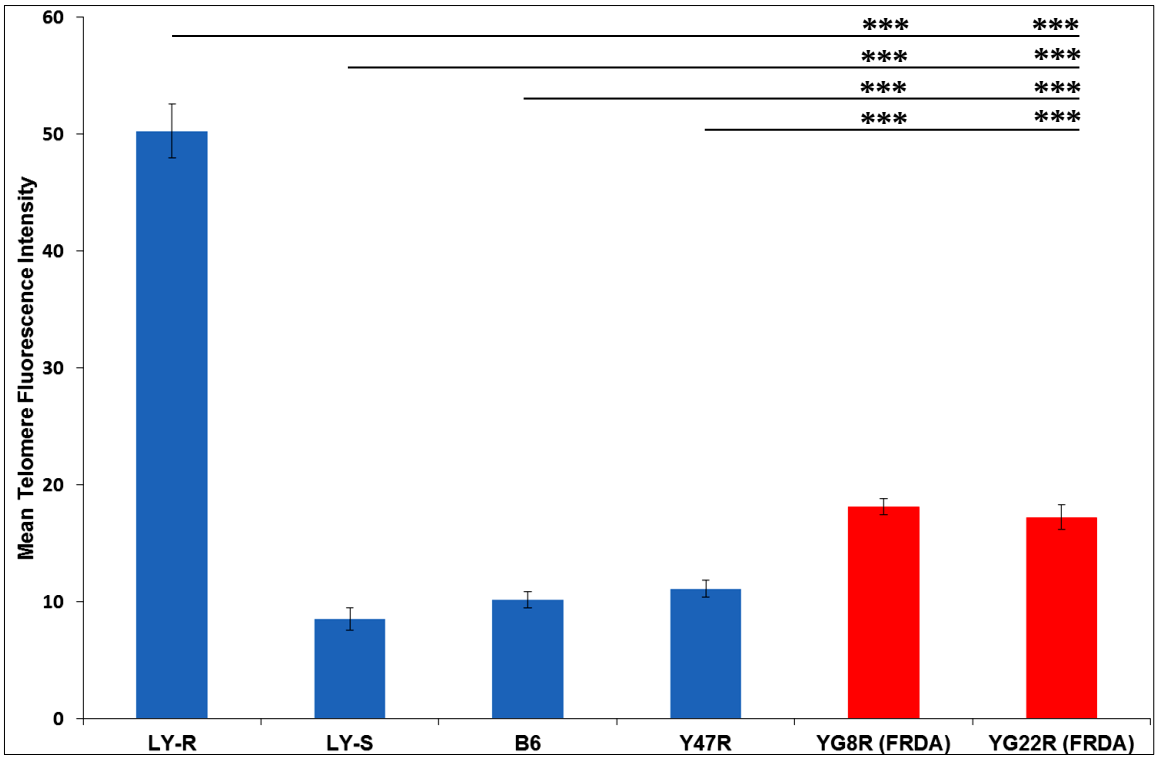

Fig. 5.6 Telomere length analysis of FRDA mouse models by Q-FISH. YG8R and YG22R mice showed to have significantly increased telomeric repeat fluorescence compared to Y47R and B6 controls. LY-R control also showed to have 6 times greater telomere fluorescence than LY-S control which further confirmed the accuracy of the technique. Error bars indicate SEM and values represent mean ± SEM. Asterisks indicate significant differences between the mutant and control mice ($^{***}P<0.001$).

5.3.1.2 Telomere Length Analysis in Human FRDA Fibroblast Cells

Subsequently, telomere fluorescence intensity of PNA probes was analysed in human FRDA (GM03665, GM04078 and GM03816) and control (GM07492, GM04503 and GM07545) fibroblast cell lines at the same growth stage, passage 7. The results indicated that the mean telomere fluorescence intensity of the PNA probes in all the FRDA cell lines was significantly greater ($P<0.001$) than those of the controls, Fig. 5.7.

5.3.2 Telomere Length Measurement by qPCR

To further confirm the Q-FISH results, qPCR technique was performed to evaluate the telomere length in the FRDA and control cell lines.

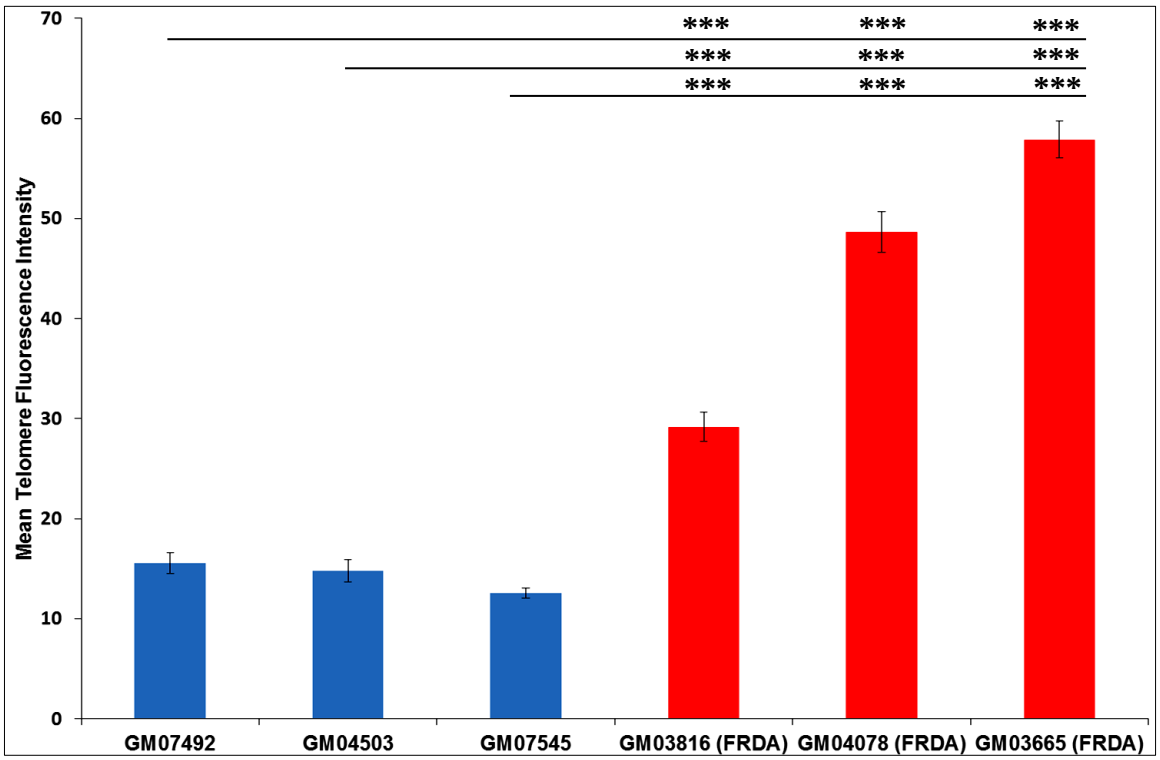

Fig. 5.7 Telomere length analysis of human FRDA cells by Q-FISH. All the FRDA cells showed to have significantly higher telomere fluorescence compared to the controls. Error bars indicate SEM and values represent mean ± SEM. Asterisks indicate significant differences between the FRDA and control cells ($^{***}P<0.001$).

5.3.2.1 Telomere Length Analysis in Human FRDA Fibroblast Cells

Telomere length was measured in human FRDA (GM03665, GM04078 and GM03816) and control (GM07492, GM07545 and human normal) fibroblast cell lines at the same growth stage, passage 7, Table 5.1. Three controls (one 21NT human breast cancer epithelial sample and two 184 normal breast epithelial samples with growth passages of 7 and 20), with known telomere length of 3kb, 15kb and 6kb respectively, were used as the controls to examine the accuracy of the technique. The telomere length of these samples was previously measured using Southern blot method by Dr. Hemad Yasaei. The results obtained by qPCR were in good agreement with those previously acquired by Q-FISH and Southern blot methods, Fig. 5.8A. The results demonstrated that the FRDA fibroblast cells had significantly higher average telomere length of 19kb compared to the normal fibroblasts (14kb, $P<0.001$) and 184 (passage 7) normal epithelial cells (15kb, $P<0.05$), Fig. 5.8B.

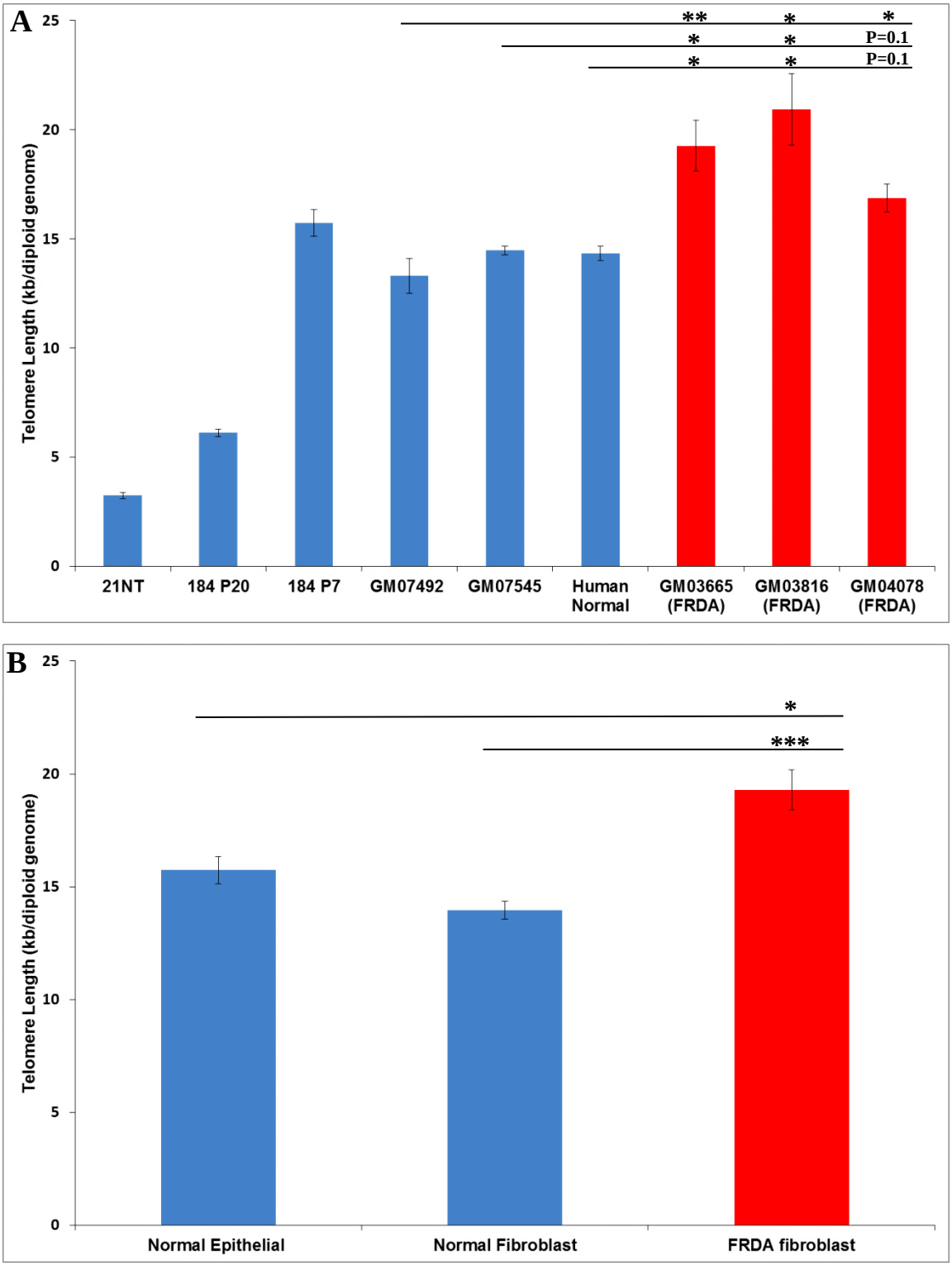

Fig. 5.8 Telomere length measurement in FRDA fibroblasts using qPCR. **A)** The FRDA fibroblasts had higher telomere length compared to the controls. 21NT breast cancer epithelial cell, 184 (passage 7) and 184 (passage 20) normal epithelial cells, with average telomere length of 3kb, 15kb and 6kb respectively, were used as the controls. **B)** Mean telomere length of the FRDA patients was significantly greater than the fibroblast and epithelial (184 passage 7) controls. Error bars indicate SEM and values represent mean telomere length per genome. Asterisks indicate significant differences between the FRDA and control cells ($^{*}P<0.05$ and $^{***}P<0.001$).

5.3.2.2 Telomere Length Analysis in Human FRDA Lymphocyte Cells

Genomic DNA samples, previously extracted from blood samples of 18 FRDA patients and 12 healthy controls, were used to measure the telomere length by qPCR method,

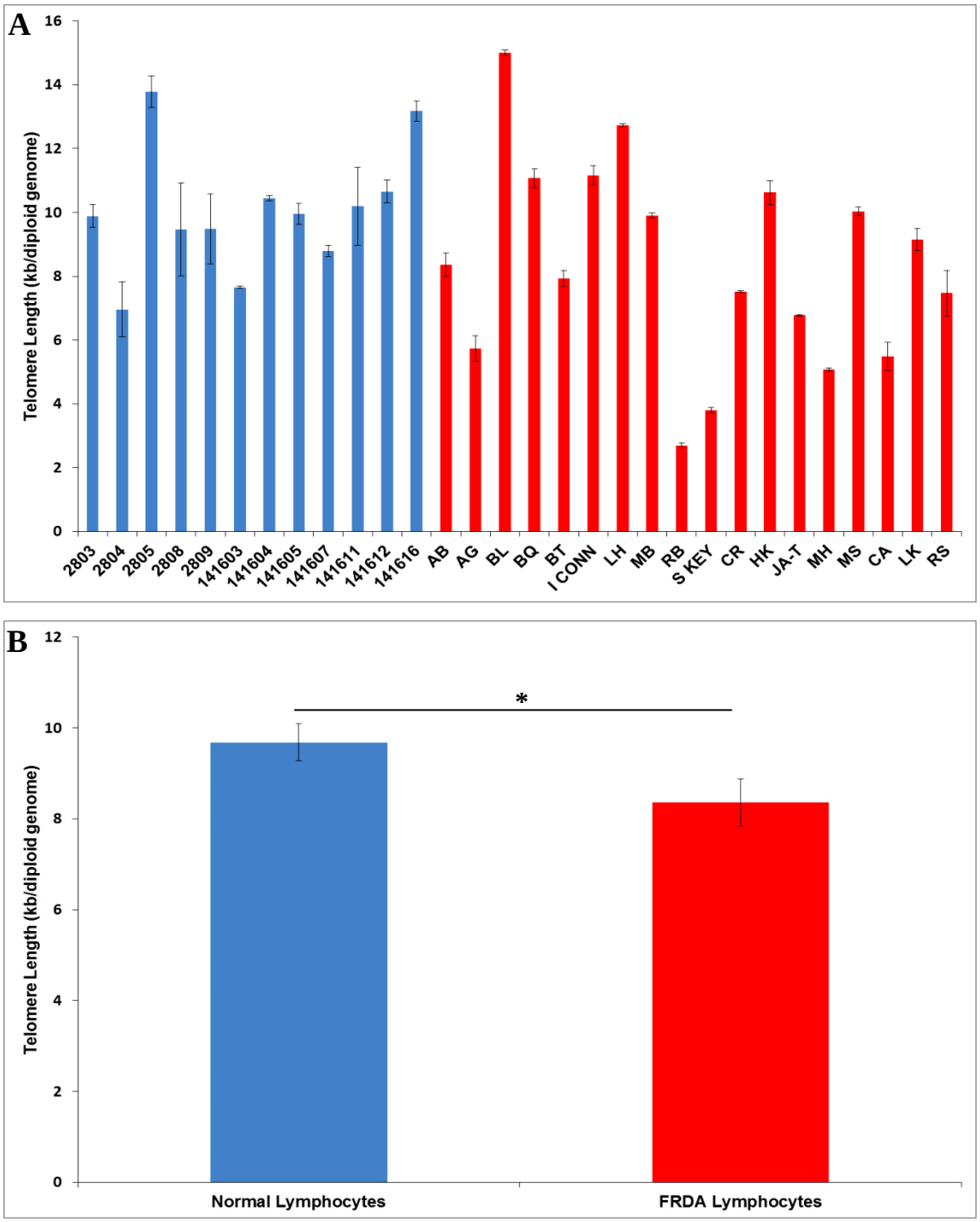

Fig. 5.9 Telomere length measurement in FRDA lymphocytes using qPCR. **A)** There was a variation in the telomere length of the FRDA patients and control lymphocytes. **B)** Mean telomere length of the FRDA lymphocyte cells was significantly lower compared to the controls. Error bars indicate SEM and values represent mean telomere length per genome. Asterisk indicates significant difference between the FRDA and control cells ($^{*}P<0.05$).

Table 5.2. The results indicated that although there was a considerable variation in the telomere length of the patients, Fig. 5.9 A, the mean telomere length was significantly ($P<0.05$) shortened in the FRDA lymphocyte cells compared to the controls, Fig. 5.9 B. These results were in good agreement with those previously reported [214].

5.3.3 Investigation of Telomerase Activity in Human FRDA Fibroblast Cells Using the TRAP Assay

As previously discussed, the FRDA fibroblast cells were found to have chromosomes with relatively longer telomeric repeats. Therefore, these cells might have overcome telomere shortening through activation of telomerase. To validate this hypothesis, cells were screened for expression of telomerase activity using the TRAP assay. In this method, telomerase adds telomeric repeats to the forward primer provided that it is active in these cells. The extended primer would then be amplified by qPCR with a reverse primer complementary to the telomeric repeat. Telomerase activity was assessed in each sample at the same growth stage, passage 7. The results revealed that telomerase activity was not present in the FRDA fibroblasts, Fig. 5.10. The positive control and 21NT showed telomerase activity while the FRDA cells exhibited the same level of telomerase activity as the negative controls. Such observed activity in the FRDA cells was presumed to be due to the background since the higher number of PCR amplification cycles will enhance the sensitivity as well as the background. Consequently, the FRDA cell lines were considered to be negative for telomerase activity.

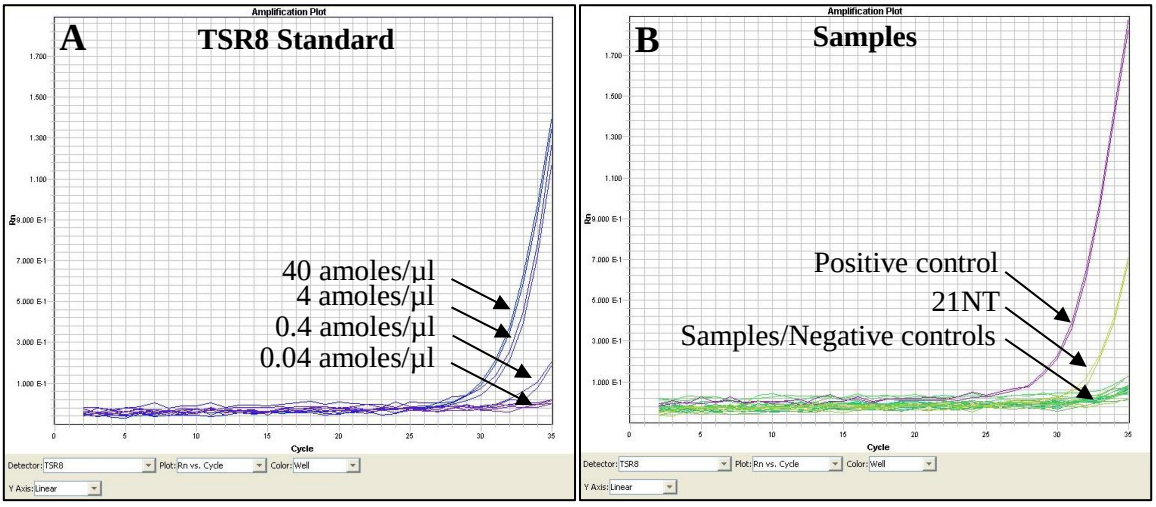

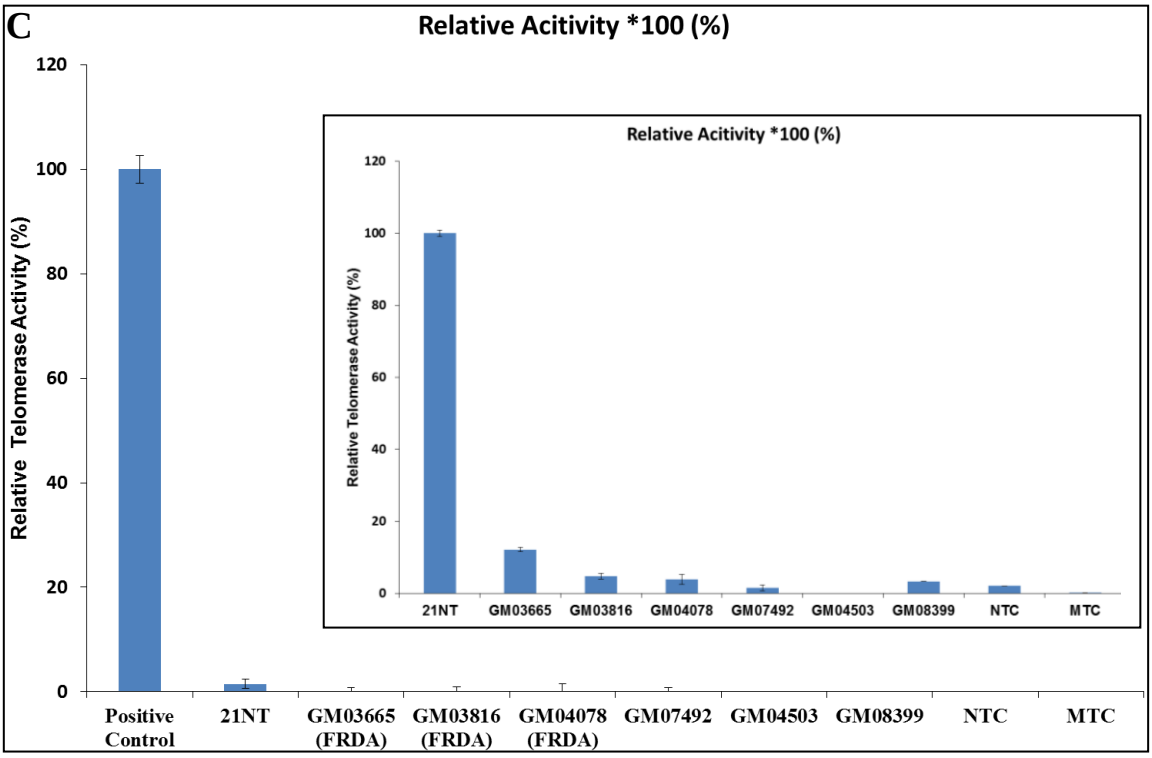

Fig. 5.10 Telomerase activity determined by the TRAP assay in FRDA cells. **A)** Ten-fold serial dilutions of TSR8 quantitation control from 40 amoles to 0.04 amoles were used. **B-C)** FRDA cells showed to be negative for telomerase activity. The breast cancer cell line 21NT and telomerase positive control provided in the kit were used as the positive controls. No template control (NTC), heat treated telomerase negative control and minus telomerase control (MTC) served as the negative controls.

5.3.4 Investigation of hTERT Expression in Human FRDA Fibroblast Cells

Since the TRAP assay is a semi-quantitative method and there exists a strong correlation between hTERT mRNA expression levels and telomerase activity [237], hTERT (human Telomerase Reverse Transcriptase) mRNA expression was measured in the FRDA cells. The quantitative assay for hTERT mRNA expression in the FRDA cells (GM03665, GM03816 and GM04078) was conducted using TaqMan qRT-PCR. Two human breast cancer epithelial samples, 21MT and 21NT, were used as the positive controls while a normal breast epithelial sample, 184, and two normal human fibroblasts, GM07492 and GM08399, served as the negative controls. The results indicated that the FRDA cells did not express hTERT gene, further confirming that the telomerase was negative in these cells, Fig. 5.11.

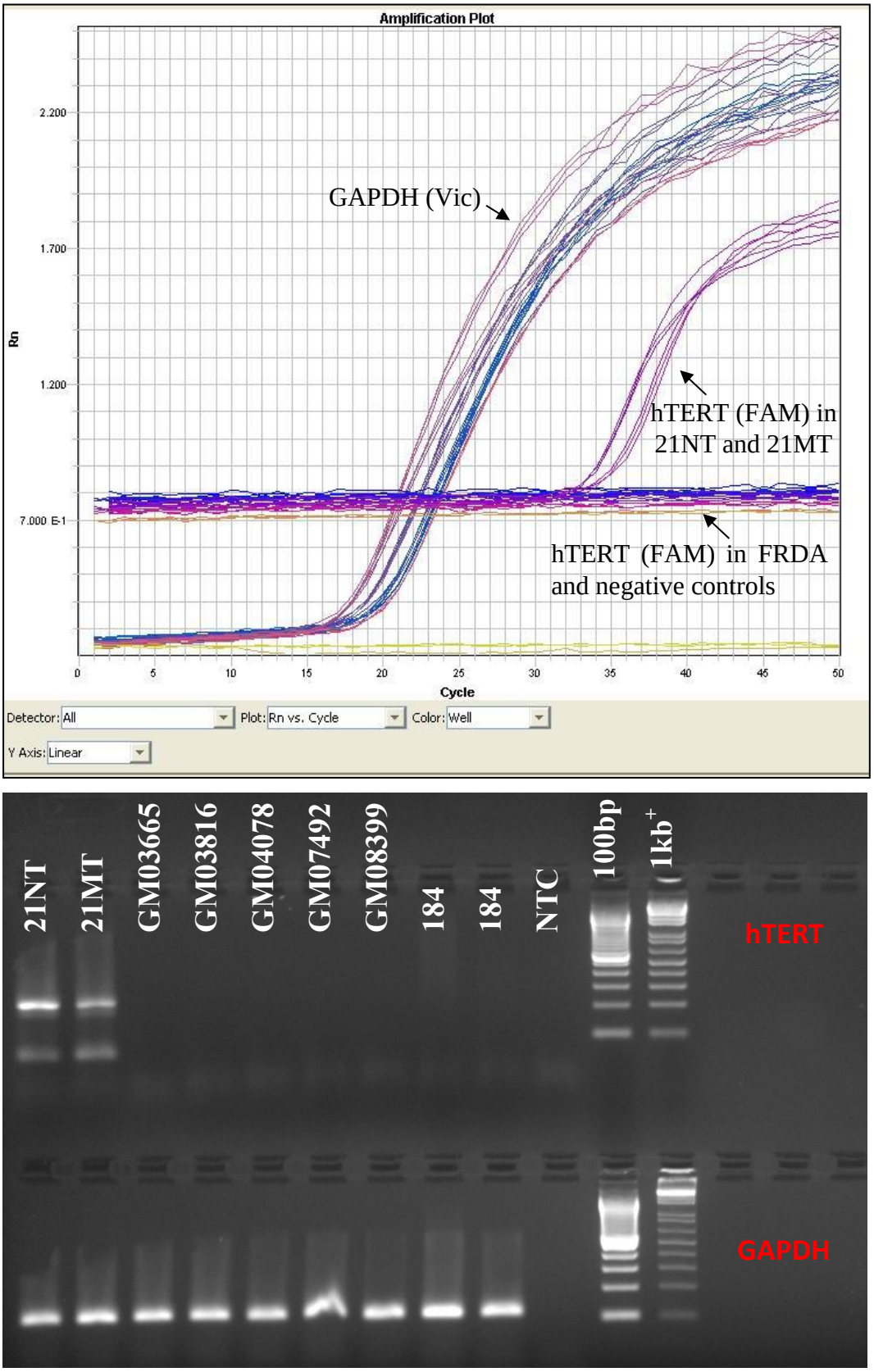

Fig. 5.11 Quantification of hTERT transcripts in FRDA cells. Amplification plot (above) and results in gel electrophoresis (below) indicated that FRDA cells did not express hTERT. The breast cancer cell lines 21NT and 21MT were used as the positive controls. Normal human fibroblast GM07492 and GM08399 cell lines, normal breast epithelial cell line 184 and NTC (No Template Control) served as the negative controls.

5.3.5 Co-localisation of PML Bodies and Telomeres in Human FRDA Fibroblast Cells

As previously stated, the FRDA fibroblast cells exhibited a marked telomere lengthening with no detectable telomerase activity. To investigate whether the FRDA cells maintain their telomeres by ALT associated PML bodies (APBs), the FRDA cells were first examined for the presence of PML bodies using immunofluorescence. No difference was detected in the number and distribution of PML nuclear foci in the FRDA cells compared to the controls. Furthermore, co-localisation of PML bodies with telomeres was investigated in these cells using combined immunofluorescence to PML followed by Q-FISH for telomere detection, Fig. 5.12. The results indicated that in 50 randomly analysed FRDA cells (GM03665, GM03816 and GM04078), approximately 35% of the PML foci co-localised with telomeric DNA. However, the mean co-localisation of PML and telomeres in ALT positive U2OS cell and; GM07492 and HeLa negative controls were 99%, 11% and 8% respectively, Fig. 5.13A. These results suggested that the ALT mechanism was involved in the FRDA cells but it was not as frequent as the ALT positive cells. Subsequently, the size of co-localised PML bodies with telomeres was examined in the aforementioned cells. The results indicated that larger PML bodies in the FRDA cells were associated with telomeres, Fig. 5.13B. However, similar results were obtained in

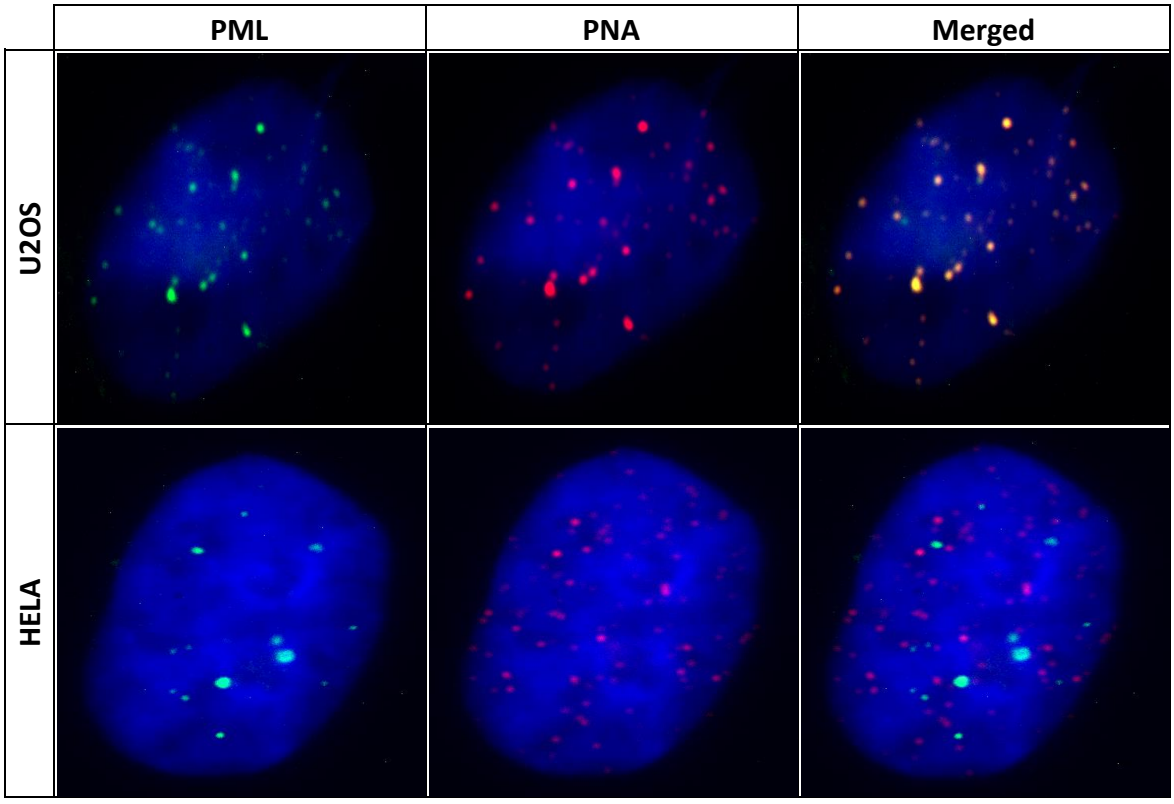

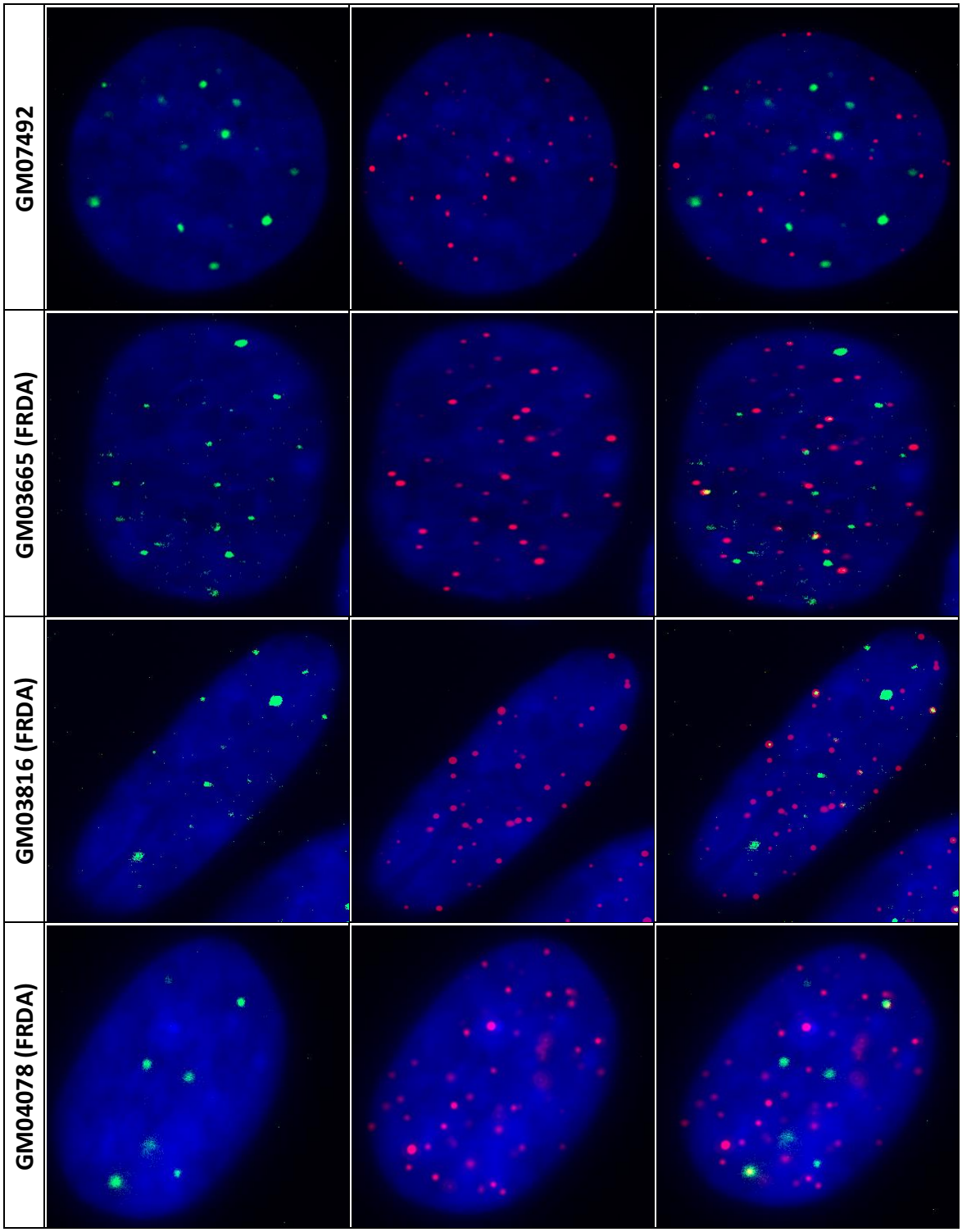

Fig. 5.12 Detection of APBs by immuno-FISH in FRDA cell lines. PML bodies co-localised with telomeres in the FRDA cell lines GM03665, GM03816 and GM04078. U2OS was used as the positive control while GM07492 and HeLa served as the negative controls. Interphase cells were permeabilised and stained with anti-PML (green) and telomeric Cy3-labeled PNA probes (red). Nuclei were counterstained with DAPI.

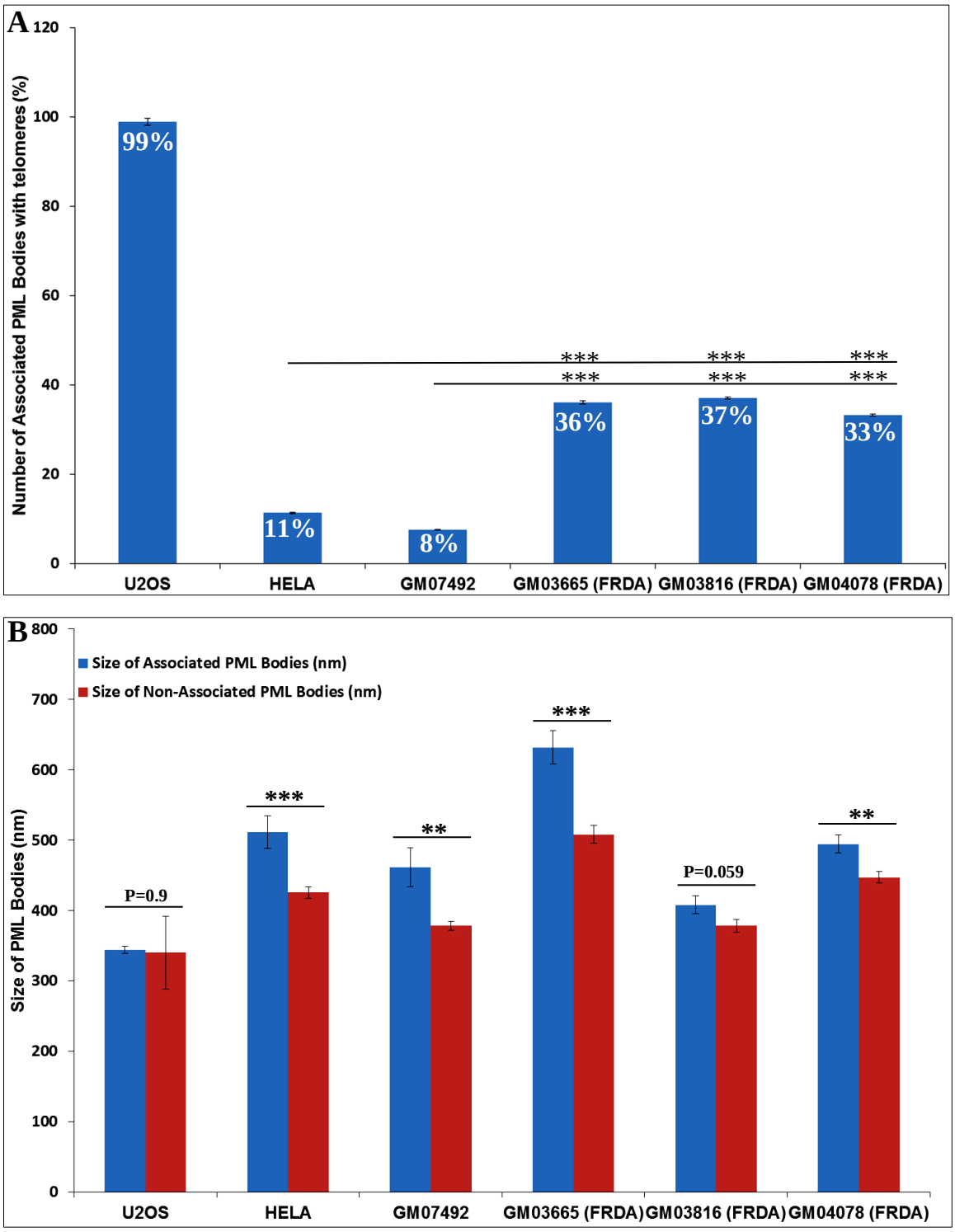

Fig. 5.13 Co-localisation of PML bodies with telomeres in FRDA cells. **A)** Percentage of the PML bodies associated with telomeres demonstrate high co-localisation in all the FRDA cells, GM03665, GM03816 and GM04078, compared to GM07492 and HeLa controls. 99% of the telomere foci co-localised with the PML bodies in the positive control U2OS. **B)** Size analysis of associated and non-associated PML bodies with telomeres. Asterisks indicate significant differences between the FRDA and control cell lines ($^{**}P<0.01$ and $^{***}P<0.001$).

the negative controls (HeLa and GM07492). In addition, no significant difference was detected in the ALT positive control U2OS. Previous results showed that cellular stress may promote aggregation of PML bodies or conversely disperse them into microspeckles [238]. However, in the current study similar results were obtained in the normal cells even though there was an increase in the size of PML bodies associated with telomeres in the FRDA cells. Consequently, these results did not provide any further information regarding the assembly or disassembly of PML bodies in the FRDA cells due to cellular stress. In order to further validate these results, it is of great importance to assess the co-localisation of other PML components such as Sp100 and Daxx with telomeres in the FRDA cells [239].

5.3.6 CO-FISH Analysis of FRDA Fibroblast Cells

Subsequently, telomere recombination frequencies between sister telomeres were analysed in the human FRDA (GM03665, GM04078 and GM03816) and control (GM07492 and GM08399) primary fibroblast cell lines at the same growth stage, passage 7, using the CO-FISH method. A total of 20 metaphases per cell line was analysed to examine the frequencies of T-SCEs in each cell line. The results indicated a significant increase ($P<0.001$) in T-SCE levels of the FRDA cell lines compared to the controls, Fig. 5.14 and Fig. 5.15. These results suggested that T-SCEs occur much more frequently in the FRDA cells than the normal cells, further confirming the existence of ALT mechanism in these cells.

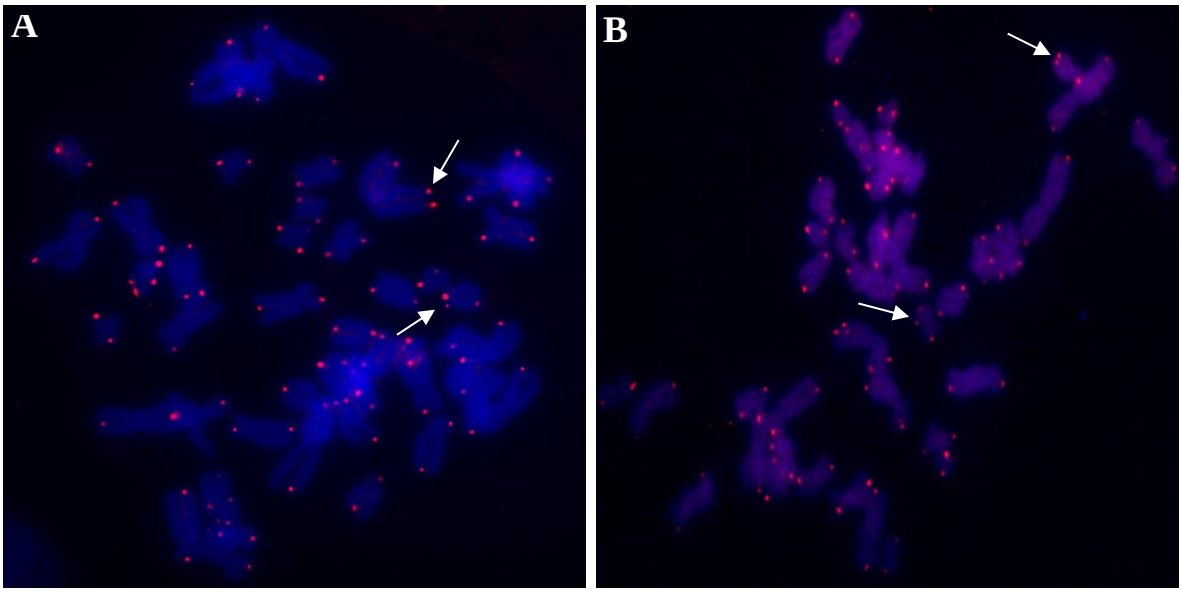

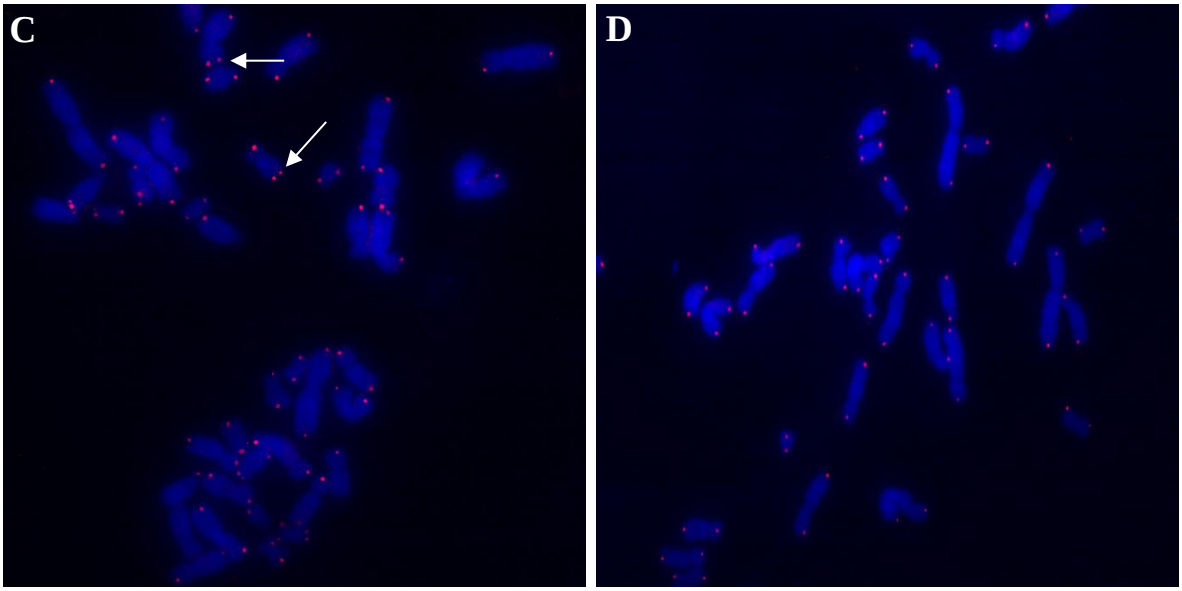

Fig. 5.14 T-SCE frequency in FRDA fibroblasts by CO-FISH. **A)** GM03665, **B)** GM04078 and **C)** GM03816 FRDA cells showed multiple T-SCEs events indicated by arrows. The process effectively removes the newly synthesised DNA strands and leaves behind the two parental strands which are located on sister chromatids. A single-stranded probe hybridises to complementary telomeric DNA on one chromatid of each chromosome arm producing a two-signal pattern instead of the four signals seen with ordinary FISH. **D)** In the normal GM07492 and GM08399 fibroblast cells T-SCE is a very rare event.

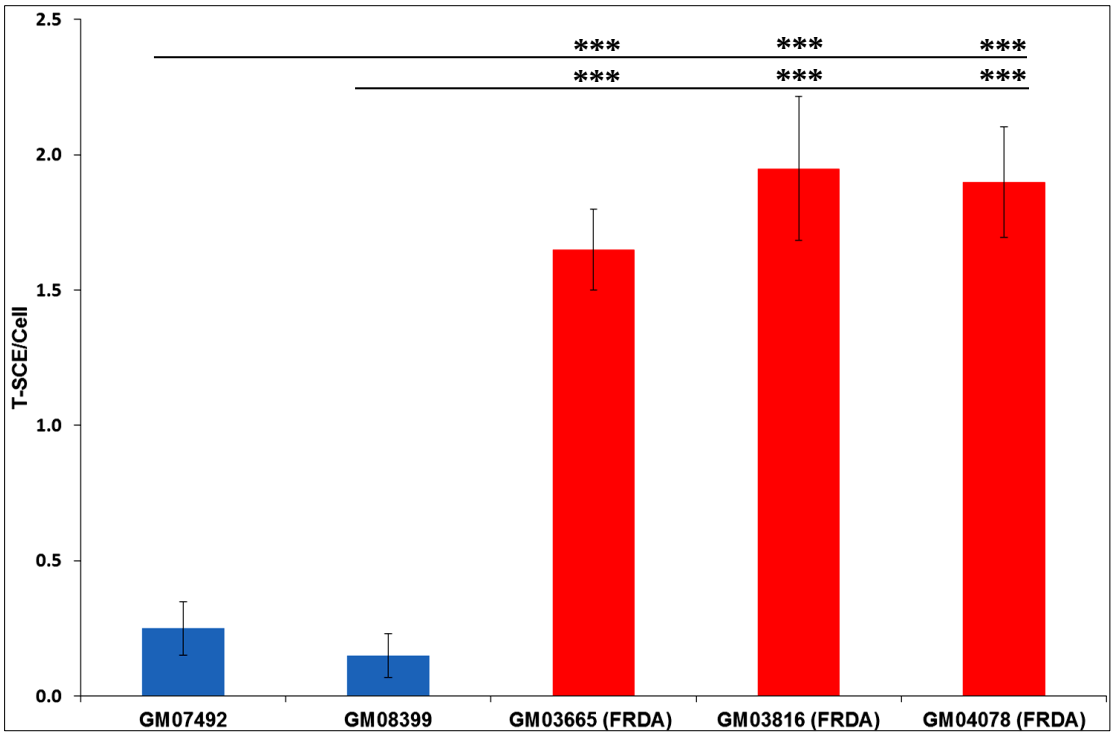

Fig. 5.15 T-SCE analysis of human FRDA cells by CO-FISH. All FRDA cells showed a significant increase ($P<0.001$) in T-SCE levels compared to the controls. Error bars indicate SEM and values represent mean ± SEM. Asterisks indicate significant differences between the FRDA and control cell lines ($^{***}P<0.001$).

5.3.7 Population Doubling and Growth Curve of Human FRDA Fibroblast Cells

To investigate whether the FRDA cells activate ALT during culturing *in vitro* and become immortalised, growth curves and cumulative population doubling analysis were performed. Growth curve analysis of the human FRDA and control fibroblasts was carried out from the earliest passage number for each cell line. The cells harvested from the earliest passage were counted by a Countess^{TM} automated cell counter and were reseeded at 100,000 cells/25cm^2 flasks every 6-7 days. As evident in Fig. 5.16A and Table 5.5, GM03816 and GM04078 FRDA fibroblast cell cultures underwent growth arrest after 175 days with average cumulative population doubling of 57 and 52 respectively. In contrast, the normal fibroblast cells exhibited earlier growth arrest, after approximately 138 days, with an average of 36 cumulative population doubling, Fig. 5.16B and Table 5.5. GM03665 FRDA fibroblast cell showed growth arrest with cumulative population doubling of 33 after 133 days, Fig. 5.16A. However, the earliest passage number of this cell line was not provided at the beginning of culturing and was assumed to be at passage 7. In addition, such subtle differences in the cellular ageing process of different primary human fibroblasts can be due to different cellular processes. Therefore, the analysis of variation in growth rate requires additional studies. These results indicated that the FRDA cells were unable to become immortalised by the ALT mechanism alone, suggesting that the frequency of the PML bodies may not have been sufficient to prevent senescence. However, the FRDA cells senesced approximately 11

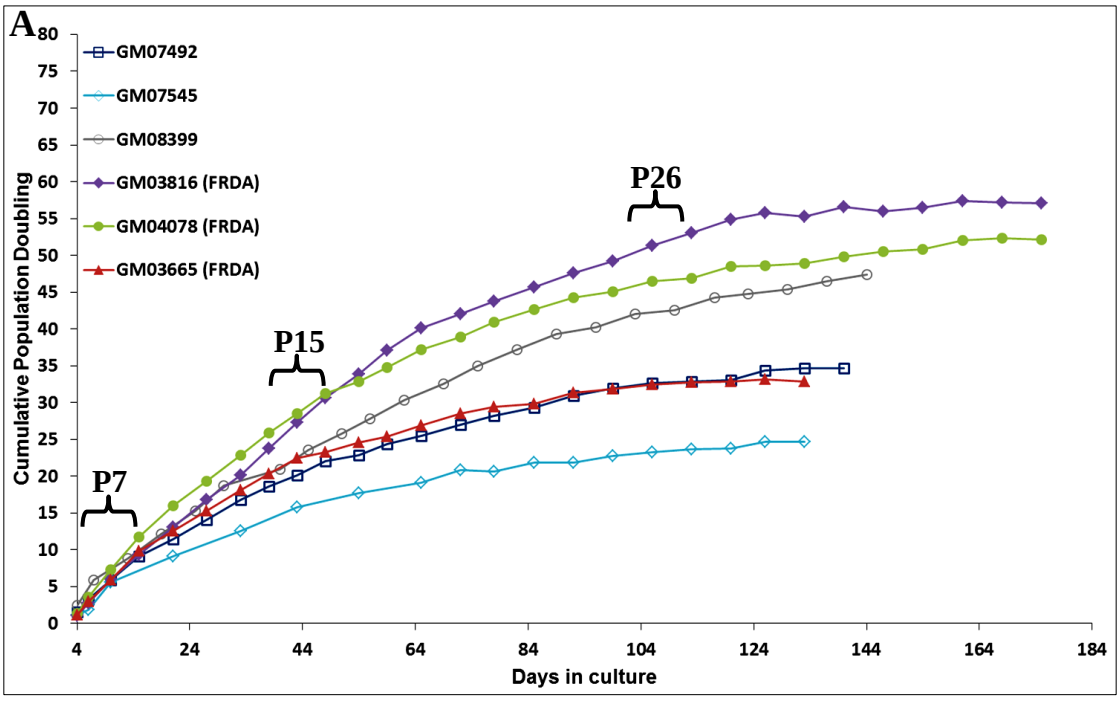

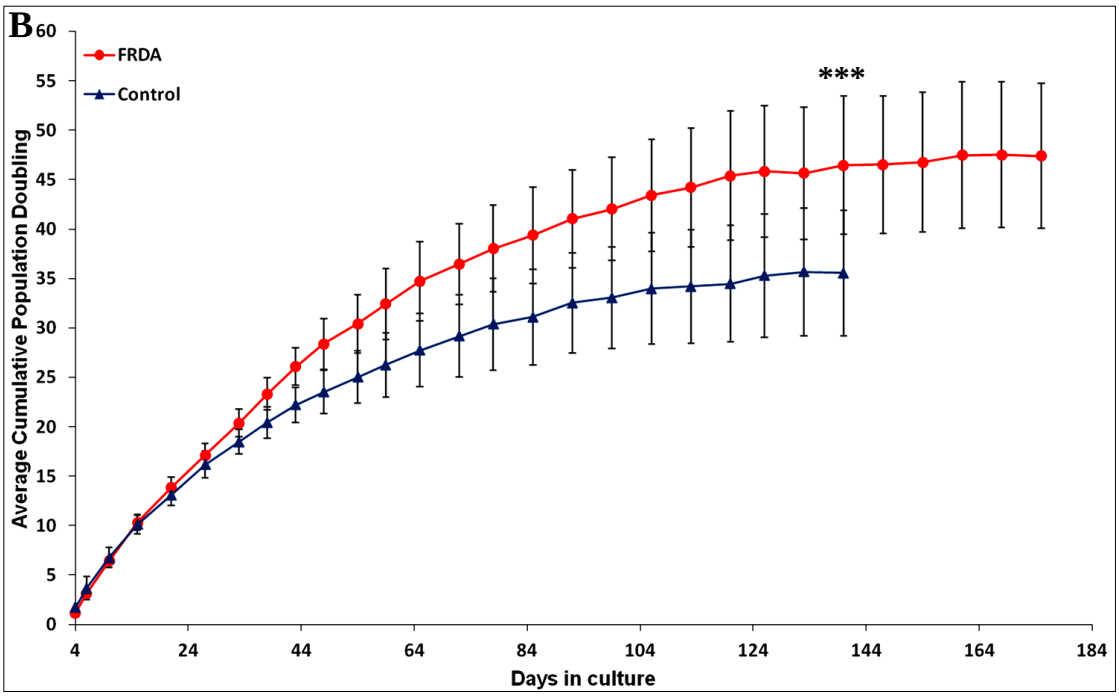

Fig. 5.16 Growth curves of human fibroblast cells. **A)** CPD of the human FRDA and normal fibroblast cell lines. **B)** The FRDA cells senesced approximately 11 population doublings later than the control cells. Every cell passage is indicated by a point and the CPD was calculated based on the average sum of the cell proliferations over the cumulative time taken from the earliest passages until cells underwent senescence. Error bars indicate SEM and values represent mean ± SEM. Asterisks indicate significant differences between the FRDA and control fibroblasts ($^{***}P<0.001$), evaluated by two-way ANOVA.

population doublings later than the controls (P<0.001). This delay in transition from proliferation to senescence in the FRDA cells could be due to the difference in the original telomere lengths of these cell lines.

Table 5.5 CPDs of the human fibroblasts at different passages

Cell line	Duration in culture (Day)	CPD at earliest passage (P-7)	CPD at passage 15th	CPD at passage 26th	CPD at final passage
GM07492	140	3	20	34	35
GM07545	133	1	19	22	25
GM08399	144	2	26	45	47
GM03816 (FRDA)	175	3	27	56	57
GM04078 (FRDA)	175	4	33	49	52
GM03665 (FRDA)	133	1	20	32	33

CPD, Cumulative Population Doubling; P, Passage number

5.3.8 Telomere Length Shortening Rate Analysis in Human FRDA Fibroblast Cells

The effect of replicative aging of culture cells at the 7th, 15th and 26th passages was studied by qPCR telomere length assay to determine telomeric DNA loss due to cell divisions. Three FRDA fibroblast cell lines (GM03665, GM03816 and GM04078) and two normal fibroblasts (GM07492 and GM07545) were monitored for telomere length loss, Fig. 5.17A and Table 5.6. The results from this study revealed an accelerated rate of telomere shortening in the FRDA fibroblasts, Fig. 5.17B. Although preliminary results indicated that the FRDA fibroblast cells had relatively longer telomeres at growth stage of passage 7 compared to the controls, further analysis of telomere length at different time points of passages 15 and 26 revealed that these cells lost telomeres more rapidly in culture than the normal cells, Fig. 5.17C and Fig 5.17D. The accelerated telomere shortening observed in the FRDA fibroblast cells suggested that telomeres were dysfunctional in these cells. In addition, it is possible that genetic changes or recruitment of other proteins at telomeres may alter the heterochromatic state of ALT telomeres, resulting in the repression of telomeric recombination [155].

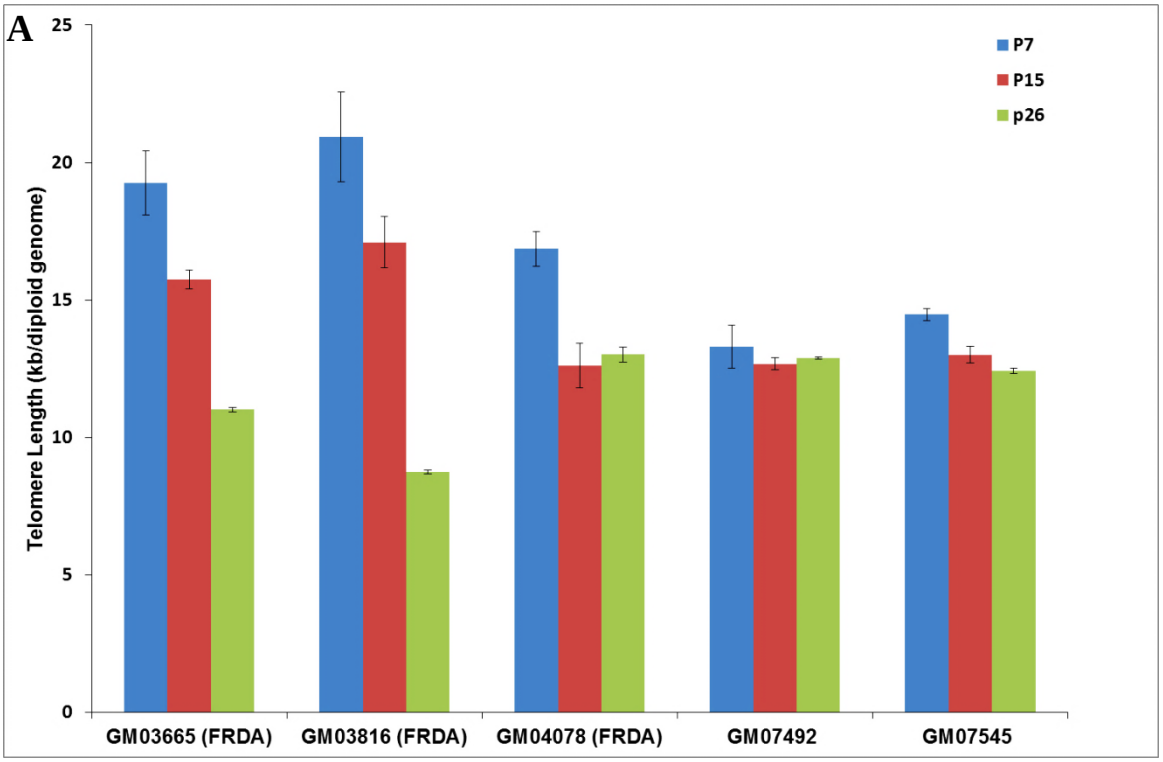

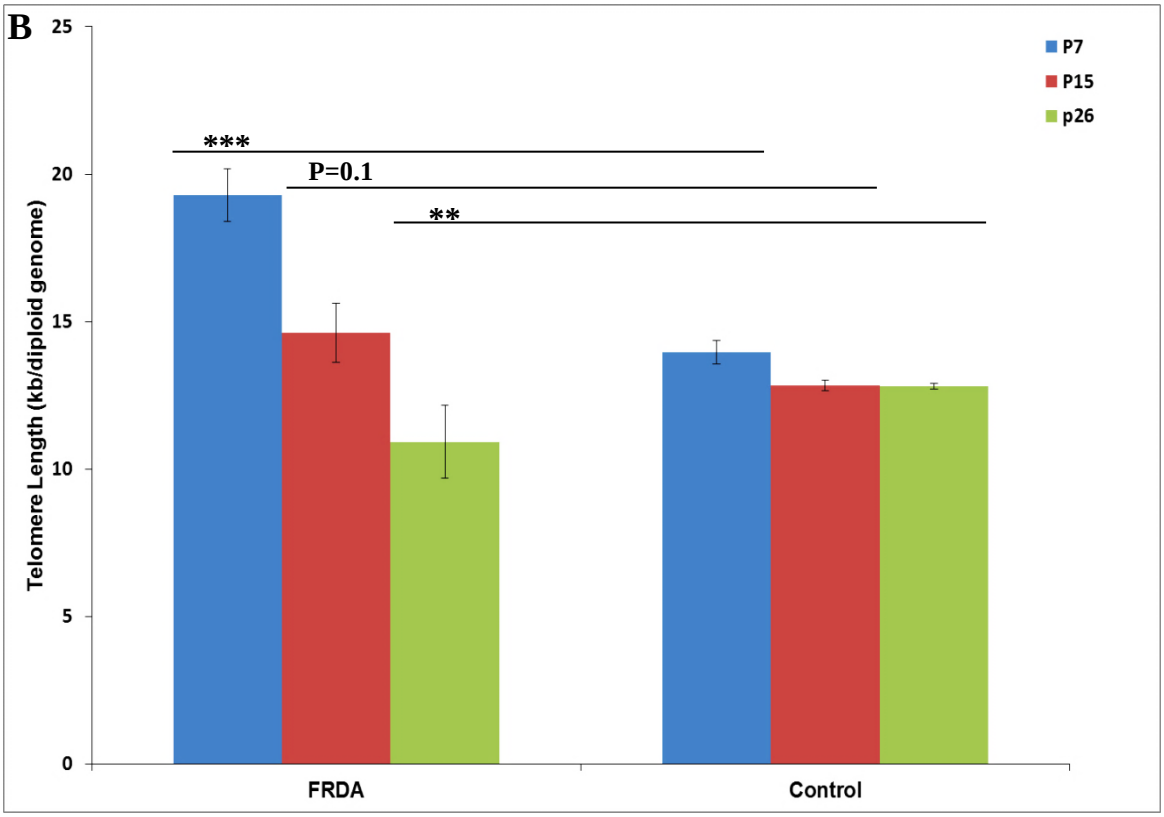
B
25
20
15
10
5
0
Telomere Length (kb/diploid genome)
P7
P15
p26
***
P=0.1
**
FRDA
Control

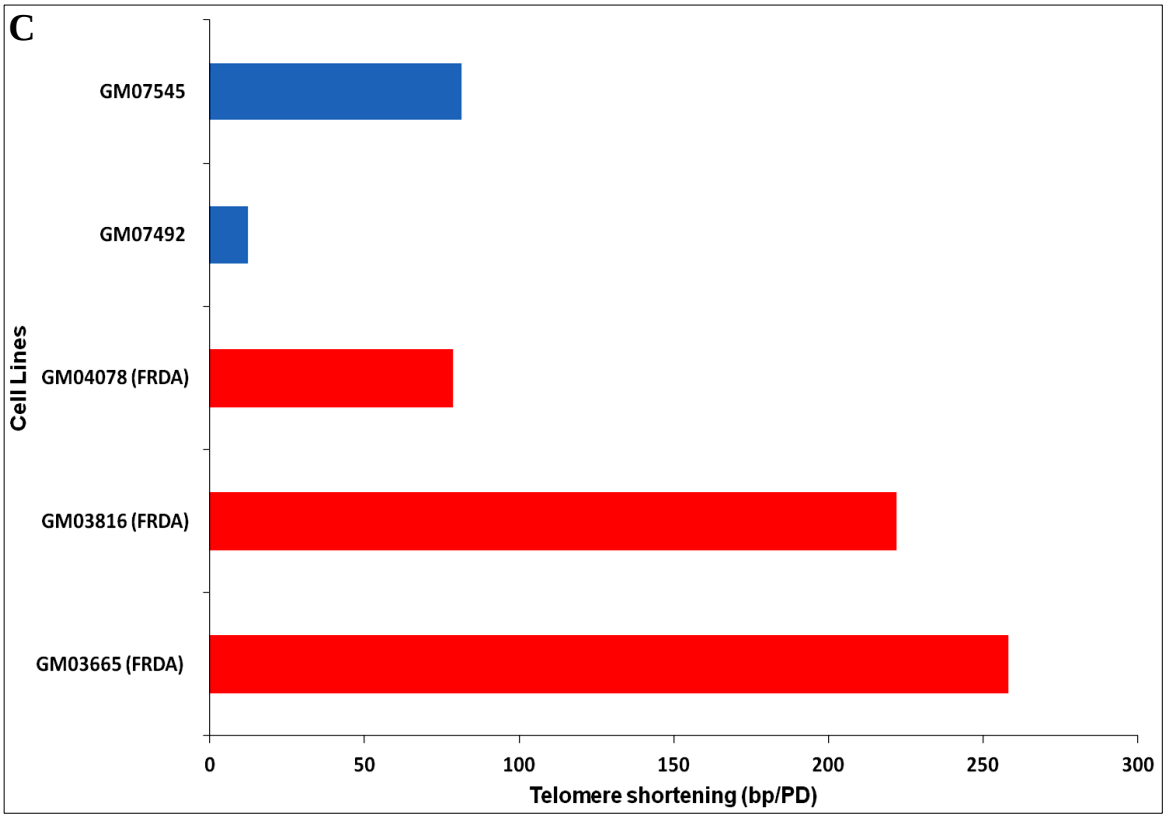
C
GM07545
GM07492
GM04078 (FRDA)
GM03816 (FRDA)
GM03665 (FRDA)
Cell Lines
0
50
100
150
200
250
300
Telomere shortening (bp/PD)

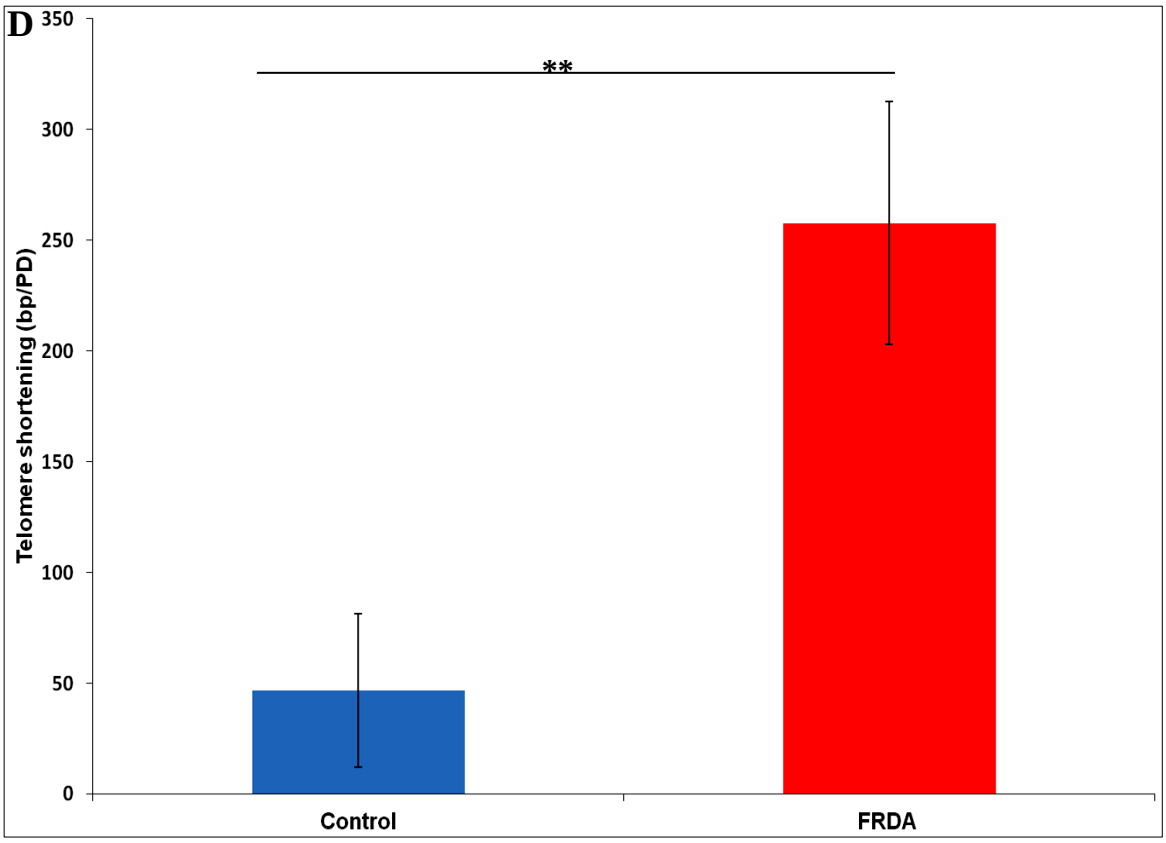

Fig. 5.17 Rates of telomere shortening in human FRDA fibroblast cells. **A)** Telomere length analysis by qPCR in the FRDA fibroblast cells (GM03665, GM03816 and GM04078) compared to normal fibroblasts (GM07492 and GM07545) at different growth passages of 7, 15 and 26. **B)** The average telomere length of the FRDA cells compared to the controls at different growth passages. **C)** Rates of telomere shortening in the human FRDA and normal fibroblasts in bp/population doubling. **D)** The average rates of telomere shortening in the human FRDA and normal fibroblasts in bp/population doubling. Error bars indicate SEM and values represent mean ± SEM. Asterisks indicate significant differences between the FRDA and control cell lines (**P<0.01 and ***P<0.001).

Table 5.6 Student's *t* test analysis of telomere length shortening in FRDA fibroblasts

Cell line	Passage number	Versus GM07492	Versus GM07545
GM03665	7	P= 0.01	P= 0.05
	15	P= 0.004	P= 0.01
	26	P= 0.0001	P= 0.003
GM03816	7	P= 0.02	P= 0.05
	15	P= 0.03	P= 0.03
	26	P= 5.30E-06	P= 0.0008
GM04078	7	P= 0.04	P= 0.1
	15	P= 0.1	P= 0.3
	26	P= 0.05	P= 0.1

5.3.9 TIF Analysis in Human FRDA Fibroblast Cells

To confirm the presence of a telomere dysfunction phenotype in the FRDA cells, the telomere dysfunction-induced foci (TIF) assay was performed using an antibody against DNA damage marker γ-H2AX together with the synthetic PNA telomere probe. As evident in Fig. 5.18 and Fig. 5.19A, the frequency of γ-H2AX foci was significantly higher in the FRDA cells compared to the controls ($P<0.001$). Similarly, the FRDA cells had greater TIF frequencies in comparison to the controls ($P<0.001$), Fig. 5.19B, suggesting that the FRDA cells may have induced telomere dysfunction relative to the controls.

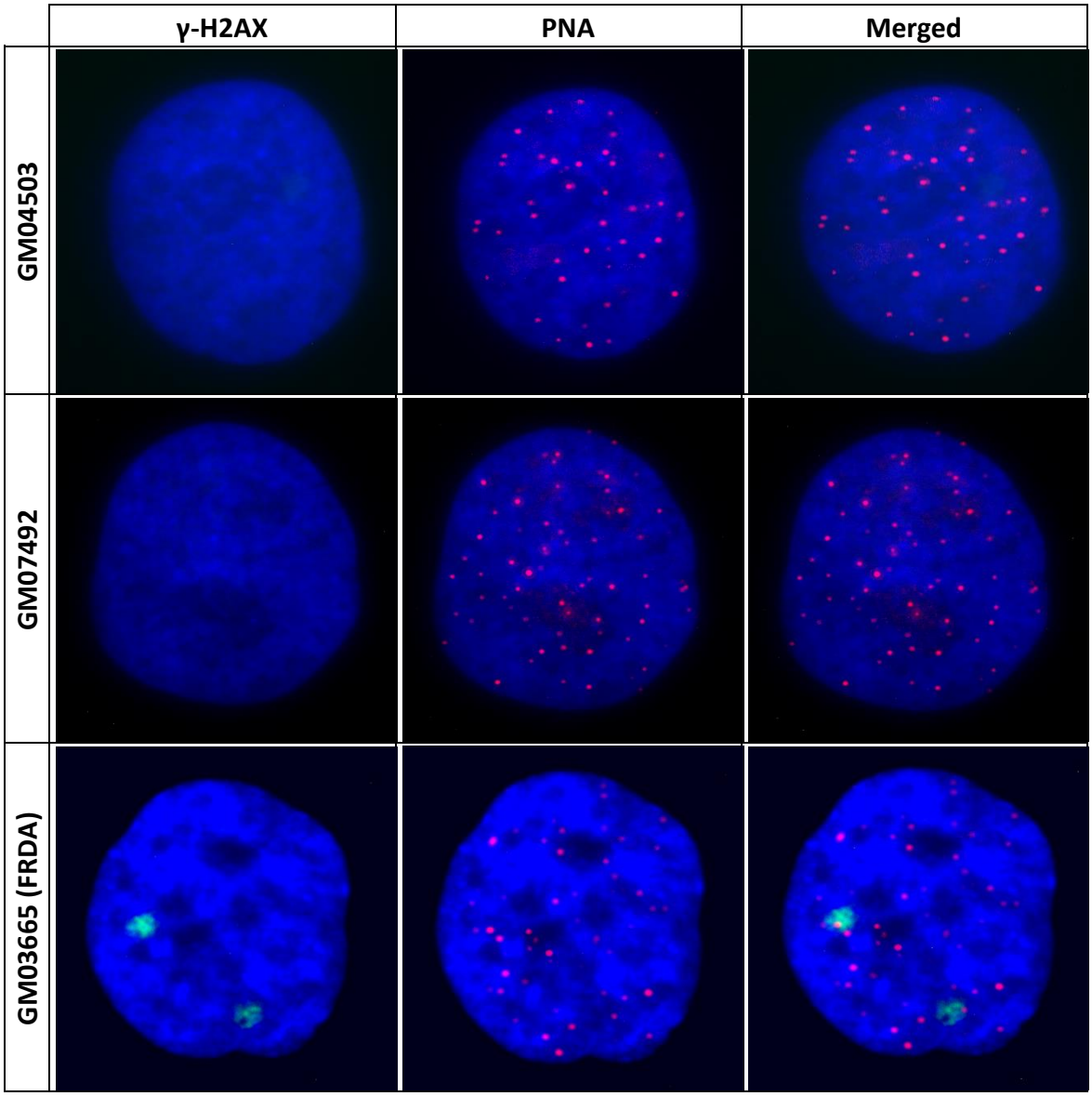

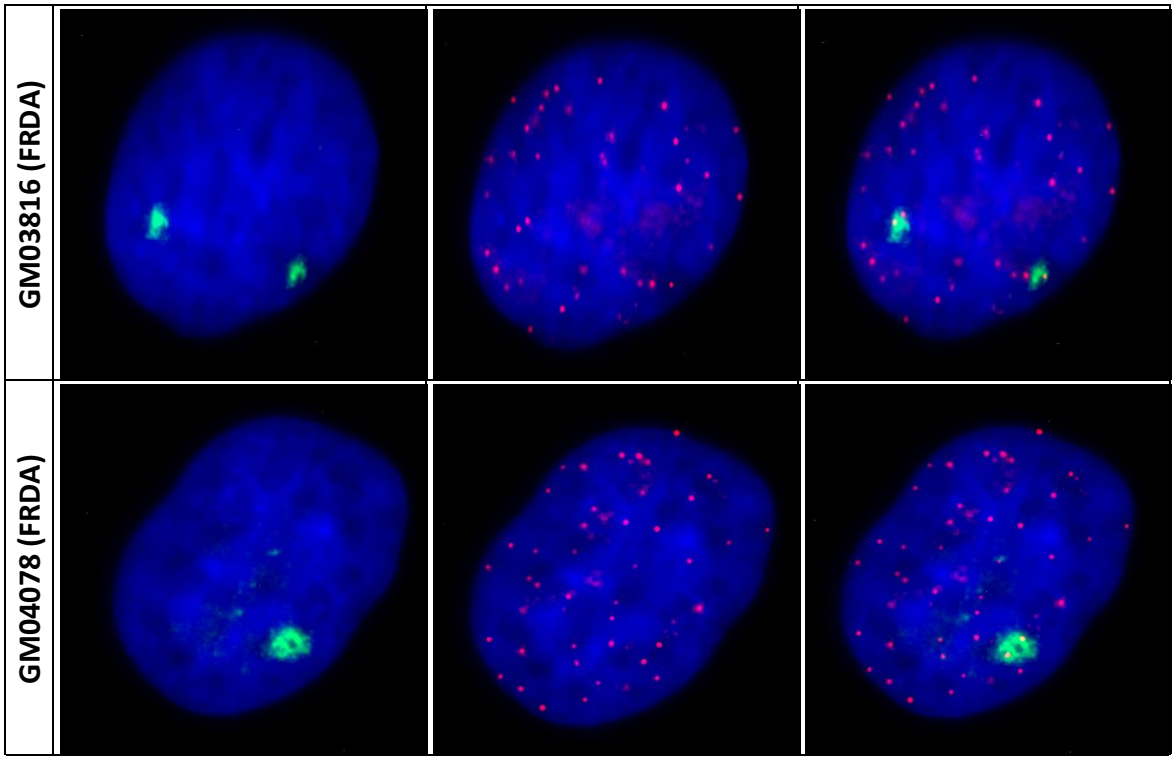

Fig. 5.18 Detection of γ-H2AX by immuno-FISH in FRDA cell lines. Cell nucleus in the FRDA cell lines (GM03665, GM03816 and GM04078) exhibiting a TIF. GM07492 and GM04503 cell lines were used as the negative controls. Interphase cells were permeabilised and stained with antiphospho-histone γ-H2AX (green) and telomeric Cy3-labeled PNA probes (red). Nuclei were counterstained with DAPI.

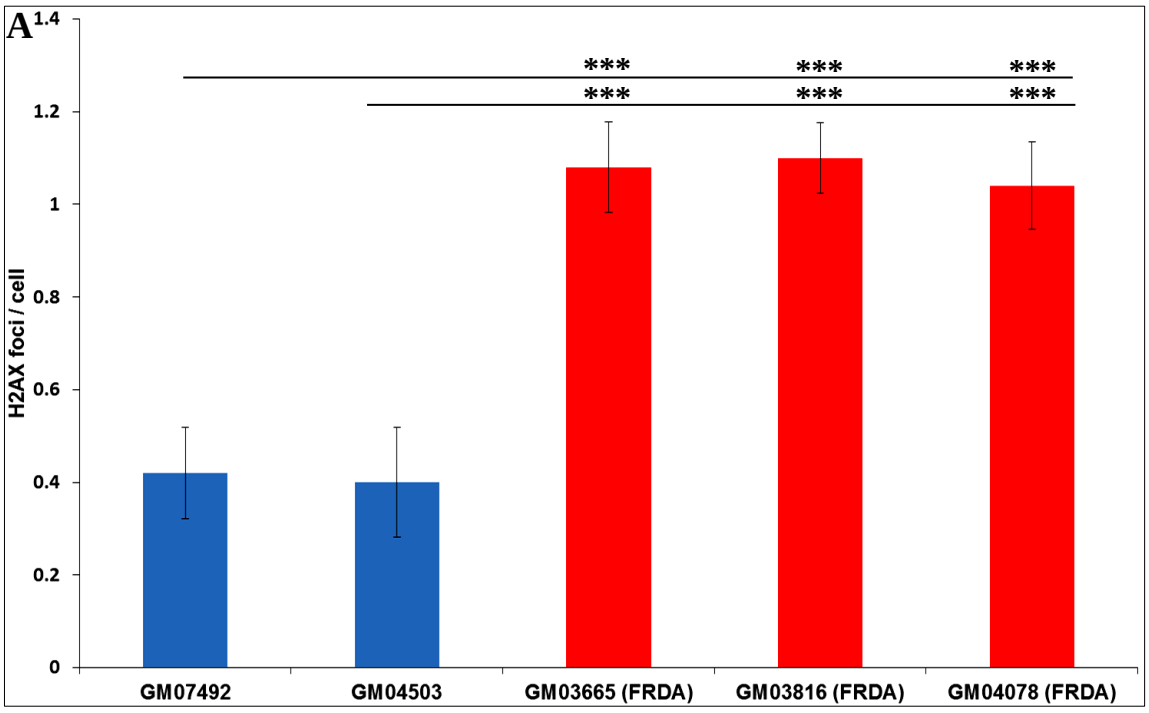

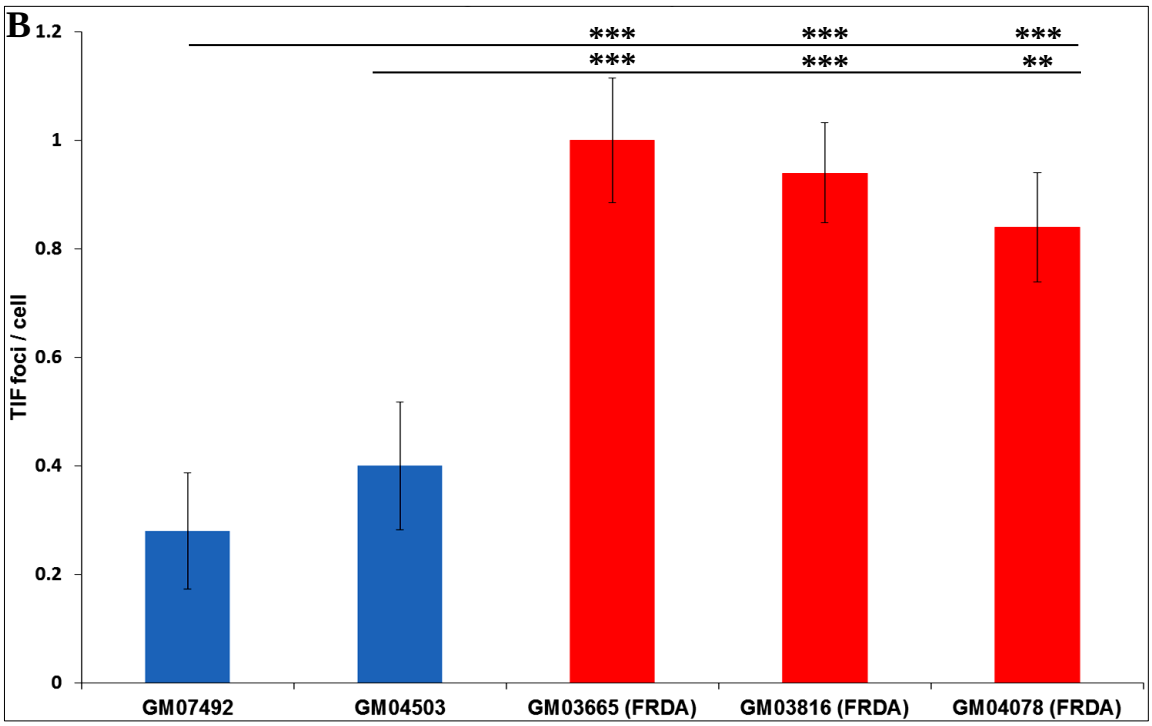

Fig. 5.19 Frequencies of γ-H2AX positive foci and TIFs in FRDA cells. **A)** Average γ-H2AX positive foci in each cell line. **B)** Average TIFs in each cell line. The results were obtained based on two independent experiments with an average of 50 cell nuclei scored per cell line. Asterisks indicate significant differences between the FRDA and control cell lines (**P<0.01 and ***P<0.001).

5.4 Discussion

FRDA is caused by a GAA triplet repeat expansion within the first intron of the frataxin gene. This expansion impairs the transcription of the gene, leading to deficiency of frataxin. This protein is a ubiquitous mitochondrial protein involved in mitochondrial iron transport and/or in the assembly of iron-sulphur cluster enzymes. Frataxin deficiency is associated with iron dysregulation and severe disruption of iron-sulphur cluster proteins. Lack of iron detoxification and the increase in the level of bioavailable iron are likely to enhance cellular sensitivity to oxidative stress, an important modulator of telomere length. Therefore, it was hypothesised that telomere length might be shortened in the FRDA patients.

This study, which is to my knowledge the first to report on telomere length in the FRDA fibroblast cells, showed that human FRDA fibroblast cells had significantly higher telomere length compared to normal fibroblasts of the same growth passage. Similar results were obtained in the mouse FRDA fibroblast cells. However, the results published in a recent study using human FRDA lymphoblast cells indicated significant telomere

shortening in these cells [214]. Consequently, telomere length was also examined in the genomic DNA from FRDA lymphocytes in order to investigate such a discrepancy. The results indicated that the mean telomere length was significantly shortened in the FRDA lymphocytes relative to the controls which were in good agreement with the recently published results [214]. Nevertheless, there was a considerable variation in the telomere length of the patients. Therefore, the mean results cannot serve as a reliable biomarker of the FRDA disease as proposed by the authors [214]. The results from the fibroblast and lymphocyte cells revealed that telomere length varies within different cell types. This may be due to the different environmental conditions as the former was derived from *in vitro* culture while the latter was generated from *in vivo* cells. However, an explicit conclusion can only be drawn provided that a sufficiently large sample size is examined and the fibroblast cells are matched for age. Therefore, larger age matched sample sizes are required to evaluate the reliability and validity of the results presented in this study.

To investigate the mechanisms which induce telomere lengthening in the human FRDA primary fibroblasts, cells were screened for the expression of telomerase activity using the TRAP assay. The results indicated that the observed telomere elongation in the FRDA fibroblasts did not involve the telomerase enzyme. A quantitative assay for hTERT mRNA expression in the FRDA cells was also conducted using TaqMan qRT-PCR. The results showed that the FRDA cells did not express hTERT, further confirming the finding that telomerase activity was negative in these cells. Therefore, it was hypothesised that the ALT mechanism may be responsible for the observed telomere lengthening in the FRDA fibroblasts. To investigate whether FRDA cells maintain their telomeres by ALT associated PML bodies (APBs), co-localisation of PML bodies with telomeres was investigated in these cells using combined immunofluorescence and Q-FISH. The results indicated that the FRDA fibroblast cells had significantly higher co-localised PML foci with telomeric DNA compared to the normal fibroblast cells. However, the mean co-localisation of PML and telomeres was more pronounced in the U2OS ALT positive control. These results suggested that the ALT mechanism was involved in the FRDA cells but it was not as frequent as the ALT positive cells. Subsequently, the size of co-localised PML bodies with telomeres was examined in the FRDA cells. The results indicated that larger PML bodies in the FRDA cells were associated with telomeres. However, similar results were obtained in the negative controls. In addition, no significant difference was detected in the ALT positive control U2OS. Previous results showed that cellular stress

may promote aggregation of PML bodies or conversely disperse them into microspeckles [238]. However, in the current study similar results were obtained in the normal cells even though there was an increase in the size of PML bodies associated with telomeres in the FRDA cells. Consequently, these results did not provide any further information regarding assembly or disassembly of PML bodies in the FRDA cells due to cellular stress. In order to further validate these results, it is of great importance to assess the co-localisation of other PML components such as Sp100 and Daxx with telomeres in the FRDA cells [239]. T-SCE frequencies were also analysed in the human FRDA cell lines. The results exhibited a significant increase in T-SCE levels of the FRDA cell lines relative to the controls, further confirming the existence of ALT mechanism in these cells.

To investigate whether the FRDA cells activate ALT during culturing *in vitro* and become immortalised, growth curves and cumulative population doubling analysis were performed. The results showed that the FRDA fibroblast cell cultures underwent growth arrest with higher cumulative population doubling compared to the controls. These results indicated that the FRDA cells were unable to become immortalised by the ALT mechanism alone, suggesting that the frequency of the PML bodies may not have been sufficient to prevent senescence. However, the FRDA cells senesced approximately 11 population doublings later than the controls. This promotion of the transition from proliferation to senescence in the FRDA cells could be due to the difference in the original telomere lengths of these cell lines or the activation of the ALT mechanism by which the mean cell population doubling may have been exceeded. In addition to the growth behaviour and the number of cells, the state of replicative senescence can also be determined by increased numbers of γ-H2AX DNA repair foci at telomeres as a result of cell-specific stress responses. Therefore, further analysis is required to confirm the senescent phenotype in the fibroblasts cells.

Subsequently, the effect of replicative ageing of culture cells at 7^{th}, 15^{th} and 26^{th} passages was studied by telomere length assay to determine telomeric DNA loss due to cell divisions. Analysis of telomere length results at different passage numbers revealed that the FRDA cells lost telomeres faster than the controls. These results suggested that dysfunctional telomeres in the FRDA cells, possibly due to oxidative stress, were responsible for the increased rate of telomere attrition [156]. In addition, previous studies have also shown that the FRDA cells were more sensitive to ionising radiation than the control cells, suggesting that FRDA is a DNA repair-deficient disorder [216].

Furthermore, it is possible that genetic changes or recruitment of other proteins at telomeres may alter the heterochromatic state of ALT telomeres, resulting in the repression of telomeric recombination [155].

Finally, to confirm the presence of a telomere dysfunction phenotype in the FRDA cells, the TIF assay was performed. The results demonstrated that the frequency of γ-H2AX foci was significantly higher in the FRDA cells compared to the controls, indicating a higher degree of DNA damage. Similarly, the FRDA cells had greater frequencies of TIFs in comparison to the controls. Therefore, these results suggested that the FRDA cells may have induced telomere dysfunction relative to the control cells.

The results presented in this chapter demonstrated a telomere dysfunction phenotype and accelerated telomere shortening in the FRDA fibroblasts. In addition, the results suggested that intertelomeric recombination was initiated in the FRDA cells but was not capable of maintaining the telomeres and preventing accelerated telomere shortening.

CHAPTER VI

GENERAL DISCUSSION AND CONCLUSIONS

VI GENERAL DISCUSSION AND CONCLUSIONS

FRDA is an autosomal recessive neurodegenerative disorder caused by a reduction in frataxin expression. The reduction in frataxin expression leads to oxidative stress, mitochondrial iron accumulation and consequential cell death with the primary sites of neurons of the dorsal root ganglia and the dentate nucleus of the cerebellum. To recapitulate such features of FRDA disease in the mouse, the Ataxia Research Group at Brunel University established GAA repeat expansion-based *FXN* YAC transgenic mouse models, YG8R and YG22R, containing 190+90 and 190 GAA repeat sequence respectively. A new line, designated YG8sR (YG8R with a small GAA band), line was recently generated from YG8R breeding.

6.1 Determination of Amplification of the *FXN* Gene Using TaqMan Copy Number and Fluorescence *In Situ* Hybridisation Assays

To determine the copy number of the *FXN* transgene in the enhanced GAA repeat expansion-based FRDA mouse lines, a TaqMan qPCR assay was developed. The results indicated that the YG22 and Y47 lines had a single copy of the *FXN* gene, while the YG8 line was shown to have two copies. The YG8s line showed less than one copy of the target gene, indicating deletion of the *FXN* gene. Single integration sites of all transgenes were confirmed by dual colour FISH analysis of metaphase and interphase chromosomes. However, in YG8s, at least 25% of the YG8s cells had no signals, while the remaining cells showed one signal corresponding to the transgenic *FXN* gene. In addition, the analysis of *FXN* exons in YG8s mice by PCR confirmed the presence of all *FXN* exons in this line. These results suggest the incidence of somatic mosaicism in YG8sR cells. Further investigation of the somatic mosaicism in YG8sR mice could be carried out in the future studies using the BAC probes together with mouse centromere- and/or telomeres specific probe to confirm the incidence of mosaicism in this line. In addition, results from the Jackson Laboratory using SNP assay showed that the transgenes are localised on Chr. 16 of the YG8R mouse chromosomes. Accordingly, it would be of particular interest to determine how the *FXN* transgenes in the YG8R line have become distributed at this locus. However, both TaqMan copy number and FISH assays are not capable of providing such information. Therefore, other techniques such as Fibre FISH should be utilised in future investigations to characterise the organisation of FRDA transgenes in different mouse models.

6.2 Functional Studies of FRDA Mouse Models

Subsequently, extended functional analysis was carried out on different groups of mice from 4 to 12 months of age to determine the effect of reduced frataxin level on FRDA-like pathological phenotype and functional deficits. Coordination ability of YG8R, YG8sR and YG22R 'FRDA-like' mice, together with Y47R and C57BL6/J wild-type control mice, was assessed using accelerating rotarod analysis. The results indicated a progressive decrease in the motor coordination ability of YG8R, YG22R and YG8sR mice compared to Y47R or C57BL6/J controls. Locomotor activity was also assessed using an open field beam-breaker, beam-walk, hang wire, grip strength and foot print tests. The results indicated substantial functional deficits in the FRDA mouse models. The body weight analysis of YG22R, YG8R and YG8sR demonstrated an increase in weight compared to C57BL6/J which may be attributed to the observed decreased locomotor activity of the mice. The identified functional deficits in the FRDA mouse models may be due to the reduced levels of frataxin, inducing an FRDA-like phenotype. If so, then these functional tests provide an experimental approach capable of detecting the phenotypic consequences of the reduced level of frataxin in the FRDA mice, making them amenable to novel therapeutic strategies. Another symptom of FRDA disease is susceptibility to diabetes. Consequently, glucose and insulin tolerance tests were performed to determine the prevalence of abnormalities in glucose handling and insulin sensitivity. The glucose tolerance results indicated that the FRDA mice were glucose intolerant and insulin secretion following a glucose injection was delayed. Furthermore, the glucose-lowering effect of exogenous insulin was enhanced in the FRDA mouse models during insulin tolerance test, suggesting insulin hypersensitivity in these lines. These results suggested that mitochondrial dysfunction due to frataxin deficiency in the FRDA mouse models may contribute to pancreatic ß cell dysfunction. Therefore, it would be of particular interest to assess the relative contribution of insulin resistance and ß cell dysfunction or deficiency in genes of the IRS family in the future studies. This may provide a novel treatment strategy for the FRDA patients.

6.3 GAA Repeat Instability and *FXN* Gene and Protein Expression in FRDA Mouse Models

Following comprehensive functional analysis of the FRDA mice, frataxin mRNA and protein levels as well as somatic GAA repeat instability were examined in the FRDA mouse models in order to investigate the correlation between FRDA-like pathological

phenotype and frataxin deficiency. The results revealed GAA repeat somatic instability in the brain, cerebellum and liver of all the FRDA mouse models. However, the pattern and size of the GAA repeats differed between males and females, indicative of gender-specific differences in repeat sizes. Subsequently, frataxin mRNA and protein levels were investigated. Significant reduction in the levels of the *FXN* mRNA and protein in the liver of YG8R and YG22R compared to Y47R was detected. However, in the case of the YG8sR line, a significant decrease in *FXN* mRNA was observed in all the tissues compared to both Y47R human *FXN* and C57BL6/J mouse *Fxn* mRNA. Protein expression levels were also considerably decreased in all the tissues of YG8sR mice compared to Y47R mice. Of all FRDA mouse models studied, the greatest *FXN* reduction was detected in the YG8sR tissues compared to both Y47R human *FXN* and C57BL6/J mouse *Fxn* mRNA. In addition, GAA repeat analysis identified a single GAA repeat band in the YG8sR line with no complexity compared to the other FRDA lines. Therefore, YG8sR can be considered to be the most suitable YAC transgenic GAA repeat-based mouse model for the investigation of potential FRDA therapies.

6.4 Telomere Length Analysis in FRDA Cells

Since oxidative stress is considered to be an important modulator of telomere length and is reported to increase the rate of telomere attrition [156], it was hypothesised that telomere length might be shortened in the FRDA patients. The qPCR telomere length measurements revealed that the human FRDA fibroblast cells had significantly higher telomere length compared to the normal fibroblasts. Similar results were obtained in the mouse FRDA fibroblast cells. However, the results published in a recent study using human FRDA lymphoblast cells indicated significant telomere shortening in these cells [214]. Consequently, telomere length was also examined in the genomic DNA from FRDA lymphocytes in order to investigate such a discrepancy. The results indicated that the mean telomere length was significantly shortened in the FRDA lymphocytes relative to the controls which were in good agreement with the recently published results [214]. Nevertheless, there was a considerable variation in the telomere length of the patients. Therefore, the mean results cannot serve as a reliable biomarker of the FRDA disease as proposed by the authors [214]. The results from the fibroblast and lymphocyte cells revealed that telomere length varies within different cell types. This may be due to the different environmental conditions as the former was derived from *in vitro* culture while the latter was generated from *in vivo* cells. However, an explicit conclusion can only be

drawn provided that a sufficiently large sample size is examined and the fibroblast cells are matched for age. Therefore, larger age matched sample sizes are required to evaluate the reliability and validity of the results presented in this study. In addition, the human FRDA primary fibroblasts were screened for the expression of telomerase activity using the TRAP assay and a quantitative assay for hTERT mRNA expression using TaqMan qRT-PCR to investigate the mechanisms which induce telomere lengthening in these cells. The results indicated that the observed telomere elongation in the FRDA fibroblasts did not involve the telomerase enzyme. Therefore, it was presumed that ALT mechanism may be responsible for the observed telomere elongation and co-localisation of PML bodies with telomeres was investigated in these cells using immunoFISH. The results demonstrated that the FRDA fibroblast cells had significantly higher co-localised PML foci with telomeric DNA compared to the normal fibroblast cells. However, the mean co-localisation of PML and telomeres were more pronounced in U2OS ALT positive control. These results suggested that the ALT mechanism was involved in the FRDA cells but it was not as frequent as the ALT positive cells. Subsequently, the size of co-localised PML bodies with telomeres was examined in the FRDA cells to investigate the effect of cellular stress on aggregation or dispersion of PML bodies. The results did not provide any information regarding assembly or disassembly of PML bodies due to cellular stress. In order to further validate these results, it is of great importance to assess the co-localisation of other PML components such as Sp100 and Daxx with telomeres in the FRDA cells [239]. T-SCE frequencies were also analysed in the human FRDA cell lines. The results exhibited a significant increase in T-SCE levels of the FRDA cell lines relative to the controls, further confirming the existence of ALT mechanism in these cells. To investigate whether the FRDA cells activate ALT during culturing *in vitro* and become immortalised, growth curves and cumulative population doubling analysis were performed. The results showed that the FRDA fibroblast cell cultures underwent growth arrest with higher cumulative population doubling compared to the controls. These results indicated that the FRDA cells were unable to become immortalised by the ALT mechanism alone, suggesting that the frequency of the PML bodies may not have been sufficient to prevent senescence. However, the FRDA cells senesced approximately 11 population doublings later than the controls. This promotion of the transition from proliferation to senescence in the FRDA cells could be due to the difference in the original telomere lengths of these cell lines or the activation of the ALT mechanism by which the mean cell population doubling may have been exceeded. In addition to the

growth behaviour and the number of cells, the state of replicative senescence can also be determined by increased numbers of γ-H2AX DNA repair foci at telomeres as a result of cell-specific stress responses. Therefore, further analysis is required to confirm the senescent phenotype in the fibroblasts cells. Subsequently, the effect of replicative ageing of culture cells at different passages was studied by telomere length assay to determine telomeric DNA loss due to cell divisions. Analysis of telomere length results at different passage numbers indicated that the FRDA cells lost telomeres faster than the controls. These results suggested that dysfunctional telomeres in the FRDA cells, possibly due to oxidative stress, were responsible for the increased rate of telomere attrition. In addition, it has been reported that the FRDA cells are more sensitive to ionising radiation than the control cells, suggesting that FRDA is a DNA repair-deficient disorder [216].

Finally, to confirm the presence of a telomere dysfunction phenotype in the FRDA cells, the TIF assay was performed. The results demonstrated that the frequency of γ-H2AX foci was significantly higher in the FRDA cells compared to the controls, indicating a higher degree of DNA damage. Similarly, the FRDA cells had greater frequencies of TIFs in comparison to the controls. Therefore, these results suggested that the FRDA cells may have induced telomere dysfunction relative to the control cells. In conclusion, the results demonstrated a telomere dysfunction phenotype and accelerated telomere shortening in the FRDA fibroblasts. In addition, the results suggested that intertelomeric recombination was initiated in the FRDA cells but was not capable of maintaining the telomeres and preventing accelerated telomere shortening.

REFERENCES

[1] Greenfield J.G. (1954). "The spino-cerebellar degenerations." Oxford: Blackwell 21-34.

[2] Berciano J., Pascual J. and Polo J.M. (2000). "History of Ataxia Research. Handbook of Ataxia Disorder." Klockgether, T. New York, Marcel Dekker, INC. 77-100.

[3] Pearce J.M. (2004). "Friedreich's ataxia." J Neurol Neurosurg Psychiatry **75**(5): 688.

[4] Harding A.E. (1981). "Friedreich's ataxia: a clinical and genetic study of 90 families with an analysis of early diagnostic criteria and intrafamilial clustering of clinical features." Brain **104**(3): 589–620.

[5] Harding A.E. and Zilkha K.J. (1981). "Pseudo-dominant' inheritance in Friedreich's ataxia." J Med Genet **18**(4): 285-287.

[6] Campuzano V., Montermini L., Molto M. D., *et al.* (1996). "Friedreich's ataxia: autosomal recessive disease caused by an intronic GAA triplet repeat expansion." Science **271**(5254): 1423-1427.

[7] Harding A.E. (1983). "Classification of the hereditary ataxias and paraplegias." Lancet **1**(8334): 1151-1155.

[8] Filla A., De Michele G., Cavalcanti F., *et al.* (1996). "The relationship between trinucleotide (GAA) repeat length and clinical features in Friedreich ataxia." Am J Hum Genet **59**(3): 554-560.

[9] Epplen C., Epplen J. T., Frank G., *et al.* (1997). "Differential stability of the (GAA)n tract in the Friedreich ataxia (STM7) gene." Hum Genet **99**(6): 834-836.

[10] Koeppen A. H. (2011). "Friedreich's ataxia: Pathology, pathogenesis, and molecular genetics." J Neurol Sci **303**(1-2):1-12.

[11] Durr A., Cossee M., Agid Y., *et al.* (1996). "Clinical and genetic abnormalities in patients with Friedreich's ataxia." N Engl J Med **335**(16): 1169-1175.

[12] Geoffroy G., Barbeau A., Breton G., *et al.* (1976). "Clinical description and roentgenologic evaluation of patients with Friedreich's ataxia." Can J Neurol Sci **3**(4): 279-286.

[13] Pandolfo M. (1998). "Molecular genetics and pathogenesis of Friedreich ataxia." Neuromuscul Disord **8**(6): 409-415.

[14] De Michele G., Filla A., Cavalcanti F., *et al.* (1994). "Late onset Friedreich's disease: clinical features and mapping of mutation to the FRDA locus." J Neurol Neurosurg Psychiatry **57**(8): 977-979.

[15] Coppola G., De Michele G., Cavalcanti F., *et al.* (1999). "Why do some Friedreich's ataxia patients retain tendon reflexes? A clinical, neurophysiological and molecular study." J Neurol **246**(5): 353-357.

[16] Wessel K., Schroth G., Diener H. C., *et al.* (1989). "Significance of MRI-confirmed atrophy of the cranial spinal cord in Friedreich's ataxia." Eur Arch Psychiatry Neurol Sci **238**(4): 225-230.

[17] Klockgether T., Petersen D., Grodd W., *et al.* (1991). "Early onset cerebellar ataxia with retained tendon reflexes. Clinical, electrophysiological and MRI observations in comparison with Friedreich's ataxia." Brain **114**(4): 1559-1573.

[18] Wullner U., Klockgether T., Petersen D., *et al.* (1993). "Magnetic resonance imaging in hereditary and idiopathic ataxia." Neurology **43**(2): 318-325.

[19] De Michele G., Di Salle F., Filla A., *et al.* (1995). "Magnetic resonance imaging in "typical" and "late onset" Friedreich's disease and early onset cerebellar ataxia with retained tendon reflexes." J Neurol Sci **16**(5): 303-308.

[20] Lamarche J. B., Lemieux B. and Lieu H. B. (1984). "The neuropathology of "typical" Friedreich's ataxia in Quebec." Can J Neurol Sci **11**(4): 592-600.

[21] Said G., Marion M. H., Selva J., *et al.* (1986). "Hypotrophic and dying-back nerve fibers in Friedreich's ataxia." Neurology **36**(10): 1292-1299.

[22] Wells R. and Ashizawa T. (2006). "Genetic Instabilities and Neurological Diseases." Elsevier 277-290.

[23] Hewer R. L. and Robinson N. (1968). "Diabetes mellitus in Friedreich's ataxia." J Neurol Neurosurg Psychiatry **31**(3): 226-231.

[24] Sanchez-Casis G., Cote M. and Barbeau A. (1976). "Pathology of the heart in Friedreich's ataxia: review of the literature and report of one case." Can J Neurol Sci **3**(4): 349-354.

[25] Lamarche J. B., Cote M. and Lemieux B. (1980). "The cardiomyopathy of Friedreich's ataxia morphological observations in 3 cases." Can J Neurol Sci **7**(4): 389-396.

[26] Chamberlain, S., Shaw, J., Rowland, A., *et al.* (1988). "Mapping of mutation causing Friedreich's ataxia to human chromosome 9." Nature **334**(6179): 248-249.

[27] Fujita R., Agid Y., Trouillas P., *et al.* (1989). "Confirmation of linkage of Friedreich ataxia to chromosome 9 and identification of a new closely linked marker." Genomics **4**(1): 110-111.

[28] Chamberlain S., Farrall M., Shaw J., *et al.* (1993). "Genetic recombination events which position the Friedreich ataxia locus proximal to the D9S15/D9S5 linkage group on chromosome 9q." Am J Hum Genet **52**(1): 99-109.

[29] Delatycki M. B., Williamson R. and Forrest S. M. (2000). "Friedreich ataxia: an overview." J Med Genet **37**(1): 1-8.

[30] Cossee M., Campuzano V., Koutnikova H., *et al.* (1997). "Frataxin fracas." Nat Genet **15**(4): 337-338.

[31] Al-Mahdawi S., Pinto R. M., Varshney D., *et al.* (2006). "GAA repeat expansion mutation mouse models of Friedreich ataxia exhibit oxidative stress leading to progressive neuronal and cardiac pathology." Genomics **88**(5): 580-590.

[32] Montermini L., Richter A., Morgan K., *et al.* (1997). "Phenotypic variability in Friedreich ataxia: Role of the associated GAA triplet repeat expansion." Ann Neurol **41**(5): 675-682.

[33] Bidichandani S. I., Ashizawa T. and Patel P. I. (1998). "The GAA triplet-repeat expansion in Friedreich ataxia interferes with transcription and may be associated with an unusual DNA structure." Am J Hum Genet **62**(1): 111-121.

[34] Sakamato N., Chastain P. D., Parniewski P., *et al*. (1999). "Sticky DNA: Self-association properties of long GAA TTC repeats in RR Y triplex structures from Friedreich's ataxia." Mol Cell **3**(4): 465-475.

[35] Pandolfo M. (1999). "Molecular pathogenesis of Friedreich ataxia." Arch Neurol **56**(10): 1201-1208.

[36] Cossee M., Durr A., Scmitt M., *et al.* (1999). "Friedreich's ataxia: Point mutations and clinical presentations of compound heterozygotes." Ann Neurol **45**(2): 200-206.

[37] Forrest S. M., Knight M., Delatcyki M., *et al.* (1998). "The correlation of clinical phenotype with the site of point mutations in FRDA gene." Neurogenetics **1**(4): 253-257.

[38] Montermini L., Andermann E., Labuda M., *et al.* (1997). "The Friedreich ataxia GAA triplet repeat: premutation and normal alleles." Hum Mol Genet **6**(8): 1261-1266.

[39] Monticelli A., Giacchetti M., De Biase I., *et al.* (2004). "New clues on the origin of the Friedreich ataxia expanded alleles from the analysis of new polymorphisms closely linked to the mutation." Hum Genet **114**(5): 458-463.

[40] Campuzano V., Montermini L., Lutz Y., *et al.* (1997). "Frataxin is reduced in Friedreich ataxia patients and is associated with mitochondrial membranes." Hum Mol Genet **6**(11): 1771-1780.

[41] Clark R. M., De Biase I., Malykhina A. P., *et al.* (2007). "The GAA triplet-repeat is unstable in the context of the human FXN locus and displays age-dependent expansions in cerebellum and DRG in a transgenic mouse model." Hum Genet **120**(5): 633-640.

[42] Puccio H. and Koenig M. (2000). "Recent advances in the molecular pathogenesis of Friedreich ataxia." Hum Mol Genet **9**(6): 887-892.

[43] Koutnikova H., Campuzano V., Foury F., *et al.* (1997). "Studies of human, mouse and yeast homologues indicate a mitochondrial function for frataxin." Nat Genet **16**(4): 345-351.

[44] Wilson R. B. and Roof D. M. (1997). "Respiratory deficiency due to loss of mitochondrial DNA in yeast lacking the frataxin homologue." Nat Genet **16**(4): 352-357.

[45] Babcock M., de Silva D., Oaks R., *et al.* (1997). "Regulation of mitochondrial iron accumulation by Yfh1p, a putative homolog of frataxin." Science **276**(5319): 1709-1712.

[46] Delatcycki M., Camakaris M., Brooks H., *et al.* (1999). "Direct evidence that mitochondrial iron accumulation occurs in Friedreich ataxia." Ann Neurol **45**(5): 673-675.

[47] Rotig A., de Lonlay P., Chretien D., *et al.* (1997). "Aconitase and mitochondrial iron-sulphur protein deficiency in Friedreich ataxia." Nat Genet **17**(2): 215-217.

[48] Bradley J. L., Blake J. C., Chamberlain S., *et al.* (2000). "Clinical, biochemical and molecular genetic correlations in Friedreich's ataxia." Hum Mol Genet **9**(2): 275-282.

[49] Lobmayr L., Brooks D. G. and Wilson R. B. (2005). "Increased IRP1 activity in Friedreich ataxia." Gene **354**: 157-161.

[50] Condo I., Malisan F., Guccini I., *et al.* (2010). "Molecular control of the cytosolic aconitase/IRP1 switch by extramitochondrial frataxin." Hum Mol Genet **19**(7): 1221-1229.

[51] Shan Y. and Cortopassi G. (2012). "HSC20 interacts with frataxin and is involved in iron-sulfur cluster biogenesis and iron homeostasis." Hum Mol Genet **21**(7): 1457-1469.

[52] Rai M., Soragni E., Jenssen K., *et al.* (2008). "HDAC inhibitors correct frataxin deficiency in a Friedreich ataxia mouse model." PLoS One **3**(4): e1958.

[53] Thierbach R., Schulz T. J., Isken F., *et al.* (2005). "Targeted disruption of hepatic frataxin expression causes impaired mitochondrial function, decreased life span and tumor growth in mice." Hum Mol Genet **14**(24): 3857-3864.

[54] Chantrel-Groussard K., Geromel V., Puccio H., *et al.* (2001). "Disabled early recruitment of antioxidant defenses in Friedreich's ataxia." Hum Mol Genet **10**(19): 2061-2067.

[55] Alper G. and Narayanan V. (2003). "Friedreich's ataxia." Pediatr Neurol **28**(5): 335-341.

[56] Branda S. S., Yang Z. Y., Chew A., *et al.* (1999). "Mitochondrial intermediate peptidase and the yeast frataxin homolog together maintain mitochondrial iron homeostasis in Saccharomyces cerevisiae." Hum Mol Genet **8**(6): 1099-1110.

[57] Gordon D. M., Shi Q., Dancis A., *et al.* (1999). "Maturation of frataxin within mammalian and yeast mitochondria: one-step processing by matrix processing peptidase." Hum Mol Genet **8**(12): 2255-2262.

[58] Cavadini P., Adamec J., Taroni F., *et al.* (2000). "Two-step processing of human frataxin by mitochondrial processing peptidase. Precursor and intermediate forms are cleaved at different rates." J Biol Chem **275**(52): 41469-41475.

[59] Condo I., Ventura N., Malisan F., *et al.* (2007). "In vivo maturation of human frataxin." Hum Mol Genet **16**(13): 1534-1540.

[60] Dhe-Paganon S., Shigeta R., Chi Y. I., *et al.* (2000). "Crystal structure of human frataxin." J Biol Chem **275**(40): 30753-30756.

[61] Musco G., Stier G., Kolmerer B., *et al.* (2000). "Towards a structural understanding of Friedreich's ataxia: the solution structure of frataxin." Structure **8**(7): 695-707.

[62] Cho S. J., Lee M. G., Yang J. K., *et al.* (2000). "Crystal structure of Escherichia coli CyaY protein reveals a previously unidentified fold for the evolutionarily conserved frataxin family." Proc Natl Acad Sci **97**(16): 8932-8937.

[63] Bidichandani S. I., Ashizawa T. and Patel P. I. (1997). "Atypical Friedreich ataxia caused by compound heterozygosity for a novel missense mutation and the GAA triplet-repeat expansion." Am J Hum Genet **60**(5): 1251-1256.

[64] Bartolo C., Mendell J. R. and Prior T.W. (1998). "Identification of a missense mutation in a Friedreich's ataxia patient: implications for diagnosis and carrier studies." Am J Med Genet **79**(5): 396-399.

[65] Labuda M., Poirier J. and Pandolfo M. (1999). "A missense mutation (W155R) in an American patient with Friedreich ataxia." Hum Mut **13**: 506-507.

[66] Yariv J., Kalb A. J., Helliwell J. R., *et al.* (1988). "Chemical and Mossbauer spectroscopic evidence that iron-containing concanavalin A is a ferritin." J Biol Chem **263**(27): 13508-13510.

[67] Al-Mahdawi S., Pinto R. M., Ismail O., *et al.* (2008). "The Friedreich ataxia GAA repeat expansion mutation induces comparable epigenetic changes in human and transgenic mouse brain and heart tissues." Hum Mol Genet **17**(5): 735-746.

[68] Toth G., Gaspari Z. and Jurka J. (2000). "Microsatellites in different eukaryotic genomes: survey and analysis." Genome Res **10**(7): 967-981.

[69] Cummings C. J. and Zoghbi H. Y. (2000). "Fourteen and counting: unraveling trinucleotide repeat diseases." Hum Mol Genet **9**(6): 909-916.

[70] Jasinska A. J., Kozlowski P. and Krzyzosiak W. J. (2008). "Expression characteristics of triplet repeat-containing RNAs and triplet repeat-interacting proteins in human tissues." Acta Biochim Pol **55**(1): 1-8.

[71] Kunst C. B. and Warren S. T. (1994). "Cryptic and polar variation of the fragile X repeat could result in predisposing normal alleles." Cell **77**: 853–861.

[72] Kang S., Jaworski A., Ohshima K., *et al.* (1995). "Expansion and deletion of CTG repeats from human disease genes are determined by the direction of replication in E. coli." Nat Genet **10**(2): 213-218.

[73] Freudenreich C. H., Stavenhagen J. B. and Zakian V. A. (1997). "Stability of a CTG/CAG trinucleotide repeat in yeast is dependent on its orientation in the genome." Mol Cell Biol **17**(4): 2090-2098.

[74] Bambara R. A., Murante R. S. and Henricksen L. A. (1997). "Enzymes and reactions at the eukaryotic DNA replication fork." J Biol Chem **272**(8): 4647-4650.

[75] Waga S. and Stillman B. (1998). "The DNA replication fork in eukaryotic cells." Annu Rev Biochem **67**: 721-751.

[76] Trinh T. Q. and Sinden R. R. (1991). "Preferential DNA secondary structure mutagenesis in the lagging strand of replication in E coli." Nature **352**(6335): 544-547.

[77] Mirkin S. M. (2007). "Expandable DNA repeats and human disease." Nature **447**(7147): 932-40.

[78] Mitas M., Yu A., Dill J., *et al.* (1995). "Hairpin properties of single-stranded DNA containing a GC-rich triplet repeat $(CTG)_{15}$." Nucleic Acids Res **23**(6): 1050-1059.

[79] Chen X., Mariappan S. V., Catasti P., *et al.* (1995). "Hairpins are formed by the single DNA strands of the fragile X triplet repeats: structure and biological implications." Proc Natl Acad Sci **92**(11): 5199-5203.

[80] Nadel Y., Weisman-Shomer P. and Fry M. (1995). "The fragile X syndrome single strand $d(CGG)_n$ nucleotide repeats readily fold back to form unimolecular hairpin structures." J Biol Chem **270**(48): 28970-28977.

[81] Usdin K. (1998). "NGG-triplet repeats form similar intrastrand structures: implications for the triplet expansion diseases." Nucleic Acids Res **26**(17): 4078-4085.

[82] Veaute X. and Fuchs R. P. P. (1993). "Greater susceptibility to mutations in lagging strand of DNA replication in Escherichia coli than in leading strand." Science **261**(5121): 598-600.

[83] Tishkoff D. X., Filosi N., Gaida G. M., *et al.* (1997). "A novel mutation avoidance mechanism dependent on S. cerevisiae RAD27 is distinct from DNA mismatch repair." Cell **88**(2): 253-263.

[84] Gordenin D. A., Kunkel T. A., Resnick M. A., *et al.* (1997). "Repeat expansion -all in a flap?" Nat Genet **16**(2): 116-118.

[85] Schweitzer J. K. and Livingston D. M. (1998). "Expansions of CAG repeat tracts are frequent in a yeast mutant defective in Okazaki fragment maturation." Human Mol Genet **7**(1): 69-74.

[86] Spiro C., Pelletier R., Rolfsmeier M. L., *et al.* (1999). "Inhibition of FEN- 1 processing by DNA secondary structure at trinucleotide repeats." Mol Cell **4**(6): 1079-1085.

[87] White P. J., Borts R. H. and Hirst M. C. (1999). "Stability of the human fragile X (CGG)(n) triplet repeat array in Saccharomyces cerevisiae deficient in aspects of DNA metabolism." Mol Cell Biol **19**(8): 5675-5684.

[88] Moore H., Greenwell P. W., Liu C. P., *et al.* (1999). "TD Triplet repeats form secondary structures that escape DNA repair in yeast." Proc Natl Acad Sci **96**(4): 1504-1509.

[89] Henricksen L. A., Tom S., Liu Y., *et al.* (2000). "Inhibition of flap endonuclease 1 by flap secondary structure and relevance to repeat sequence expansion." J Biol Chem **257**(22): 16420-16427.

[90] Gacy A. M., Goellner G. M., Juranic N., *et al.* (1995). "Trinucleotide repeats that expand in human disease form hairpin structures in vitro." Cell **81**(4): 533-540.

[91] Leproust, E. M., Pearson C. E., Sinden R. R., *et al.* (2000). "Unexpected formation of parallel duplex in GAA and TTC trinucleotide repeats of Friedreich's ataxia." J Mol Biol **302**(5): 1063-1080.

[92] Suen I. S., Rhodes J. N., Christy M., *et al.* (1999). "Structural properties of Friedreich's ataxia d(GAA) repeats." Biochim Biophys Acta **1444**(1): 14-24.

[93] Gacy A. M., Goellner G. M., Spiro C., *et al.* (1998). "GAA instability in Friedreich's Ataxia shares a common, DNA-directed and intraallelic mechanism with other trinucleotide diseases." Mol Cell **1**(4): 583-593.

[94] Sakamoto N., Chastain P., Parniewski P., *et al.* (1999). "Sticky DNA: self-association properties of long GAA.TTC repeats in R.R.Y triplex structures from Friedreich's ataxia." Mol Cell **3**(4): 465-475.

[95] Schmucker S. and Puccio H. (2010). "Understanding the molecular mechanisms of Friedreich's ataxia to develop therapeutic approaches." Hum Mol Genet **19**(R1): R103-110.

[96] Gottesfeld J. M. (2007). "Small molecules affecting transcription in Friedreich ataxia." Pharmacol Ther **116**(2): 236-248.

[97] Saveliev A., Everett C., Sharpe T., *et al.* (2003). "DNA triplet repeats mediate heterochromatin-protein-1-sensitive variegated gene silencing." Nature **422**(6934): 909-913.

[98] Elgin S. C. and Grewal S. I. (2003). "Heterochromatin: silence is golden." Curr Biol **13**(23): R895-898.

[99] Aguilera A. and Go´mez-Gonza´lez B. (2008). "Genome instability: a mechanistic view of its causes and consequences." Nat Rev Genet **9**(3): 204-217.

[100] Hahn M., Dambacher S. and Schotta G. (2010). "Heterochromatin dysregulation in human diseases." J Appl Physiol **109**(1): 232-42.

[101] Reddy K., Tam M., Bowater R. P., *et al.* (2011). "Determinants of R-loop formation at convergent bidirectionally transcribed trinucleotide repeats." Nucleic Acids Res 39(5): 1749-1762.

[102] Lin Y., Dent S. Y., Wilson J. H., *et al.* (2010). "R loops stimulate genetic instability of CTG.CAG repeats." Proc Natl Acad Sci USA 107(2): 692-697.

[103] Al-Mahdawi S., Pinto R. M., Ruddle P., *et al.* (2004). "GAA repeat instability in Friedreich ataxia YAC transgenic mice." Genomics **84**(2): 301-310.

[104] Bidichandani S. I., Purandare S. M., Taylor E. E., *et al.* (1999). "Somatic sequence variation at the Friedreich ataxia locus includes complete contraction of the expanded GAA triplet repeat, significant length variation in serially passaged lymphoblasts and enhanced mutagenesis in the flanking sequence." Hum Mol Genet **8**(13): 2425-2436.

[105] Sharma R., Bhatti S., Gomez M., *et al.* (2002). "The GAA triplet-repeat sequence in Friedreich ataxia shows a high level of somatic instability in vivo, with a significant predilection for large contractions." Hum Mol Genet **11**(18): 2175-2187.

[106] Miranda C. J., Santos M. M., Ohshima K., *et al.* (2002). "Frataxin knockin mouse." FEBS Lett **512**(1-3): 291-297.

[107] Parniewski P. and Staczek P. (2002). "Molecular mechanisms of TRS instability." Adv Exp Med Biol **516**: 1-25.

[108] Cleary J. D., Nichol K., Wang Y. H., *et al.* (2002). "Evidence of cisacting factors in replication-mediated trinucleotide repeat instability in primate cells." Nat Genet **31**(1): 37-46.

[109] Libby R. T., Monckton D. G., Fu Y. H., *et al.* (2003). "Genomic context drives SCA7 CAG repeat instability, while expressed SCA7 cDNAs are intergenerationally and somatically stable in transgenic mice." Hum Mol Genet **12**(1): 41-50.

[110] Lia, A. S., Seznec H., Hofmann-Radvanyi H., *et al.* (1998). "Somatic instability of the CTG repeat in mice transgenic for the myotonic dystrophy region is age dependent but not correlated to the relative intertissue transcription levels and proliferative capacities." Hum Mol Genet **7**(8): 1285-12891.

[111] Di Prospero N. A. and Fischbeck K. H. (2005). "Therapeutics development for triplet repeat expansion diseases." Nat Rev Genet **6**(10): 756-765.

[112] Cooper J. M. and Schapira A. H. (2007). "Friedreich's ataxia: coenzyme Q10 and vitamin E therapy." Mitochondrion **7 Suppl**: S127-135.

[113] Kelso G. F., Porteous C. M., Coulter C. V., *et al.* (2001). "Selective targeting of a redox-active ubiquinone to mitochondria within cells: antioxidant and antiapoptotic properties." J Biol Chem **276**(7): 4588- 4596.

[114] Jauslin M. L., Meier T., Smith R. A., *et al.* (2003). "Mitochondria-targeted antioxidants protect Friedreich Ataxia fibroblasts from endogenous oxidative stress more effectively than untargeted antioxidants." FASEB J **17**(13): 1972-1974.

[115] Lodi R., Hart P. E., Rajagopalan B., *et al.* (2001). "Antioxidant treatment improves in vivo cardiac and skeletal muscle bioenergetics in patients with Friedreich's ataxia." Ann Neurol 49(5): 590-596.

[116] Rustin P., Rötig A., Munnich A., *et al.* (2002). "Heart hypertrophy and function are improved by idebenone in Friedreich's ataxia." Free Radic Res **36**(4): 467-9.

[117] Lynch D. R., Perlman S. L. and Meier T. (2010). "A phase 3, double-blind, placebo- controlled trial of idebenone in Friedreich ataxia." Arch Neurol **67**(8): 941-947.

[118] Lynch D. R., Willi S. M., Wilson R. B., *et al.* (2012). "A0001 in Friedreich ataxia: Biochemical characterization and effects in a clinical trial." Mov Disord **27**(8):1026-1033.

[119] Enns G. M., Kinsman S. L., Perlman S. L., *et al.* (2012). "Initial experience in the treatment of inherited mitochondrial disease with EPI-743." Mol Genet Metab **105**(1): 91-102.

[120] Richardson D. R. (2003). "Friedreich's ataxia: iron chelators that target the mitochondrion as a therapeutic strategy?" Expert Opin Invest Drugs **12**(2): 235-245.

[121] Sturm B., Stupphann D., Kaun C., *et al.* (2005). "Recombinant human erythropoietin: effects on frataxin expression in vitro." Eur J Clin Invest **35**(11): 711-717.

[122] Napoli E., Morin D., Bernhardt R., *et al.* (2007). "Hemin rescues adrenodoxin, heme a and cytochrome oxidase activity in frataxin-deficient oligodendroglioma cells." Biochim Biophys Acta **1772**(7): 773-780.

[123] Goncalves S., Paupe V., Dassa E. P., *et al.* (2008). "Deferiprone targets aconitase: implication for Friedreich's ataxia treatment." BMC Neurol **8**: 20.

[124] Puccio H. and Koenig M. (2000). "Recent advances in the molecular pathogenesis of Friedreich ataxia." Hum Mol Genet **9**(6): 887-892.

[125] Fleming J., Spinoulas A., Zheng M., *et al.* (2005). "Partial correction of sensitivity to oxidant stress in Friedreich ataxia patient fibroblasts by frataxin-encoding adeno-associated virus and lentivirus vectors." Hum Gene Ther **16**(8): 947- 956.

[126] Grabczyk E. and Usdin K. (2000). "The GAA*TTC triplet repeat expanded in Friedreich's ataxia impedes transcription elongation by T7 RNA polymerase in a length and supercoil dependent manner." Nucleic Acids Res **28**(14): 2815-2822.

[127] Grabczyk E., and Usdin K. (2000). "Alleviating transcript insufficiency caused by Friedreich's ataxia triplet repeats." Nucleic Acids Res **28**(24): 4930- 4937.

[128] Dervan P. B. and Edelson B. S. (2003). "Recognition of the DNA minor groove by pyrrole-imidazole polyamides." Curr Opin Struct Biol **13**(3): 284-299.

[129] Burnett R., Melander C., Puckett J. W., *et al.* (2006). "DNA sequence-specific polyamides alleviate transcription inhibition associated with long GAA.TTC repeats in Friedreich's ataxia." Proc Natl Acad Sci **103**(31): 11497-11502.

[130] Langley B., Gensert J. M., Beal M. F., *et al.* (2005). "Remodeling chromatin and stress resistance in the central nervous system: histone deacetylase inhibitors as novel and broadly effective neuroprotective agents." Curr Drug Targets CNS Neurol Disord **4**(1): 41-50.

[131] Festenstein R. (2006). "Breaking the silence in Friedreich's ataxia." Nat Chem Biol **2**(10): 512-513.

[132] Herman D., Jenssen K., Burnett R., *et al.* (2006). "Histone deacetylase inhibitors reverse gene silencing in Friedreich's ataxia." Nat Chem Biol **2**(10): 551-558.

[133] Biacsi R., Kumari D. and Usdin K. (2008). "SIRT1 inhibition alleviates gene silencing in Fragile X mental retardation syndrome." PLoS Genet **4**(3): e1000017.

[134] Bedalov A., Gatbonton T., Irvine W. P., *et al.* (2001). "Identification of a small molecule inhibitor of Sir2p." Proc Natl Acad Sci U S A **98**(26): 15113-15118.

[135] Chan P. K., Torres R., Yandim C., *et al.* (2013). "Heterochromatinization induced by GAA-repeat hyperexpansion in Friedreich's ataxia can be reduced upon HDAC inhibition by vitamin B3." Hum Mol Genet **22**(13): 2662-2675.

[136] Chiurazzi P., Pomponi M. G., Pietrobono R., *et al.* (1999). "Synergistic effect of histone hyperacetylation and DNA demethylation in the reactivation of the FMR1 gene." Hum Mol Genet **8**(12): 2317-2323.

[137] Hebert M. D. and Whittom A. A. (2007). "Gene-based approaches toward Friedreich ataxia therapeutics." Cell Mol Life Sci **64**(23): 3034-43.

[138] Cossee M., Puccio H., Gansmuller A., *et al.* (2000). "Inactivation of the Friedreich ataxia mouse gene leads to early embryonic lethality without iron accumulation." Hum Mol Genet **9**(8): 1219-1226.

[139] Puccio H., Simon D., Cossee M., *et al.* (2001). "Mouse models for Friedreich ataxia exhibit cardiomyopathy, sensory nerve defect and Fe-S enzyme deficiency followed by intramitochondrial iron deposits." Nat Genet **27**(2): 181-186.

[140] Seznec H., Lia-Baldini A. S., Duros C., *et al.* (2000). "Transgenic mice carrying large human genomic sequences with expanded CTG repeat mimic closely the DM CTG repeat intergenerational and somatic instability." Hum Mol Genet **9**(8): 1185-1194.

[141] Wheeler V. C., Auerbach W., White J. K., *et al.* (1999). "Length-dependent gametic CAG repeat instability in the Huntington's disease knock-in mouse." Hum Mol Genet **8**(1): 115-122.

[142] Shelbourne P. F., Killeen N., Hevner R. F., *et al.* (1999). "A Huntington's disease CAG expansion at the murine Hdh locus is unstable and associated with behavioural abnormalities in mice." Hum Mol Genet **8**(5): 763-774.

[143] Peier A. M. and Nelson D. L. (2002). "Instability of a premutation-sized CGG repeat in FMR1 YAC transgenic mice." Genomics **80**(4): 423-432.

[144] Monckton D. G., Coolbaugh M. I., Ashizawa K. T., *et al.* (1997). "Hypermutable myotonic dystrophy CTG repeats in transgenic mice." Nat Genet **15**(2): 193-196.

[145] Watase K., Venken K. J., Sun Y., *et al.* (2003). "Regional differences of somatic CAG repeat instability do not account for selective neuronal vulnerability in a knock-in mouse model of SCA1." Hum Mol Genet **12**(21): 2789-2795.

[146] Lorenzetti D., Watase K., Xu B., *et al.* (2000). "Repeat instability and motor incoordination in mice with a targeted expanded CAG repeat in the Sca1 locus." Hum Mol Genet **9**(5): 779-785.

[147] Ishiguro H., Yamada K., Sawada H., *et al.* (2001). "Age-dependent and tissue-specific CAG repeat instability occurs in mouse knock-in for a mutant Huntington's disease gene." J Neurosci Res **65**(4): 289-297.

[148] Bontekoe C. J., Bakker C. E., Nieuwenhuizen I. M., *et al.* (2001). "Instability of a (CGG)98 repeat in the Fmr1 promoter." Hum Mol Genet **10**(16): 1693-1699.

[149] Pook M. A., Al-Mahdawi S., Carroll C. J., *et al.* (2001). "Rescue of the Friedreich's ataxia knockout mouse by human YAC transgenesis." Neurogenetics **3**(4): 185-193.

[150] Cemal C. K., Huxley C. and Chamberlain S. (1999). "Insertion of expanded CAG trinucleotide repeat motifs into a yeast artificial chromosome containing the human Machado– Joseph disease gene." Gene **236**(1): 53-61.

[151] Riha K., Heacock M. L. and Shippen D. E. (2006). "The role of the nonhomologous end-joining DNA double-strand break repair pathway in telomere biology." Ann Rev Genet **40**: 237-277.

[152] Meier A., Fiegler H., Munoz P., *et al.* (2007). "Spreading of mammalian DNA-damage response factors studied by ChIP-chip at damaged telomeres." EMBO J **26**(11): 2707-2718.

[153] Olovnikov A. M. (1971). "Principle of marginotomy in template synthesis of Polynucleotides." Dokl Akad nauk SSSR **201**(6): 1496-1499.

[154] Watson J. D. (1972). "Origin of concatemeric T7 DNA." Nat New Biol **239**(94): 197-201.

[155] Conomos D., Pickett H. A. and Reddel R. R. (2013). "Alternative lengthening of telomeres: remodelling the telomere architecture." Front Oncol **3**: 27.

[156] von Zglinicki T. (2002). "Oxidative stress shortens telomeres." Trends Biochem Sci **27**(7): 339-344.

[157] Lansdorp P. M. (2005). "Major cutbacks at chromosome ends." Trends Biochem Sci **30**(7): 388-395.

[158] de Lange T., Shiue L., Myers R. M., *et al.* (1990). "Structure and variability of human chromosome ends." Mol Cell Biol **10**(2): 518-527.

[159] Starling J. A., Maule J., Hastie N. D., *et al.* (1990). "Extensive telomere repeat arrays in mouse are hypervariable." Nucleic Acids Res **18**(23): 6881-688.

[160] Klobutcher L. A., Swanton M. T., Donini P., *et al.* (1981). "All genesized DNA molecules in four species of hypotrichs have the same terminal sequence and an unusual 3' terminus." Proc Natl Acad Sci **78**(5): 3015-3019.

[161] Wellinger R. J., Wolf A. J. and Zakian V. A. (1993). "Saccharomyces telomeres acquire single strand TG1-3 tails late in S phase." Cell **72**(1): 51-60.

[162] Riha K., McKnight T. D., Fajkus J., *et al.* (2000). "Analysis of the G-overhang structures on plant telomeres: evidence for two distinct telomere architectures." Plant J **23**(5): 633-641.

[163] Makarov V. L., Hirose Y. and Langmore J. P. (1997). "Long G tails at both ends of human chromosomes suggest a C strand degradation mechanism for telomere shortening." Cell **88**(5): 657-666.

[164] Wright W. E., Tesmer V. M., Huffman K. E., *et al.* (1997). "Normal human chromosomes have long G-rich telomeric overhangs at one end." Genes Dev **11**(21): 2801-2809.

[165] Chai W., Sfeir A. J., Hoshiyama H., *et al.* (2006). "The involvement of the Mre11/Rad50/Nbs1 complex in the generation of Goverhangs at human telomeres." EMBO Rep **7**(2): 225-230.

[166] Price C.M. (1997). "Synthesis of the telomeric C-strand. A review." Biochemistry (Mosc) 62**(11)**: 1216-1223.

[167] Munoz-Jordan J. L., Cross G. A., de Lange T., *et al.* (2001). "T-loops at trypanosome telomeres." EMBO J **20**(3): 579-588.

[168] Hohensinner P. J., Goronzy J. J. and Weyand C. M. (2011). "Telomere dysfunction, autoimmunity and aging." Aging Dis **2**(6): 524-537.

[169] Cesare A. J., Quinney N., Willcox S., *et al.* (2003). "Telomere looping in P. sativum (common garden pea)." Plant J **36**(2): 271-279.

[170] Tomaska L., Willcox S., Slezakova J., *et al.* (2004). "Taz1 binding to a fission yeast model telomere: formation of telomeric loops and higher order structures." J Biol Chem **279**(49): 50764-50772.

[171] Wei C. and Price M. (2003). "Protecting the terminus: t-loops and telomere end-binding proteins." Cell Mol Life Sci **60**(11): 2283-2294.

[172] de Lange T. (2005). "Shelterin: the protein complex that shapes and safeguards human telomeres." Genes Dev **19**(18): 2100-2110.

[173] Wai L. K. (2004). "Telomeres, telomerase, and tumorigenesis--a review." MedGenMed **6**(3): 19.

[174] Hayflick L. (1965). "The limited in vitro lifetime of human diploid cell strains." Exp Cell Res **37**(3): 614-636.

[175] Wright W. E. and Shay J. W. (2000). "Telomere dynamics in cancer progression and prevention: Fundamental differences in human and mouse telomere biology." Nat Med **6**(8): 849-851.

[176] Youngren K., Jeanclos E., Aviv H., *et al.* (1998). "Synchrony in telomere length of the human fetus." Hum Genet **102**(6):640-643.

[177] Vaziri H., Dragowska W., Allsopp R. C., *et al.* (1994). "Evidence for a mitotic clock in human hematopoietic stem cells: loss of telomeric DNA with age." Proc Natl Acad Sci **91**(21): 9857-9860.

[178] Graakjaer J., Bischoff C., Korsholm L., *et al.* (2003). "The pattern of chromosome-specific variations in telomere length in humans is determined by inherited, telomerenear factors and is maintained throughout life." Mech Ageing Dev **124**(5): 629-640.

[179] Graakjaer J., Pascoe L., Der-Sarkissian H., *et al.* (2004). "The relative lengths of individual telomeres are defined in the zygote and strictly maintained during life." Aging Cell **3**(3): 97-102.

[180] Greider C. W. (1996). "Telomere length regulation." Annu Rev Biochem **65**: 337-365.

[181] Allsopp R. C., Vaziri H., Patterson C., *et al.* (1992). "Telomere length predicts replicative capacity of human fibroblasts." Proc Natl Acad Sci **89**(21): 10114-10118.

[182] Lustig A. J. (2003). "Clues to catastrophic telomere loss in mammals from yeast telomere rapid deletion." Nat Rev Genet **4**(11): 916-923.

[183] Thomson J. A., Itskovitz-Eldor J., Shapiro S. S., *et al.* (1998). "Embryonic stem cell lines derived from human blastocysts." Science **282**(5395): 1145-1147.

[184] Ingram D. A., Mead L. E., Tanaka H., *et al.* (2004). "Identification of a novel hierarchy of endothelial progenitor cells using human peripheral and umbilical cord blood." Blood **104**(9): 2752-2760.

[185] Autexier C. and Lue N. F. (2006). "The structure and function of telomerase reverse transcriptase." Ann Rev Biochem **75**: 493-517.

[186] Cohen S. B., Graham M. E., Lovrecz G. O., *et al.* (2007). "Protein composition of catalytically active human telomerase from immortal cells." Science **315**(5820: 1850-1853.

[187] Legassie J. D. and Jarstfer M. B. (2006). "The unmasking of telomerase." Structure **14**(11): 1603-1609.

[188] Mason P. J., Wilson D. B. and Bessler M. (2005). "Dyskeratosis congenita—A disease of dysfunctional telomere maintenance." Curr Mol Med **5**(2): 159-170.

[189] Feng J., Funk W. D., Wang S. S., *et al.* (1995). "The RNA component of human telomerase." Science **269**(5228): 1236-1241.

[190] Smogorzewska A. and de Lange T. (2004). "Regulation of telomerase by telomeric proteins." Ann Rev Biochem **73**: 177-208.

[191] Liu Y., Snow B. E., Hande M. P., *et al.* (2000). "The telomerase reverse transcriptase is limiting and necessary for telomerase function in vivo." Curr Biol **10**(22): 1459-1462.

[192] Yuan X., Ishibashi S., Hatakeyama S., *et al.* (1999). "Presence of telomeric G-strand tails in the telomerase catalytic subunit TERT knockout mice." Genes Cells **4**(10): 563-572.

[193] Allsopp R. C., Morin G. B., DePinho R., *et al.* (2003). "Telomerase is required to slow telomere shortening and extend replicative lifespan of HSCs during serial transplantation." Blood **102**(2): 517-520.

[194] Fitzgerald M. S., McKnight T. D. and Shippen D. E. (1996). "Characterization and developmental patterns of telomerase expression in plants." Proc Natl Acad Sci **93**(25): 14422-14427.

[195] Lee M. S. and Blackburn E. H. (1993). "Sequence-specific DNA primer effects on telomerase polymerization activity." Mol Cell Biol **13**(10): 6586-6599.

[196] Bryan T. M. and Reddel R. R. (1997). "Telomere dynamics and telomerase activity in in vitro immortalised human cells." Eur J Cancer **33**(5): 767-73.

[197] Hande M. P., Samper E., Lansdorp P., *et al.* (1999). "Telomere length dynamics and chromosomal instability in cells derived from telomerase null mice." J Cell Biol **144**(4): 589-601.

[198] Royle N. J., Foxon J., Jeyapalan J. N., *et al.* (2008). "Telomere length maintenance--an ALTernative mechanism." Cytogenet Genome Res **122**(3-4): 281-291.

[199] Bryan T. M., Englezou A., Gupta J., *et al.* (1995). "Telomere elongation in immortal human cells without detectable telomerase activity." EMBO J **14**(17): 4240-4248.

[200] Henson J. D., Neumann A. A., Yeager T. R., *et al.* (2002). "Alternative lengthening of telomeres in mammalian cells." Oncogene **21**(4): 598-610.

[201] Jeyapalan J. N., Mendez-Bermudez A., Zaffaroni N., *et al.* (2008). "Evidence for alternative lengthening of telomeres in liposarcomas in the absence of ALT-associated PML bodies." Int J Cancer **122**(11): 2414-2421.

[202] Cesare A.J. and Reddel R.R. (2010). "Alternative lengthening of telomeres: models, mechanisms and implications." Nat Rev Genet **11**(5): 319-330.

[203] Fasching C.L., Neumann A.A., Muntoni A., *et al.* (2007). "DNA damage induces alternative lengthening of telomeres (ALT) associated promyelocytic leukemia bodies that preferentially associate with linear telomeric DNA." Cancer Res **67**(15):7072–7077.

[204] Henson J. D., Neumann A. A., Yeager T. R., *et al.* (2002). "Alternative lengthening of telomeres in mammalian cells." Oncogene **21**(4): 598-610.

[205] Ching R. W., Dellaire G., Eskiw C. H., *et al.* (2005). "PML bodies: a meeting place for genomic loci?" J Cell Sci **118**(5):847-854.

[206] Johnson R. D. and Jasin M. (2000). "Sister chromatid gene conversion is a prominent double-strand break repair pathway in mammalian cells." EMBO J **19**(13): 3398-3407.

[207] Petersen S., Saretzki G. and Von Zglinicki T. (1998). "Preferential accumulation of single-stranded regions in telomeres of human fibroblasts." Exp Cell Res **239**(1): 152-160.

[208] Muntoni A. and Reddel R.R. (2005). "The first molecular details of ALT in human tumor cells." Hum Mol Genet **14**: 191-196.

[209] Blagoev K. B. and Goodwin E. H. (2008). "Telomere exchange and asymmetric segregation of chromosomes can account for the unlimited proliferative potential of ALT cell populations." DNA Repair (Amst) **7**(2): 199-204.

[210] Shay J. W. and Wright W. E. (2001). "Aging. When do telomeres matter?" Science **291**(5505): 839-840.

[211] Shay J. W. and Wright W. E. (2001). "Telomeres and telomerase: implications for cancer and aging." Radiat Res **155**(1 pt 2):188-193.

[212] Shin J. S., Hong A., Solomon M. J., *et al.* (2006). "The role of telomeres and telomerase in the pathology of human cancer and aging." Pathology **38**(2): 103-113.

[213] Cai Z., Yan L. J. and Ratka A. (2013). "Telomere shortening and Alzheimer's disease." Neuromolecular Med **15**(1):25-48.

[214] Castaldo I., Vergara P., Castaldo I., *et al.* (2012). "Can Telomere Shortening in Human Peripheral Blood Leukocytes Serve as a Disease Biomarker of Friedreich's Ataxia?" Antioxid Redox Signal **18**(11):1303-1306.

[215] Cnop M., Igoillo-Esteve M., Rai M., *et al.* (2012). "Central role and mechanisms of β-cell dysfunction and death in friedreich ataxia-associated diabetes." Ann Neurol **72**(6):971-82.

[216] Chamberlain S. and Lewis P. D. (1982). "Studies of cellular hypersensitivity to ionising radiation in Friedreich's ataxia." J Neurol Neurosurg Psychiat **45**(12): 1136-1138.

[217] Hastings P. J., Lupski J. R., Rosenberg S. M., *et al.* (2009). "Mechanisms of change in gene copy number." Nat Rev Genet **10**(8):551-564.

[218] Henrichsen C. N., Chaignat E. and Reymond A. (2009). "Copy number variants, diseases and gene expression." Hum Mol Genet **18**(R1): R1-R8.

[219] Stankiewicz P. and Lupski J. R. (2010). "Structural variation in the human genome and its role in disease." Annu Rev Med **61**: 437-455.

[220] Wang K., Li M., Hadley D., *et al.* (2007). "PennCNV: An integrated hidden Markov model designed for high-resolution copy number variation detection in whole-genome SNP genotyping data." Genome Res **17**(11): 1665-1674.

[221] Xie C. and Tammi M. T. (2009). "CNV-seq, a new method to detect copy number variation using high-throughput sequencing." BMC Bioinformatics **10**: 80.

[222] Applied Biosystems (2010). "TaqMan Copy Number Assays Protocol, accessed February 2011
URL<http://www.invitrogen.com/search/global/searchAction.action?query=taqman+copy+number+protocol&resultsPerPage=15&show_seproductcategorynavigator=true&show_productcategorynavigator=true&show_taxonomynavigator=true&show_brandnavigator=true&show_sedocumenttypenavigator=true&mode=and&navigator=sedocumenttypenavigator&modifier=Manuals+%26+Protocols."

[223] Gomes-Pereira M. and Monckton D. G. (2004). "Mouse tissue culture models of unstable triplet repeats." Methods Mol Biol **277**: 215-227.

[224] Sarsero J. P., Li L., Wardan H., *et al.* (2003). "Upregulation of expression from the FRDA genomic locus for the therapy of Friedreich ataxia." J Gene Med **5**(1): 72-81.

[225] Montermini L., Rodius F., Pianese L., *et al.* (1995). "The Friedreich ataxia critical region spans a 150-kb interval on chromosome 9q13." Am J Hum Genet **57**(5): 1061-1067.

[226] Mowery-Rushton P. A., Hanchett J. M., Zipf W. B., *et al.* (1996). "Identification of mosaicism in Prader-Willi syndrome using fluorescent in situ hybridization." Am J Med Genet **66**(4): 403-412.

[227] Korenberg J. R., Chen X. N., Devon K. L., *et al.* (1999). "Mouse molecular cytogenetic resource: 157 BACs link the chromosomal and genetic maps." Genome Res **9**(5): 514-523.

[228] Koehler K. E., Millie E. A., Cherry J. P., *et al.* (2004). "Meiotic exchange and segregation in female mice heterozygous for paracentric inversions." Genetics **166**(3): 1199-1214.

[229] Ristow M., Mulder H., Pomplun D., *et al.* (2003). "Frataxin deficiency in pancreatic islets causes diabetes due to loss of beta cell mass." J Clin Invest **112**(4): 527-534.

[230] Mollá B., Bolinches-Amorós A., Riveiro R., *et al.* (2012). "Molecular and cellular changes in spinal nerve roots support dying-back axonopathy as a primary defect in Friedreich's ataxia pathophysiology." Ataxia Research Conference, London Stansted Airport, UK.

[231] Blackburn E. H. (2000). "Telomere states and cell fates." Nature **408**(6808): 53-56.

[232] Olovnikov A. M. (1973). "A theory of marginotomy. The incomplete copying of template margin in enzymic synthesis of polynucleotides and biological significance of the phenomenon." J Theor Biol **41**(1): 181-190.

[233] Wellinger R. J., Ethier K., Labrecque P., *et al.* (1996). "Evidence for a new step in telomere maintenance." Cell **85**(3): 423-433.

[234] d'Adda di Fagagna F., Reaper P. M., Clay-Farrace L., *et al.* (2003). "A DNA damage checkpoint response in telomere-initiated senescence." Nature **426**(6963): 194-198.

[235] O'Callaghan N. J. and Fenech M. (2011). "A quantitative PCR method for measuring absolute telomere length." Biol Proced Online, 13:3.

[236] McIlrath J., Bouffler S. D., Samper E., *et al.* (2001). "Telomere length abnormalities in mammalian radiosensitive cells." Cancer Res **61**(3): 912-915.

[237] Meyerson M., Counter C. M., Eaton E. N., *et al.* (1997). "hEST2, the putative human telomerase catalytic subunit gene, is up-regulated in tumour cells and during immortalization." Cell **90**(4): 785-795.

[238] Valérie Lallemand-Breitenbach and Hugues de Thé (2010). "PML Nuclear Bodies." Cold Spring Harb Perspect Biol **2**(5): a000661.

[239] Jiang W. Q., Zhong Z. H., Henson J. D., *et al.* (2005). "Suppression of alternative lengthening of telomeres by Sp100-mediated sequestration of the MRE11/RAD50/NBS1 complex." Mol Cell Biol **25**(7): 2708-2721.

APPENDIX

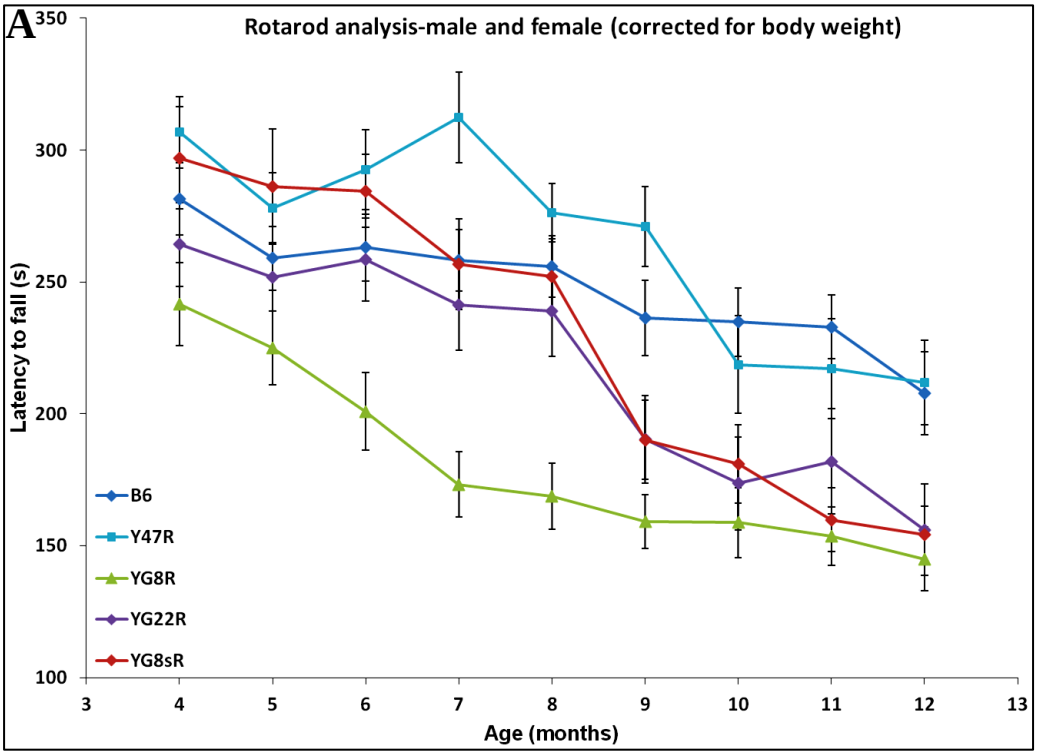
A
Rotarod analysis-male and female (corrected for body weight)
Latency to fall (s)
350
300
250
200
150
100
3
4
5
6
7
8
9
10
11
12
13
Age (months)
B6
Y47R
YG8R
YG22R
YG8sR

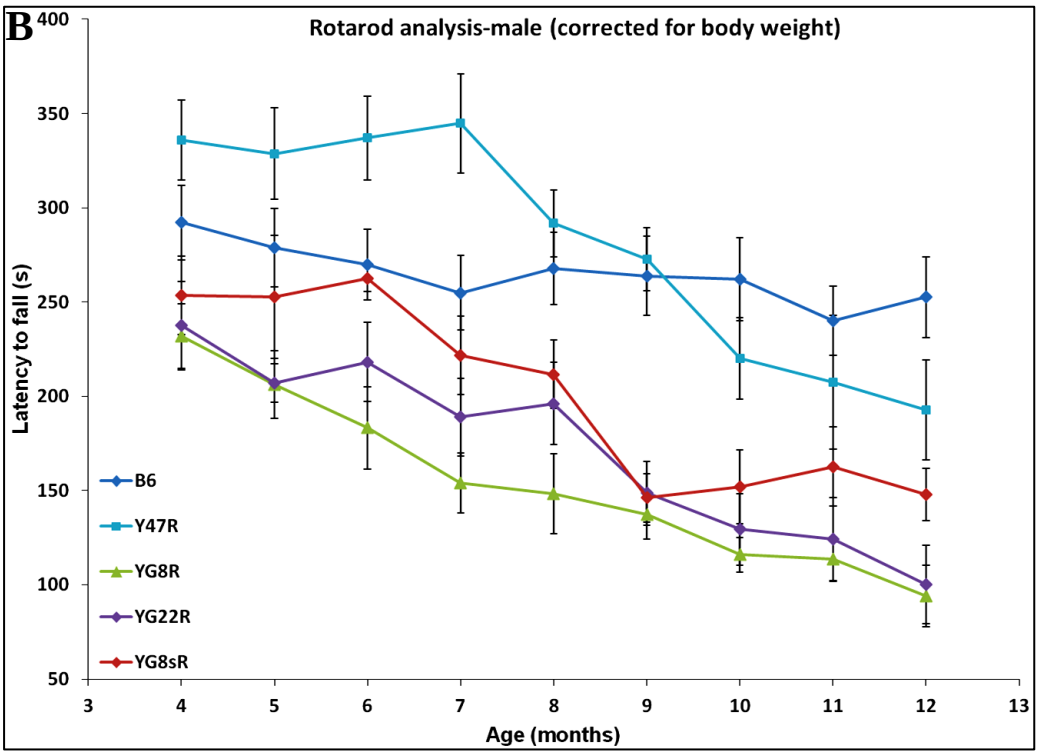
B
Rotarod analysis-male (corrected for body weight)
Latency to fall (s)
400
350
300
250
200
150
100
50
3
4
5
6
7
8
9
10
11
12
13
Age (months)
B6
Y47R
YG8R
YG22R
YG8sR

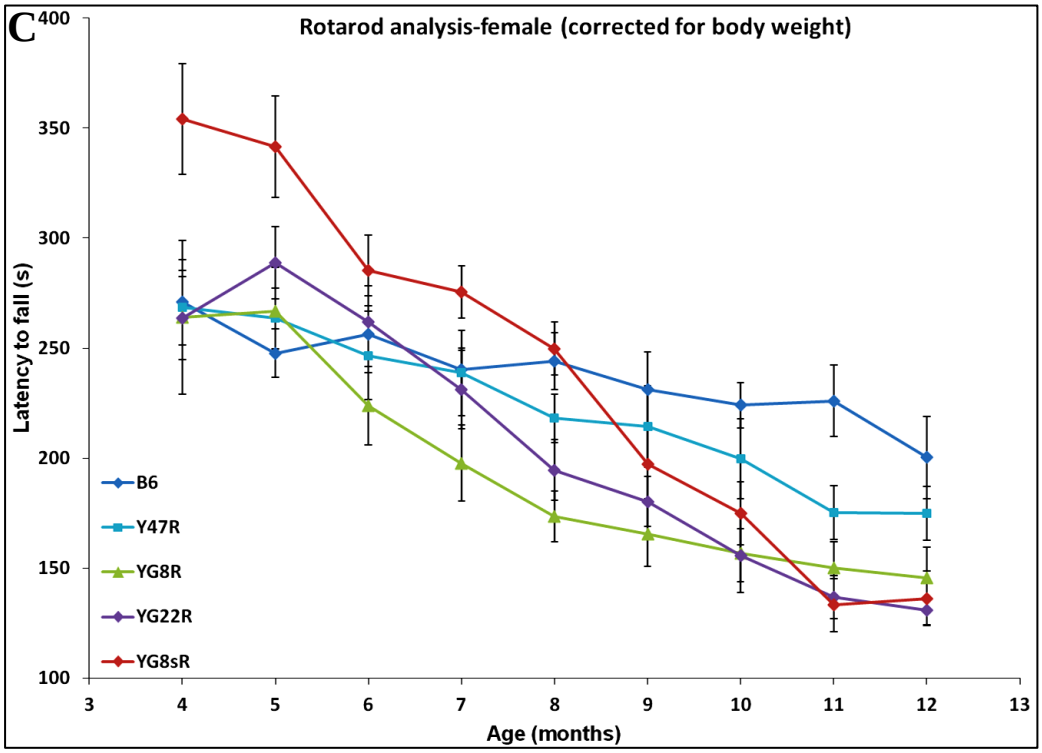

Fig. S.1 Rotarod performance of mice (corrected for body weight). **A)** Rotarod analysis of YG22R, YG8R and YG8sR compared to B6 and Y47R controls shows a coordination deficit in all three rescue mice (*n*=10 mice per genotype) when both male and female values were taken together. Analysis of **B)** males and **C)** females separately (*n*=5 mice per genotype). Error bars indicate SEM and values represent mean ± SEM.

Table S.1 Two-way ANOVA analysis of rotarod performance (corrected for body weight) in FRDA mice

Mouse	Genotype	Gender	Versus B6	Versus B6 (Male & Female)	Versus Y47R	Versus Y47R (Male & Female)
YG22R	FRDA YG22 Rescue	Male	P=2.22E-21	P=0.0007	P=1.08E-20	P=9.7E-08
		Female	P=0.092		P=0.006	
YG8R	FRDA YG8 Rescue	Male	P=3.1E-24	P=2.94E-24	P=4.76E-23	P=1.02E-30
		Female	P=8.22E-05		P=0.005	
YG8sR	FRDA YG8 Small Rescue	Male	P=0.021	P=3.28E-05	P=0.769	P=0.081
		Female	P=3.84E-11		P=5.84E-14	

Table S.2 Student's *t* test analysis of rotarod performance (corrected for body weight) in FRDA mice from 4 to 12 months

Mouse	Male and Female	4m	5m	6m	7m	8m	9m	10m	11m	12m
YG22R	Vs B6	0.41	0.24	0.81	0.72	0.41	0.05	0.006	0.03	0.03
	Vs Y47R	0.04	0.15	0.12	0.004	0.96	0.0005	0.08	0.55	0.02
YG8R	Vs B6	0.000395	0.75	0.001	0.0009	2.23E-06	7.58E-05	0.0001	7.29E-06	0.002
	Vs Y47R	3.47E-06	0.007	3.78E-05	7.94E-09	0.0002	5.04E-08	0.01	0.04	0.001
YG8sR	Vs B6	0.51	0.03	0.25	0.28	0.83	0.04	0.008	6.45E-05	0.006
	Vs Y47R	0.62	0.63	0.61	0.027	0.37	0.0003	0.09	0.09	0.003

Mouse	Male	4m	5m	6m	7m	8m	9m	10m	11m	12m
YG22R	Vs B6	0.08	0.04	0.07	0.02	0.01	1.02E-05	1.43E-06	0.0002	9.8E-06
	Vs Y47R	0.003	9.83E-05	0.0003	4.27E-05	0.04	3.46E-07	0.009	0.15	0.009
YG8R	Vs B6	0.02	0.08	0.004	0.0003	0.0001	8.48E-05	2.95E-06	0.002	0.0001
	Vs Y47R	0.0004	0.0002	1.59E-05	6.76E-07	0.0006	2.38E-06	0.02	0.46	0.05
YG8sR	Vs B6	0.18	0.97	0.71	0.24	0.19	3.64E-05	0.0007	0.009	0.0002
	Vs Y47R	0.008	0.07	0.003	0.0008	0.37	8.21E-07	0.42	0.63	0.14

Mouse	Female	4m	5m	6m	7m	8m	9m	10m	11m	12m
YG22R	Vs B6	0.46	7.85E-05	0.19	0.05	0.47	0.76	0.23	0.09	0.86
	Vs Y47R	0.38	0.002	0.033	0.44	0.07	0.82	0.50	0.42	0.42
YG8R	Vs B6	0.01	0.03	0.20	0.49	0.0002	0.08	0.51	0.0006	0.73
	Vs Y47R	0.01	0.30	0.75	0.12	0.54	0.03	0.83	0.61	0.29
YG8sR	Vs B6	0.01	0.0001	0.23	0.001	0.74	0.84	0.08	6.29E-05	0.24
	Vs Y47R	0.01	0.001	0.03	0.11	0.001	0.48	0.28	0.16	0.03

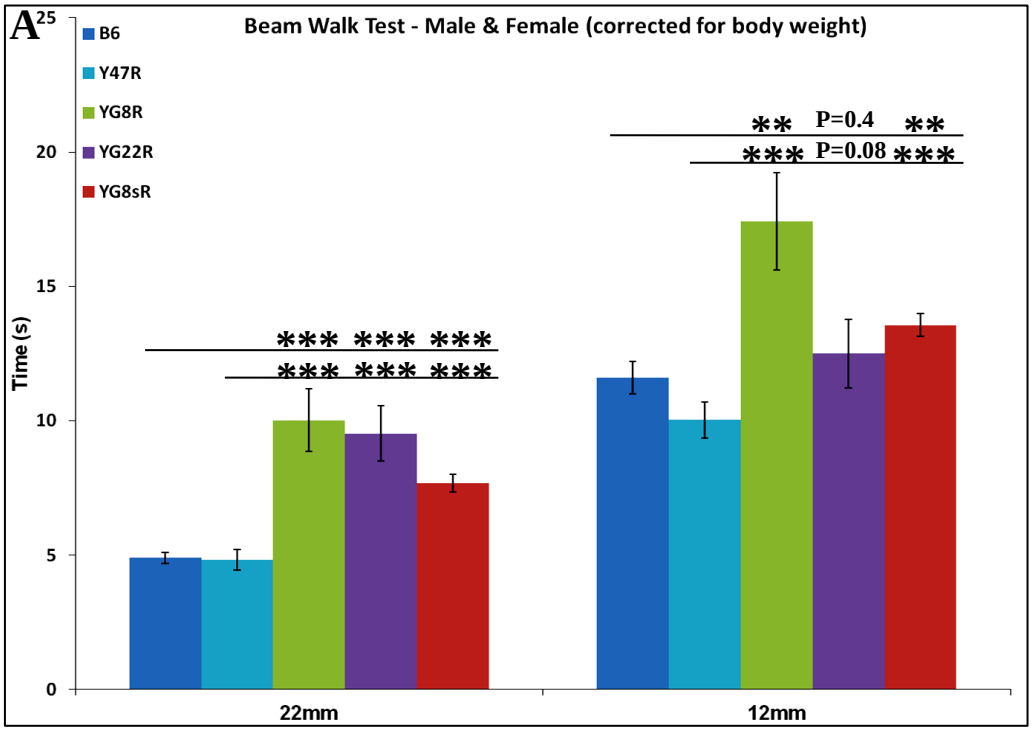
A
Beam Walk Test - Male & Female (corrected for body weight)
B6
Y47R
YG8R
YG22R
YG8sR
Time (s)
25
20
15
10
5
0
** P=0.4 **
*** P=0.08 ***
*** *** ***
*** *** ***
22mm
12mm

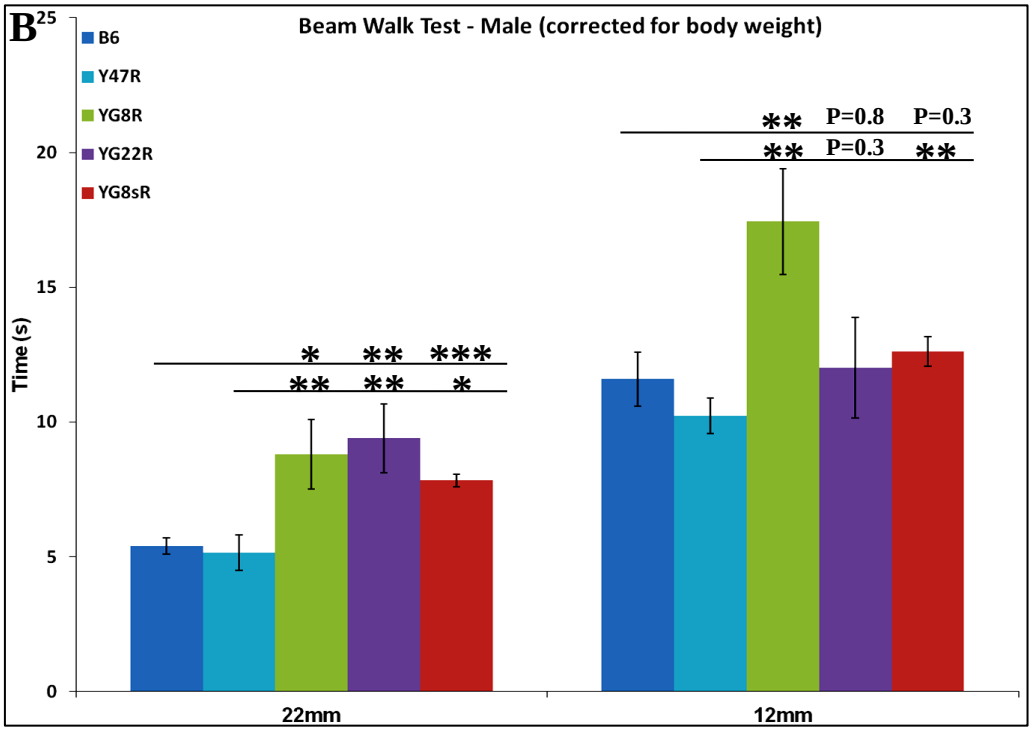
B
Beam Walk Test - Male (corrected for body weight)
B6
Y47R
YG8R
YG22R
YG8sR
Time (s)
25
20
15
10
5
0
** P=0.8 P=0.3
** P=0.3 **
* ** ***
** ** *
22mm
12mm

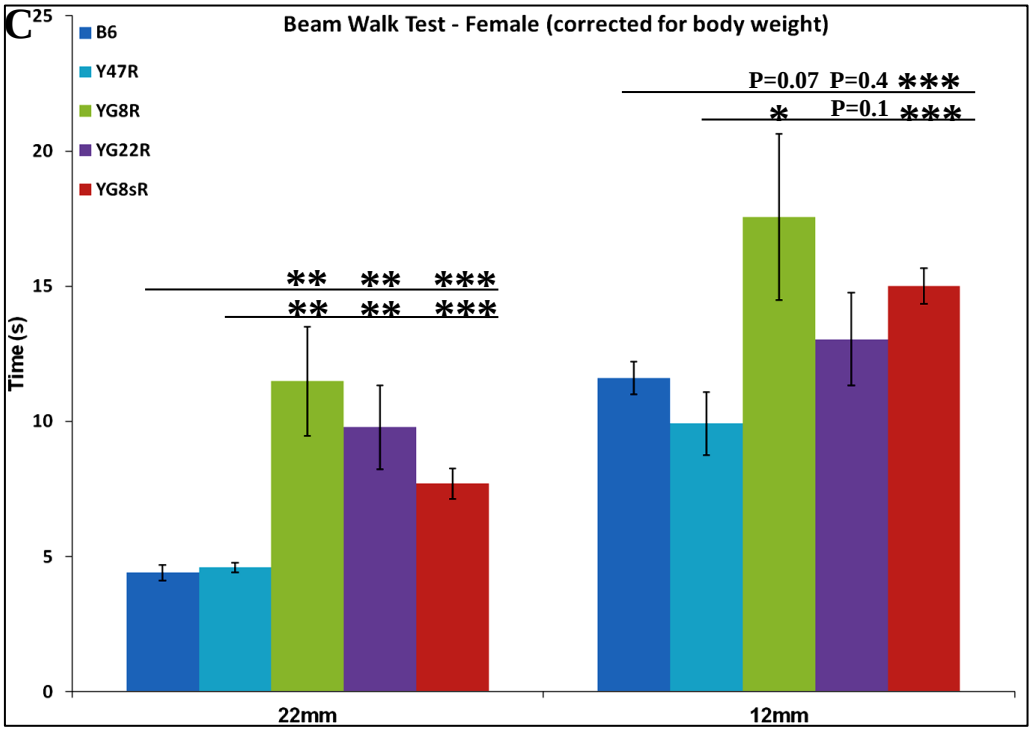

Fig. S.2 Beam-walk analysis of mice (corrected for body weight). **A)** Body weight corrected beam-walk analysis of YG8R, YG22R and YG8sR FRDA mice compared with B6 and Y47R controls (*n*=10 mice per genotype) when both male and female values were taken together. **B)** Analysis of male and **C)** female littermates (*n*=5 mice per genotype). Error bars indicate SEM and values represent mean ± SEM. Asterisks indicate significant differences between mutant and control mice (*P<0.05, **P<0.01 and ***P<0.001). Statistical differences between mutant and B6 control mice are indicated by the top line drawn over the bars while the bottom line indicates the differences between mutant and Y47R control mice.

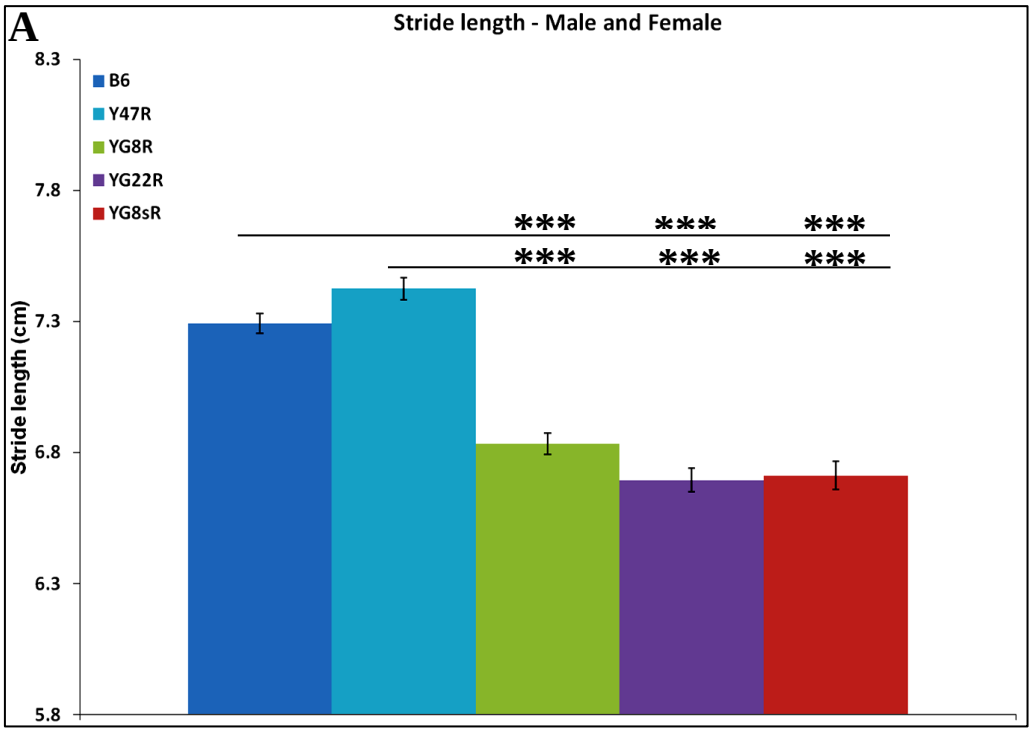

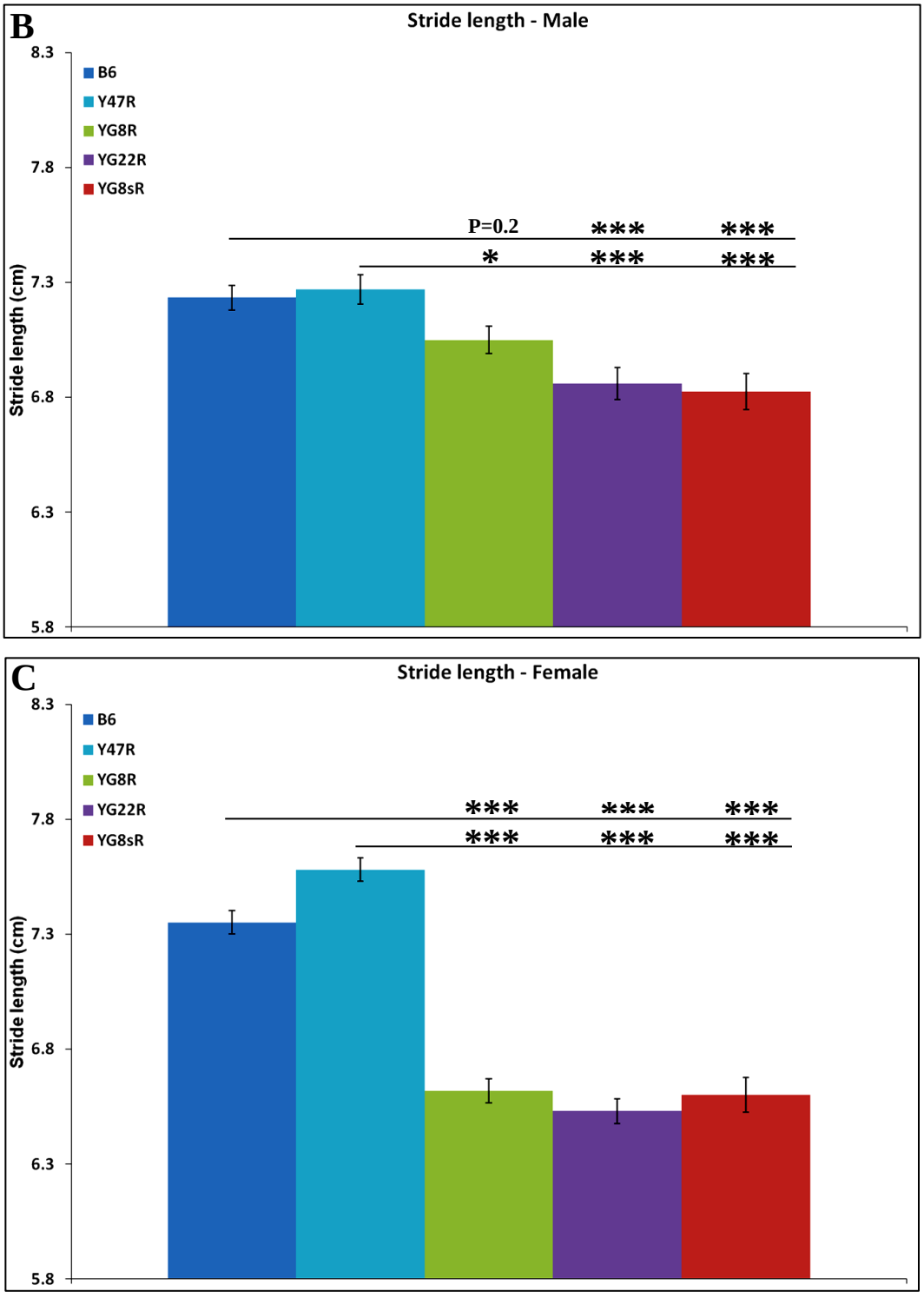

Fig. S.3 Stride length (average of left and right hindlimb; and left and right forelimb) analysis of mice. **A)** Analysis of YG8R, YG22R and YG8sR mice revealed significantly reduced stride length compared to B6 and Y47R controls when both male and female values were taken together (*n*=10 mice per genotype). Analysis of **B)** males and **C)** females separately (*n*=5 mice per genotype). Error bars indicate SEM and values represent mean ± SEM. Asterisks indicate significant differences between mutant and control mice (*P<0.05, **P<0.01 and ***P<0.001). Statistical differences between mutant and B6 control mice are indicated by the top line drawn over the bars while the bottom line indicates the differences between mutant and Y47R control mice.

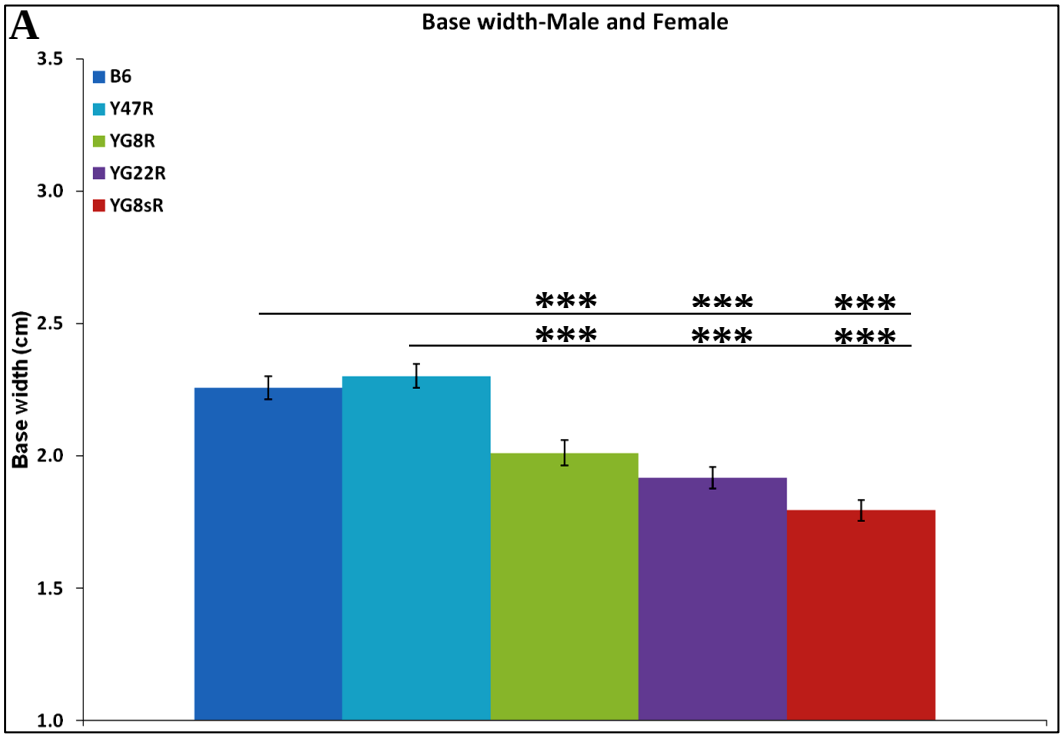
A
Base width-Male and Female
B6
Y47R
YG8R
YG22R
YG8sR
Base width (cm)
3.5
3.0
2.5
2.0
1.5
1.0
***
***
***
***
***
***

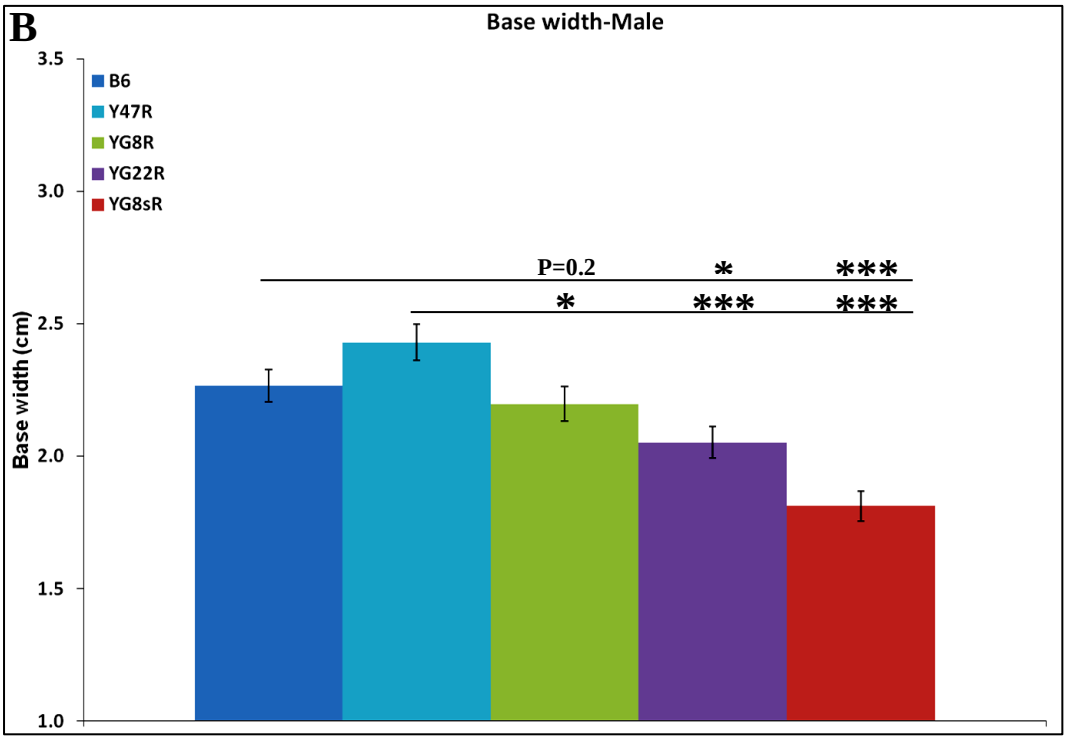
B
Base width-Male
B6
Y47R
YG8R
YG22R
YG8sR
Base width (cm)
3.5
3.0
2.5
2.0
1.5
1.0
P=0.2
*
***
*
***
***

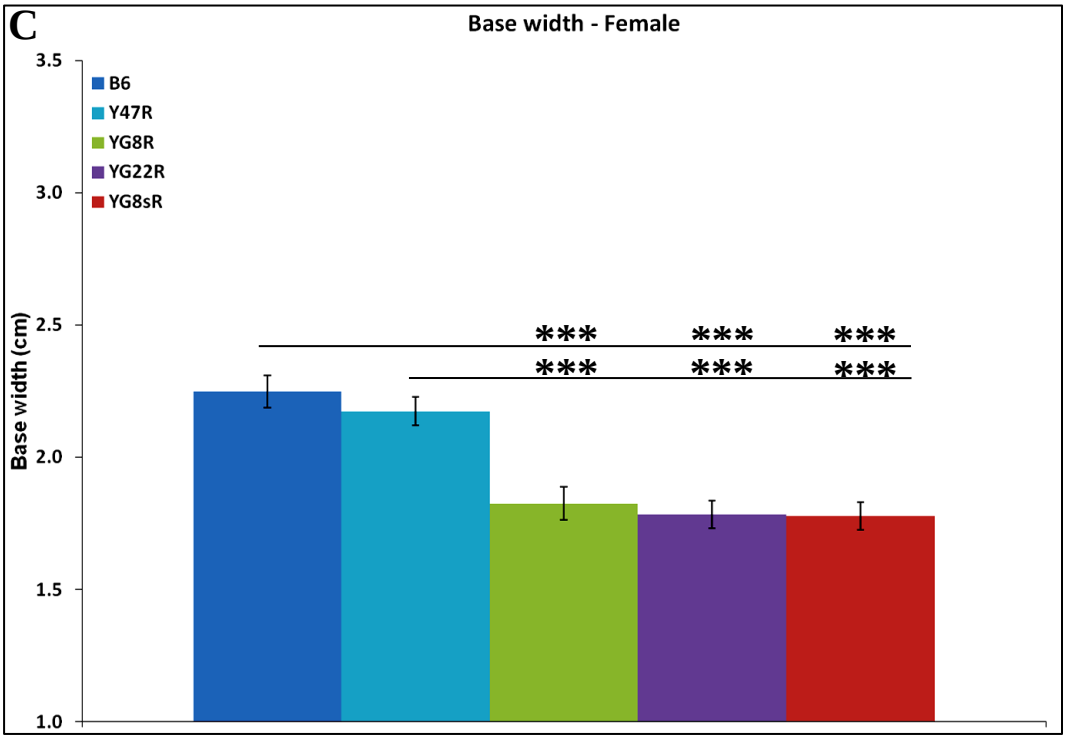

Fig. S.4 Base width (average of fore and hind base width) analysis of mice. **A)** Analysis of YG8R, YG22R and YG8sR mice revealed significantly shorter base width compared to B6 and Y47R controls when both male and female values were taken together (*n*=10 mice per genotype). Analysis of **B)** males and **C)** females separately (*n*=5 mice per genotype) revealed a significant decrease in base width of all mutant mice compared to controls. Error bars indicate SEM and values represent mean ± SEM. Asterisks indicate significant differences between mutant and control mice (*P<0.05, **P<0.01 and ***P<0.001). Statistical differences between mutant and B6 control mice are indicated by the top line drawn over the bars while the bottom line indicates the differences between mutant and Y47R control mice.

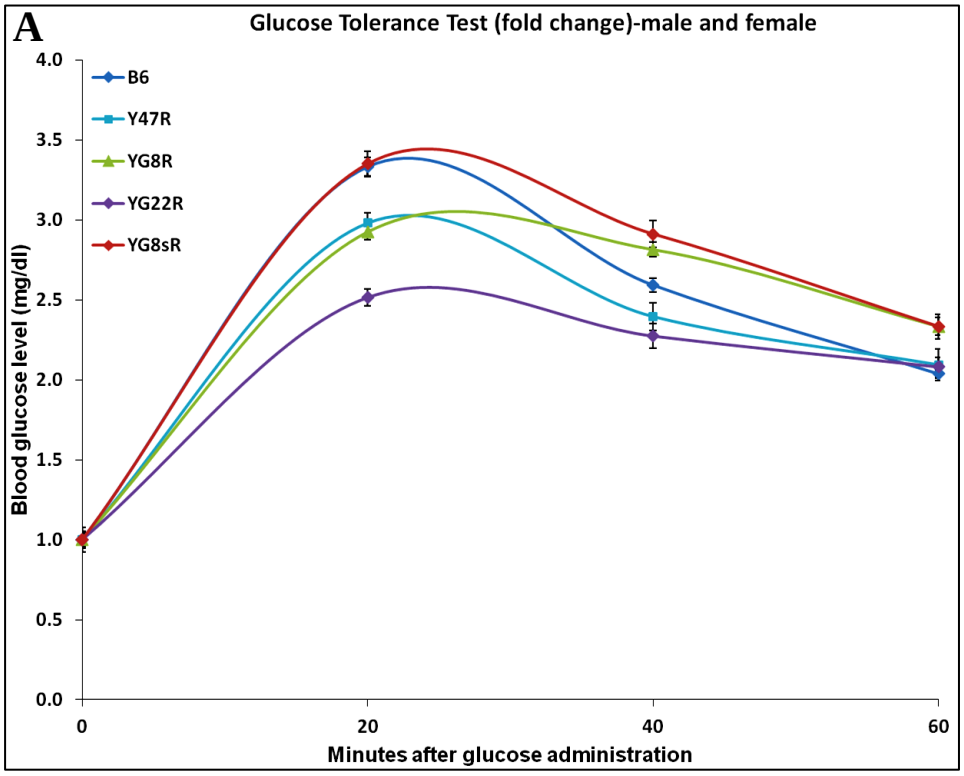
A
Glucose Tolerance Test (fold change)-male and female
B6
Y47R
YG8R
YG22R
YG8sR
Blood glucose level (mg/dl)
4.0
3.5
3.0
2.5
2.0
1.5
1.0
0.5
0.0
0
20
40
60
Minutes after glucose administration

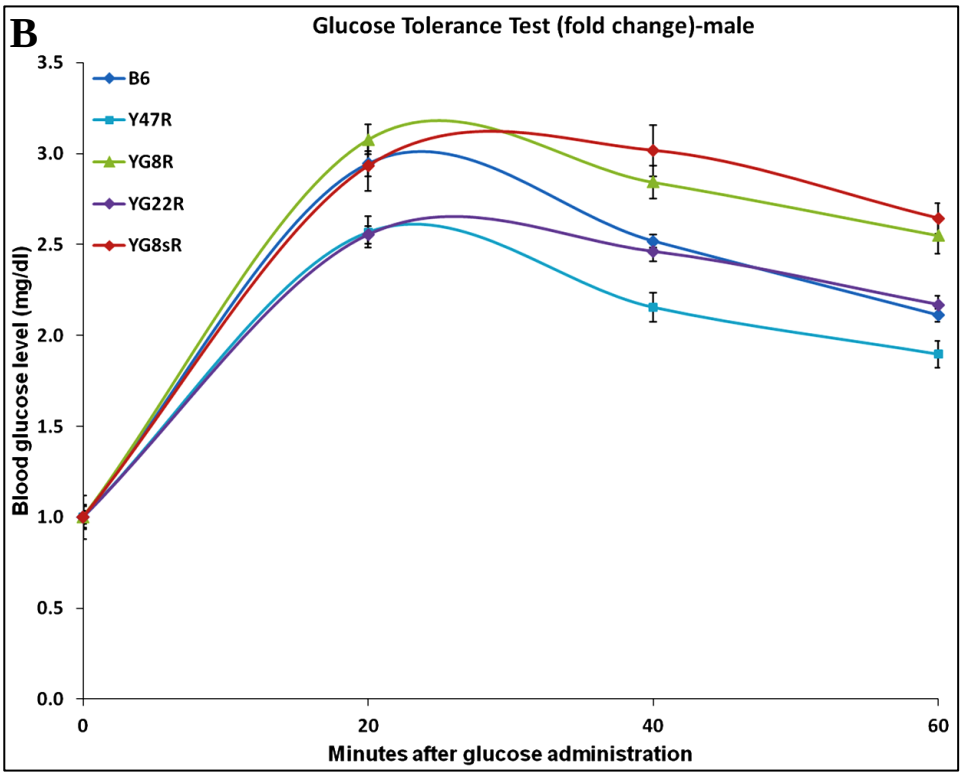
B
Glucose Tolerance Test (fold change)-male
B6
Y47R
YG8R
YG22R
YG8sR
Blood glucose level (mg/dl)
3.5
3.0
2.5
2.0
1.5
1.0
0.5
0.0
0
20
40
60
Minutes after glucose administration

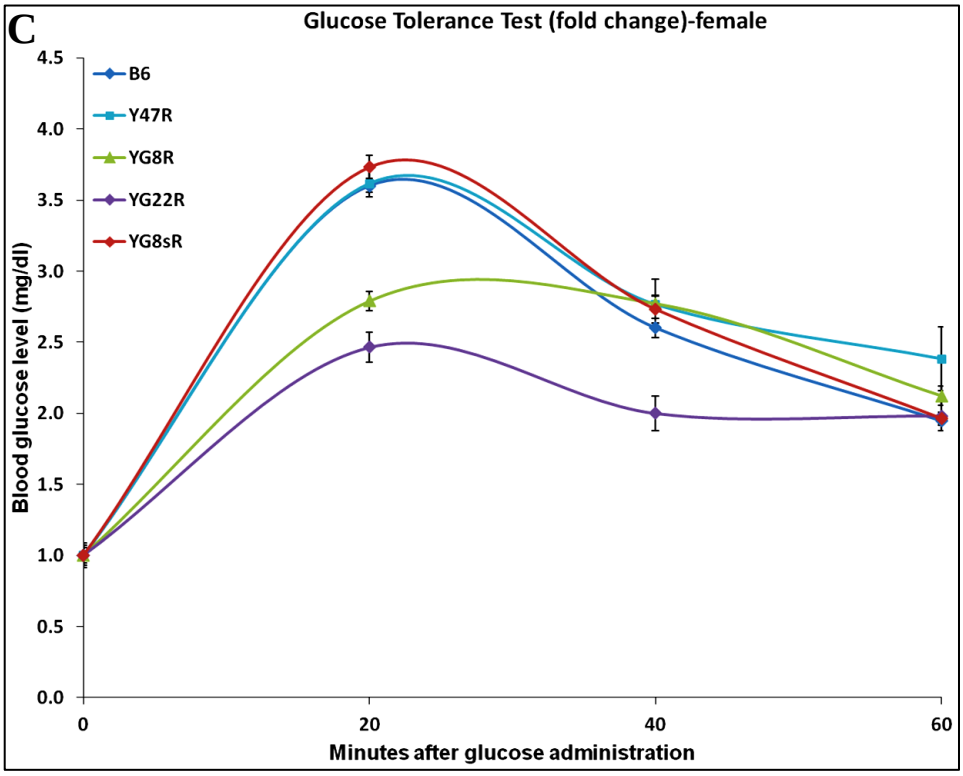

Fig. S.5 Fold change analysis of glucose tolerance test in mice. **A)** Glucose concentration in YG8R, YG22R and YG8sR mice compared to B6 and Y47R controls when both male and female values were taken together (*n*=10 mice per genotype). Analysis of **B)** males and **C)** females separately (*n*=5 mice per genotype). Error bars indicate SEM and values represent mean ± SEM.

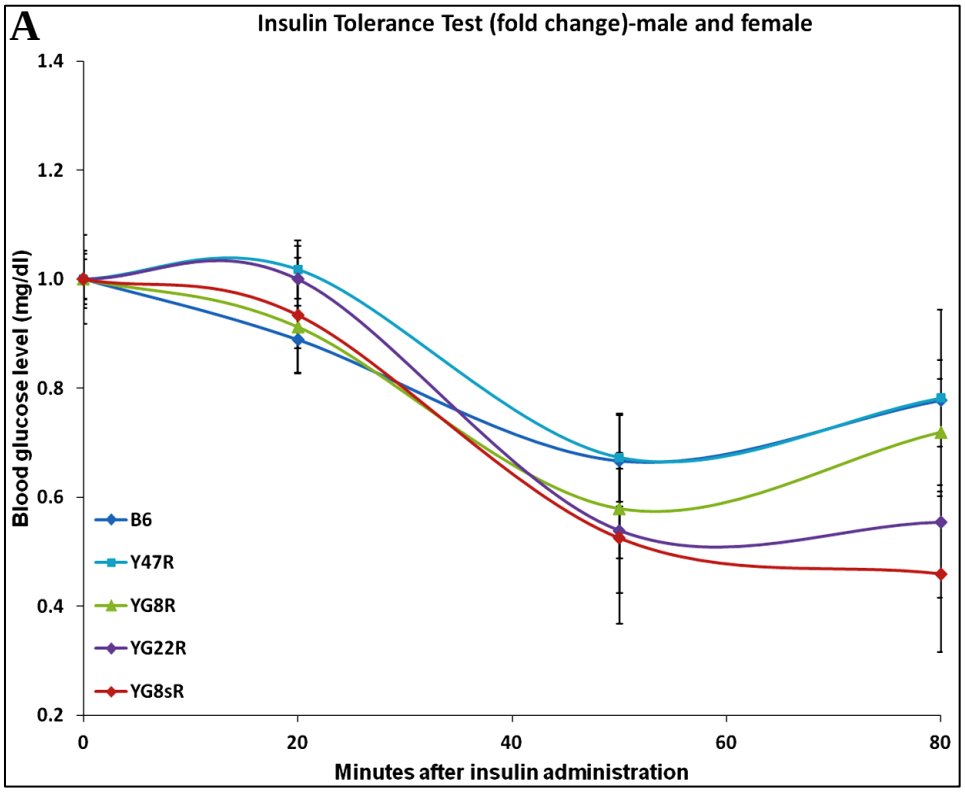

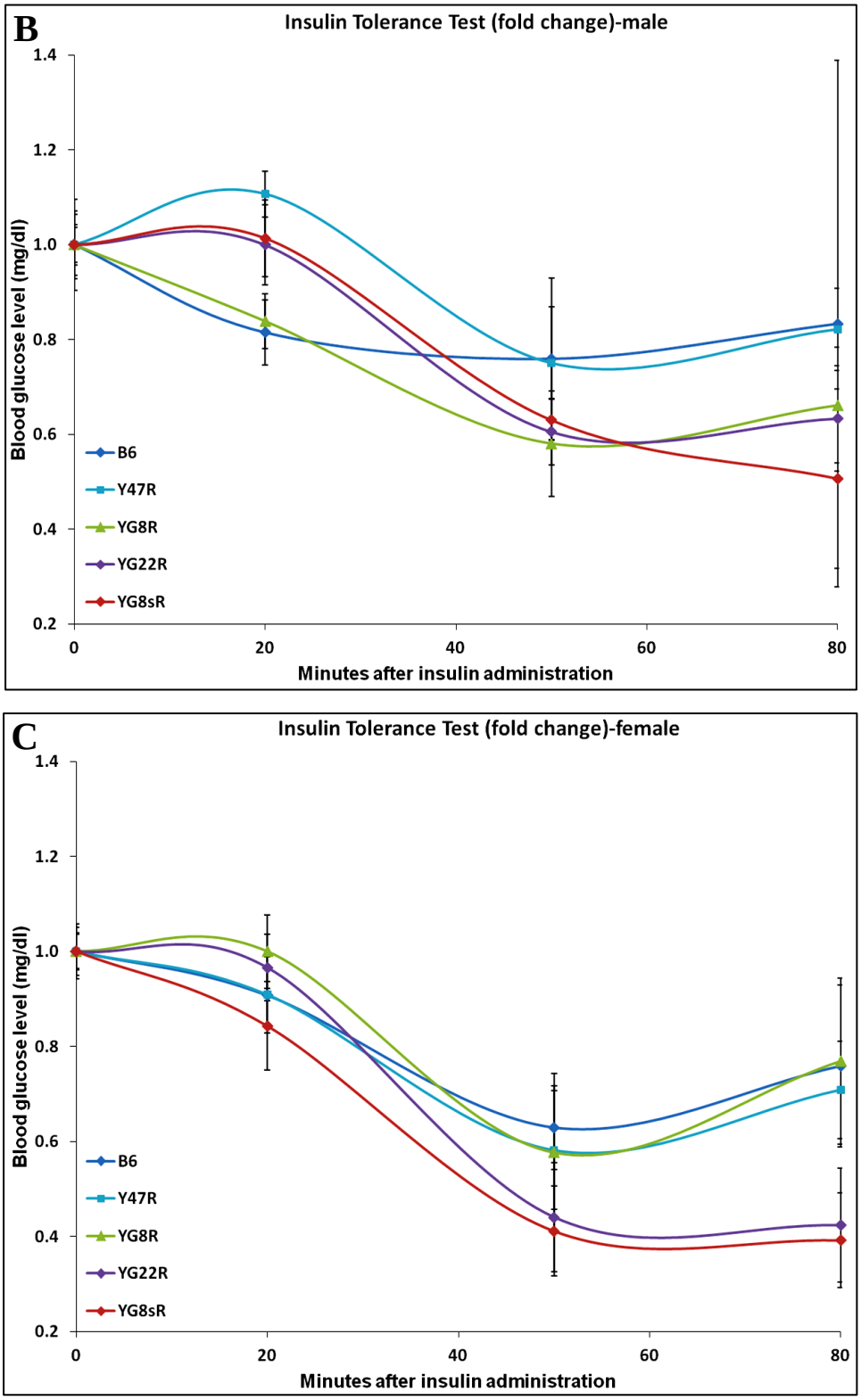

Fig. S.6 Fold change analysis of insulin tolerance test in mice. **A)** YG8R, YG22R and YG8sR mice showed lower blood glucose level after insulin injection compared to B6 and Y47R controls when both male and female values were taken together. A similar tendency was observed when **B)** males and **C)** females were considered alone, except YG8R female mice that showed a similar response as controls. Error bars indicate SEM and values represent mean ± SEM.